

Computational Engineering of PET-degrading Enzymes

Inaugural Dissertation
by

Anna Jäckering

from
Nordhorn, Germany

for the attainment of the title of doctor
in the Faculty of Mathematics and Natural Sciences
at
Heinrich-Heine-Universität Düsseldorf

Frechen, April 2024

Supervisor:
Prof. Dr. Birgit Strodel

From the Institute for Biological Information Processing: Structural Biochemistry (IBI-7) at the Forschungszentrum Jülich

Published by permission of the
Faculty of Mathematics and Natural Sciences at
Heinrich-Heine-Universität Düsseldorf

1. Reviewer: Prof. Dr. Birgit Strodel
2. Reviewer: Prof. Dr. Holger Gohlke

Date of the oral examination: 17th of June, 2024

Selbstständigkeitserklärung / Declaration of Authorship

Hiermit erkläre ich, Anna Jäckering, dass ich die vorliegende Arbeit mit dem Titel
„*Computational Engineering of PET-degrading Enzymes*“
selbstständig verfasst und keine anderen als die angegebenen Quellen benutzt habe. Die Stellen der Arbeit sowie eventuell beigefügte Zeichnungen, Skizzen, graphische Darstellungen oder Daten, die anderen Werken entnommen oder an diese angelehnt sind, habe ich unter Angabe der Quelle als Entlehnung kenntlich gemacht.

I, Anna Jäckering, hereby declare that I have authored the thesis entitled
“*Computational Engineering of PET-degrading Enzymes*”.
No other person’s work has been used without due acknowledgement in this thesis. Where I have quoted from or adapted the work of others, the source is always given. This includes the sources of graphs and data.

Düsseldorf, _____ _____

Anna Jäckering

Contents

Acknowledgements vii

Abstract ix

Publications xi

List of Abbreviations xvi

List of Figures xviii

List of Tables xviii

1 Introduction 1

1.1 Plastics: Boon or Bane? 1

1.2 Enzymes in Industry: Opportunities and Challenges for the Circular Economy of PET 4

1.3 The Power of Computational Enzyme Engineering to Improve PET-degrading Enzymes 7

1.4 LCC and PES-H1 14

1.5 Motivation and Problem Statement 16

2 Methods 17

2.1 Molecular Dynamics Simulation 18

2.1.1 Numerical Integration of the Equation of Motion 20

2.1.2 Force Field 22

2.2 Enhanced Sampling 26

2.2.1 Hamiltonian Replica Exchange MD Simulation 27

2.2.2 Umbrella Sampling MD Simulation 30

2.3 Quantum Mechanical / Molecular Mechanical Simulations 32

2.3.1 QM Method 34

2.3.2 Adaptive String Method 36

3 Interactions and Binding Poses of PET in the Active Site of PES-H1 39

3.1 Résumé of Publication I 40

3.2 Conclusion of Publication I 42

4 From PET Adsorption to Productive Binding **43**
4.1 PET Adsorption to the Enzyme's Surface 44
4.1.1 Résumé of publication II, Section 2.1 45
4.1.2 Conclusion of publication II, Section 2.1 49
4.2 PET's entry to the binding site 50
4.2.1 Résumé of publication II, Section 2.2 51
4.2.2 Conclusion of publication II, Section 2.2 56

5 Acylation of PET **59**
5.1 Résumé of manuscript I 60
5.2 Conclusion of manuscript I 65

6 Conclusion **67**

Bibliography **71**

A Appendix **93**
A.1 Supplementary Figures 93
A.2 Supplementary Tables 101
A.3 Publication I: Multiple substrate binding mode-guided engineering of a thermophilic PET hydrolase 102
A.4 Publication II: From bulk to binding: Decoding the entry of PET into hydrolase binding pockets. 151
A.5 Manuscript I: Influence of Wobbling Tryptophan and Mutations on PET Degradation Explored by QM/MM Free Energy Calculations. . . 223

Acknowledgement

I would like to take a moment to express my profound gratitude to the individuals and institutions that have made this doctoral journey possible.

First and foremost, my heartfelt appreciation goes to my supervisor, Prof. Birgit Strodel. Beyond her exceptional expertise and guidance, Birgit's unwavering support, understanding of personal challenges, and friendly manner have been a constant source of motivation. Conversations with her have always been enlightening, both academically and personally.

My sincere gratitude extends to Prof. Dr. Holger Gohlke for kindly agreeing to be my second reviewer and providing his valuable time and expertise to thoroughly examine my thesis.

I am deeply grateful to the additional members of my thesis committee, Jun.-Prof. Dr. Jan Meisner, Prof. Dr. Vlada Urlacher and Prof. Dr. Sander Smits, for generously dedicating their time and expertise to discuss my work.

I would additionally like to express my profound appreciation to Prof. Dr. Vlada Urlacher for being my mentor and valuable collaboration partner. Additionally, I would like to acknowledge Alessandra, whose vibrant personality made our collaboration a joy.

The expertise on PET degrading enzymes and the experimental support from our collaborators in Greifswald, including Prof. Uwe Bornscheuer, Dr. Ren Wei, Dr. Mark Doerr, Dr. Lara Pfaff, and Frederike Göttsch, have been indispensable to my research.

Dr. Marc van der Kamp and Dr. Kirill Zinovjev, despite our interactions being primarily virtual, provided invaluable guidance on QM/MM and the ASM method. Your unwavering kindness and support motivated me every time I was feeling overwhelmed when experiencing the hurdles of QM/MM simulations.

My gratitude extends to all my colleagues, who have made this academic journey a memorable one. I would like to point out a few individuals: Hebah, your bright smile and positive personality have brightened each day we've shared in our office and during our conference trips. Lara, a long-time friend, has consistently been a source of inspiration and strength and the one receiving most Discord messages throughout the time to share joy and desperation. Wibke, despite the physical distance, our shared struggles and mutual support have been a pillar of strength. Moritz, your expertise and relaxed attitude have been a constant reassurance. Jennifer, your guidance during my master's thesis and unwavering support during my PhD journey was invaluable. Additionally, I am thankful to Hebah, Lara and Moritz for proofreading my thesis and providing valuable feedback.

I would like to extend my heartfelt thanks to the students who have been instrumental in supporting my work, particularly Tilman, who generously shared his expertise in machine learning, and Miro, who embarked on the machine learning journey with me.

Acknowledgements are also due to the IT and administrative staff at Heinrich-Heine University Düsseldorf and Forschungszentrum Jülich, especially Mrs. Stobbe, Gudrun, both Sabines, both Nicoles, Tugba, and Jolanta, who exhibited patience and support when I was facing bureaucratic challenges, and to Fritz and Volker, who assisted me with hardware and software issues.

Furthermore, I would like to express my gratitude to Jun.-Prof. Dr. Jan Meissner and his group for their warm welcome as office neighbours. I enjoyed the coffee chats with Jan and I am thankful for his support, sharing his expertise on QM calculations.

I extend my sincere thanks to the Deutsche Bundesstiftung Umwelt (DBU) for funding my research, which deepened my commitment to environmental sustainability. Dr. Hans-Christian Schaefer and Sabine Dannhauer provided invaluable mentorship and guidance during this journey. Furthermore, Dr. Schaefer made the DBU seminars in Bad-Bederkesa and Ostritz memorable experiences I really enjoyed.

I gratefully acknowledge the computing time granted through JARA-HPC (project PETaseMD) on the supercomputer JURECA at Forschungszentrum Jülich,[1] the hybrid computer cluster purchased from funding by the Deutsche Forschungsgemeinschaft (DFG, German Research Foundation) project number INST 208/704-1 FUGG, and the Centre for Information and Media Technology at Heinrich Heine University Düsseldorf and the Regional Computing Center of the University of Cologne (RRZK) for providing computing time on the DFG-funded (Funding number: INST 216/512/1FUGG) High Performance Computing (HPC) system CHEOPS. The dedicated staff of the HPC facilities were always supportive and facilitated my research.

Last but certainly not least, heartfelt thanks are owed to my family and friends who have provided unwavering support throughout this journey and patiently listened to my Mimimi's during hard times. To Ben, for the rides to the FZJ that spared me from lonely train station nights during DB disruptions. And to Pierre, who has been a constant source of support through both the highs and lows of this journey.

Abstract

The escalating climate crisis necessitates innovative solutions, among which eco-friendly enzymatic degradation of plastic waste, particularly the widely used polymer Poly(Ethylene Terephthalate) (PET), stands out as a promising avenue. Despite this, the intricate mechanisms of PET hydrolases remain incompletely understood, hindering the development of uniform enzyme engineering strategies to enhance degradation activity on an industrially viable scale. This study seeks to bridge this knowledge gap by exploring the PET binding and conversion mechanisms of PET hydrolases through advanced computational methodologies.

We focused on two thermophilic PET hydrolases, PolyESter Hydrolase I (PES-H1) and Leaf-branch Compost Cutinase (LCC), along with their highly active variants PES-H1 L92F/Q94Y (PES-H1^{FY}) and LCC F243I/D238C/S283C/Y127G (LCC^{ICCG}), with the LCC F243I/Y127G (LCC^{IG}) variant serving as a representative for LCC^{ICCG} in this study. We conducted a comprehensive computational analysis, ranging from substrate adsorption and final productive binding using extensive conventional Molecular Dynamics (MD) simulations and enhanced sampling Hamiltonian Replica Exchange Molecular Dynamics (HREMD) simulations, to the initial stage of catalysed PET degradation, known as acylation, explored via hybrid Molecular Mechanics / Quantum Mechanics (QM/MM) simulations. This effort resulted in the compilation of approximately 55 μs of simulation data, positioning our study as one of the most exhaustive computational examinations of PET hydrolases to date, further validated by experimental assessments.

Our findings emphasised the critical roles of enzyme surface electrostatics and hydrophobicity in PET adsorption. Additionally, a few distal mutations significantly impaired *in vitro* functionality, highlighting the pivotal role of adsorption in PET degradation. We bridged the gap between adsorption and productive PET binding by employing HREMD simulations and Principle Component Analysis to sample and identify previously unexplored entry pathways of PET into the active site, a methodology with potential applications in studying active site entries of other polymers. Our simulations elucidated the crucial role of PET conformational flexibility in overcoming the energy barrier upon entry, and Free Energy Surface analyses facilitated the identification of hindering residues. These insights guided the enhancement of experimentally determined kinetic properties of LCC^{ICCG} and PES-H1^{FY} variants. Furthermore, our QM/MM simulations revealed a concerted conformational shift in the PET benzene ring, changing its interaction with the 'wobbling' tryptophan from T-stacking to face-to-face π-π interactions. Addressing methodological challenges,

our research advocated for incorporating this previously overlooked conformational change and selecting appropriate QM methods to improve the consistency of future QM/MM investigations.

In conclusion, this thesis has significantly advanced our understanding of the atomistic details underlying enzymatic PET degradation, offering novel approaches to investigate the elusive polymer entry pathways into enzyme binding sites. The methodologies and insights derived from this study lay a robust foundation for future holistic research, promoting consistency and facilitating the optimisation of PET hydrolases and potentially other polymer-degrading enzymes. This knowledge transfer holds transformative potential for large-scale industrial applications, paving the way for efficient and environmentally-responsible recycling of plastic waste.

Publications

Publications that are part of the thesis

[I] L. Pfaff, J. Gao, Z Li, A. Jäckering, G. Weber, J. Mican, Y. Chen, W. Dong, X. Han, C. G. Feiler, Y. Ao, C. P. S. Badenhorst, D. Bednar, G. J Palm, M. Lammers, J. Damborsky, B. Strodel, W. Liu, U. T. Bornscheuer, R. Wei: Multiple substrate binding mode-guided engineering of a thermophilic PET hydrolase. *ACS Catal* **12**, 9790-9800 (2022).

[II] A. Jäckering, F. Göttsch, M. Schäffler, M. Doerr, U.T. Bornscheuer, R. Wei and B. Strodel: From bulk to binding: Decoding the entry of PET into hydrolase binding pockets. *bioRxiv*, 2024.04.21.590457 (2024).

Manuscripts that are part of the thesis

[I] A. Jäckering, M. van der Kamp, B. Strodel and K. Zinovjev: Influence of Wobbling Tryptophan and Mutations on PET Degradation Explored by QM/MM Free Energy Calculations. *submitted*

Publications beyond the scope of this thesis

[I] J. Loschwitz, A. Jäckering, M. Keutmann, M. Olagunju, R.J. Eberle, M. A. Coronado, O. O. Olubiyi, and B. Strodel: Novel inhibitors of the main protease of SARS-CoV-2 identified via a molecular dynamics simulation-guided *in vitro* assay. *Bioorg Chem* **111**, 104862 (2021).

[II] J. Loschwitz, A. Jäckering, M. Keutmann, M. Olagunju, O. O. Olubiyi, and B. Strodel: Dataset of AMBER force field parameters of drugs, natural products and steroids for simulations using GROMACS. *Data in Brief* **35**, 106948 (2021).

List of Abbreviations

AE Acyl-Enzyme Intermediate. 12, 13, 36, 61–64, 66, 99

AM1 Austin Model 1. 36, 63

AMBER Assisted Model Building with Energy Refinement. 25, 26

AO Atomic Orbital. 34, 35

ASM Adaptive String Method. 18, 36–38, 60, 63, 65, 67, 99

BHET Bis(2-HydroxyEthyl) Terephthalic acid. 5

CBM Carbohydrate-Binding Domains. 9

Coul Coulomb. 24, 25, 94, 96

CV Collective Variable. 27, 29–32, 36–38, 50, 56, 57, 59–66, 68, 69, 99

DFT Density Functional Theory. 34–36, 60, 62, 63

DFTB3 Density Functional Tight Binding 3. 36, 60, 62, 63, 68

DNA DeoxyriboNucleic Acid. 25, 26

EG Ethylene Glycol. 5, 45

EPS Electrostatic Potential Surface. 15, 46–48, 93

FES Free Energy Surface. ix, 29, 30, 37, 44, 52–56, 68, 69, 95–98

GGA Generalised Gradient Approximation. 35

HEMT 1-(2-HydroxyEthyl) 4-MethylTerephthalate. 11, 40

HF Hartree-Fock. 34–36

HREMD Hamiltonian Replica Exchange Molecular Dynamics. ix, 11, 14, 16, 17, 27–29, 38, 44, 51–53, 56, 61, 67–69

LCC Leaf-branch Compost Cutinase. ix, 4, 6, 7, 9, 10, 14–16, 39, 43–47, 49, 51–54, 56, 59, 60, 63, 65, 67, 68, 94–100

LCC^{ICCG} LCC F243I/D238C/S283C/Y127G. ix, 14, 15, 39, 41–44, 48, 49, 53, 55, 57, 59, 60, 65–69, 94, 101

LCC^{IG} LCC F243I/Y127G. ix, 44, 48, 49, 53–56, 60, 63, 65, 67, 68, 96, 100

LDA Local Density Approximation. 35

LINCS LINear Constraint Solver. 22

LJ Lennard–Jones. 24, 25, 28, 33, 40, 42, 94, 96

MAF Mobile Amorphous Fraction. 5, 6

MBAR Multistate Bennett Acceptance Ratio. 28, 29

MC Michaelis Complex. 13, 36, 37, 59–64, 99

MD Molecular Dynamics. ix, 9–11, 14, 16–20, 22–27, 29, 31, 37, 39, 40, 42–45, 47–49, 51, 52, 67

MEP Molecular Electrostatic Potential. 26

MFEP Minimum Free Energy Path. 37, 38, 60, 62

mGGA meta Generalised Gradient Approximation. 35

MHET Mono(2-HydroxyEthyl) Terephthalic acid. 5, 14, 45

MHETA MHET Analogue. 40

ML Machine Learning. 9

MM Molecular Mechanics. 17, 18, 22, 23, 32–34, 36, 61, 67, 99

MO Molecular Orbital. 34, 35

NMR Nuclear Magnetic Resonance. 26

NMWE Natural Mineral Waters Europe. 2

pbc Periodic Boundary Conditions. 24

PBE Perdew–Burke–Ernzerhof. 63

PC Principle Component. 30, 55–57, 98

PCA Principle Component Analysis. ix, 29, 30, 44, 55–57, 68, 69

PES-H1 PolyESter Hydrolase I. ix, 4, 6, 9, 10, 14–16, 39–47, 49, 51, 53, 54, 56, 57, 59–61, 63–65, 67–69, 94–100

PES-H1^{FY} PES-H1 L92F/Q94Y. ix, 14, 15, 39, 41–44, 48–50, 53–57, 59, 60, 63–69, 94, 96, 97, 100, 101

PET Poly(Ethylene Terephthalate). ix, x, 1–18, 30, 32, 36, 39–57, 59–61, 63–69, 93–100

PETCORE PET COntainer Recycling Europe. 2

PHL7 Polyester Hydrolase Leipzig 7. 39

PME Particle-Mesh Ewald. 25

PMF Potential of Mean Force. xvii, 29, 31, 32, 37, 38, 60, 62–66, 68, 69, 100

pNP *p*-Nitrophenyl Butyrate. 11

PrC Product Complex. 13, 36, 37

PRE Plastic Recyclers Europe. 2

QM Quantum Mechanics. x, 13, 17, 18, 22, 26, 32–34, 36, 59, 60, 63, 66, 68, 69, 99

QM/MM Molecular Mechanics / Quantum Mechanics. ix, x, 11–14, 16, 18, 20, 22, 32, 33, 59, 60, 63, 65–69, 99

RAF Rigid Amorphous Fraction. 5, 6

REMD Replica Exchange Molecular Dynamics. 27, 28

RESP Restrained ElectroStatic Potential. 25, 26

RMSD Root-Mean-Square-Deviation. 40

SEM Standard Error of the Mean. 46

T_g Glass transition Temperature. 5, 6

T_m Melting Temperature. 9, 15

TI Tetrahedral Intermediate. 12, 13

TIP3P Transferable Intermolecular Potential with 3 Points. 26

TIPS Transferable Intermolecular Potential functions. 26

TM Triple Mutant. 48

TPA TerePhthalic Acid. 2, 5, 39, 45

TS Transition State. 36, 64, 66

UI Umbrella Integration. 32, 37, 38

UNESDA UNion of European Soft Drinks Association. 2

US Umbrella Sampling. 37, 38

USMD Umbrella Sampling Molecular Dynamics. 27, 30–32, 37, 38

vdW van–der–Waals. 24, 33

WHAM Weighted Histogram Analysis Method. 32

WT Wild-Type. 4, 5, 7, 39, 48, 53–55, 57, 59–61, 63, 64, 67, 69, 97

$\mathbf{X_C}$ Degree of Crystallinity. 6, 10

List of Figures

1.1 Schematic representation of the different recycling and waste management routes for plastic products. . . . 3
1.2 PET degradation reaction resulting in the products BHET, MHET, TPA and EG. . . . 5
1.3 Comparison of secondary structure and binding cleft composition of type I and II PET hydrolases. . . . 6
1.4 Schematic process of enzymatic plastic degradation. . . . 8
1.5 Exemplary pro-*S* (left) and pro-*R* (right) poses sampled during LCC simulations in this study. . . . 12
1.6 Mechanism of PET-degradation as proposed by Boneta *et al.*. . . . 13
1.7 Comparison of secondary structure and EPS of LCC and PES-H1. . . . 15

2.1 Illustration of the MD cycle. . . . 19
2.2 Bonded and nonbonded interaction terms considered by the force field. 23
2.3 Schematic representation of the principle of replica exchange simulations. . . . 27
2.4 Schematic representation of the principle of PCA. . . . 30
2.5 Schematic 2D PMF profiles highlighting the probability distribution of unbiased vs. biased sampling including harmonic potentials. . . . 31
2.6 Scheme highlighting the separation of the QM and MM regions. . . . 33
2.7 Workflow of the ASM schematically shown on a 2D-FES. . . . 37
2.8 Biasing potentials and sampled ensemble for the original string method and the ASM. . . . 38

3.1 Representative binding pose of the most prominent cluster for the productive binding of a PET analogue in the active site of PES-H1. . . . 41

4.1 Representative starting structure for the MD simulations of enzyme adsorption on amorphous PET. . . . 45
4.2 Analysis of LCC and PES-H1 adsorption on amorphous PET. . . . 46
4.3 Results for the *in silico* mutation of surface residues. . . . 48
4.4 Setup for HREMD simulations and PET entry results. . . . 52
4.5 FESs of the intermolecular PET–residue interactions over the SER–C distance. . . . 54
4.6 The three preferred entry pathways of a PET-5mer. . . . 56

5.1 Dihedral angle and the angle between the 'wobbling' tryptophan and PET ring planes. 61
5.2 Comparison of simulations with or without the dihedral CV. 62
5.3 PMFs and CV progression of PES-H1 and PES-H1^{FY}. 64
5.4 PMFs and CV progression of LCC and LCC^{IG}. 65

A1 EPS of an amorphous PET bulk. 93
A2 PET film weight loss of the original and variants of LCC^{ICCG} and PES-H1^{FY}. 94
A3 Examples of intramolecular PET–PET interactions. 94
A4 Free energy surfaces of PET–PET interactions over the SER–C distance. 95
A5 Mutation sites of variants addressed using FES. 96
A6 Examples of intermolecular PET–residue interactions. 96
A7 FESs of PET–residue interactions over the SER–C distance. 97
A8 FESs of PET–residue interactions at position 68 of PES-H1^{FY} variants over the SER–C distance. 97
A9 FESs over PC1 and PC2 and the contribution profile of amino acid positions to PC1. 98
A10 Comparison of the PET conformations after thorough relaxation with the input structures for PES-H1. 99
A11 QM region and CVs employed in this study 99
A12 Uncorrected PMFs of the final acylation simulations. 100

List of Tables

A1 Kinetic parameters obtained from conventional and inverse Michaelis–Menten approaches. 101

Master has presented Dobby with clothes.
Dobby is . . . free.
— Harry Potter and the Chamber of Secrets

1 Introduction

1.1 Plastics: Boon or Bane?

In our contemporary lives, it is challenging to imagine a day without products made from synthetic organic polymers, commonly referred to as plastics, although these materials have only been in production for approximately seven decades [2]. Since then, the global demand for plastics has skyrocketed, reaching a production of 390.7 million metric tonnes (mt) in 2021 [3]. But what drives our strong preference for plastic materials?

Beyond their cost-effectiveness, plastics offer valuable physical and chemical properties, including lightweight construction, adaptability in shaping, flexibility, and impressive durability due to their robustness and chemical inertness [4]. With these characteristics, plastic materials play a pivotal role in numerous industrial applications, notably in packaging, which accounts for 44% of global production, as well as in the building and construction sector, making up 18% of global production [3]. However, alongside the vast opportunities they offer, plastics also carry substantial risks that have garnered increased public scrutiny. In the ensuing discussion, I will delve into these risks, with particular attention directed towards Poly(Ethylene Terephthalate) (PET), which is one of the most common plastic materials and is central to this thesis project.

Littering Perhaps the most widely debated issue associated with plastics is littering, a problem that captures public attention through powerful imagery in the media. Plastic waste disperses across oceans and land, persisting for centuries and posing a threat to biodiversity due to plastics' inherent durability, which inhibits biodegradation [5, 6]. However, plastics, especially oxo-degradable plastics, undergo decomposition through processes like photodegradation, resulting in the formation of small microplastic fragments. These fragments can serve as carriers of toxins due to their high capacity to absorb organic compounds. Furthermore, they accumulate in the environment and within the gastrointestinal tracts of organisms, causing ecological concerns [7, 8]. The significant volume of plastic waste polluting our environment is, to a large extent, attributed to the high production rate of single-use products [9]. Notably, the packaging sector contributes significantly to our plastic footprint, accounting for up to 27.9% in the EU in 2014 [10]. Consequently, the EU has introduced new regulations aimed at curbing the production of single-use plastic products and, as of the 3rd of July 2021, has imposed a complete ban on the manufacturing of oxo-degradable plastics in an effort to combat plastic packaging waste and mitigate littering [11]. One of the primary plastics utilised in this sector is PET, notably renowned for its application in the production of bottles for water and soft drinks [12].

Virgin Plastic vs. Recyclates Virgin plastic primarily relies on fossil fuels, a non-renewable resource that could be depleted within the next 35 years. Its production involves high energy consumption and leads to substantial greenhouse gas emissions [13, 14]. In a bid to reduce plastic waste and address the extensive production of virgin plastic, regulations from the EU compel plastic bottle manufacturers to incorporate 25% and 30% recycled plastic material by 2025 and 2030, respectively [11]. According to a recent report by EUNOMIA for organisations including Plastic Recyclers Europe (PRE), PET COntainer Recycling Europe (PETCORE), Natural Mineral Waters Europe (NMWE), and UNion of European Soft Drinks Association (UNESDA), approximately 2.4 mt out of the 5.1 mt of produced PET were recycled in the EU27+3 in 2020, with Germany alone accounting for 21% of this figure [15]. However, in 2021, only 8.3% of global plastic production involved post-consumer recycled plastics. The disparity between supply and demand, coupled with the need for sophisticated recycling techniques, has driven up the price of recyclates [3, 16].

Waste Management Techniques Plastic waste does not only accumulate after reaching the market, but may already arise during industrial manufacturing. This pre-consumer waste may be directly recovered and reprocessed, termed *primary recycling*, whereas post-consumer waste needs to be collected and most often pre-processed before being submitted to degradation, which is further explained in the next paragraph [17]. The pre-processed waste can undergo secondary recycling, such as mechanical recycling, which involves processing polymeric waste to granules of lower molecular weight. This technique is cost-efficient and applicable at scale [18]. However, mechanical recycling is not suitable for materials like thermosets and elastomers due to their crosslinked structures. Impurities can also degrade the recyclate's quality by causing polymer scission, branching, and cross-linking. While measures like adding radical quenchers or using solid-state polymerisation can help mitigate quality loss, mechanical recycling has limitations, including a restricted number of reprocessing cycles and high processing temperatures, making it less eco-friendly [19–22]. In addition to mechanical recycling, tertiary or chemical recycling allows for polymer-to-monomer degradation. This includes methods like glycolysis, methanolysis, and hydrolysis to yield monomers and oligomers, enabling the production of high-quality polymers [23–26]. Unlike secondary recycling, tertiary recycling's monomeric compounds enable the production of high-quality polymers. However, it is important to note that efficient, cost-effective, and large-scale chemical recycling methods are currently limited to a few polymers. Full depolymerisation is time-consuming, requires hazardous compounds, and is accompanied by high energy consumption. Additionally, the purification of degradation products such as TerePhthalic Acid (TPA) is challenging and expensive [27–32].

In cases where mechanical or chemical degradation is not feasible, *quaternary recycling* is applied which involves incinerating plastic waste for energy recovery, emitting CO_2 and hazardous substances like dioxins and polycyclic aromatic hydrocarbons [33, 34].

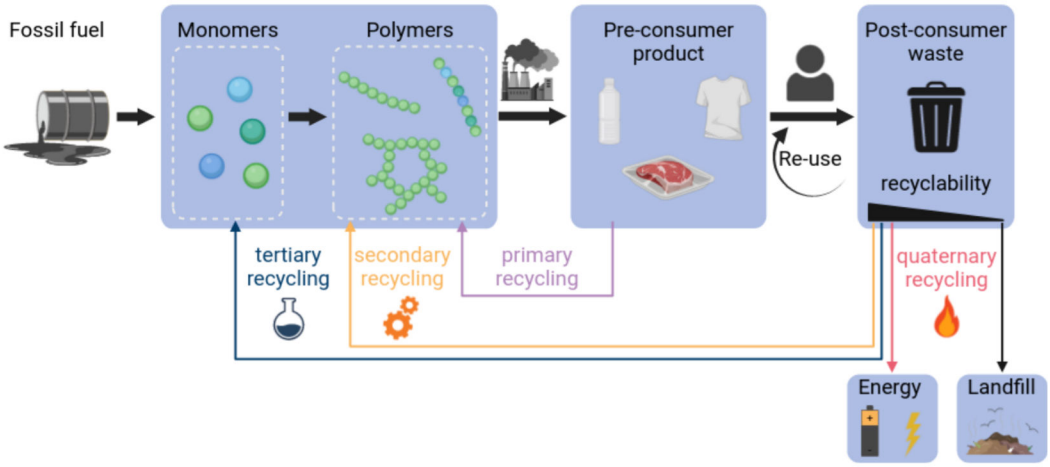


Fig. 1.1.: Schematic representation of the different recycling and waste management routes for plastic products. Created with BioRender.com.

The least environmentally friendly waste management option is *landfilling*, releasing CO_2, methane, and microplastics into the environment [35, 36]. From all these degradation methods, only the primary, secondary, or tertiary recycling routes allow for the desired material recovery.

Recycling Routes Recyclate quality determines its suitability for *open-loop* or *closed-loop* manufacturing of new products [37] (Fig. 1.1). In closed-loop recycling, the original product's properties are preserved during recycling, allowing for the same product type to be made from recyclate instead of virgin polymers. Closed-loop recycling of food packaging, particularly in mechanical recycling, remains challenging due to material exposure to hazardous substances and contaminants, preventing recyclate from reaching food-grade quality [38]. Semi-closed-loop systems often blend recycled PET with high-quality virgin plastic, e.g., 70/30 virgin to recyclate ratio for PET bottles [19, 39–41]. If the properties of recyclate change, open-loop recycling occurs, which includes *downcycling*, where the product's value decreases, and *upcycling*, yielding value-added products. For example, PET bottle recyclate in open-loop can become textiles or concrete reinforcement [42–44]. PET recyclate can also be upcycled into valuable products like carbon fibers, fuels, or vanillin [45–48].

However, not all collected plastic waste is suitable for recycling. it is crucial to avoid contamination by additives and different polymer types, especially hardly recyclable ones such as thermosets, to ensure processing to high-quality recyclate [49, 50]. For recyclable post-consumer plastic waste, separate collection, such as in the case of PET bottles, provides a sorted plastic waste feedstock allowing for production of high quality recyclate, though this is not always feasible [51]. Mixed waste is sorted by polymer type and cleaned from contaminants based on various methods, including sieves, optical recognition cameras, and washing with detergents [52–57]. In the EU27+3 in 2020, only 1% of the 7.9 mt of collected mixed waste was recycled, with 62% undergoing energy recovery and 37% disposed in landfills. In contrast, 80% of separately collected waste was recycled, 18% used for energy

recovery, and only 2% ended up in landfills [3]. Of the 2.4 mt PET waste recycled, approximately 71% was recovered as recyclate according to EUNOMIA [15]. These statistics highlight the inefficiency and environmental concerns associated with current recycling techniques, emphasising the need for alternative, eco-friendly methods such as enzymes for large-scale plastic waste recycling [58].

1.2 Enzymes in Industry: Opportunities and Challenges for the Circular Economy of PET

Enzymes have emerged as essential biocatalysts in various industrial sectors over the past century, leading to significant advancements in pharmaceuticals, laundry detergents, food processing, and chemical transformations, often referred to as 'green chemistry' [59–64]. One of the pivotal advantages of enzymes lies in their environmental friendliness, contributing to the imperative shift towards a sustainable industry to combat climate change [65–67]. These environmental benefits stem from the enzymes' specificity, often performing one-step, enantioselective processes rapidly, and their ability to function under mild conditions, including lower temperatures, neutral pH, and aqueous systems, often requiring minimal or no additives [68–73]. As a result, enzyme utilisation leads to reduced energy consumption, greenhouse gas emissions, byproduct formation, and overall waste generation, partly due to the biodegradability of the enzymes themselves [74–76]. Additionally, the high purity achieved with enzymes reduces the need for extensive purification steps, simplifies downstream processing, and enhances product quality, ultimately reducing costs when compared to chemical or mechanical processes in industry [77–79]. Given the challenges outlined in the previous section regarding plastic degradation, involving waste mixtures, high energy consumption, and the presence of hazardous compounds or byproducts resulting in low-quality recyclate, enzymes indeed appear to offer a promising solution. However, it is important to note that certain limitations currently restrict the widespread application of enzymes. The following section provides an overview over these limitations, focusing on enzymatic PET degradation and the two model enzymes under study, Leaf-branch Compost Cutinase (LCC) and PolyESter Hydrolase I (PES-H1).

Substrate Specificity Enzymes, while adept at degrading mixtures, pose a challenge when targeting non-natural substrates. Naturally derived enzymes typically process naturally occurring compounds [80]. Plastics, being synthetic human-made polymers absent in nature, may not be readily recognised by Wild-Type (WT) enzymes [81]. Nevertheless, nature hosts polyesters like cutin, resembling the polymer PET closely enough to be susceptible to degradation by various cutinases, including LCC and the *Thermobifida fusca* cutinase, which was the first PET-degrading enzyme described by Müller *et al.* in 2005 [82–84].

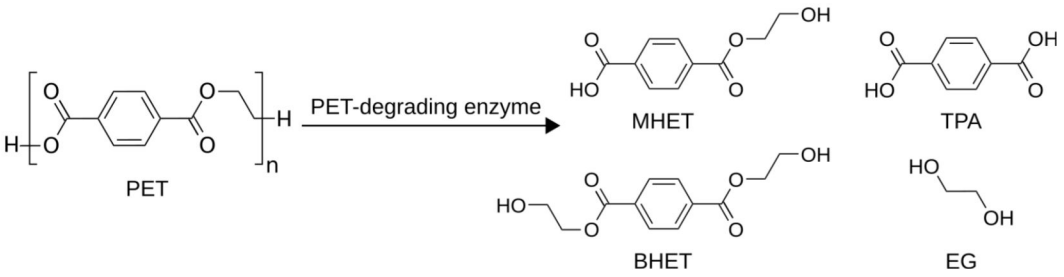


Fig. 1.2.: PET degradation reaction resulting in the products BHET, MHET, TPA and EG.

In 2016, Yoshida *et al.* made a remarkable discovery concerning *Ideonella sakaiensis* 201-F6, a bacterium demonstrating the ability to metabolise PET utilising a dual-enzyme system consisting of *Is*PETase and MHETase. These two enzymes enable the conversion of PET to Mono(2-HydroxyEthyl) Terephthalic acid (MHET) and Bis(2-HydroxyEthyl) Terephthalic acid (BHET) and the monomers TPA and Ethylene Glycol (EG), thereby pioneering the innovative enzyme class of polyester hydrolases (Fig. 1.2) [85]. Enzymes classified as polyester hydrolases feature a designated α/β-hydrolase fold, characterised by an α/β-sheet core consisting of eight β-strands and six α-helices with a surface-exposed catalytic triad typically composed of serine, aspartate, and histidine, enabling the hydrolysis of PET (Fig. 1.3) [86, 87]. Polyester hydrolases are suggested to contain two subsites following the catalytic triad, each binding one PET unit [88, 89]. For polyester hydrolases of type I, the catalytic serine lies within a GHSXG-motif, subsite II contains a phenylalanine and the extended loop following subsite II is missing [89]. In contrast, type II polyester hydrolases comprise a GWSXG-motif and an extended loop, which is stabilised by a second disulfide bridge absent in type I and connecting this loop to a neighbouring β-strand, while subsite II contains either phenylalanine or tyrosine (IIa) or a serine (IIb) at the corresponding position of the phenylalanine of type I polyester hydrolases (Fig. 1.3).

Catalytic Efficiency WT enzymes usually exhibit exceptionally high reaction rates, surpassing those of chemical reactions in solution by a significant margin [90]. However, this remarkable efficiency typically applies to their natural substrates, finely tuned over centuries of evolution, and may not extend to non-natural substrates [91]. For enzymes to become economically viable and widely applicable, their turnover rates must compete with conventional industrial methods. Unfortunately, this is not yet the case for PET biodegradation when compared to mechanical or chemical degradation [92, 93]. PET is a semi-crystalline thermoplastic, with linear polymer strands forming both amorphous and crystalline regions. These regions affect PET's thermal liquefaction, with the amorphous regions being either mobile (Mobile Amorphous Fraction (MAF), mostly *gauche*) or rigid (Rigid Amorphous Fraction (RAF) mostly *trans*), and the crystalline regions (mostly *trans*) having a melting point below the decomposition temperature [94–97]. Moreover, the mobility of the PET chains is temperature-dependent, transitioning from rigidity below the Glass transition Temperature (T_g) to flexibility above it.

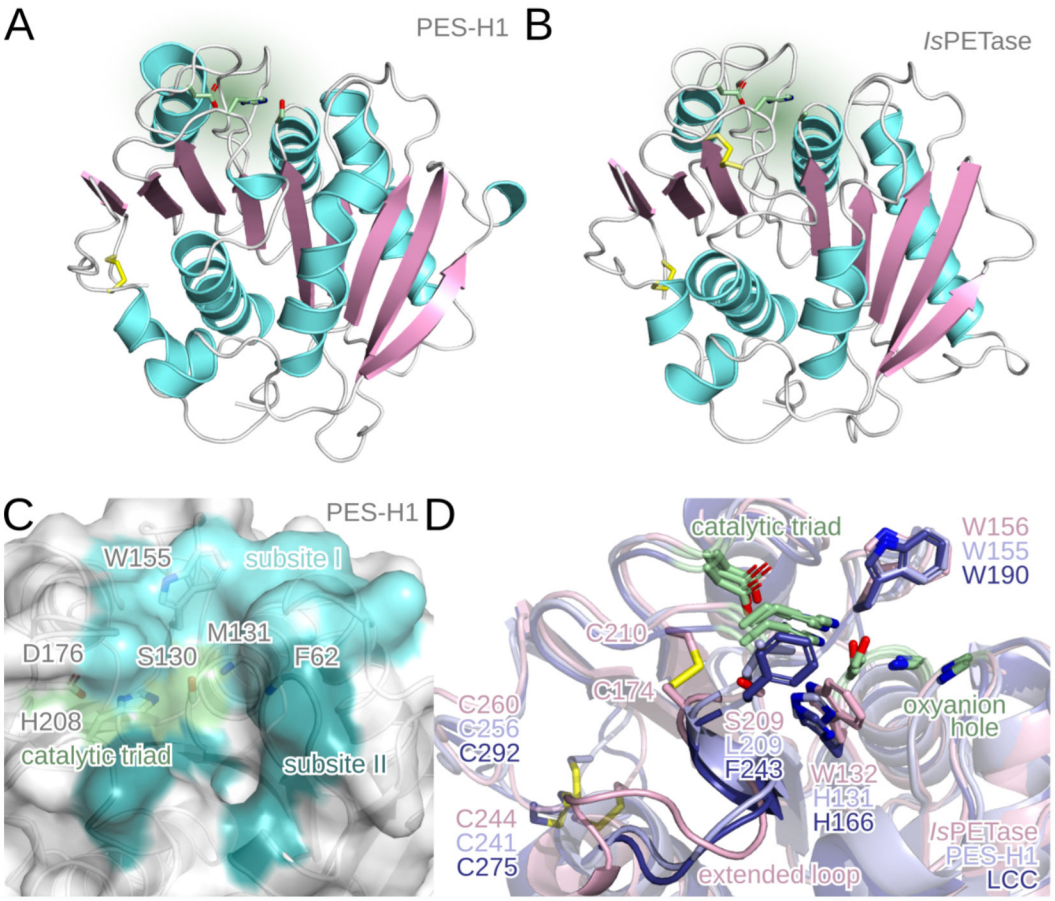


Fig. 1.3.: Comparison of secondary structure and binding cleft composition of type I and II PET hydrolases. The secondary structure is highlighted for type I polyester hydrolase PES-H1 (A) and type II polyester hydrolase *Is*PETase (B), showcasing the α/β-hydrolase fold with α-helices depicted in aquamarine, β-sheets in pink, the disulfide bridges in yellow and the catalytic triad in green. A magnified view of the active site of PES-H1 is provided in surface representation, featuring the catalytic triad residues (S130, D176, H208), the oxyanion hole (M131, F62), and the 'wobbling' tryptophan (W155) highlighted as sticks (C). The surface representation shows the catalytic triad in green, subsite I in aquamarine, and subsite II in teal, respectively. The secondary structures of thermophilic type I polyester hydrolases PES-H1 (light blue) and LCC (dark blue) are compared to the mesophilic type II polyester hydrolase *Is*PETase (pink) (D). Disulfide bridges are emphasised, with type II hydrolases containing an additional one to stabilise the extended loop. Notably, two residues vary between type I and type II hydrolases, represented as sticks: One residue of subsite II, which is either a phenylalanine (type I, IIa, LCC), a tyrosine (type IIa), or a serine (IIb, *Is*PETase). Additionally, either a GHSXG motif (type I) or a GWSXG motif (type II) defines the vicinity of the catalytic serine.

The T_g differs between the regions (MAF, RAF, crystalline) and between the PET bulk and the PET surface due to the plasticization effect of water [98–101] Increased flexibility grants better access to ester bonds, thereby enhancing enzymatic turnover [102]. Conversely, increased polymer mobility enables recrystallisation – a process known as physical ageing –, and higher Degree of Crystallinity (X_C) impedes access, diminishing turnover [101, 103, 104]. This so-called physical ageing process starts

at temperatures above 72°C for amorphous PET in aqueous environment [105]. Hence, the need for highly efficient enzymes capable of outperforming the competing physical ageing process is crucial [99, 100].

Stability Substrate specificity is not the only double-edged aspect; the preference for mild conditions also carries both advantages and disadvantages. Industrial processes often demand elevated temperatures, far from neutral pH, or solvation in hydrophobic environments such as organic solvents to achieve high conversion rates and facilitate product extraction [106–109]. Despite some enzymes originating from extremophiles, capable of enduring extreme conditions, most enzymes tend to denature under industrial operating conditions, resulting in a loss of activity and rendering them less applicable [110–112]. In the case of PET, optimal results are expected at 68-72°C, where the mobility of PET and, thus, its accessibility increases [98, 101, 105, 113, 114]. This preference excludes WT mesophilic enzymes, which remain stable at 15-45°C, in favour of thermophilic enzymes, which exhibit stability within the 45-80°C range [115]. To this end, enabling an elevated thermostability arose as a promising engineering strategy for PET-degrading enzymes.

Despite the promise that enzymes hold for environmentally friendly PET degradation, their industrial application for a circular economy of PET faces significant economic and operational challenges [116]. In September 2021, the French company CARBIOS launched the first enzymatic PET recycling demonstration plant, with a pre-industrial scale capable of treating 100 t of PET waste annually, paving the way for further expansion [117]. However, achieving the necessary specificity, activity, and stability for this pre-industrial application required advanced enzyme engineering techniques, resulting in the enhanced LCC variant ICCG (F243I/D238C/S283C/Y127G) [105].

1.3 The Power of Computational Enzyme Engineering to Improve PET-degrading Enzymes

Despite the discovery of numerous PET-degrading enzymes, their limited activity and stability preclude their industrial application [99, 118]. Enzyme design is a widely adopted approach to tailor the properties of enzymes to the specific target process, thereby rendering them efficiently deployable [119]. In the case of PET-degrading enzymes, the thermostability could be successfully enhanced to enable enzyme operation at a temperature optimal for PET degradation, which is approximately 68-72°C [98, 101, 105, 113, 114]. Increasing the catalytic efficiency of PET degrading enzymes is also of utmost importance, notably to counteract the heightened PET crystallisation rate at elevated temperatures. However, despite being able to engineer variants with increased activity, reaching an industrial applicable activity still constitutes a major challenge [120, 121]. The mechanism of action

and, consequently, the activity of PET-degrading enzymes encompass the following processes which are subject of engineering approaches (Fig. 1.4):

1. Adsorption of the enzyme onto PET.
2. Binding of PET within the enzyme's active site.
3. Catalysis of PET hydrolysis.
4. Release of the products.

The following sections will present enzyme design approaches and achievements relevant for PET-degrading enzymes including thermostability and the four steps defining an enzyme's activity, with a particular emphasis on the contribution of computer-assisted methods.

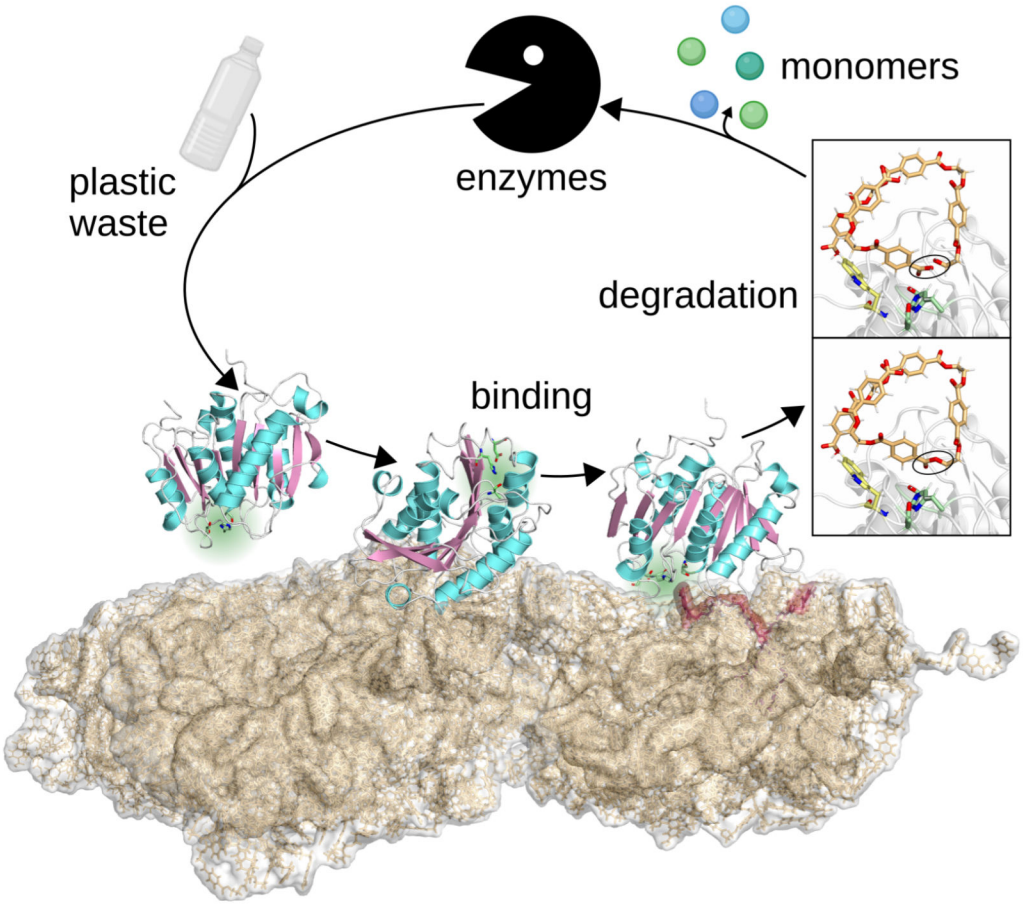


Fig. 1.4.: Schematic process of enzymatic plastic degradation. The enzyme binds the plastic polymers in orange at the active site highlighted in green. The ester bonds are hydrolysed so that monomers can be retrieved. After isolating the monomers and enzymes, the enzyme can be reused in another cycle to degrade more plastic waste.

Thermostability The thermostability of enzymes often increases in the presence of stabilising additives, such as divalent cations like Ca^{2+} or Mg^{2+} [82, 122]. These cations coordinate at specific binding sites, leading to conformational changes and the stabilisation of previously flexible regions [123, 124], resulting in an increase in the Melting Temperature (T_m). For instance, in *Thermobifida fusca* esterases, T_m increased by 10.8–14.1°C upon addition of Ca^{2+} or Mg^{2+} cations [125]. Mutations in the binding sites can stabilise enzymes independently of divalent cations. In the same study by Then *et al.*, Molecular Dynamics (MD) simulations identified binding sites for divalent cations, enabling the introduction of stabilising mutations to arginine, raising T_m even without divalent cations [125]. A stronger stabilising effect was achieved by introducing covalent disulfide bridges, elevating the T_m of TfCut2 (*T. fusca* Cutinase 2) to 92.8°C [126]. Disulfide bridges have frequently been employed for successful stabilisation of PET-degrading enzymes, resulting in T_m increases of 20–30°C [127–129]. The T_m of LCC was raised from 84.7 to 94.5°C through the D238C and S283C disulfide bridge mutations [105], and the T_m of PES-H1 increased from 84.9 to 91.3°C [130], making them, alongside TfCut2, the PET-degrading enzymes with the highest T_m. In addition to stabilising divalent cation binding sites, an increase in general intramolecular interactions, especially in flexible regions, can result in enhanced thermostability. This includes substitutions with rigid amino acids like proline or hydrophobic amino acids, which increase hydrophobic intramolecular interactions of β-sheets [122, 131–133].

Apart from rational enzyme design based on current knowledge, modern methods can generate variants with increased thermostability without such prior knowledge. An example is directed evolution, for which the Nobel Prize was awarded to Frances Arnold in 2018 [134–136]. Its application led to one of the most thermostable *Is*PETase variant, HotPETase, with a T_m of 82.5°C [137]. Additionally, Cui *et al.*, using the computer-assisted greedy accumulated strategy for protein engineering (GRAPE), generated another *Is*PETase variant with increased thermostability, DuraPETase [138]. Lu *et al.* employed protein structure-based Machine Learning (ML) to create FAST-PETase [139]. In another study, along with structural data, additional information from the system's dynamics obtained from MD trajectories was provided to ML algorithms, enabling the prediction of TfCut2 variants with enhanced thermostability [140].

Adsorption of Enzymes onto PET To initiate the desired reaction, the first step involves the binding of PET to the enzyme. In the case of PET-degrading enzymes, no explicit PET recognition site has been identified so far. Instead, the results suggest adsorption based on general surface interactions, which is why modifications of surface characteristics or fusion to binding domains has been attempted to enhance adsorption [141]. For example, Carbohydrate-Binding Domains (CBM)s, known for efficiently binding polymers like synthetic plastics [142, 143], have been fused terminally with PET-degrading enzymes [144–147]. Furthermore, fusion with hydrophobins or their addition as free molecules has improved adsorption as they

create an amphipathic phase between hydrophobic regions like the PET surface and hydrophilic areas like enzyme surfaces [148–152]. Surfactants serve a similar function, with their hydrophobic part binding to PET, while the charged part mediates contact with the enzyme. The charge of the surfactant matches the surface electrostatics of the target enzyme, with anionic surfactants mediating the adsorption of positively charged *Is*PETase [153] and cationic surfactants facilitating that of negatively charged TfCut2 [154]. Additionally, precise orientation of the active site towards PET can be achieved when areas near it bear the opposite charge to the surfactants used, contributing significantly to enzyme activity [153]. The surface properties also influence direct PET contact, but this effect appears highly individual. Nakamura *et al.* increased adsorption through a more positive PET2 surface [155]. Sagong *et al.* revealed a positive effect by introducing negative charges in surface regions away from the catalytic centre, although substitutions with negatively charged amino acids near the catalytic centre resulted in reduced activity [156]. Thomsen *et al.* observed the formation of craters at the PET surface upon PES-H1 and suggested the low affinity of PES-H1 towards PET with high X_C and the negative surface charge opposite to the binding site of PES-H1 to be responsible [157]. They assume that a repulsion of the negative enzyme surface at the distal site of PES-H1 and the negatively charged carboxylic termini surrounding the enzyme after hydrolysis limits the mobility of PES-H1 at the PET surface, which results in craters rather than uniform degradation and highlighting the importance of the charge location. Several studies also indicate a positive impact of a more neutral, hydrophobic enzyme surface [122, 123, 158]. MD simulations conducted by our research group have additionally demonstrated the influence of aromatic interactions between PET and tryptophan, as well as the significance of hydrogen bonding with PET esters and the general interplay between polar and hydrophobic interactions [142]. However, enhancing adsorption does not always result in increased activity. Arnling Bååth *et al.* demonstrated that, according to the Sabatier principle, an optimal binding affinity exists, yielding the highest corresponding activity, which in the case of LCC is achieved with lowered affinity due to the presence of cationic surfactants [159]. Furthermore, Thomsen *et al.* stated that unproductive binding on the PET surface impedes formation of productive enzyme-substrate complexes needed for substrate conversion [157]. In summary, more detailed investigations are required to establish consistent principles for the productive adsorption of PET-degrading enzymes onto PET.

Binding of PET in the Enzyme's Active Site Successful substrate binding in a productive pose within the enzyme's active site is crucial for its activity as only then subsequent hydrolysis is ensured. Indicators for productive poses include small distances between the catalytic serine's γ-oxygen and PET's esters carbon, as well as the ester's carbonyl oxygen residing within the oxyanion hole. Therefore, many studies focused on the interaction between PET and amino acids near the active centre. To achieve this, crystal structures of enzymes in complex with PET analogues have been

examined [89, 130, 133, 155, 160–163], along with structures based on docking [88, 105, 162, 164, 165], often followed by short MD simulations [130, 166–170]. One approach highlights the accessibility of the active site for bulky aromatic polyesters like PET [171]. Several studies have substituted sterically demanding amino acids with smaller ones to widen the binding cleft of PET-degrading enzymes, increasing activity due to improved accessibility [164, 172–174]. However, such substitutions might lead to the loss of specific interactions with PET, weakening binding. In one study by Austin *et al.*, narrowing the binding site and introduction of amino acids with stronger PET interactions has led to increased activity [170]. Notably, increased aromaticity [172] and hydrophobicity [174, 175] near the active centre were shown to positively affect the activity.

Apart from general characteristics of the active site promoting PET binding, the precise binding position of PET and the influence of individual amino acids are disputed. Particular importance is attributed to a tryptophan positioned at one end of the catalytic binding cleft, directly adjacent to the catalytic triad. This tryptophan, also known as 'wobbling' tryptophan, is conserved among all PET-degrading enzymes. However, it adopts a different conformation in *Is*PETase compared to other PET-degrading enzymes. This difference is attributed to steric hindrance by a nearby histidine, which in *Is*PETase is replaced by a serine [162, 176]. This conformation allows T-shaped π-π interactions with PET's benzene ring and the tested substrate analogue 1-(2-HydroxyEthyl) 4-MethylTerephthalate (HEMT), expanding the free space within the active site, which favours PET binding, and face-to-face stacking with the tested product analogue and *p*-Nitrophenyl Butyrate (pNP), which might facilitate product liberation [162, 176]. Extensive MD and metadynamics simulations, along with experimental analyses, have demonstrated that the presence of this serine and an adjacent isoleucine in *Is*PETase, instead of histidine and phenylalanine in other PET-degrading enzymes, increases the flexibility of the tryptophan and loop regions within the active site, positively impacting activity [177, 178]. Flexibility of the active site, in general, is believed to be crucial for successful substrate conversion [166, 179]. Joo *et al.*, based on docking studies, postulated an elongated, L-shaped hydrophobic binding cleft with multiple subsites that can simultaneously bind four PET units in defined positions [88]. Other studies also suggested such extended PET binding in the active site, where multiple units are bound simultaneously [167, 168, 170, 180]. However, NMR data and extensive classical MD and Hamiltonian Replica Exchange Molecular Dynamics (HREMD) simulations revealed high flexibility of PET in the active site [167, 180], contrary to the notion of a defined binding position with several simultaneously bound subunits [100, 181]. Two principal binding poses are proposed: the pro-*S* conformation where the benzene ring is adjacent to the ester bond of PET, facing the 'wobbling' tryptophan [162, 168, 181], and the pro-*R* conformation where the benzene ring points in the opposite direction (Fig. 1.5)[105, 166]. Molecular Mechanics / Quantum Mechanics (QM/MM) analyses by Boneta *et al.* as well as Zheng *et al.* detected an energetic preference for catalysis starting

from the pro-*S* pose [182, 183]. These studies demonstrate the importance of computer-assisted methods in making statements about binding positions, dynamics, and the influence of individual amino acids. However, it is crucial to differentiate between comprehensive simulations and less informative docking modelling. The fewer factors are considered in theoretical calculations, the less certain are the results obtained, which in the case of studies solely based on docking can lead to incorrect assumptions about the system.

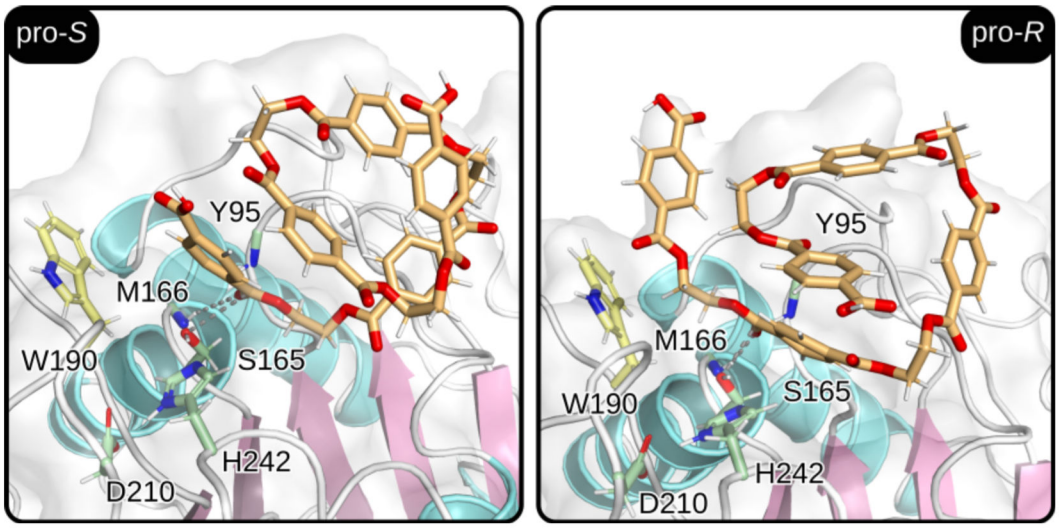


Fig. 1.5.: Exemplary pro-*S* (left) and pro-*R* (right) poses sampled during LCC simulations in this study. The side-chains of the catalytic triad residues (S165, D210, H242) and the backbone-amine of the oxyanion hole residues (Y95, M166) are highlighted as green sticks. The 'wobbling' tryptophan (W190) is shown as yellow sticks and PET in orange. The distance between the PET ester's carbon and the catalytic serine's γ-oxygen, as well as the distances between the PET ester's carbonyl oxygen and the backbone amines of both oxyanion hole residues are displayed as grey dashed lines.

Catalysis of PET Hydrolysis The first computer-assisted studies of PET hydrolysis were published in 2021 and included several QM/MM simulation studies [182, 184, 185], whereas prior to that, only assumptions about the mechanism could be made based on crystal structures and docking [162]. The mechanism can be divided into two processes: acylation and deacylation (Fig. 1.6) [182, 186–189]. In acylation, the nucleophilicity of the catalytic serine is increased by a proton transfer to the catalytic histidine, which is polarised by the catalytic aspartate. This allows the nucleophilic attack on the ester's carbonyl carbon, and the resulting oxyanion of the TI is stabilised by the oxyanion hole. Subsequently, the ester bond is cleaved, yielding the AE and, after a proton transfer from the catalytic histidine to the resulting oxyanion, an alcohol, which is the first product to leave the active site. In deacylation, the oxygen of a water molecule nucleophilically attacks the carbonyl carbon of the AE, resulting in a second TI and the re-protonation of the catalytic histidine. In the final step, the AE bond is broken, yielding the second product with a carboxyl group, and the serine is re-protonated, restoring the initial state.

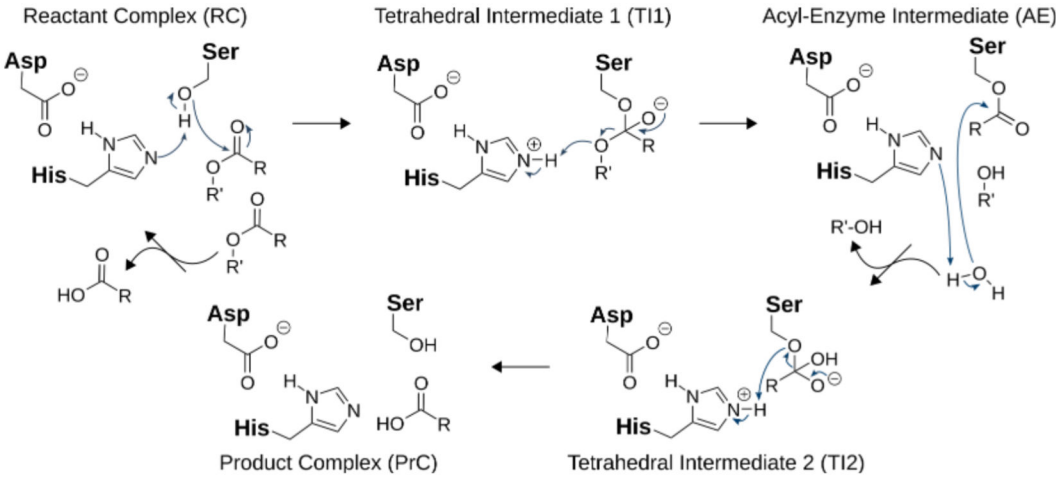


Fig. 1.6.: Mechanism of PET-degradation as proposed by Boneta *et al.* [182]. The mechanism can be divided into two steps: First, the acylation of the Michaelis Complex (MC) yielding the Acyl-Enzyme Intermediate (AE) and second, the hydrolysis yielding the Product Complex (PrC), both incorporating a Tetrahedral Intermediate (TI).

It is disputed whether acylation and deacylation occur in a one- or two-step manner, leaving the TI to be a potential tetrahedral transition state [182, 189]. Instead of pure polarisation of the catalytic histidine by the catalytic aspartate [182, 185], some studies describe a proton transfer to the aspartate [162, 184, 190]. One QM/MM study focuses on three amino acids (SER, ILE, ALA) near the catalytic aspartate, stabilising it and thereby preventing proton transfer [186]. This stabilisation can only be observed when these three amino acids are part of the QM region, highlighting the significance of the choice of the Quantum Mechanics (QM) region [186, 191]. The larger it is, the more accurately the results reflect reality, but the computational cost also increases massively. The importance of the isoleucine's stabilisation was confirmed by mutation to alanine, resulting in activity loss [186]. Furthermore, a dynamic hydrogen bond network has been postulated as an important factor [187, 188]. The rate-determining step could not be consistently identified for the mechanism or any enzyme [188]. Acylation is often described as the rate-determining step, as it was shown to have a higher free activation energy [182, 184, 185], while other identified the deacylation [186, 187, 192] or the product release [190] as the rate-determining step. An analysis of the contribution of surrounding amino acids to the energy barriers suggests negatively charged aspartates near the oxyanion formed during TI as potential mutation sites for substitutions with positively charged amino acids to further stabilise the first TI [185]. Furthermore, such an analysis may be essential to evaluate potential mutation sites, especially since many enzyme design approaches aim to stabilise substrate binding, but they also must stabilise transition states to lower the free activation energy [193, 194]. QM/MM calculations further offer the possibility to determine the preference for specific binding poses, as discussed before [182, 183], and thus to distinguish between exo- and endo-hydrolysis. Exo-hydrolysis describes the cleavage of a terminal ester bond

instead of endo-hydrolysis, where an ester bond within the polymer is cleaved [195]. It is suspected that PET-degrading enzymes mainly mediate endo-hydrolysis, yet evidence of exo-activity has been found [98, 101, 196–198]. This exo-activity is believed to occur mainly after endo-hydrolysis, where the subsequent ester group of the just cleaved polymer is addressed [101, 198]. Such a mechanism aligns with the stepwise degradation proposed in an extensive MD and HREMD study [181].

Product Release After successful hydrolysis, the products must exit the active site to make room for the hydrolysis of the next substrate. This step can be the rate-determining step of a reaction, as suggested by Shrimpton-Phoenix *et al.* based on QM/MM simulations [190]. However, the results of other MD simulations do not suggest an energetic hindrance to the diffusion of products into solution [185]. It is believed that conformational changes of the 'wobbling' tryptophan, as well as conformational changes of the PET benzene ring altering the interactions with the 'wobbling' tryptophan from T-stacked to face-to-face stacking also facilitate product release [162, 176–178]. Even if the product diffuses freely into solution, it can exhibit an inhibitory effect on PET-degrading enzymes which increases with product accumulation as PET depolymerisation progresses [179, 199]. To counteract this product inhibition, the product can be removed from the solution, for example, through ultrafiltration [199] or a two-enzyme system, consisting of a PET-degrading enzyme and, for example, MHETase, which further breaks down the PET degradation products like MHET into monomeric building blocks [116, 200]. Furthermore, enzyme design can be employed to enhance the binding of the PET substrate compared to product binding, thereby mitigating the inhibitory effect, as demonstrated by a glycine-to-alanine mutation within the binding cleft in TfCut2 [201]. A pH-dependent shift in substrate preference was shown in a QM/MM study, which could strengthen the binding to PET over products without enzyme design [192].

The above mentioned achievements highlight the importance of detailed studies investigating and engineering PET-degrading enzymes, which yielded the two up-to-date most active variants: the LCC F243I/D238C/S283C/Y127G (LCC^{ICCG}) and PES-H1 L92F/Q94Y ($PES\text{-}H1^{FY}$).

1.4 LCC and PES-H1

This section provides an introduction of the two target enzymes of the underlying study, LCC and PES-H1. The LCC (PDB: 4EB0[82]) and PES-H1 (PDB: 7CUV[130]) enzymes were derived from compost metagenome libraries in 2014 [82] and 2022 [202], respectively, and assigned to the type I polyester hydrolases. Consequently, both enzymes exhibit a closely resembling α/β-hydrolase fold (RMSD: 1.08 Å) featuring a catalytic SER-ASP-HIS triad (LCC: S165, D210, H242; PES-H1: S130, D176, H208) [202], and encompassing a single disulfide bridge (Fig. 1.7).

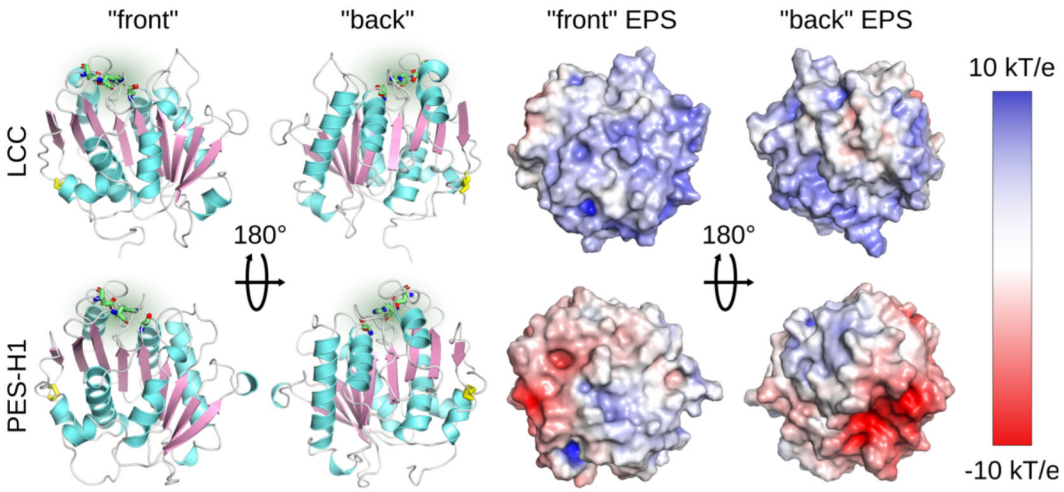


Fig. 1.7.: Comparison of secondary structure and Electrostatic Potential Surface (EPS) of LCC and PES-H1. The α/β-hydrolase fold is depicted by β-sheets in pink and α-helices in aquamarine. The catalytic triad is shown in green and the disulfide bridges in yellow. A negative surface potential is coloured in red and a positive one in blue.

Furthermore, both enzymes harbor the conserved 'wobbling' tryptophan (LCC: W190; PES-H1: W155). Despite structural similarity, there exists a disparity in net charge; LCC bears a positive surface charge of $+5$, while PES-H1 exhibits a negative net charge of -5 (Fig. 1.7). The thermostability of these thermophilic enzymes was enhanced by mutagenesis: Introduction of an additional disulfide bridge at the calcium binding site (D238C and S283C) and two mutations proximal to the active site (I243G and Y127G) elevated the T_m of LCC from 84.7 to 94.5°C in the resultant LCC^{ICCG} variant [105]. For PES-H1, incorporation of two contiguous mutations near the active site (L92F and Q94Y) elevated the T_m from 84.9 to 91.3°C in the PES-H1 L92F/Q94Y ($PES\text{-}H1^{FY}$) variant, albeit introduction of a disulfide bridge at the calcium binding site augmented the T_m while concurrently reducing activity [130]. Notably, a tyrosine residue at an analogous position in both enzymes yields divergent effects despite their structural similarity: Depletion of tyrosine (Y127G) alongside other mutations enhanced LCC activity, whereas an activity enhancement was observed in PES-H1 following introduction of tyrosine at the expense of glutamine at the corresponding position (Q94Y) together with the L92F mutation. Thus, these highly active PET-degrading enzymes pose a formidable challenge in contemporary research on PET-degrading enzymes, necessitating exploration of concepts and attributes among closely related enzymes that uniformly enhance activity, rendering them suitable model enzymes for the present investigation.

1.5 Motivation and Problem Statement

A climate-friendly disposal of our abundant plastic waste is a significant challenge in today's world. The question is: Can we enhance the activity of PET-degrading enzymes to the extent that their industrial application becomes viable for environmentally friendly PET recycling? The activity of PET-degrading enzymes fundamentally depends on the individual steps of the PET degradation mechanism, which are not yet fully understood. A detailed elucidation of the enzymatic PET degradation mechanism will enable targeted, rational enzyme design, with great potential to significantly boost enzyme activity. Particularly, the complete binding pathway of PET, including adsorption, entry into the active centre, and productive binding to enable subsequent hydrolysis, has not been fully clarified. Computer-assisted analyses allow for a precise examination of these processes at the atomic level to identify the involvement of individual amino acids. However, very few detailed simulation studies have been conducted thus far. This study aims to address this research gap through comprehensive MD, HREMD, and QM/MM simulations, contributing to our understanding of enzymatic PET degradation and advancing the design of efficient, eco-friendly, and industrially applicable PET-degrading enzymes. The precise goals of this research project include the elucidation of the following aspects using two model PET-degrading enzymes, LCC and PES-H1:

1. Adsorption of Enzymes onto PET
2. Entrance of PET into the Enzyme's Active Site
3. Binding of PET in the Enzyme's Active Site
4. PET Degradation Mechanism

The company Carbios is currently evaluating their PET-degrading enzyme's industrial applicability, however, the large amount of plastic waste demands for maximally efficient and widely applicable enzymes for diverse types of plastic waste. By providing knowledge about and approaches to analyse single steps of enzymatic PET degradation, which will be transferable to other plastic types, this research constitutes a significant step toward a more sustainable strategy to tackling the plastic waste problem.

2 Methods

Numerous vital biological processes, such as the adsorption of polymers onto enzyme surfaces or the favoured binding sites of ligands, present experimental challenges of no small significance. However, a comprehensive understanding of these processes is of paramount importance in the realm of enzyme engineering. The ever-expanding computational power at our disposal empowers us to probe these phenomena theoretically at the atomic level. This endeavour employs the application of static methodologies, including the visualisation of a crystalline structure alongside a ligand in a binding pose derived from docking, as well as the utilisation of Molecular Dynamics (MD) simulations. MD simulations, a powerful asset in our scientific arsenal, prove to be invaluable for the exploration of dynamic processes, such as the behaviour of enzymes during binding. it is worth noting, however, that these simulations rely on a classical approximation in which atoms are treated as partially charged point charges [203–207]. While this Molecular Mechanics (MM) approximation may not capture the minutiae of binding events and bond breakages, it nevertheless facilitates the evaluation of theoretical predictions through experimental validation, particularly when dealing with large biological systems. These systems pose a significant challenge for exact Quantum Mechanics (QM) treatment due to the persistent limitations in computing capabilities. Consequently, MM MD simulations, hereafter referred to as MD simulations, are employed to investigate the adsorption of Poly(Ethylene Terephthalate) (PET) onto the surface of enzymes capable of PET degradation. This approach sheds light on the entry of PET into the binding site and its subsequent binding behaviour within the active site, all of which are processes fundamentally reliant on non-covalent interactions [208].

Traditional MD simulations offer insight into the dynamic behaviour of a system in a state of thermal equilibrium, where the system explores the local free energy landscape. In theory, given an exceedingly long run time, it is possible to sample the complete free energy landscape [209]. Nevertheless, in practice, this endeavour demands a significant amount of computational time, rendering it unaffordable if substantial energy barriers impede transitions to other regions of the energy landscape. In order to facilitate the exploration of so-called 'rare events', several enhanced sampling methods have been developed, making it possible to overcome energy barriers within a practical time frame. Among these methods, the Hamiltonian Replica Exchange Molecular Dynamics (HREMD) simulation technique [210], as described in Section 2.2.1, is employed to sample the entry of PET into the active site of enzymes responsible for PET degradation. This is necessary due to the assumed presence of an energy barrier that hinders entry, and which cannot be overcome within the simulated duration through conventional MD simulations. Both, conventional and enhanced sampling MD simulations are realised using the software GROMACS [211], complemented with PLUMED [212–215] to facilitate

enhanced sampling.

As previously mentioned, MM MD simulations fall short in their ability to simulate the breaking and formation of chemical bonds. Meanwhile, the substantial computational demands of a QM representation, which would indeed allow such simulations, render it infeasible for large biological systems. However, the imperative need to investigate the details of enzymatic catalysis mechanisms necessitates the adoption of a hybrid approach known as Molecular Mechanics / Quantum Mechanics (QM/MM) MD simulations, hereafter referred to as QM/MM simulations. In this method, only the specific region requiring QM treatment to address the research question is treated quantum mechanically, while the remainder of the system is simulated classically, thereby mitigating computational expenses [216]. To investigate the energy barriers associated with the enzymatic degradation of PET, QM/MM simulations have been conducted in collaboration with Dr. Marc van der Kamp (University of Bristol, GBR) and Dr. Kirill Zinovjev (University of Valencia, ESP). These simulations utilise the Adaptive String Method (ASM) developed by our collaboration partners as described in Section 2.3 [217]. All QM/MM simulations were executed using the AmberTools and Amber software [218], augmented with the incorporation of the ASM code [217].

Our computational efforts and predictions are assessed through *in vitro* investigations conducted in collaboration with the University of Greifswald in Germany. This partnership involves Prof. Dr. Uwe Bornscheuer, Dr. Ren Wei, Dr. Mark Dörr, Dr. Lara Pfaff and Frederike Göttsch. The upcoming sections provide an in-depth explanation of the methodological approaches utilised in this PhD project.

2.1 Molecular Dynamics Simulation

MD simulation is a powerful computational technique that allows us to investigate the dynamic behaviour of molecules at the atomic scale, providing invaluable insights into their structural and thermodynamic properties. The theoretical background for MD simulations explained in this section is based on my master's thesis [219] and extensive literature sources [206, 207, 220–222]. Conducting an MD simulation involves several essential steps (Fig. 2.1):

1. **System Setup:** This phase entails configuring the system, including the biological molecules under investigation, such as proteins. Additionally, it typically comprises the inclusion of water and ions to replicate physiological or experimental conditions and ensure charge neutrality.

2. **Energy Minimisation:** Before performing the MD simulation itself, it is crucial to conduct energy minimisation. This process aims to find a local minimum on the potential energy surface, close to the chosen starting configuration. This is important to avoid artificially high forces at the start of the MD simulation. Techniques like the steepest descent algorithm are employed for this purpose [223]. This algorithm guides all atoms along the energy gradient direction,

continuously minimising the force until a predefined convergence criterion is met [220].

3. **Equilibration:** During this step, the system is supposed to reach a state of equilibrium. This entails the relaxation of solvent molecules and the adjustment of temperature and pressure to the desired values. Notably, the position of the solute is usually restrained during this stage.

4. **Production Run:** The final step involves the actual MD simulation, during which data is sampled to analyse the processes of interest.

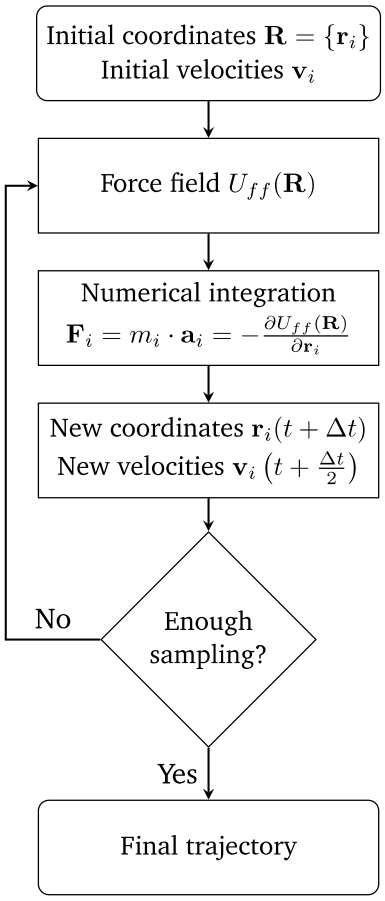


Fig. 2.1.: Illustration of the MD cycle. The MD cycle commences with the utilisation of initial coordinates and velocities to compute the potential energy. This potential energy calculation, in turn, serves as the basis for determining the forces and subsequently numerically integrating Newton's second law. The outcome of this integration process yields updated coordinates and velocities.

The initial coordinates are often derived from sources such as a crystal structures, and initial velocities are assigned based on the equipartition theorem and a desired temperature. Consequently, a Maxwellian velocity distribution is attained after equilibrating the system during which the conditions required to accurately represent the system under study are established. For biological systems, a canonical NVT

(constant number of atoms N, volume V, and temperature T) or an isothermic-isobaric NpT (constant N, pressure p, and T) ensemble are often chosen instead of a microcanonical NVE (constant N, V, and total energy E) ensemble, as they better reflect physiological conditions [206, 207, 220]. Too maintain a fixed temperature and pressure as required to sample NVT and NpT ensembles, thermostat and barostat algorithms are applied, respectively. For equilibration, fast but less accurate algorithms are utilised, such as the velocity-rescaling thermostat [224] or the Berendsen barostat [225], which are applied in this study. Both introduce factors to scale the velocity of the atoms and cell volume and inter-atom vectors to adjust the temperature and pressure, respectively. For the production run, we opt for slower but more accurate algorithms, which are able to accurately represent the canonical and isothermic-isobaric ensembles. Specifically, the Nosé-Hoover thermostat [226, 227] and the Parinello-Rahman barostat [228–230] were employed, which couple the system to an imaginary external heath bath and piston, respectively. For QM/MM simulations using the AMBER software, Langevin dynamics and the Berendsen barostat [225] are used to control the temperature and pressure, respectively, as these are commonly used together with the AMBER software and the before named thermostats and barostats are only available in GROMACS. Langevin dynamics [231] addresses the dynamics of large target molecules in a system of smaller particles such as proteins in water and is able to represent the canonical ensemble [220]. Here, the temperature is adjusted by modifying Newton's second law of motion, $\mathbf{F}_i = m_i\mathbf{a}_i = m_i\dot{\mathbf{v}}_i = \dot{\mathbf{p}}_i$, describing the force $\mathbf{F}_i$ acting on atom i based on the mass m_i and acceleration $\mathbf{a}_i$ or momentum $\mathbf{p}_i$ of atom i, by a friction or damping factor γ and a Gaussian distributed random force f_i mimicking the collisions of the solute with the smaller solvent particles and, thus, a coupling to a heat bath (Eq. 2.1).

$$\dot{\mathbf{p}}_i = \mathbf{F}_i - \gamma_i\mathbf{p}_i + \mathbf{f}_i \tag{2.1}$$

The key stages of the MD cycle, as highlighted in Figure 2.1, are explained in detail in the following sections.

2.1.1 Numerical Integration of the Equation of Motion

Newton's second law of motion is a fundamental component of conducting MD simulations. It enables the calculation of the force $\mathbf{F}_i$ acting on each atom i, which is determined from the potential energy U_{ff} of the system with coordinate vector $\mathbf{R}$ (Eq. 2.2).

$$\mathbf{F}_i = m_i \cdot \mathbf{a}_i = \frac{\mathrm{d}(m_i\mathbf{v}_i)}{\mathrm{d}t} = m_i\frac{\mathrm{d}^2\mathbf{r}_i}{\mathrm{d}t^2} = -\frac{\partial U_{ff}(\mathbf{R})}{\partial \mathbf{r}_i} \tag{2.2}$$

This potential energy is derived from the force field function as discussed in Section 2.1.2. However, to obtain the new positions $\mathbf{r}_i$ and velocities $\mathbf{v}_i$ for each atom i after a specific time step Δt, a numerical integration approach must be employed. In this

process, a set of $3N$ differential equations is solved for a system composed of N atoms. Several algorithms are available for this purpose.

The Verlet algorithm, introduced by Loup Verlet in 1968 [232], relies on a Taylor expansion of the coordinate vector $\mathbf{r}$ at time t, progressing both forwards and backwards by a time step Δt (Eq. 2.5).

$$\mathbf{r}(t+\Delta t) = \mathbf{r}(t) + \mathbf{v}(t)\Delta t + \frac{1}{2}\mathbf{a}(t)\Delta t^2 + \frac{1}{6}\dddot{\mathbf{r}}(t)\Delta t^3 \tag{2.3}$$

$$\mathbf{r}(t-\Delta t) = \mathbf{r}(t) - \mathbf{v}(t)\Delta t + \frac{1}{2}\mathbf{a}(t)\Delta t^2 - \frac{1}{6}\dddot{\mathbf{r}}(t)\Delta t^3 \tag{2.4}$$

$$\mathbf{r}(t+\Delta t) = 2\mathbf{r}(t) - \mathbf{r}(t-\Delta t) + \mathbf{a}(t)\Delta t^2 + \mathcal{O}(\Delta t^4) \tag{2.5}$$

$$\Rightarrow \mathbf{v}(t) \quad = \frac{\mathbf{r}(t+\Delta t) - \mathbf{r}(t-\Delta t)}{2\Delta t} + \mathcal{O}(\Delta t^2) \tag{2.6}$$

This summation allows us to access the new coordinates with an error on the order of $\mathcal{O}(\Delta t^4)$. The velocity is computed based on the new position $\mathbf{r}(t+\Delta t)$, resulting in reduced accuracy to the order of Δt^2. This limitation necessitates the use of short time steps, typically around 1 fs (Eq. 2.6). The velocity at time t is essential for calculating the kinetic energy and temperature T at time t. Consequently, obtaining these parameters is only possible after knowing $\mathbf{r}(t+\Delta t)$, making the application of a thermostat challenging.

The leap-frog algorithm, developed by van Gunsteren and Berendsen in 1988 [233], builds upon the Verlet algorithm to address the limitation of indirect velocity calculation and the consequent challenge of temperature scaling. In this approach, velocities $\mathbf{v}$ are computed at half-integer time steps $t + \frac{\Delta t}{2}$ via a Taylor expansion and are then employed to generate new coordinates $\mathbf{r}$ at full integer time steps $t + \Delta t$ (Eq. 2.7 and 2.8).

$$\mathbf{v}\left(t + \frac{\Delta t}{2}\right) = \mathbf{v}\left(t - \frac{\Delta t}{2}\right) + \Delta t\mathbf{a} + \mathcal{O}(\Delta t^3) \tag{2.7}$$

$$\mathbf{r}(t+\Delta t) \quad = \mathbf{r}(t) + \Delta t\mathbf{v}\left(t + \frac{\Delta t}{2}\right) + \mathcal{O}(\Delta t^4) \tag{2.8}$$

This separation of velocity and position updates has implications; kinetic and potential energy cannot be calculated simultaneously, and consequently, neither can the total energy. However, this algorithm allows for temperature and pressure coupling, all while producing the same trajectories as the Verlet algorithm, which is why it was employed in this study [222].

The velocity Verlet algorithm is similar to the leap frog algorithm [233] but computes velocities $\mathbf{v}$ and coordinates $\mathbf{r}$ at the same time t. The forces $\mathbf{F}(t)$ determine the new coordinates at time $t + \Delta t$ (Eq 2.9) [234].

$$\mathbf{r}(t+\Delta t) = \mathbf{r}(t) + \Delta t \cdot \mathbf{v} + \frac{\Delta t^2}{2m}\mathbf{F} \tag{2.9}$$

Subsequently, these updated coordinates guide the computation of new forces $\mathbf{F}(t + \Delta t)$, essential for determining velocities $\mathbf{v}$ at time $t + \Delta t$ after two half-step velocity calculations (Eq. 2.12) [234].

$$\mathbf{v}\left(t + \frac{\Delta t}{2}\right) = \mathbf{v}(t) + \frac{\Delta t}{2m}\mathbf{F}(t) \tag{2.10}$$

$$\mathbf{v}\left(t + \frac{\Delta t}{2}\right) = \mathbf{v}(t + \Delta t) - \frac{\Delta t}{2m}\mathbf{F}(t + \Delta t) \tag{2.11}$$

$$\Rightarrow \mathbf{v}(t + \Delta t) = \mathbf{v}(t) + \frac{\Delta t}{2m}\left[\mathbf{F}(t) + \mathbf{F}(t + \Delta t)\right] \tag{2.12}$$

Despite its effective energy conservation, the Velocity Verlet algorithm is computationally more demanding than the leap frog algorithm due to the inclusion of two additional half-step velocity calculations (Eq. 2.10 and 2.11). For the two MD simulation softwares used in this study, we adhered to the default integration scheme: the leap frog algorithm for simulations in GROMACS and the Velocity Verlet algorithm for QM/MM simulations in AMBER.

The time step, denoted as Δt, is not solely dependent on the precision of the integration algorithm utilised but is also dictated by the fastest interactions or motions occurring within the system. This consideration assumes constant interactions throughout the Δt duration. In many instances, the fastest interactions relate to bond vibrations, requiring a time step as short as 1 fs. However, it is important to acknowledge that for numerous biomolecular motions, the impact of bond vibrations is negligible. In such scenarios, bond constraint techniques like the LINear Constraint Solver (LINCS) [235] or SHAKE [236] can be applied, facilitating an increase in the time step to 2 fs [207].

2.1.2 Force Field

In MD simulations, the fundamental objective is to determine the forces acting on each atom, enabling the prediction of molecular motions. In the framework of the MM approximation, these forces are calculated based on the potential energy of the system, utilising what is known as a force field. This force field is a mathematical construct that defines the functional relationship for computing the potential energy U_{ff} of the system $\mathbf{R}$ (Eq. 2.13).

$$\begin{aligned} U_{ff}(\mathbf{R}) = &\sum_{bonds} U_{ij}^{Bonds} + \sum_{angles} U_{ijk}^{Angles} + \sum_{dihedrals} U_{ijkl}^{Dihedrals} \\ &+ \sum_{improper} U_{ijkl}^{Improper} + \sum_{atom\ pairs} U_{ij}^{LJ} + \sum_{atom\ pairs} U_{ij}^{Coul} \end{aligned} \tag{2.13}$$

Generally, this potential energy is expressed as the sum of all interactions present within the system. To compute these interactions, the force field incorporates parameters that describe the relationships between all particles in the system. These parameters are typically derived from experiments or QM calculations to ensure an accurate representation during MD simulations. In the context of all-atom force

fields, the individual particles correspond to single atoms, each associated with specific atom types. These interactions are categorised into bonded and non-bonded contributions, as illustrated in Fig. 2.2 [222]. The choice and parameterisation of the force field significantly impact the accuracy and predictive power of the simulations.

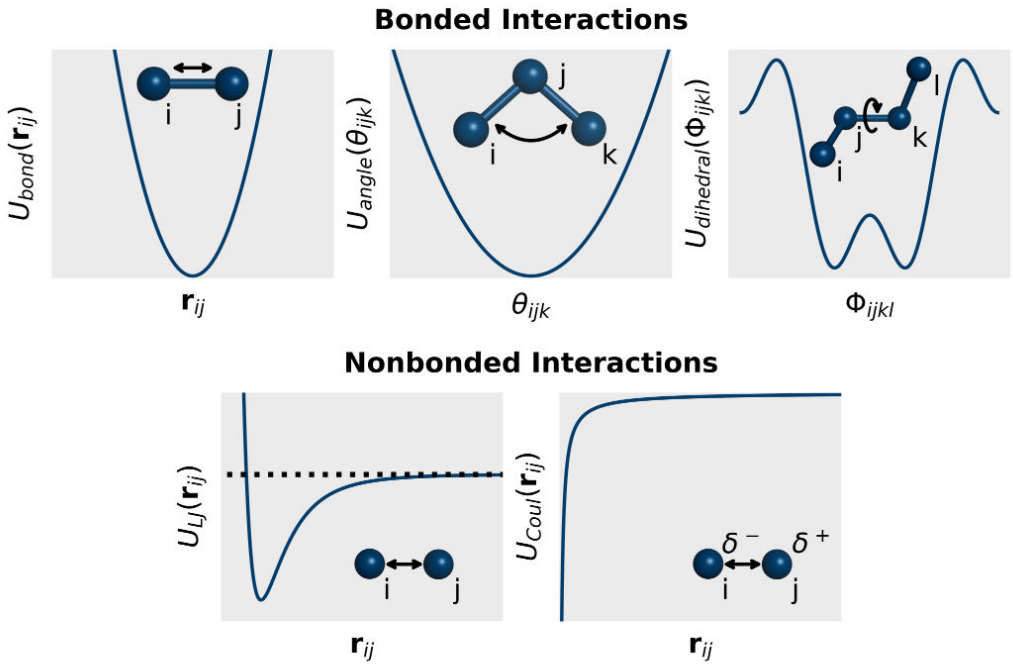


Fig. 2.2.: Bonded and nonbonded interaction terms considered by the force field.

The bonded interactions encompass three fundamental types of interactions in MD simulations:

Bond vibration is described by the harmonic potential governing the interatomic distance r_{ij} between atoms i and j (Eq. 2.14).

$$U_{bond}(r_{ij}) = \frac{k^b_{ij}(r_{ij} - b^0_{ij})^2}{2} \tag{2.14}$$

It involves two key parameters: the stretching force constant k^b_{ij} and the equilibrium bond length b^0_{ij}, both specific to the bond between the atom types of atoms i and j. it is important to note that the use of a harmonic oscillator model precludes the sampling of bond breaking and formation in the MM approximation.

Bond angle bending relates to the harmonic potential characterising the bending between consecutive atoms i, j, and k. It is defined by the bending force constant k^θ_{ijk} and the equilibrium angle θ^0_{ijk} between the atom types of i, j, and k (Eq. 2.15).

$$U_{angle}(\theta_{ijk}) = \frac{k^\theta_{ijk}(\theta_{ijk} - \theta^0_{ijk})^2}{2} \tag{2.15}$$

Dihedral angle torsion describes the interaction involving four consecutive atoms i, j, k, and l and is typically represented by a periodic cosine function (Eq. 2.16).

$$U_{dihedral}(\Phi_{ijkl}) = \sum k^{\Phi}_{ijkl}[1 + cos(n\Phi_{ijkl} - \Phi^0)] \tag{2.16}$$

The force field provides parameters including the phase or equilibrium angle Φ^0, the periodicity n, and the torsion force constant k^{Φ}_{ijkl}. In some cases, multiple functions may be required for a comprehensive representation of *trans/gauche/cis* energy states.

Improper dihedral angle torsion describes out-of-plane bending of planar geometries within a molecule, such as in aromatic rings or peptide bonds. It is usually described using a harmonic potential enforced by the improper torsion force constant k^{ω}_{ijkl} and the equilibrium angle, which is typically ω^0_{ijk} (Eq. 2.17).

$$U_{improper}(\omega_{ijkl}) = k^{\omega}_{ijkl}[1 + cos(n\omega_{ijkl} - \omega^0_{ijk})] \tag{2.17}$$

Non-bonded interactions encompass two primary types of interactions:

The Lennard–Jones (LJ) 12–6 potential characterises the van–der–Waals (vdW) interaction. It comprises two terms: the repulsive r^{-12} term, representing the Pauli exclusion principle and internuclear repulsion at close interatomic distances, and the attractive r^{-6} term, accounting for dispersion or London interactions at greater distances (Eq. 2.18).

$$U_{LJ}(r_{ij}) = 4\epsilon_{ij}\left[\left(\frac{\sigma_{ij}}{r_{ij}}\right)^{12} - \left(\frac{\sigma_{ij}}{r_{ij}}\right)^{6}\right] \tag{2.18}$$

The LJ potential is defined by parameters σ_{ij} and ϵ_{ij}, which establish the interatomic distance where the LJ potential equals zero and the depth of the LJ well, respectively.

The Coulomb's law describes electrostatic interactions and relies on the partial point charges q of two atoms i and j, as well as the distance r_{ij} between them (Eq. 2.19).

$$U_{Coul} = \frac{q_i q_j}{4\pi\epsilon_0\epsilon_r r_{ij}} \tag{2.19}$$

The vacuum permittivity ϵ_0 and the relative permittivity ϵ_r, which is typically set to 1 for MD simulations, are essential components in this description. Coulomb (Coul) interactions are repulsive for atoms with like charges and attractive for opposite charges, with a slow decay of $\frac{1}{r}$ [207].

In practice, non-bonded interactions, particularly electrostatic interactions, contribute significantly to the computational costs as they scale with N^2 unlike the bonded interactions scaling with N, especially when considering Periodic Boundary Conditions (pbc) for simulations involving periodic systems with infinite number of images [220].

Cutoff methods are used to enhance convergence, especially regarding the Coulomb potential decaying much slower than the LJ potential, which is truncated using a strict cutoff at 8–12 Å. The Coulomb potential is managed at extended distances using the Particle-Mesh Ewald (PME) method [237, 238]. To enhance convergence, the total potential energy contribution of Coul interactions is divided into three components:

1. A short-range potential $U_{short-range}$, calculated in real space, represents charges as point charges q and as oppositely charged Gaussian densities $-q$.

2. A long-range potential $U_{long-range}$ is computed in Fourier space and accounts for the sum of Gaussian densities with charge q, which compensates for the addition of the $-q$ densities.

3. A correction term for self-interaction U_{self} is included to ensure accurate calculations.

Using a cubic box length L and volume V, a wave vector $\mathbf{k} = (2\pi/L)\mathbf{l}$ with the lattice factor $\mathbf{l} = l_x, l_y, l_z$ in Fourier space, the Gaussian charge distribution ρ, and the complementary error function $erfc$, the final expression for PME is derived (Eq. 2.20). The prime included in the short-range potential defines the summation over all periodic images n and atoms, except for the same atom ($i = j$) of the unit cell with $n = 0$. By introducing a grid for mesh interpolation of the long-range potential and optimising the Gaussian width α, the computational scaling is reduced from $\mathcal{O}(N^2)$ without PME to $\mathcal{O}(N\cdot)$. This significant reduction in computational demand is a key advantage of the PME method [237–240].

$$\begin{aligned} U_{Coul} =& U_{short-range} + U_{long-range} - U_{self} \\ =& \frac{1}{2} \sum_{i,j=1}^{N} {\sum_{n}}' \frac{q_i q_j erfc(\sqrt{\alpha}|\mathbf{r}_{ij} + nL|)}{|\mathbf{r}_{ij} + nL|} \\ &+ \frac{1}{2V} \sum_{\mathbf{k}\neq 0} \frac{4\pi}{\mathbf{k}^2} |\rho(\mathbf{k})|^2 exp\left(\frac{-\mathbf{k}^2}{4\alpha}\right) \\ &- \left(\frac{\alpha}{\pi}\right)^{\frac{1}{2}} \sum_{i=1}^{N} q_i^2 \end{aligned} \tag{2.20}$$

The general force field expression (Eq. 2.13) can be expanded by incorporating additional terms to introduce restraints, cross terms, and other correction terms, as detailed in the literature [220].

The AMBER14SB_parmbsc1 force field was used in this study to determine the potential energy of the system. Force fields used in MD simulations can vary in their functional terms and parameters, tailored to accurately represent specific types of systems such as proteins, lipid membranes, or DeoxyriboNucleic Acid (DNA) [241–243]. The Assisted Model Building with Energy Refinement (AMBER) force field series relies on Restrained ElectroStatic Potential (RESP) charges [244, 245].

The RESP program fits the quantum mechanically calculated Molecular Electrostatic Potential (MEP) at molecular surfaces using an atom-centred point charge model while incorporating a restraint function that modifies charges and associated bond polarity. It also preserves molecular dipole moments and ion net charges [246]. The initial parameter set for AMBER dates back to 1980 [247–249] and has undergone continuous refinement over the years. This process culminated in the development of the first all-atom AMBER force field in 1986 [250]. The AMBER14SB force field [251] was introduced in 2015, and it has been further enhanced with the parmbsc1 corrections specifically designed for DNA simulations, resulting in the AMBER14SB_parmbsc1 force field, which was the most recent and recommended choice for protein simulations at the outset of this PhD project. AMBER14SB_parmbsc1 is rooted in the AMBER99SB force field [252] but features improved amino acid side chain dihedral parameters obtained through QM calculations. Additionally, slight adjustments of backbone dihedral parameters were made, guided by evaluation against Nuclear Magnetic Resonance (NMR) data.

The Transferable Intermolecular Potential with 3 Points (TIP3P) water model is an explicit 3-site rigid water model that is based on the earlier Transferable Intermolecular Potential functions (TIPS) model [253], which was subsequently reparameterised [254]. In the TIP3P model, each water molecule is represented by three interaction sites, each corresponding to an atom. These sites carry partial point charges: a negative charge for the oxygen atom and positive charges for the two hydrogen atoms related by $q_O = -2q_H$. it is worth noting that there are more complex water models, such as TIP4P, which include an additional dummy atom to provide a more accurate representation of the electrostatic distribution within water molecules. While TIP4P offers a better representation of water, it comes at the cost of significantly increased computational time, as the non-bonded interactions between water molecules are a computationally intensive part of molecular simulations. AMBER14SB is a force field that was specifically developed to be used with the TIP3P water model. It includes empirical corrections designed to be compatible with TIP3P, especially focusing on backbone corrections that are specific to this water model.

2.2 Enhanced Sampling

MD simulations aim to replicate the dynamic behaviour of a system in thermal equilibrium, allowing exploration of the free energy landscape and the configurational states of the system. The free energy (G) of a macrostate s can be determined using Boltzmann's constant (k_B), temperature (T), and the probability (P) of finding the system in state s (Eq. 2.21).

$$G(s) = -k_B T \ln P(s) \tag{2.21}$$

However, for this to hold true, the simulation must be ergodic, meaning that the ensemble average matches the time average. In theory, with a sufficiently long runtime, it is possible to sample the entire phase space and achieve ergodicity [209]. In practice, this approach is computationally impractical and, thus, calculations are limited to the free energy difference ΔG of two adequately sampled states. Some processes, the 'rare events', have high energy barriers, making their occurrence improbable in typical MD simulations. As a result, the system becomes trapped in energetically favourable minima, exhaustively exploring these minima while inadequately sampling high-energy states (Fig. 2.5 left). This leads to insufficient statistical significance to calculate the free energy difference between these states. To address this sampling problem, enhanced sampling methods are employed [255]. These methods either bias the system along a specified Collective Variable (CV), such as the Umbrella Sampling Molecular Dynamics (USMD) approach, which requires prior knowledge of the process being analysed, or uniformly enhance sampling of a system, as in HREMD simulations, where no prior knowledge is necessary.

2.2.1 Hamiltonian Replica Exchange MD Simulation

In **Replica Exchange Molecular Dynamics (REMD)** simulations, the same system is simultaneously simulated in multiple replicas, with each replica corresponding to a different temperature or energy state (Fig. 2.3) [256, 257].

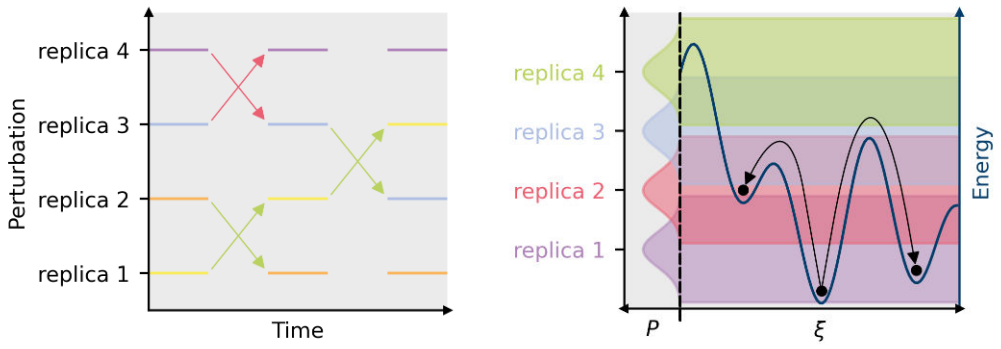


Fig. 2.3.: Schematic representation of the principle of replica exchange simulations. Left: Schematic exchange profile depicting accepted (green) and rejected (red) exchanges of conformations (coloured) between different replicas with perturbed energy. Right: Schematic 2D free energy profile along the CV ξ with the projection of the populated areas per replica and the respective distribution of probability P. Exchanges of conformations between replicas allows for transition to other local minima and better exploration of the sampling space.

The exchange of configurations between replicas is attempted at regular intervals. To ensure that despite this exchange an equilibrium ensemble is sampled, the Metropolis-Hastings criterion is employed [258, 259]. This criterion dictates that an

exchange is accepted only if the energy of the replica at higher T is lower than that of the replica at lower T or with a probability defined by $e^{-\Delta}$ (Eq. 2.22).

$$P_{i\to j} = \begin{cases} 1 & \text{if } \Delta \leq 0 \\ e^{-\Delta} & \text{if } \Delta > 0 \end{cases} \quad \text{with } \Delta = \left(\frac{1}{k_B T_i} - \frac{1}{k_B T_j} \right) (U_j - U_i) \tag{2.22}$$

For such an exchange to occur, the potential energy distributions of both states must overlap. The extent of the overlap region can be adjusted to increase the exchange acceptance ratio, aiming for a desired range of 0.2 to 0.4. This ratio depends on the choice of the exchange interval and the number of replicas, which scales with the square root of the number of atoms in the system ($\sqrt{N}$). The exchange of configurations to a replica with a higher temperature allows for exploration of conformational changes associated with high energy barriers.

HREMD simulations follow a similar approach to REMD but focus on perturbing the effective potential energy function provided by the force field (U_{ff}) and therewith the Hamiltonian H (Eq. 2.23) between the replicas, rather than changing the temperature [210, 260, 261]. This perturbation occurs in a specific part of the system, referred to as the 'hot' region, while the rest of the system remains unperturbed, forming the 'cold' region. This approach significantly reduces the number of replicas needed and thus the computational effort.

$$H(\mathbf{R}, \mathbf{p}) = E_{kin} + U_{ff} \quad \text{with } E_{kin} = \sum_{i}^{N} \frac{\mathbf{p}_i^2}{2m_i} \tag{2.23}$$

After perturbing the Hamiltonian of the 'hot' region of replica i with a scaling factor $0 < \lambda_i \leq 1$, an effective temperature of $\frac{T}{\lambda_i}$ is achieved for the 'hot' region and $\frac{T}{\sqrt{\lambda_i}}$ for the 'hot/cold' interface region. The 'cold' region maintains the target temperature T. The unperturbed replica always retains an effective temperature of T for both the 'hot' and 'cold' regions as $\lambda = 1$. To perturb the entire Hamiltonian, the scaling is applied differently to the interaction terms:

1. Dihedral angle torsion: The dihedral angle torsion energy $U_{dihedral}$ is scaled by λ for the 'hot' region and by $\sqrt{\lambda}$ for the interface.
2. LJ potential: The depth of the LJ well, ϵ_{ij}, is scaled by λ.
3. Coulomb potential: The atomic charges q_i and q_j are each scaled by $\sqrt{\lambda}$.

Similar to REMD simulations, HREMD simulations enable the exploration of energy barriers by reducing their height, allowing for more conformational transitions.

Multistate Bennett Acceptance Ratio (MBAR) is a statistical estimator commonly used to estimate the free energy barrier between two states, denoted as A and B, when dealing with configurations obtained from enhanced sampling simulations in a thermodynamic ensemble which require reweighting for free energy calculations [262–265]. In MBAR, a state A out of K states including N_i uncorrelated samples

is defined by a reduced potential energy $u_A(\mathbf{R})$, which encompasses the potential energy $U_A(\mathbf{R})$ of state A and configurations $\mathbf{R}$ [262]. For simulations in the NpT ensemble, it also includes the external pressure p_A and the volume of the system $V(\mathbf{r})$ (Eq. 2.24). In the grand-canonical μVT ensemble, the definition incorporates the vector of chemical potentials μ_A^T and the number of particles $\mathbf{n}(\mathbf{R})$. The dimensionless free energy of state A can be computed by integrating the Boltzmann weight of the reduced potential energy $u_A(\mathbf{R})$. The estimated free energy of state A, denoted as $\hat{f}_A$, is provided by the MBAR equation with $\mathbf{R}_{jn}{}_{n=1}^{N_j}$ describing the sample n of all uncorrelated samples N_i in each state j of all states K (Eq. 2.25). As the MBAR equation includes a sum over all states K, $\hat{f}_A$ is present at both sites of the equation and the equation must be solved self-consistently. However, the absolute free energy $\hat{f}_A$ of a state A is arbitrary, as it is only defined up to an additive constant, which cancels out when computing the free energy difference between two states, denoted as $\Delta\hat{f}_{AB}$.

$$u_A(\mathbf{R}) = k_B T[U_A(\mathbf{R}) + p_A V(\mathbf{R}) + \mu_A^T \mathbf{n}(\mathbf{R})] \tag{2.24}$$

$$\hat{f}_A = -\ln \sum_{j=1}^{K} \sum_{n=1}^{N_j} \frac{e^{-u_A(\mathbf{R}_{jn})}}{\sum_{k=1}^{K} N_k e^{\hat{f}_k - u_k(\mathbf{R}_{jn})}} \quad \text{with } f_A = -\ln e^{u_A(\mathbf{R})} d\mathbf{R} \tag{2.25}$$

$$\tag{2.26}$$

The MBAR method allows to estimate the thermodynamic averages of a CV ξ in unsampled states ξ_u through interpolation of Eq. 2.25 from the sampled states (Eq. 2.27).

$$\langle \xi \rangle_u = \frac{\int \xi(\mathbf{r}) e^{-u_u(\mathbf{r})} d\mathbf{r}}{e^{-u_u(\mathbf{r})} d\mathbf{r}} = \frac{e^{-f_{u,\xi}}}{e^{-f_u}} \tag{2.27}$$

To access the free energy on ξ_u, also known as the Potential of Mean Force (PMF), a Dirac delta function $\delta(\xi_u)$ is introduced. This method can be extended to be used with enhanced sampling techniques such as HREMD, where $u_{A,i}(\mathbf{R})$ incorporates the potential energy U_{ff} scaled by the λ_i factor of the respective replica i. Furthermore, a 3D-Free Energy Surface (FES) can be generated by free energy decomposition along two CVs.

Principle Component Analysis (PCA) is a method that uncovers the large scale dynamics of a system by reducing its dimensionality while retaining as much variance, and thus information, as possible [266–272]. Typically, the input dataset from MD trajectories comprises the atomic Cartesian coordinates of the molecule of interest over time, although other descriptors, such as distances, as employed in this study, can also be used. In this context, we obtain S m-dimensional vectors $\mathbf{q}(s)$ for conformations (or frames) s from a trajectory containing a total of S conformations. Each element $\mathbf{q}_i(s)$ relates to the value of the chosen descriptor of atom i among all n atoms in the system considered for PCA. Using this data, a covariance matrix C is

constructed, where each element contains the descriptor correlation between atom i and j, denoted as the variance σ_{ij} (Eq. 2.28).

$$C_{ij} = \frac{1}{S}\sum_{s=1}^{S}(\mathbf{q}_i(s) - \langle \mathbf{q}_i \rangle)(\mathbf{q}_j(s) - \langle \mathbf{q}_j \rangle) \tag{2.28}$$

Here, $\langle \mathbf{q_i} \rangle$ represents the ensemble average of the descriptor for atom i across all S conformations, equivalent to the time average if the conformations form a continuous trajectory. Diagonalising the covariance matrix C yields m pairs of eigenvectors, also called Principle Component (PC), and their corresponding eigenvalues λ_p. The eigenvectors are ordered with respect to the magnitude of their eigenvalue, such that the lower the index p, the higher the eigenvalue, and the more variance explained by the corresponding PC (Fig. 2.4). Typically, the first few PCs already account for 70% to 90% of the overall variance and, thus, the most significant motions sampled in the trajectory, significantly reducing the degrees of freedom [273]. Hence, the first two PCs can be utilised as CVs to create a FES for identifying dominant motions, such as PET entry modes [274]. To enhance the statistical significance of the results, several independent yet equivalent trajectories can be concatenated and used to perform the PCA, as applied in the current study, where multiple PET entry snippets for diverse enzyme variants were combined.

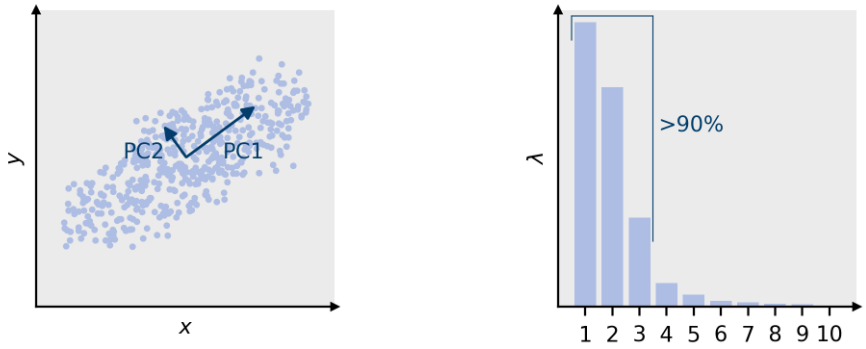


Fig. 2.4.: Schematic representation of the principle of PCA. Left: Schematic representation of the first two PCs with respect to the CV value y per sample x. The first two PCs explaining most variance are highlighted. Right: Schematic barplot of the Eigenvalues λ_p ordered by the index p. The lower the index p, the higher the eigenvalue, and the more variance explained by the corresponding PC. Here, the first three Eigenvalues explain more than 90% of the variance.

2.2.2 Umbrella Sampling MD Simulation

USMD is an enhanced sampling method that requires prior knowledge of the system and involves the definition of a CV, denoted as ξ [275, 276]. The choice of the CV is crucial as it must effectively describe the transition between two states of interest. To compute the free energy profile along a specific CV ξ_0, the CV ξ is separated from

all other degrees of freedom. This is achieved via a Dirac delta function $\delta(\xi - \xi_0)$ (Eq. 2.29).

$$G(\xi_0) = -k_B T \ln P(\xi_0) = -k_B T \ln(\langle \delta(\xi - \xi_0) \rangle) \tag{2.29}$$

The ensemble average of this probability distribution corresponds to the probability of finding the system in state ξ_0 and is equivalent to the time average of extensively sampled MD simulations. However, extensive sampling of all states along the entire pathway is necessary to obtain the probability $P(\xi_0)$ with statistical significance. To achieve this, the system is constrained in multiple states, known as 'windows,' positioned uniformly along the ξ dimension (Fig. 2.5).

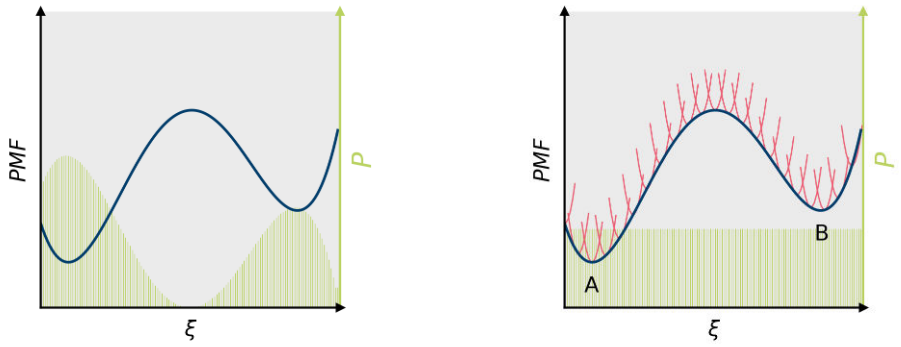


Fig. 2.5.: Schematic 2D PMF profiles highlighting the probability distribution of unbiased vs. biased sampling including harmonic potentials. The PMF profiles of an unbiased, conventional MD simulation (left) and a USMD biased along the CV ξ connecting state A and B are shown. The PMF is displayed in blue, the probability distribution P in green and the harmonic biasing potentials of each umbrella window in red.

In each window, an arbitrary potential, referred to as an 'umbrella', is added to the unbiased PMF, resulting in a biased PMF (Eq. 2.30). This biased PMF ($G^b(\xi_0)$) can be calculated from the data collected in the USMD simulation to obtain the unbiased PMF for each window, $G_i(\xi_0)$ (Eq. 2.31).

$$G_i^b(\xi_0) = G_i(\xi_0) + V_i^a(\xi_0) + F_i \tag{2.30}$$

$$\begin{aligned} \Rightarrow G_i(\xi_0) &= G_i^b(\xi_0) - V_i^a(\xi_0) - F_i \\ &= -k_B T \ln P_i^b(\xi_0) - \frac{K_i}{2}(\xi - \xi_0)^2 + k_B T \ln \left\langle e^{\frac{V_i^a}{k_B T}} \right\rangle^b \end{aligned} \tag{2.31}$$

The biased probability distribution $P^b(\xi_0)$ for state ξ_0 can be obtained from the USMD simulation data after sufficient sampling. The arbitrary potential used in the windows is typically a harmonic potential that confines the CV ξ close to a target equilibrium value ξ_0 for each window (Fig. 2.5). The value of the biasing force constant K_i should strike a balance between driving the system across energy barriers to explore the entire range of the CV ξ and ensuring that the probability distributions $P_i^b(\xi)$ are not overly narrow resulting in a larger number of windows

to enable sufficient overlap of the sampling space. A correction factor F_i is included to account for the shift in the PMF due to the addition of the arbitrary potential V_i^a, and this correction factor is independent of ξ.

Umbrella Integration (UI) [277–279] is one of two principal methods for calculating the PMF across the CV ξ, denoted as $G(\xi)$, besides Weighted Histogram Analysis Method (WHAM) [280]. In order to determine the global PMF not just for a single state ξ_0 but for the entire ξ phase space, information from all windows is accumulated. Umbrella Integration (UI) calculates the unbiased mean force $\frac{\partial G_i}{\partial \xi}$ for each window i based solely on the mean $\langle \xi_i \rangle^b$ and the variance $(\sigma_i^b)^2$ of ξ, approximating the biased probability with a normal distribution (Eq. 2.32).

$$\frac{\partial G_i}{\partial \xi} = -k_B T \frac{\partial \ln P_i^b(\xi)}{\partial \xi} - \frac{-dV_i^a}{d\xi} = -k_B T \frac{\xi - \langle \xi_i \rangle^b}{(\sigma_i^b)^2} - K(\xi - \xi_i^0) \tag{2.32}$$

This formulation is independent of F_i and therefore non-iterative, allowing for faster convergence compared to methods like WHAM. The overall PMF is obtained by numerically integrating the sum of the weighted unbiased mean forces across all I windows, employing normalised weights p_i and considering the number of degrees of freedom N_i per window (Eq. 2.33).

$$\frac{\partial G}{\partial \xi} = \sum_i^I p_i(\xi) \frac{\partial G_i}{\partial \xi} \quad \text{with } p_i(\xi) = \frac{a_i}{\sum_j a_j} \text{ and } a_i(\xi) = N_i P_i^b(\xi) \tag{2.33}$$

The UI method offers the advantage of deriving statistical measures to estimate key parameters such as the force constant K or to assess the sufficiency of the sampling. In this study, USMD simulations combined with the UI method are employed to sample the PMF for the initial step of the PET degradation mechanism, i.e. acylation. This approach utilises a hybrid QM/MM description of the system.

2.3 Quantum Mechanical / Molecular Mechanical Simulations

The hybrid QM/MM method was developed by Warshel and Levitt [216] to facilitate the simulation of biological systems. Traditional computational methods reliant solely on QM descriptions become computationally infeasible for such large systems. Moreover, QM/MM enables the simulation of processes involving bond breaking and formation, a task not achievable through the application of MM force fields alone. This section provides a concise overview of QM/MM simulations and outlines the methodology adopted in this study, drawing upon relevant literature [281–283].

In this methodology, the system is partitioned into two distinct regions: the QM region, encompassing all atoms relevant to the process under investigation at the QM level (e. g. , bond breaking and formation in enzymatic catalysis), and the MM level, which includes all other atoms in the system (e. g. , solvent and the remaining

portion of the enzyme). This division serves to optimise computational efficiency (Fig. 2.6).

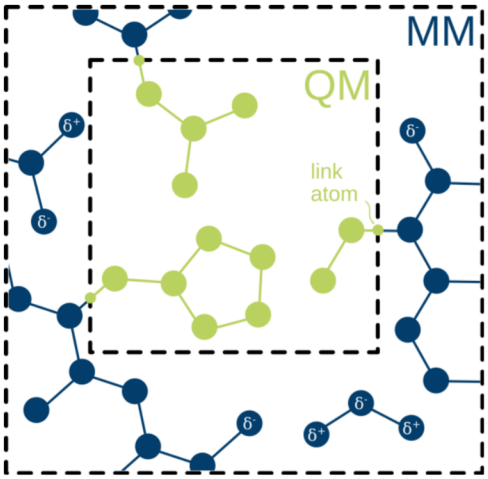


Fig. 2.6.: Scheme highlighting the separation of the QM and MM regions. The regions interact via link atoms and electrostatic embedding enables polarisation of the QM region by the MM region.

To account for interactions between the QM and MM regions and to compute the energy of the hybrid system, the herein used AMBER software employs an additive QM/MM coupling approach. This entails deriving the total energy of the combined QM/MM system ($U_{QM/MM}$) by summing the energies of the QM region obtained through QM calculations ($U_{QM}(QM)$), the MM region obtained via the MM force field ($U_{ff}(MM)$), and the interaction energy between the QM and MM regions at the QM/MM boundary ($U_{int}(QM-MM)$) (Eq. 2.34).

$$U_{QM/MM} = U_{QM}(QM) + U_{ff}(MM) + U_{int}(QM-MM) \tag{2.34}$$

The former is applicable only when a covalent bond crosses the QM/MM boundary. In such instances, the electrons of the MM atom engaged in bonding orbitals must be considered in the QM calculation, necessitating the introduction of a cap for the QM region. One approach involves the addition of monovalent link atoms along the bond vector at an appropriate distance from the QM atom bonding partner, typically hydrogen (Fig. 2.6). This link atom is exclusively considered in QM calculations for the QM region, and the force acting on this atom is distributed across both bond partners. These bonded interactions are addressed using the MM force field terms governing bond vibrations, angle bending, and dihedral torsions. Nonbonded interactions are computed using the force field LJ term for vdW interactions, while electrostatic interactions are treated through electrostatic embedding. This involves an additional term in the QM Hamiltonian, accommodating electrostatic interactions with MM atoms carrying partial charges. These atoms are modelled as point charges surrounding the QM region, enabling polarisation of the QM region by the MM region (Fig. 2.6).

2.3.1 QM Method

In addition to selecting the MM force field, like the protein-optimised AMBER14SB_parmbsc1 force field chosen in this study, the choice of the QM level of theory holds significance, impacting both accuracy and computational demand. Broadly, the QM method offers a framework for deriving Molecular Orbitals (MOs), which involves evaluating the energy and probability distribution of electrons, represented by its wave function. The MOs serve as an approximate solution to the time-independent Schrödinger equation, describing the wave function (Φ) using the Hamilton operator $\hat{H}$ and the energy of the wave function E (Eq. 2.35).

$$\hat{H}|\Phi\rangle = E|\Phi\rangle \tag{2.35}$$

The MOs are described as a linear combination of Atomic Orbitals (AOs) with the overlap $\mathbf{S}_{ij}$ between AOs i and j and their coefficients $\mathbf{c}_i$ and $\mathbf{c}_j$ to the MO in question. This process involves minimising the energy of the groundstate MO wave function to yield the secular equation (Eq. 2.37).

$$\mathbf{H}\mathbf{c}_n = E_n\mathbf{S}\mathbf{c}_n \tag{2.36}$$

$$0 = \begin{bmatrix} H_{11} - ES_{11} & \dots & H_{1N} - ES_{1N} \\ \vdots & \vdots & \vdots \\ H_{N1} - ES_{N1} & \dots & H_{NN} - ES_{NN} \end{bmatrix} \tag{2.37}$$

Various approaches exist for solving the secular equation, differing in how they simplify the matrix and address Hamiltonian calculations. In this context, three main categories of QM methods are distinguished, characterised by increasing accuracy in estimating the Schrödinger equation and, correspondingly, increasing computational demand: semi-empirical methods, Density Functional Theory (DFT), and *ab initio* methods.

The *ab initio* methods rely on fundamental physical constants and aim to solve Schrödinger's equation. The most widely used method in this category is the Hartree-Fock (HF) method, which explicitly computes the overlap term $\mathbf{S}$ and utilises the Fock matrix $\mathbf{F}$ to characterise the Hamiltonian $\mathbf{H}$ within the secular equation (Eq. 2.38) [284–289].

$$\mathbf{F}\mathbf{c}_n = E_n\mathbf{S}\mathbf{c}_n \tag{2.38}$$

In this context, the interaction of MOs is addressed in a stationary state through a linear combination of AOs, which are defined by the chosen basis set. For instance, using the popular Pople split-valence double-zeta basis set 6-31+G(d,p), the core orbitals are represented by 6 Gaussian-type orbitals, while the valence orbitals are described by a linear combination of 3 Gaussian-type orbitals, supplemented by an additional Gaussian-type orbital, diffuse functions for heavy atoms and polarisation

functions on all atoms [290–294]. To obtain the MO resulting from the overlap of AOs μ and ν, the Fock matrix incorporates terms for calculating the kinetic energy of electrons, the attraction of electrons to all nuclei k, and the repulsion between the electrons of AO $\mu\nu$ and all other AOs $\lambda\sigma$ incorporating an electron exchange function to avoid double-counting of electrons (Eq. 2.39).

$$\mathbf{F}_{\mu\nu} = \langle\mu| - \frac{1}{2}\nabla^2|\nu\rangle - \sum_k Z_k\langle\mu|\frac{1}{\mathbf{r}_k}|\nu\rangle + \sum_{\lambda\sigma} P_{\lambda\sigma}\left[(\mu\nu|\lambda\sigma) - \frac{1}{2}(\mu\lambda|\nu\sigma)\right] \tag{2.39}$$

This calculation accounts for the indistinguishability of electrons and the occupation of orbitals, resulting in a four-indexed integral. However, the HF approach is constrained by its scaling with N^4, where N represents the number of basis sets used. This scaling contributes to the method's substantial computational demand. Moreover, the HF method overlooks correlation effects in dynamic systems, including London Dispersion effects, thereby limiting its accuracy.

DFT methods focus on the interaction of each electron with the overall electron density, employing the Kohn-Sham matrix instead of the Fock matrix describing the electron-electron interactions considered by HF (Eq. 2.40) [295–299].

$$\mathbf{K}\mathbf{c}_n = E_n\mathbf{S}\mathbf{c}_n \tag{2.40}$$

While the descriptions of kinetic energy and nuclei attraction are similar to HF, the repulsion term diverges to account for the repulsion of the electrons in the MO of interest using the electron density $\rho(\mathbf{r})$ while V_{XC} is the exchange-correlation potential (Eq. 2.41).

$$\mathbf{K}_{\mu\nu} = \langle\mu| - \frac{1}{2}\nabla^2|\nu\rangle - \sum_k\langle\mu|\frac{1}{\mathbf{r}_k}|\nu\rangle + \langle\mu|\int\frac{rho(\mathbf{r}')}{\mathbf{r}-\mathbf{r}'}ds\mathbf{r}'|\nu\rangle + \langle\mu|V_{XC}|\nu\rangle \tag{2.41}$$

This leads to a more favourable scaling of N^3. Moreover, DFT introduces the exchange(X)–correlation(C) term V_{XC} to address correlation effects, which are neglected in the HF method, and to consider the indistinguishability of electrons. While HF perfectly describes the latter, DFT approximates it by the electron density. Various functionals exist to approximate the exchange–correlation term, depending on the local electron density (Local Density Approximation (LDA)), and, for increased precision, on the gradient of the electron density (Generalised Gradient Approximation (GGA)) and the second derivative of the density (meta Generalised Gradient Approximation (mGGA)). Further improvement is achieved through a hybrid approach, where a portion α of the exchange–correlation DFT energy is described by the HF exchange energy (Eq. 2.42).

$$E_{XC} = (1-\alpha)E_{XC}^{DFT} + \alpha E_X^{HF} \tag{2.42}$$

An example is the Minnesota functional M06-2X, a hybrid functional incorporating 54% HF exchange [300].

Semi-empirical methods rely on empirically derived parameters and approximations to simplify the secular equation, making them the least accurate QM method. However, they offer significant computational time savings and are well-suited for very large systems. The overlap term $\mathbf{S}$ is typically addressed by applying pre-solved terms for known orbital types, as seen in semi-empirical molecular orbital methods like the Austin Model 1 (AM1) [301]. The calculation of the Hamiltonian is simplified by using parameters tailored to fit the energy to experimental data. These parameters may include overlap integrals β combined with a statistical term to account for electron exchange of electrons i and j of atoms A and B (Eq. 2.43) or the approximation of electronic density, as seen in Density Functional Tight Binding 3 (DFTB3), which is derived from DFT [302].

$$\mathbf{H}_{ij} = \frac{1}{2}(\beta_i + \beta_j)\mathbf{S}_{ij} - \frac{1}{2}\sum_{i\in A}\sum_{j\in B} P_{kl}\langle ik|jl\rangle \tag{2.43}$$

Unlike HF and DFT, semi-empirical methods are defined based on a specific basis set, which therefore does not require further specification when employing such a method.

2.3.2 Adaptive String Method

QM/MM simulations of chemical reactions involve overcoming the free energy barriers associated with these reactions. Adequate sampling across all reaction stages, including the high energy Transition State (TS), is essential to compute the free energy profile. To address this requirement, various simulation methods exist to push the reactant over the energy barrier to the product and ensuring sufficient TS sampling while maintaining reasonable computational demands. In this investigation, the ASM was employed to sample the acylation of PET, the initial step in enzymatically catalysed PET degradation [217].

The ASM is a path-based method derived from the on-the-fly string method [303, 304], mainly developed and implemented in the AMBER software by our collaboration partner Dr. Kirill Zinovjev (University of Valencia, ESP). As the name implies, the reaction is depicted by a path – referred to as a string – that connects the Michaelis Complex (MC) and the Product Complex (PrC), or in the case of acylation, the Acyl-Enzyme Intermediate (AE) as the target configuration (Fig. 2.7). This string $\mathbf{z}$ is defined in a reduced dimension of an arbitrary number of D CVs θ, encompassing all degrees of freedom involved in the reaction, such as distances between atoms that are involved in forming or breaking a bond. An initial guess of the string is defined by either a linear interpolation connecting MC and PrC or by interpolating along several points in CV space provided based on rational knowledge on the mechanism under study. To sample the whole string sufficiently, n nodes are defined in equidistant positions along this initial guess of the string. The position

of the i^{th} node $\mathbf{z}_i$ is defined by α_i based on the arc-length of the total string L (Eq. 2.44).

$$\mathbf{z}_i = \mathbf{z}(\alpha_i) \quad \text{with} \quad \alpha = \frac{i-1}{n-1} L \tag{2.44}$$

For each node, an MD simulation is initiated either from the MC or the PrC input structure, enforcing structural changes to reach the CV values of the target node. Then, the simulations are restrained to the node position by a biasing potential $V^{string}(\mathbf{x})$, with $\mathbf{x}$ comprising the three-dimensional Cartesian coordinates and $\mathbf{B}$ the biasing matrix (Eq. 2.45).

$$V_i^{string}(\mathbf{x}) = \frac{1}{2}(\theta(\mathbf{x}) - \mathbf{z}_i)^T \mathbf{B} (\theta(\mathbf{x}) - \mathbf{z}_i) \tag{2.45}$$

$$\mathbf{B} = (K^{\parallel} - K^{\perp}) \mathbf{M}^{-1} \hat{\mathbf{n}} \hat{\mathbf{n}}^T \mathbf{M}^{-1} + K^{\perp} \mathbf{M}^{-1} \tag{2.46}$$

$$\text{with} \quad \mathbf{M}_i = \langle \tilde{\mathbf{M}}(\mathbf{x}) \rangle_i = Z^{-1}$$

$\mathbf{B}$ includes force constants K, the normalisation vector $\hat{\mathbf{n}}$, and the distance metric tensor $\mathbf{M}$ defined by the inverse partition function of the biased ensemble Z^{-1} (Eq. 2.46). The initial string is optimised, allowing node positions to change in CV space according to the free energy gradient. Equidistant positioning is retained by redefining node positions after interpolating the updated string, resulting in the string converging to the Minimum Free Energy Path (MFEP). A pathCV s is defined to describe the progression from MC to PrC along the MFEP, which is used as a CV for subsequent USMD (Section 2.2.2). The USMD ensures sufficient uniform sampling, enabling the calculation of the PMF along s via UI.

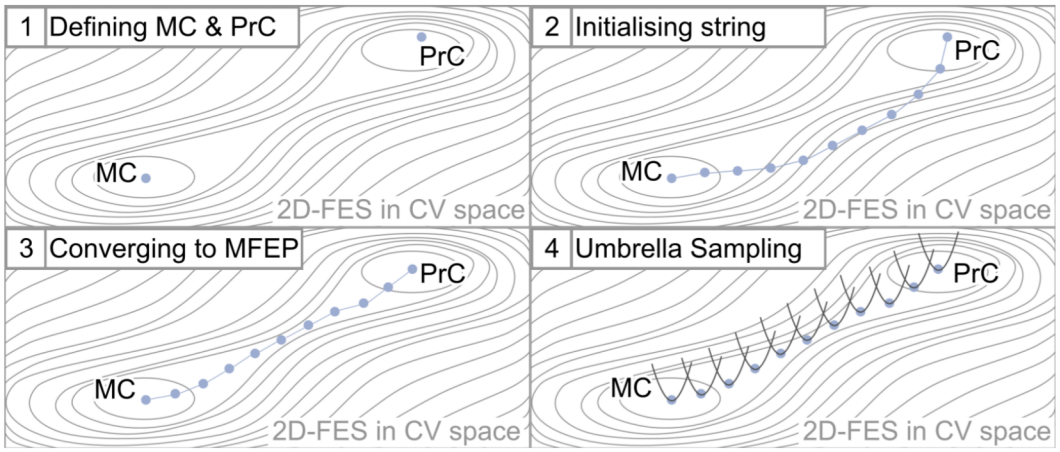


Fig. 2.7.: Workflow of the ASM schematically shown on a 2D-FES. First, initial structures of the MC and PrC states are provided. Second, the initial structures are driven towards the n equidistant node positions along the string defined based on the initial guess. Third, the position of each node is allowed to change during MD simulation to converge to the Minimum Free Energy Path (MFEP), while an equidistant positioning is ensured. Fourth, Umbrella Sampling Molecular Dynamics (USMD) simulations are conducted to enable extensive sampling at each node or US window position and to obtain the PMF.

The benefit of ASM, compared to the on-the-fly string method, lies in the introduction of the biasing matrix $\mathbf{B}$, incorporating force constants along ($K^{\parallel}$) and orthogonal ($K^{\perp}$) to the string, instead of $\mathbf{K}$ – a diagonal matrix of force constants per CV (Eq. 2.46). This way, the biasing potential and the corresponding ensemble sampled during string optimisation align with the biasing potential and ensemble of the USMD (Fig. 2.8). Consequently, the final node positions and the biasing potential parameters – α_i, the arc-length of the string up to node i, and the parallel force constant $K^{\parallel}$ – averaged over the converged part of the string optimisation corresponding to the MFEP, serve as a reference to define the position of the US windows and US biasing potential V^{US} (Eq. 2.47).

$$V_i^{US}(s(\mathbf{x}), z(\mathbf{x})) = \frac{K^{\parallel}}{2}(s(\mathbf{x}) - \alpha_i)^2 + \frac{K^{\perp}}{2} z(\mathbf{x})^2 \tag{2.47}$$

Once sufficient sampling is achieved, the final PMF can be calculated using UI (Section 2.2.2). Convergence can be enhanced by combining USMD with HREMD, utilising the optimised parameters to ensure a high replica exchange rate.

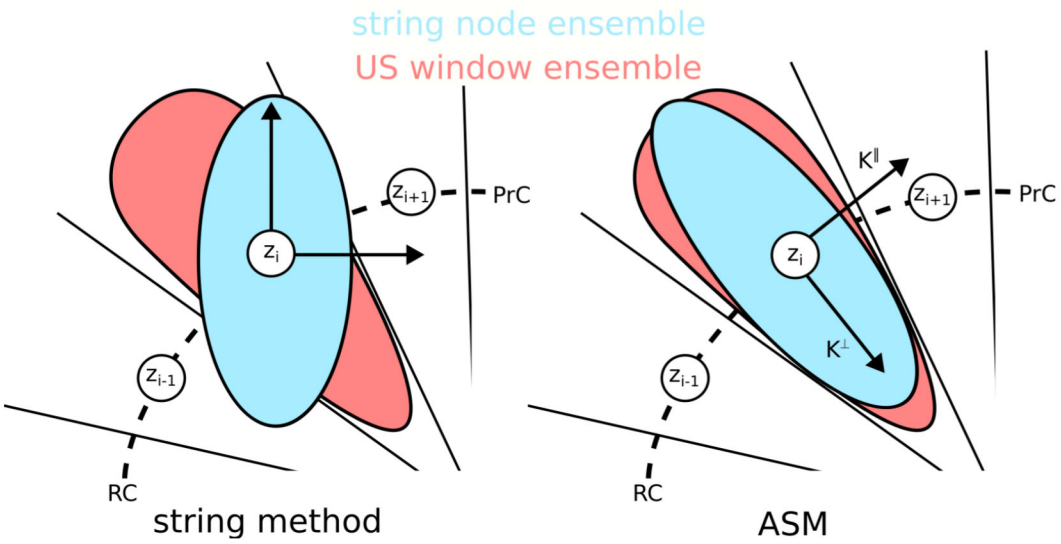


Fig. 2.8.: Biasing potentials and sampled ensemble for the original string method (left) and the ASM (right). The ASM uses a parallel ($K^{\parallel}$) and an orthogonal ($K^{\perp}$) force constant, which improves the overlap of the string node (blue) and Umbrella Sampling (US) (red) ensemble. Adapted from Zinovjev and Tuñón *et al.* [217], reproduced with permission.

3 Interactions and Binding Poses of PET in the Active Site of PES-H1

A pivotal aspect of enzymatic activity lies in the enzyme's capacity to bind substrates within its active site. Numerous investigations have scrutinised substrate binding considering the Poly(Ethylene Terephthalate) (PET)-degrading enzyme Leaf-branch Compost Cutinase (LCC), employing methodologies such as crystallographic structures and docking analyses [133, 166, 201, 305], as well as Molecular Dynamics (MD) simulations [105, 168, 182, 183, 187, 306, 307]. These studies aimed to predict potential mutational sites within the LCC to enhance its enzymatic activity, resulting in LCC variants such as LCC F243I/D238C/S283C/Y127G (LCC^{ICCG}) [105], ICCG I6M [306], $ICCG_{DAQI}$ [305], LCC F125L/F243I [307], S101N/F243T ΔLCC [168], KIP, RIP, and KRP [133]. Notably, the discovery of PolyESter Hydrolase I (PES-H1) is a recent development, and at the initial stages of this project information on PES-H1 was lacking. Consequently, our investigation focused on probing the binding of a PET analogue, incorporating three TerePhthalic Acid (TPA) units, within the active site of PES-H1 using MD simulations. This collaborative project involved Prof. Dr. Uwe Bornscheuer, Dr. Ren Wei, Dr. Mark Doerr, and Dr. Lara Pfaff from the University of Greifswald (GER). It constituted a part of the crystallisation and experimental characterisation of PES-H1, also termed Polyester Hydrolase Leipzig 7 (PHL7), and its PET-degrading activity [202]. Our computational analysis aimed to achieve the following objectives:

1. Identify the predominant binding pose and assess the flexibility of a small PET analogue within the active site of PES-H1.

2. Characterise the primary interactions influencing PET binding and identify the involved residues.

3. Validate the co-crystallised PES-H1–substrate complex structures displaying intermediate binding poses.

4. Investigate the rationale behind the increased activity of the PES-H1 L92F/Q94Y ($PES\text{-}H1^{FY}$) variant compared to the Wild-Type (WT).

Additionally, this knowledge contributes significantly to interpreting the outcomes of the PET entry mechanism addressed thereafter.

The methods and results are extensively discussed in publication I, as a part of the crystallisation and experimental characterisation of PES-H1 and its PET-degrading activity [130] (A.2):

Publication I: Multiple Substrate Binding Mode-Guided Engineering of a Thermophilic PET Hydrolase

Lara Pfaff, Jian Gao, Zhishuai Li, Anna Jäckering, Gert Weber, Jan Mican, Yinping Chen, Weiliang Dong, Xu Han, Christian G. Feiler, Yu-Fei Ao, Christoffel P. S. Badenhorst, David Bednar, Gottfried J. Palm, Michael Lammers, Jiri Damborsky, Birgit Strodel, Weidong Liu, Uwe T. Bornscheuer*, and Ren Wei**

ACS Catal, 12(15), 9790-9800 (2022), DOI: 10.1021/acscatal.2c02275

My contribution to this publication involved modelling and simulating a PET analogue with three PET units in a productively bound conformation within the active site of PES-H1, a conformation which allows for subsequent PET hydrolysis by PES-H1. This encompassed the draft writing and figure production of the relevant manuscript section. In the following, a summary of the key findings that address the previously outlined project objectives is provided.

3.1 Résumé of Publication I

The co-crystallised structures of PES-H1 and a MHET Analogue (MHETA), 4-(2-hydroxyethylcarbamoyl) benzoic acid, revealed intermediate binding poses rather than productive ones. Productive binding involves short distances between the catalytic serine (S130) and the PET ester carbon (SER–C) and between the PET ester carbonyl oxygen and the amide hydrogens of the oxyanion hole (F62, M131) (OXY-O) to allow for hydrolysis, while intermediate binding requires reorientation.

To analyse productive binding and compare it with intermediate poses observed in crystal structures, we modelled the position of the central PET unit based on the productive position of 1-(2-HydroxyEthyl) 4-MethylTerephthalate (HEMT) in the crystal structure of a related PET-degrading enzyme, *Is*PETase (PDB: 5XH3[162]). Three independent simulations each lasting for 100 ns consistently maintained a productive binding pose, as evidenced by calculations of SER–C and OXY–O distances, as well as the Root-Mean-Square-Deviation (RMSD) indicating only slight structural fluctuations during the simulation. Structural cluster analysis based on RMSD of all sampled conformations in the three MD simulations revealed predominant binding poses with minor conformational differences of mainly terminal units between them, suggesting limited substrate flexibility (Fig. 3.1).

Analysis of the representative structures of the four most prominent clusters revealed predominant hydrophobic Lennard–Jones (LJ) interactions, primarily mediated by F62, W155, and I178. Aromatic amino acids F62 and W155 exhibited T-shaped π-π interactions with the benzene ring of PET, consistent with the co-crystallised structures [130, 133, 308]. The positions of these amino acids in the co-crystallised structures of PES-H1 and MHETA also suggest a strong involvement in binding via similar hydrophobic and aromatic interactions.

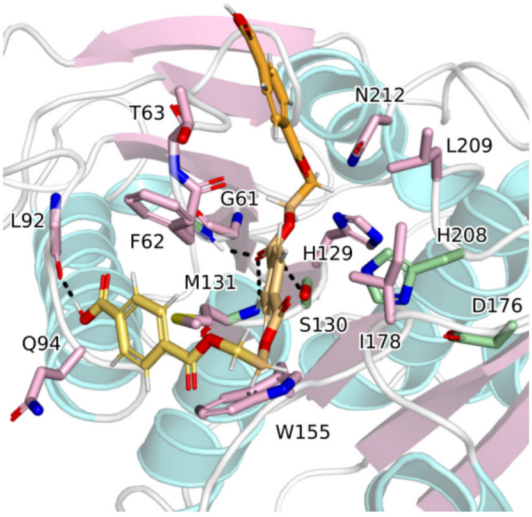


Fig. 3.1.: Representative binding pose of the most prominent cluster for the productive binding of a PET analogue in the active site of PES-H1. The side chains of the catalytic triad (S130, D176, H208) and the amide group of the oxyanion hole (F62, M131) are depicted in green, while all amino acids forming a binding interaction with PET through their side chains or backbone are shown in pink. The PET analogue, comprising three units, is shown in various shades of orange. Oxygen, nitrogen, sulfur, and hydrogen atoms are highlighted in red, blue, yellow, and white, respectively. The SER–C and OXY–O distances, as well as the hydrogen bonding of the terminal carboxyl group to L92, are indicated by black dashed lines. Adapted and modified from Pfaff *et al.* 2022 with permission [130].

It is assumed that F62 and W155 constitute an 'aromatic clamp' facilitating the correct positioning of the PET benzene ring [309]. Residues G61, T63, A64, L92, Q94, H129, M131, T157, H208, L209, and N212, making significant contributions to PET binding, were identified. Mutation sites L92F and Q94Y, present in the PES-H1^{FY} variant with notably enhanced PET-degrading activity, mainly contribute through hydrogen bonding with the terminal carboxyl group, which may be an artefact of using the shorter PET analogue in the simulations and would only be present in the case of exo-hydrolysis in polymeric PET (Fig. 3.1).

The position of the Y127G mutation in the highly active LCC^{ICCG} variant corresponds to the same position of the Q94Y mutation in the highly active PES-H1^{FY} variant. This indicates that the same amino acid, tyrosine, influences enzymatic activity differently at this position, once enhancing activity when present (PES-H1^{FY}) and once enhancing activity when removed (LCC^{ICCG}). As the mutation site is located close to, but not within the active site binding cleft, another mechanism than productive substrate binding might be affected by the mutations, which differs between the two enzymes.

3.2 Conclusion of Publication I

Our MD simulations provided valuable insights into the productive binding of a PET analogue in the active site of PES-H1, shedding light on key interactions and residues involved: (1) Identifying the predominant productive binding pose of a short PET analogue. (2) Identifying hydrophobic LJ and aromatic interactions, especially between F62, W155, I178 and the central PET unit, to be the main contributors to PET binding. (3) Validating the co-crystallised structures as potential intermediate binding poses. (4) Suggesting a potential role of the PES-H1^{FY} mutations in exo-scission and another mechanism different from productive binding to be responsible for the increased activity after comparison to LCC^{ICCG}.

We hypothesise that the PES-H1^{FY} mutations affect the entrance of the substrate to the binding site, which emphasises the significance of studying the entire binding process from initial adsorption to productive substrate binding through extensive MD simulations as aspired in the research endeavour presented next.

4 From PET Adsorption to Productive Binding

Up to date, several studies aimed to increase the activity of various Poly(Ethylene Terephthalate) (PET) hydrolases, but identifying uniform strategies appeared challenging. For example, activity can be enhanced when the binding cleft is widened or narrowed [164, 170, 172–174]. Considering the two target PET hydrolases of this study, the presence of a tyrosine at the same position exhibits different effects in variants, once increasing activity when removed (Y127G, Leaf-branch Compost Cutinase (LCC) to LCC F243I/D238C/S283C/Y127G (LCC^{ICCG})), and once increasing activity when introduced (Q94Y, PolyESter Hydrolase I (PES-H1) to PES-H1 L92F/Q94Y ($PES\text{-}H1^{FY}$)) alongside other mutations [105, 130]. A uniform strategy would immensely simplify the generation of industrially applicable PET hydrolases with improved properties. Thus, a deeper understanding of the PET degradation mechanism of PET hydrolases is required to unveil uniform activity-influencing factors. An effective PET degradation mechanism encompasses a multitude of processes: Fast and productive adsorption to the large polymer surface enabling a fast entrance of PET to the binding site and subsequent formation of a productive binding pose, constituting a pose enabling the subsequent conversion to the target product by reducing the activation free energy, and, finally, a fast liberation of the products. However, all these processes are complex on their own and might go along with slight conformational changes of the PET hydrolases and specific interactions involving single residues, which are sometimes difficult to address experimentally.

Our goal was to offer an in-depth understanding of the PET binding process, starting from the initial adsorption of LCC and PES-H1 onto an amorphous PET surface, progressing to effective PET binding within the active site, using comprehensive Molecular Dynamics (MD) simulations. Such a detailed computational analysis of the initial stages of enzymatic PET degradation, particularly the entry into the binding cleft, has not been conducted before. However, it emerges as highly promising, especially when considering the findings from the preceding section. These results led to the hypothesis that mutations in the highly active LCC^{ICCG} and $PES\text{-}H1^{FY}$ variants may enhance the entry mechanism rather than the productive binding (Sec. 3).

The methods and results for this endeavour are extensively discussed in publication II, which is currently under revision (Sec. A.2):

Publication II: From Bulk to Binding: Decoding the Entry of PET into Hydrolase Binding Pockets

Anna Jäckering, Frederike Göttsch, Moritz Schäffler, Mark Doerr, Uwe T. Bornscheuer, Ren Wei and Birgit Strodel

bioRxiv, 2024.04.21.590457, DOI: 10.1101/2024.04.21.590457,

My involvement in this publication encompasses all computational simulations and analyses, alongside the writing of the complete manuscript draft and figure creation. These efforts comprised extensive MD simulations of LCC or PES-H1 interacting with amorphous PET to investigate the adsorption process, analyse PET—enzyme interactions, and examine PET distribution on the enzyme surface, correlated with the enzyme's physicochemical properties. Furthermore, additional Hamiltonian Replica Exchange Molecular Dynamics (HREMD) simulations were carried out to explore the entry of a PET molecule into the active sites of both LCC and PES-H1. The entry pathway and the impact of individual residues on the associated energy barrier were scrutinised using Principle Component Analysis (PCA) and Free Energy Surface (FES) analyses. Based on these findings, we proposed potential mutations for the highly active LCC F243I/Y127G (LCC^{IG}) (derived from LCC^{ICCG}) and $PES\text{-}H1^{FY}$ variants, which were subsequently subjected to the same HREMD simulations and analyses.
The following sections offer an overview of the main findings presented in publication II.

4.1 PET Adsorption to the Enzyme's Surface

Efficient degradation necessitates the swift and effective adsorption of the enzyme to the PET substrate. This adsorption process is primarily governed by non-specific interactions, influenced by the physicochemical properties of the enzyme's surface, rather than specific binding sites [310–312]. While the adsorption can occur in proximity to the enzyme's active site (proximal), facilitating subsequent substrate binding, PET molecules may also first interact with regions of the enzyme's surface distant from its active site (distal). This necessitates an enzyme reorientation on the PET surface before effective substrate binding can occur [157, 313]. Enhancing the initial productive adsorption or facilitating the enzyme reorientation to transition from unproductive to productive adsorption stages would optimise enzymatic activity. Based on these insights, the objectives for this project section are delineated as follows:

1. Sample the adsorption dynamics of LCC and PES-H1 onto a substantial PET bulk, followed by the subsequent binding of PET molecules within the enzyme's active site by MD simulation.

2. Discriminate between productive and unproductive adsorption events. For instances of initial unproductive adsorption, elucidate the enzyme reorientation

process and the accompanying transition from unproductive to productive PET–enzyme interactions.

3. Characterise surface properties that facilitate either productive or unproductive adsorption and the transition from unproductive to productive binding.

4. Formulate a mutational strategy aimed at enhancing productive binding and assess the resultant enzyme variants both *in silico* and *in vitro*.

A concise overview of the principal outcomes corresponding to these objectives, as explored in section 2.1 of publication II, is presented below.

4.1.1 Résumé of publication II, Section 2.1

Adsorption was successfull sampled throughout the six MD simulations conducted over a duration of 1.5 μs for each PET hydrolase, starting from a structure containing either LCC or PES-H1 in a random orientation at least 10 Å from an amorphous PET bulk comprising 100 PET-9mers (Fig. 4.1). These simulations captured both productive and unproductive adsorption events, demonstrating extensive interactions with the enzyme's surface in both proximal and distal regions with respect to the binding site (Fig. 4.2A).

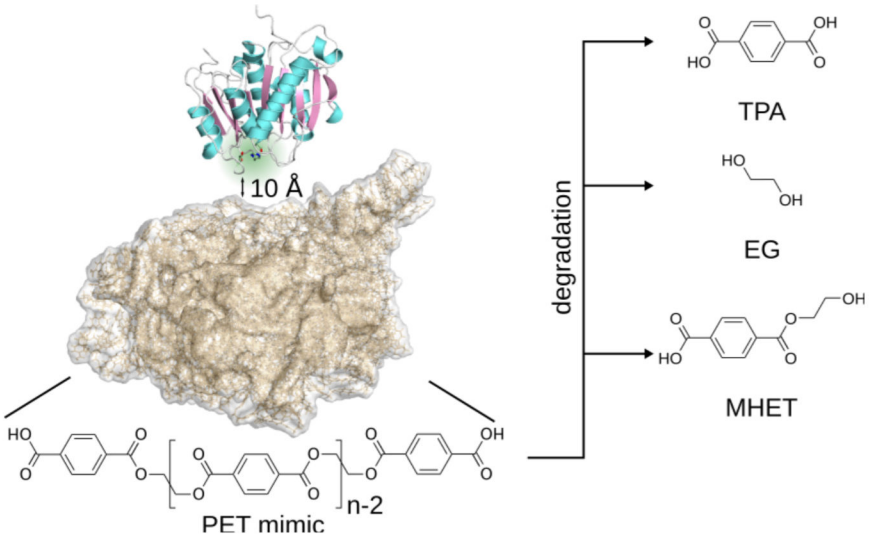


Fig. 4.1.: Representative starting structure for the MD simulations of enzyme adsorption on amorphous PET. The system comprises one PET hydrolase, either LCC or PES-H1, which is shown as cartoon and with the catalytic triad highlighted in green. Water and ions are not shown. The enzyme was randomly oriented and placed at least 10 Å away from the PET bulk, which is shown as brown surface and consists of 100 PET-9mers (n=9). The chemical structure of PET is shown at the bottom and the degradation products of PET, TerePhthalic Acid (TPA), Ethylene Glycol (EG), and Mono(2-HydroxyEthyl) Terephthalic acid (MHET) are shown on the right. Adapted from publication II (Sec. A.2).

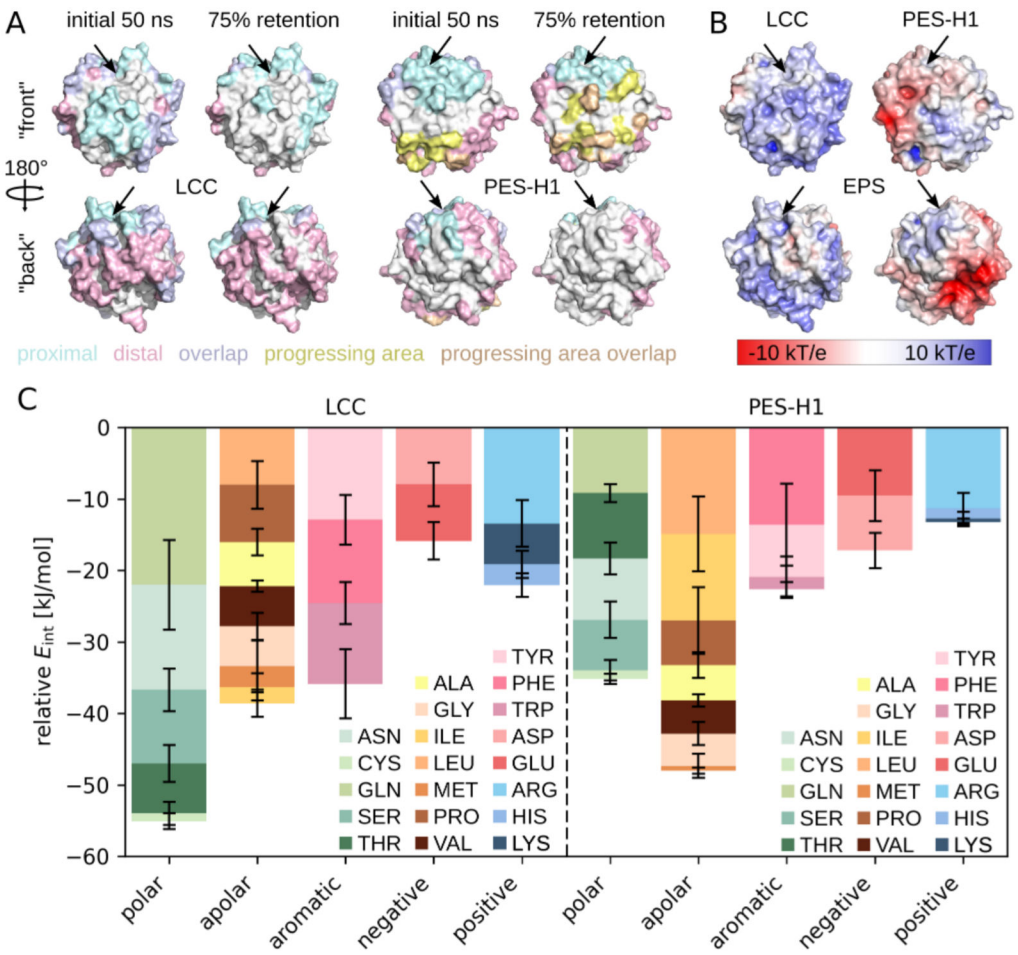


Fig. 4.2.: Analysis of LCC and PES-H1 adsorption on amorphous PET. (A) Residues contacting PET are highlighted on LCC (left) and PES-H1 (right) surfaces, using all six simulations per enzyme with a 3 Å PET–residue distance cutoff. Contacts during the initial 50 ns (left) and stable contacts present for at least 75% of the full duration (right) are distinguished, with proximal (blue) and distal (rose) binding sites. Overlapping areas are coloured violet. Some simulations show enzyme reorientation on PET bulk, with limited progression from distal to proximal binding, except in one PES-H1 simulation (highlighted in yellow). Overlaps with proximal or distal contact areas are highlighted in brown. The position of the catalytic triad is denoted by an arrow. (B) Electrostatic Potential Surface (EPS) for LCC (left, net charge: $+5$) and PES-H1 (right, net charge: -5). (C) PET interaction energies E_{int} with amino acid types in LCC and PES-H1 are shown relative to the number of the corresponding residues within 3 Å, averaged over all simulations. Energies for amino acid types with the same physicochemical characteristics are summed up, with Standard Error of the Mean (SEM) shown as error bars. Adapted from publication II (Sec. A.2).

The regions of adsorption displayed minimal movement, with the majority of interactions being established for at least 75% of the overall simulation period. Among the simulations, only one involving PES-H1 demonstrated a transition in PET–enzyme contacts from distal to proximal sites. This enabled a shift from unproductive to productive adsorption through enzyme reorientation. Despite extending the most promising simulations, which displayed productive adsorption, to 2 μs, no pene-

tration of a PET-9mer into the binding cleft was observed, and consequently, no productive binding configuration was sampled. This suggests the presence of an energy barrier during PET entry into the active site, which could not be surmounted using comprehensive conventional MD simulations. This phenomenon will be elaborated upon in the subsequent section (Sec. 4.2).

Analysis of the enzyme's surface characteristics revealed an Electrostatic Potential Surface (EPS) corresponding to the protein's net charge: A notably negative surface potential was observed for PES-H1, possessing a net charge of -5, whereas LCC exhibits a relatively positive surface potential with a net charge of $+5$ (Fig. 4.2B). Comparative examination with the contact distribution indicated a significant alignment of negative surface potentials with regions showing sparse or no PET contacts, notably exemplified by a large, strongly negative distal surface patch of PES-H1 (Fig. 4.2A and B). Considering the EPS of PET, which predominantly presents a negative surface potential on convex and exposed areas, while buried segments exhibit relatively positive potentials (Fig. Appendix 1(A1)), a scenario of repulsion between the negative PET and the enzyme surface seems plausible. Conversely, a positively charged or hydrophobic enzyme surface appears to facilitate PET contacts, a notion supported by existing literature [155–157].

In addition to surface charge, the identification of amino acids that either enhance or hinder PET interactions is crucial for guiding a mutation strategy. For this purpose, the interaction energy E_{int} between PET and individual amino acid types was computed and normalised based on the number of residues of the corresponding type in contact with PET. This accounts for the specific presence and accessibility of polar amino acids on protein surfaces. The contribution profile, categorised by groups of amino acids sharing similar physicochemical properties, indicates a preference for apolar residues over polar ones in PES-H1, and conversely, a preference for polar residues over apolar ones in LCC. In both cases, interactions with charged amino acids are least favoured, followed by aromatic residues (Fig. 4.2C). The stronger overall interaction observed with LCC, coupled with the exclusive contact progression in PES-H1, implies that weaker interactions, especially in distal regions, promote contact progression, leading to enhanced proximal binding and enzymatic activity. Based on these findings, we postulate that promoting a contribution profile akin to that of PES-H1, characterised by a stronger hydrophobic rather than polar contribution, enhances PET degradation activity. This hypothesis finds support in existing literature [122, 123, 158].

Building upon these findings, our mutation strategy focuses on altering the local surface characteristics in the distal regions of both enzymes. This is achieved by introducing three mutations in close proximity to weaken PET binding. Specifically, we aim to replace polar and positively charged residues with apolar and negatively charged counterparts of comparable size. Our approach is underpinned by the Sabatier principle, which posits the existence of an optimal relationship between interaction strength and activity [314]. In the context of LCC, this principle has

been shown to yield maximal activity with intermediate PET binding strength, which is lowered by the addition of cationic surfactants [159]. As reference and parent enzymes for incorporating the mutations, we selected the high-activity variants LCC^{ICCG} and PES-H1^{FY}. The LCC^{IG} variant is derived from LCC^{ICCG} but lacks the stabilising disulfide bridge, thereby eliminating the influence of reduced negative charge resulting from the D238C mutation. Both the LCC^{IG} and PES-H1^{FY} variants, along with their corresponding triple mutants, were subjected to MD simulations in triplicate. These simulations commenced from conformations with the shortest PET–mutation site distances, as determined from prior simulations of the Wild-Type (WT) enzymes following the introduction of the respective mutations. Comparative analysis of the EPS and interaction energy E_{int} of the residues at the mutation sites confirmed a successful local alteration in surface charge and PET binding strength, particularly when small apolar alanine residues or negatively charged residues were introduced (Fig. 4.3). These changes were more significant for LCC^{IG} as necessitated to assimilate it's surface to that of PES-H1^{FY} as aimed for in our mutation strategy.

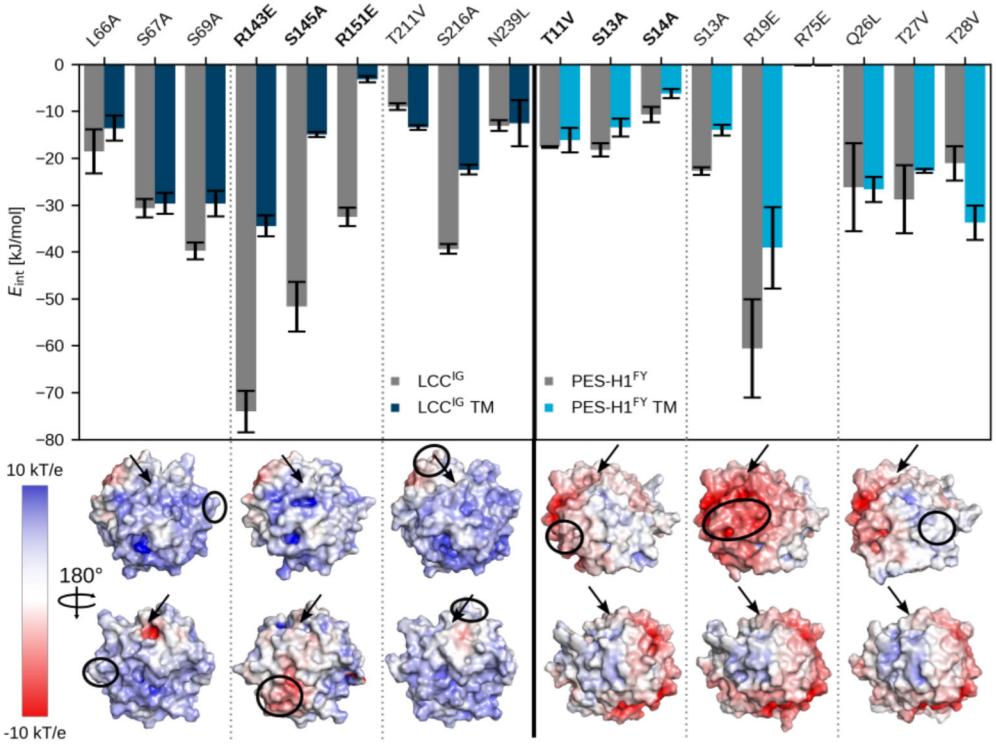


Fig. 4.3.: Results for the *in silico* mutation of surface residues. (Top) The interaction energies (E_{int}) between PET and the residues of LCC^{IG} (left) and PES-H1^{FY} (right) at mutation sites are shown for the parent enzyme LCC^{IG} or PES-H1^{FY} (gray) and the three TMs per enzyme (dark blue for LCC^{IG}, light blue for PES-H1^{FY}). The mutations are given at the top, the TMs are separated by vertical dotted lines and the TMs evaluated *in vitro* are highlighted in bold. The E_{int} values are averages over three simulations with the PET given by error bars. (Bottom) The EPS of the TMs are shown. The locations of the mutations are denoted by black circles and the catalytic site is indicated by an arrow. Adapted from publication II (Sec. A.2).

Nevertheless, no enzyme reorientation and PET–enzyme contact progression was observed during the limited simulation time of 100 ns.

The most promising triple mutants for each enzyme were subsequently evaluated experimentally by our collaborators at the University of Greifswald. For this assessment, the original LCC^{ICCG} variant was employed as a template instead of LCC^{IG} to facilitate a more accurate comparison with previously published experimental data [105, 130]. Unfortunately, the LCC^{ICCG} R143E/S145A/R151E triple mutant could not be expressed, possibly due to mutations interfering with native protein folding. Additionally, the PES-$H1^{FY}$ T11V/S13A/S14A mutant exhibited a markedly reduced percentage PET weight loss after 24 h of incubation, indicative of diminished PET degradation activity (Fig. A2). This outcome contradicts our initial hypothesis suggesting that a more negatively charged or hydrophobic surface could attenuate distal PET binding, thereby facilitating contact progression, proximal binding, productive adsorption, and ultimately, PET degradation activity. Conversely, these results underscore the significance of comprehending enzymatic adsorption to PET. It is noteworthy that even minor alterations, such as three mutations distal to the binding site that do not directly impact substrate binding and conversion, can exert a substantial influence on enzyme activity, likely mediated through their effects on adsorption.

4.1.2 Conclusion of publication II, Section 2.1

This study represents the most detailed computational investigation of PET–enzyme adsorption conducted to date, providing valuable information on the influence of enzyme surface characteristics on productive adsorption: (1) Adsorption of the target PET hydrolases, LCC and PES-H1, to an amorphous PET bulk was sampled through extensive MD simulations, while penetration of a PET-9mer into the binding site could not be captured, suggesting the existence of a considerable energy barrier upon entry. (2) Both productive and unproductive adsorption behaviours were comprehensively explored, while progression from distal to proximal contacts was observed in only one PES-H1 simulation, underscoring the significance of facilitating contact progression and productive adsorption to enhance enzymatic activity. (3) Positive surface potentials were found to promote overall PET binding, whereas negative potentials hindered it. Additionally, weak interactions with apolar residues were identified as potentially facilitating contact progression. (4) Based on these insights, our strategy aimed to attenuate distal PET binding in LCC^{IG} and PES-$H1^{FY}$ triple mutants by substituting positively charged and polar residues with negatively charged and apolar counterparts. Although the local PET interaction energy was effectively diminished *in silico*, particularly with the introduction of alanine and negative charge, the most promising variants subjected to *in vitro* evaluation either could not be expressed, potentially due to disrupted native folding, or exhibited substantially reduced activity.

Our results emphasise the critical nature of investigating this initial step in en-

zymatic PET degradation as three distal mutations largely impact the activity of PES-H1^{FY}, although it is not assumed that they directly influence activity but rather modulate adsorption behaviour. Furthermore, the presence of an obstructive energy barrier is implied, requiring further exploration of the subsequent phase in enzymatic PET degradation following productive adsorption: the penetration into the binding site.

4.2 PET's entry to the binding site

The enzymatic degradation of polymer materials presents challenges, primarily due to the difficulties associated with accessing the enzyme's binding site [102, 171]. Attack sites, such as the ester bond in PET, often remain inaccessible, particularly in polymers with a higher degree of crystallinity. For effective interaction with enzymes, a polymer chain must be sufficiently flexible to adopt a conformation that enables it to fit into the enzyme's binding cleft [101, 315, 316]. To enhance the accessibility and enzymatic turnover of PET, pre-processing methods and suitable reaction conditions are typically employed to reduce chain length, increase amorphicity and PET mobility [317–320]. However, the mechanism underlying PET entry into the active site remains incompletely understood, hindering progress in enzyme engineering aimed at facilitating productive PET binding. Although it has been demonstrated that PET can adopt either a pro-*S* or an unfavourable pro-*R* binding pose (Fig. 4.4B), the specific mode of hydrolysis – either exo-type (starting from the termini) or endo-type (originating from a central part of a PET chain) – remains ambiguous [98, 101, 181, 197, 198, 321, 322]. Additionally, debates persist regarding whether PET degradation occurs through a successive 'hopping and sliding' mechanism or a 'bind, cleave, and release' process [181]. Studying substrate entry presents significant challenges both *in vitro* and *in silico*. Commonly used computational methods, such as metadynamics, necessitate the definition of a Collective Variable (CV) to describe the entry pathway adequately [323]. This is particularly challenging with long, flexible polymers like PET, and may inadvertently bias towards a specific entry route while overlooking alternative possibilities. Consequently, the entry of PET into the binding cleft of PET hydrolases remains largely unexplored, leading to mere speculative assumptions, for example regarding the potential benefits of a wider binding cleft for facilitating easier access [164, 172–174]. Given the critical importance of unhindered substrate entry for enzyme functionality, as corroborated by our previous simulations suggesting the presence of an energy barrier obstructing entry, it is imperative to surmount these challenges and gain deeper insights into this process. In pursuit of this purpose, we aim to bridge this knowledge gap and propose an innovative approach to investigate the entry of lengthy substrates such as PET. Specifically, our objectives are as follows:

1. Utilise the enhanced sampling HREMD method to sample PET entry into the binding sites of LCC and PES-H1, and assess the presence of an energy barrier during this process.

2. Analyse factors influencing PET entry and potential associated energy barriers, including:

   a) Computational simulation setup

   b) Intramolecular PET–PET interactions

   c) Intermolecular PET–residue interactions

3. Formulate a mutation strategy to promote PET entry based on the obtained results and evaluate the corresponding variants both *in silico* and *in vitro*.

4. Identify the predominant PET entry pathways.

The following section offers a summary of the principal outcomes discussed in Section 2.2 of publication II, aligned with the objectives delineated for this project.

4.2.1 Résumé of publication II, Section 2.2

Three conformations derived from prior MD simulations, conducted for 2 μs, met the criterion of a maximum distance of 5 Å between the catalytic serine and PET. These conformations were utilised as initial structures in which all PET molecules excluding the nearest one were eliminated, and the remaining PET chain was truncated, only keeping the five PET units (PET-5mer) that are closest to the active site (Fig. 4.4A). Conformations derived from LCC MD simulations were aligned and interchanged with PES-H1, and vice versa, yielding three initial structures per enzyme. Throughout numerous HREMD simulations, executed over 115 ns with six replicas employing a modified Hamiltonian corresponding to temperatures ranging from 300 to 600 K, multiple entry events were observed. This was evidenced by a reduction from >6 Å to <4 Å in the distance between the catalytic serine's γ-oxygen and the PET-5mer ester's carbon (SER–C distance), accompanied by the adoption of a productive binding orientation (Fig. 4.4C). These orientations encompassed both pro-*S* and pro-*R* conformations, potentially leading to exo- and endo-type hydrolysis (Fig. 4.4B). The enzymes displayed interactions predominantly with a restricted set of PET units adjacent to the productively bound ester, instead of simultaneous binding of several PET units in an elongated conformation, which suggests a dynamic binding [88, 181].

Analysis of the correlation between replica number and the SER–C distance corroborated the presence of an energy barrier. This was evidenced by PET predominantly occupying high-energy replicas during the entry phase, subsequently transitioning to low-energy replicas within the binding cleft (Fig. 4.4C). First, we examined the potential impact of our computational setup choices on the observed energy barrier, with particular emphasis on pre-processing considerations such as the number of

PET chains present in the system (i.e. bulk vs. a single PET chain) or PET chain length, and reaction conditions like temperature. Conventional MD simulations of the HREMD starting structures conducted at an elevated temperature of 343 K facilitated the sampling of entry events: once, when the system retained the entire PET bulk, and multiple entries were recorded when only the nearest PET-5mer was kept. In contrast, no entry events were identified in conventional MD simulations considering a single PET-5mer at 303 K. These observations underscore the critical role of augmented PET chain mobility in enabling the adoption of a conformation capable of accessing the binding cleft. The intramolecular PET–PET interaction energy (E_{int}) between non-adjacent PET units during the entry events sampled in the HREMD simulations, coupled with the FES derived from E_{int} and the SER–C distance, corroborates this observation. These analyses suggest a predominant inhibitory influence on PET entry, attributable to the stabilisation of unbound conformations (Figs. A3 and A4). To surmount this intramolecular PET–PET interaction and increase PET mobility and accessibility, several strategies can be employed.

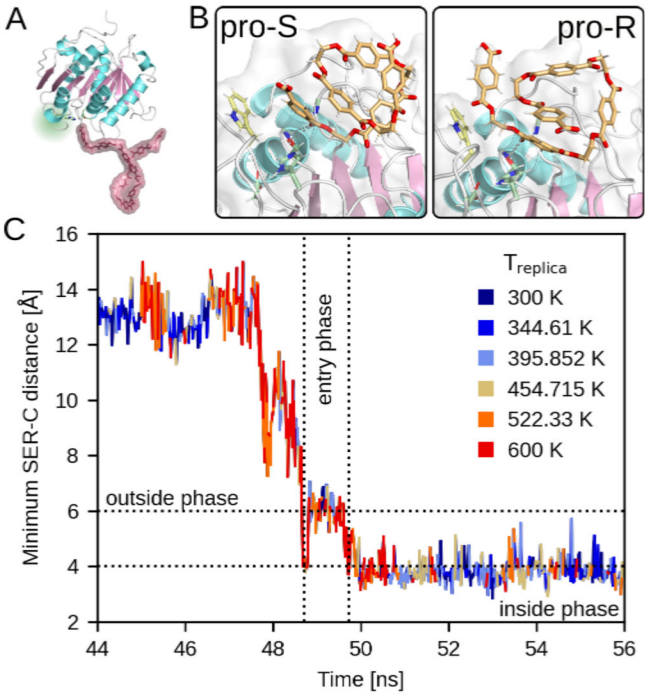


Fig. 4.4.: Setup for HREMD simulations and PET entry results. (A) An exemplary HREMD starting structure is shown to demonstrate the initial distance between the PET chain (here still with 9 units) and the enzyme. (B) PET entry into the active site resulted in pro-*S* and pro-*R* poses, for which representative snapshots are shown. (C) The entry of PET to the active site was monitored by the evolution of the SER–C distance. Here, a representative entry is shown for LCC. The entry was facilitated by the replicas at high energies/temperatures (coloured in orange to red), while conformations from replicas simulated at low energies/temperatures are coloured in shades of blue (see colour key for exact values). The dotted lines indicate the boundaries for the outside, entry, and inside phases, which are defined by the distance criteria (horizontal lines) and resulting times (vertical lines). Adapted from publication II (Sec. A.2).

These include pre-processing techniques aimed at enlargening the PET surface or increasing the surface amorphization and customised reaction conditions, such as elevating the temperature [98]. Additionally, intermolecular PET–enzyme interactions can compensate for the energy barriers. To this end, we computed the intermolecular interaction energy, E_{int}, between the PET-5mer and residues close to PET during the entry process. Similar to the intramolecular PET–PET interaction energy analysis, the E_{int} during entry revealed interactions that either promote entry by stabilising the substrate-bound states or facilitate entrance through interactions with the PET-5mer prior to and during entry, potentially compensating for the loss of intramolecular PET–PET interaction (Fig. A6). Concurrently, we identified interactions that hinder entry by stabilising the unbound states.

To condense the data for individual residues, we generated FESs using E_{int} and the SER–C distances of WT LCC and PES-H1. For comparison, we additionally investigated the impact of mutation sites in the LCC$^{\text{IG}}$ and PES-H1$^{\text{FY}}$ variants, namely PES-H1$^{\text{FY}}$ L92F (equivalent to F125 in LCC), PES-H1$^{\text{FY}}$ Q94Y and LCC$^{\text{IG}}$ Y127G, and LCC$^{\text{IG}}$ F243I (analogous to L209 in PES-H1). For LCC, the F125L variant demonstrated heightened activity due to reduced LCC binding to PET surfaces, thereby enhancing the degradation of intermediates in solution [307]. In contrast, for PES-H1, mutations at position L209 were scrutinised in two studies yielding disparate outcomes. Nevertheless, both studies reported a PET degradation activity of the L209A variant comparable to the WT [130, 202]. To comprehensively address all three mutation sites, we conducted additional HREMD simulations for the LCC$^{\text{IG}}$ and PES-H1$^{\text{FY}}$ variants, including the LCC$^{\text{IG}}$ F125L and PES-H1$^{\text{FY}}$ L209A variants. Comparative analysis of the FES for WT residues and mutated residues at the PES-H1$^{\text{FY}}$ 209/LCC$^{\text{IG}}$ 243 position unveiled entrance-promoting effects, characterised by: (1) emergence or enhancement of free energy minima at SER–C distances below 4 Å, stabilising bound states; (2) diminished minima at SER–C distances exceeding 6 Å, destabilising unbound states; (3) low-energy pathways facilitating transitions from unbound to bound states, along with the disappearance of isolated states, enabling a seamless transition towards bound states without crossing high-energy barriers (Fig. 4.5). However, the effects at the other two mutation positions diverged: the LCC$^{\text{IG}}$ Y127G mutation and the additional F125L mutation exhibited entry-promoting effects, whereas both mutations present in the PES-H1$^{\text{FY}}$ variant appeared to impede PET entry. In conclusion, we posit that the augmented PET degradation activity in LCC$^{\text{ICCG}}$ may stem from a direct enhancement of PET entry by the mutated residues, albeit through differing mechanisms in the case of PES-H1$^{\text{FY}}$.

In light of our findings, our objective is to enhance PET entry for both LCC$^{\text{IG}}$ and PES-H1$^{\text{FY}}$ variants by targeting residues that lack entry-promoting FES characteristics. Subsequently, these residues will be mutated to small residues, such as glycine or alanine, to mitigate entry-hindering interactions and sterical effects. Following HREMD simulations of the 14 resultant variants, a comparative analysis of the WT and variant FES substantiated a successful enhancement of entry-promoting FES fea-

tures (Figs. A7 and A5, and Tab. A1).The improvements manifested in: (1) Enhanced stabilisation of bound states (PES-H1^{FY}: S68A, D93A; LCC^{IG}: T211G, N246A), (2) Diminished interactions in unbound states (PES-H1^{FY}: S68A, R91A, D93A, N212A; LCC^{IG}: T192G, S241G), and (3) Facilitated smooth transitions towards bound states, lacking intermediate states where PET could become entrapped (PES-H1^{FY}: S68A, D93A; LCC^{IG}: HIS164A, T211G, S241G, N246A).

The five most promising mutations per enzyme underwent experimental evaluation by our collaboration partners at the University of Greifswald (Fig. A7).

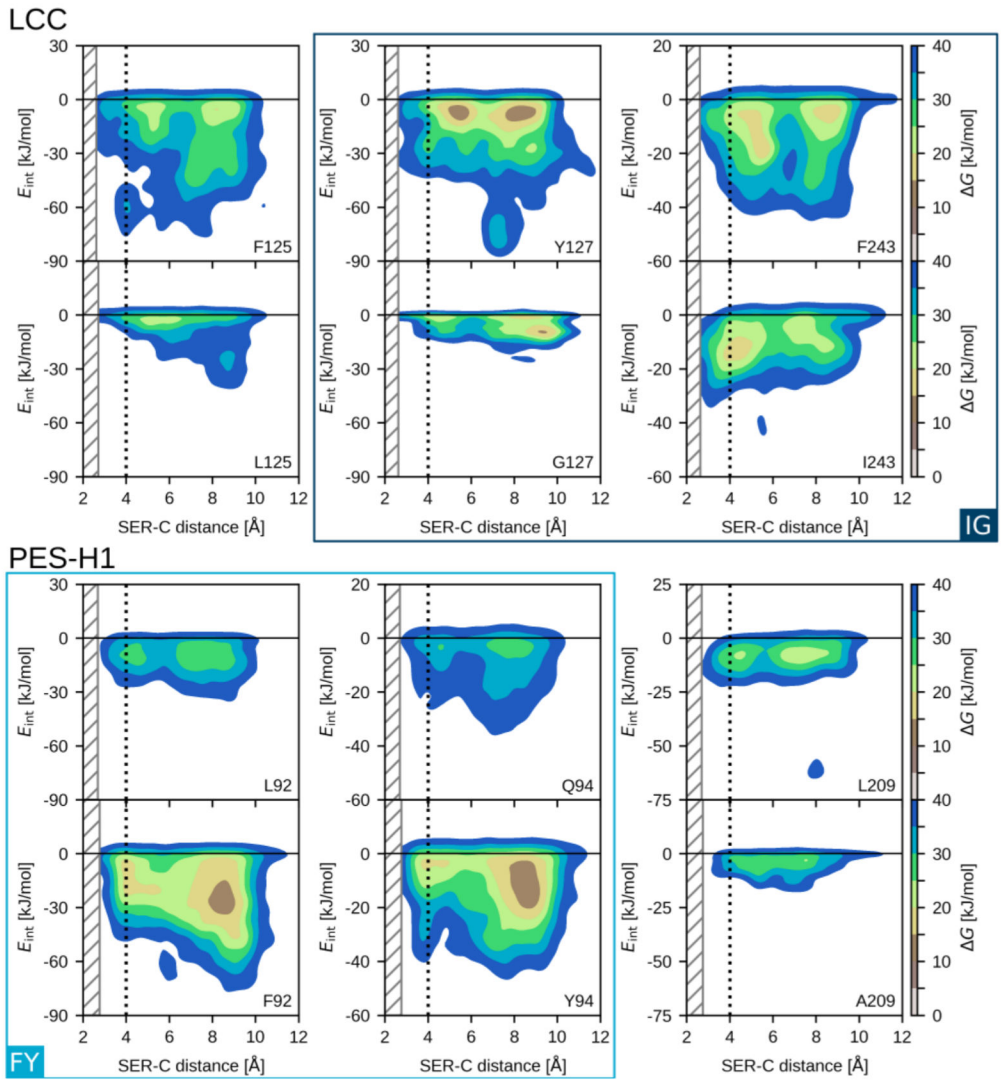


Fig. 4.5.: FESs of the intermolecular PET–residue interactions over the SER–C distance. The top row per enzyme presents the FESs for residues present in the WT LCC and PES-H1, and the bottom row for the mutated residues in the LCC^{IG}/PES-H1^{FY} variants (indicated by blue boxes) and for the LCC^{IG} F125L/PES-H1^{FY} L209A variants. The area for SER–C distance < 4 Å harbours productive poses. The grey hatched area indicates distances that were not sampled as the ester carbon atom would be too close to the catalytic serine. The free energies, ΔG are given in kJ/mol according to the colour scale on the right. Adapted from publication II (Sec. A.2).

For a more directly comparable assessment with published experimental findings [105, 202, 324], these mutations were incorporated into the LCC^{ICCG} variants instead of the LCC^{IG} variant utilised for *in silico* evaluation. The percentage PET weight loss after enzymatic degradation did not indicate increased activity for any variant. However, variants with less promising FES, predominantly characterised by destabilising effects on unbound states, demonstrated significantly reduced weight loss compared to either LCC^{ICCG} or PES-$H1^{FY}$. To delve deeper into the degradation kinetics of the top three promising variants per enzyme, a turbidimetric assay was executed [130, 325]. In addition to the conventional Michaelis–Menten (^{conv}MM) kinetics, an inverse Michaelis–Menten (^{inv}MM) approach was employed, wherein enzyme concentration was varied while maintaining a consistent substrate load (Tab. A1). This methodology is often employed for insoluble substrates like PET [159, 308, 321, 326–329].

Among these, the PES-$H1^{FY}$ S68A variant exhibited the most promising performance, demonstrating enhanced catalytic efficiency ($^{molar}\eta$) and an approximate three-fold reduction in $^{inv}K_m$, thereby indicating increased substrate affinity relative to PES-$H1^{FY}$. For LCC^{ICCG}, the LCC^{ICCG} T211G variant exhibited the most substantial enhancement in $^{molar}\eta$ compared to the wild-type LCC^{ICCG}. Encouragingly, both variants corresponded well with the most favourable FES alterations, thus affirming a high degree of alignment between computational analyses and experimental outcomes (Fig. A7).

To scrutinise the impact of side-chain characteristics such as size, polarity, charge, and aromaticity at position 68 on the most promising variant, PES-$H1^{FY}$ S68A, we computationally designed and evaluated additional variants: S68I, S68F, S68Q, S68D, and S68K (Fig. A8). The initially selected S68A variant displayed the most favourable FES, while all alternative variants exhibited features that hinder entry. Our analysis suggests that interactions at position 68 may generally be unfavourable. Specifically, side-chains larger than the small alanine might sterically impede substrate entrance, underscoring the importance of side-chain size and characteristics in modulating enzymatic activity and substrate specificity.

The aggregation of data from both the WT and variant datasets provided a comprehensive dataset, which was employed for PCA to elucidate the primary entry pathways. In this context, we computed the SER–C distances and the distances between the C_α atom of each residue and the carbon of the PET-5mer ester intended for productive binding, both during entry and the initial 1 ns of the bound state. The FES derived from the first two PCs, accounting for a cumulative variance of 86%, effectively differentiated between bound and unbound states (Fig. A9). Moreover, three predominant entry pathways were consistently identified across both enzymes (Fig. 4.6). Notably, the favoured pathway originates from the side opposite to the 'wobbling' tryptophan towards the active site, corroborating findings from previous research [181].

A detailed assessment of each residue's contribution to PC1 highlighted 49 relevant

positions. This underscores the intricacy involved in the entry of large polymers and the challenges associated with CV-based entry sampling techniques like metadynamics [323]. In contrast, our HREMD-based approach offers an easy alternative to sample polymer entries. Notably, alongside the pronounced contributions from the mutation sites of the LCC^{IG} and PES-H1^{FY} variants to PC1, position 68 of PES-H1 emerged as the most influential (Fig. A9). This residue, identified as the most promising variant through both *in silico* and *in vitro* evaluations in our study, aligns with one end of the binding cleft, alongside L209 of PES-H1 (Tab. A1, and Fig. 4.5). Our findings provide further validation to our earlier hypothesis, suggesting that this particular position could indeed serve as a steric hindrance to the primary entry pathway, which can be prevented by mutation to a small residue like alanine (Figs. 4.6 and A5).

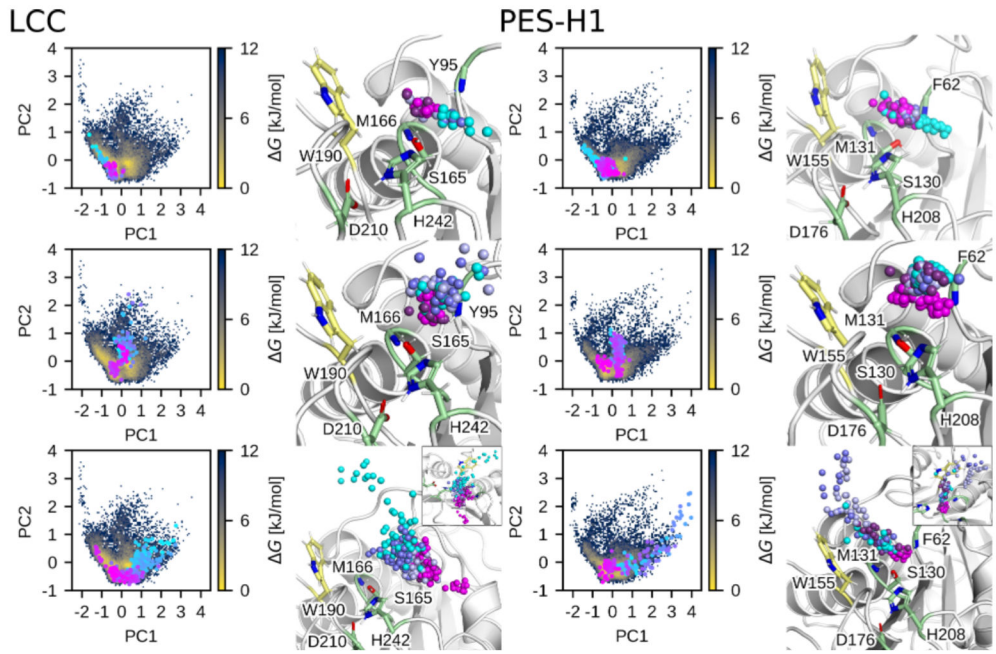


Fig. 4.6.: The three preferred entry pathways of a PET-5mer. The pathways were revealed by PCA applied to the HREMD data involving the simulations of all LCC (left) and PES-H1 (right) variants performed in this work. For each pathway, a representative example is shown. The pathways are mapped as circles on the FES in the PC1,PC2 plane of either enzyme and are also shown (as spheres) together with the corresponding enzyme structure. The progress of each pathway is highlighted by the colour change from cyan to magenta. In the structure plots, the spheres show the positions of the PET-5mer ester carbon that is finally productively bound. Adapted from publication II (Sec. A.2).

4.2.2 Conclusion of publication II, Section 2.2

In this study, we explored the entry of PET and its associated pathways for the first time, offering valuable insights into this hitherto overlooked aspect of enzymatic PET degradation: (1) Our HREMD simulations effectively facilitated the sampling of PET-5mer entries for both target PET hydrolases, LCC and PES-H1. This was achieved through exchanges to higher-energy replicas, thereby confirming the pres-

ence of an energy barrier during entry. The resultant productive binding poses comprised both pro-*R* and pro-*S* configurations, suggesting potential for both exo- and endo-type hydrolysis. (2) We elucidated several factors influencing the entry process, including: (a) The importance of PET's conformational flexibility, which is enhanced by elevated temperatures; (b) Intramolecular PET–PET interactions that predominantly impede conformational flexibility and, consequently, entry; and (c) Intermolecular PET–residue interactions, which can either facilitate or obstruct PET entry to the binding site. These interactions stabilise either the bound or unbound states or potentially aid in the required conformational changes of PET during entry by compensating for the loss of intramolecular PET–PET interactions. (3) Our mutation strategy, aimed at promoting PET entry by identifying and mutating residues that hinder entry, yielded promising variants as evidenced by *in silico* evaluations. While experimentally assessed activities were either comparable to or lower than the WT, several variants exhibited improved kinetics. Notably, PES-H1^{FY} S68A emerged as the most promising variant, followed by LCC^{ICCG} T211G. (4) Through PCA, we identified three predominant entry pathways. The different entry routes suggest a 'bind, cleave, unbind' mechanism rather than a consecutive 'hopping and sliding' process, which would take place via one defined pathway. The residue contributions to PC1 underscored the significance of the PES-H1 position 68, potentially serving as a steric hindrance for the preferred pathway.

Our comprehensive computational investigation addresses a significant research gap concerning the entry mechanism of PET hydrolases. To facilitate this, we offer a novel, unbiased approach for studying entries of large substrates such as the polymer PET, eliminating the need to define CVs. This innovation expands the computational toolkit and simplifies the exploration of a previously challenging aspect in biocatalysis: the entry of large substrates into the enzyme's binding site. Our comprehensive investigation unveiled energy barriers and entry-hindering effects, pinpointing promising targets for future enzyme engineering to enhance the PET degradation capability of these hydrolases. Nonetheless, entry into the binding site represents just one facet of the complete PET degradation mechanism. This may explain why the predicted variants aimed at promoting PET entry might not fully achieve the desired catalytic activity. Consequently, a holistic approach targeting the entire enzymatic process is essential for successful enzyme engineering.

Acylation of PET

5

A pivotal facet of biocatalysis resides in the enzymatically facilitated substrate conversion, subsequent to the aforementioned processes of adsorption, substrate entry into the active site, and productive binding. Given that the architecture of the active site is optimally configured to stabilise transition states, thereby diminishing the activation free energy for the desired chemical transformation, even minor alterations in composition or conformation can exert pronounced effects on the mechanistic pathway [330]. Advanced hybrid Molecular Mechanics / Quantum Mechanics (QM/MM) simulations at atomic resolution can delineate these nuanced effects. The first QM/MM investigation on Poly(Ethylene Terephthalate) (PET) hydrolases was published in 2021 by Boneta *et al.* [182], followed by several other studies [184, 185, 190, 192].

However, these studies exhibited inconsistencies, positing either a one- or a two-step mechanism for the acylation, and applying varying methods diverging in their choice of Quantum Mechanics (QM) method, the size of the QM region and the specific CVs considered [182, 186, 189, 191]. It remains ambiguous whether the difference in the amount of steps is a result of the differing simulation settings, necessitating clarification to enhance coherence of future research endeavours.

Furthermore, an important aspect of PET hydrolysis has not yet been fully explored: The impact of the 'wobbling' tryptophan. Han *et al.* [162] propose that a change from T-stacking to a parallel π–π interaction between this amino acid and the benzene moiety of PET facilitate product release. Although prior investigations have examined the three distinct conformations of the 'wobbling tryptophan [176–178], the conformational alteration of the PET benzene moiety has not been elucidated comprehensively.

In addition to these uncertainties, to date, no QM/MM investigation has been directed towards elucidating the catalytic mechanism of PolyESter Hydrolase I (PES-H1) and its highly active PES-H1 L92F/Q94Y (PES-H1^{FY}) variant [130]. Notably, QM/MM studies of several earlier discovered PET hydrolases encompassed only the LCC F243I/D238C/S283C/Y127G (LCC^{ICCG}) variant; however, no comparative analysis with WT Leaf-branch Compost Cutinase (LCC) has been conducted to delineate the origins of enhanced enzymatic activity [105, 182, 183, 187, 188, 191]. Consequently, our objective is to bridge this knowledge gap, which is important for developing uniform strategies for subsequent PET hydrolase engineering endeavours. Furthermore, particular attention is directed towards the potential stabilisation of the Michaelis Complex (MC), thereby testing the hypotheses posited regarding putative entry-facilitating features discussed in the previous chapter (Sec. 4.2).

In this project, our goal is to clarify both mechanistic and methodological aspects

that will greatly enhance forthcoming QM/MM investigations of PET hydrolases and associated engineering pursuits. The key objectives of our study include:

1. Sampling the initial stage of biocatalytic PET degradation, the acylation, for LCC and PES-H1, as well as their highly active variants, LCC F243I/Y127G (LCC^{IG}) (derived from LCC^{ICCG}) and PES-$H1^{FY}$, utilising QM/MM simulations employing the Adaptive String Method (ASM).
2. Systematically monitoring and analysing potential conformational changes within the PET substrate and the dynamic behaviour of the 'wobbling' tryptophan residue.
3. Scrutinising potential factors affecting the sampling procedure and the resulting Potential of Mean Force (PMF), such as the selection of QM methodologies and the Collective Variables (CVs) employed for characterising PET acylation.
4. Constructing the final PMF profiles related to the acylation process and conducting comparative assessments between WT enzymes and their respective derivatives, with a particular focus on discerning potential stabilisation of the MC.

A comprehensive discussion of the methodologies and findings can be found in manuscript I (A.2):

Manuscript I: Influence of Wobbling Tryptophan and Mutations on PET Degradation Explored by QM/MM Free Energy Calculations
Anna Jäckering, Marc van der Kamp, Birgit Strodel and Kirill Zinovjev,
(submitted to peer reviewed journal)

My contribution to this manuscript involves all computational simulations and analyses, as well as writing the initial manuscript draft and the creation of figures.

The following section provide a summary of the principal findings delineated in manuscript I.

5.1 Résumé of manuscript I

We have successfully investigated the acylation process of PET involving four enzymes: PES-H1, PES-$H1^{FY}$, LCC, and LCC^{IG}. The latter represents LCC^{ICCG} with the omission of two cysteine mutations that introduce a stabilising disulfide bridge. For these QM/MM simulations, we employed the ASM approach [217] in conjunction with the semiempirical Density Functional Tight Binding 3 (DFTB3) method [302]. Additionally, single-point Density Functional Theory (DFT) calculations were performed on the final conformations along the Minimum Free Energy Path (MFEP) using the M06-2X functional [300] and the 6-31+G(d,p) basis set. This was done to refine the PMF by applying for a higher level of theory.

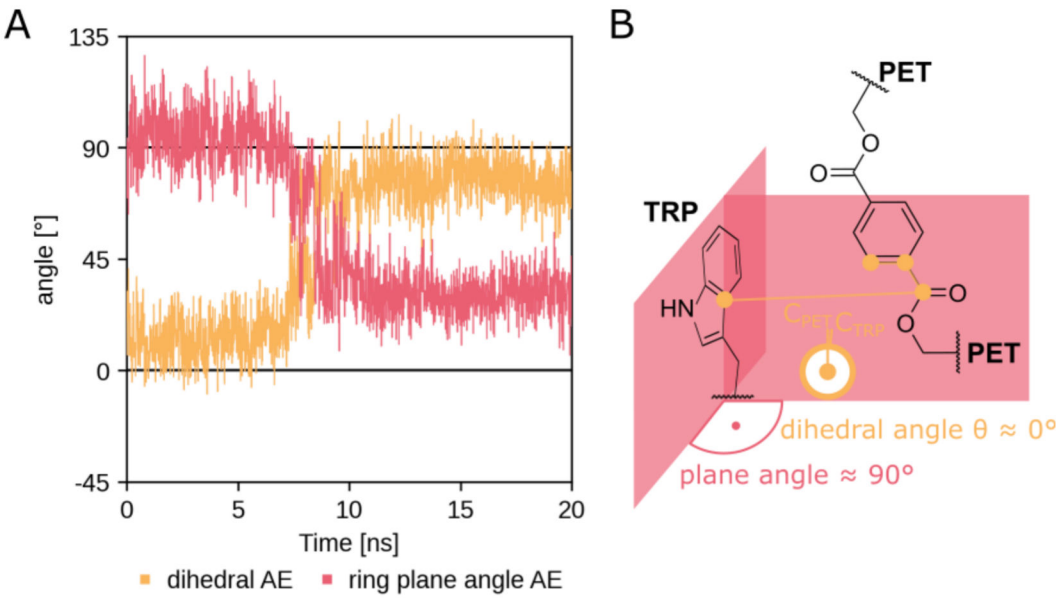


Fig. 5.1.: Dihedral angle and the angle between the 'wobbling' tryptophan and PET ring planes. The angles were calculated for the 20 ns MM production run of the AE of PES-H1 (A). The definition of the dihedral (orange) and the ring plane angles (blue) is highlighted schematically for the MC state preferring an approximate T-stacked orientation with a plane angle of approximately 90°, which correlates with a dihedral angle of approximately 0° (B). Adapted from manuscript I (Sec. A.2).

The initial structures of the MC were derived from prior Hamiltonian Replica Exchange Molecular Dynamics (HREMD) simulations of the WT enzymes choosing the pro-*S* poses with the shortest SER–C distance. Mutations were subsequently introduced to generate initial structures for the variants. The Acyl-Enzyme Intermediate (AE) states were manually generated from relaxed MC structures using PyMOL [331].

Notably, the benzene ring of PET exhibits a preference towards a parallel orientation in relation to the 'wobbling' tryptophan in the AE state during 20 ns Molecular Mechanics (MM) simulations. In contrast, the MC state predominantly favours a T-stacked orientation. Although Han *et al.* [162] initially proposed this transition in the context of product liberation, its specific association with a reaction step remained undefined. Our findings indicate that this transition predominantly occurs during the acylation phase. We have defined a dihedral angle that exhibits a strong correlation with the angle formed between the tryptophan and the PET ring plane (Fig. 5.1).

Additionally, we conducted a comparative analysis of two acylation simulations: one without and another incorporating the identified dihedral as a CV. This was in conjunction with five pertinent distance CVs and two point-to-plane distance CVs that reflect the hybridisation state of the PET ester's carbon to improve convergence (Fig. A11 and 5.2).

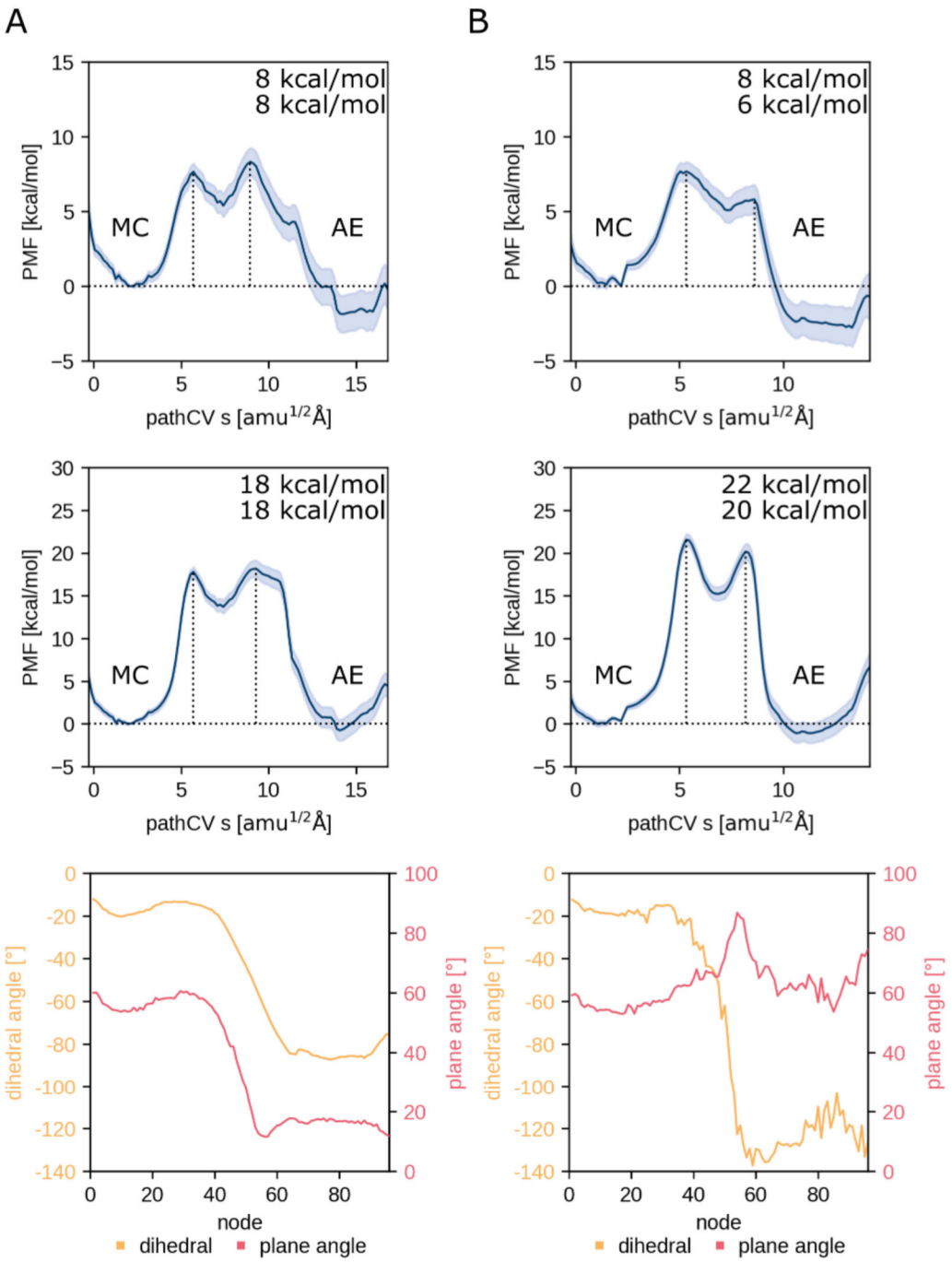


Fig. 5.2.: Comparison of simulations with or without the dihedral CV. Comparison of the PMF along the pathCV s using DFTB3 only (top) and after correction for DFT level (center), as well as the average dihedral and plane angles per node (bottom) when incorporating the dihedral as a CV (A) and without the dihedral CV (B). Adapted from manuscript I (Sec. A.2).

In contrast, the pathCV s describes the progress along the MFEP connecting MC and AE in CV space. When the dihedral was integrated as a CV, a seamless transition from approximately 0° (T-stacking) to approximately ±90° (parallel orientation) relative to the ring plane of the 'wobbling' tryptophan was observed. This transition exhibited a significant correlation with the ring plane angle alteration during the

reaction. In contrast, the simulation lacking the dihedral CV yielded a combination of parallel and T-stacked conformations when approaching the AE. These T-stacked conformations present close to the AE state arise from a 180° rotation from the T-stacked conformation in the MC state. Consequently, the PET ring atom defining the dihedral points away from, rather than towards, the 'wobbling' tryptophan as observed in the MC.

Comparison of the PMF from the ASM runs with and without the dihedral CV revealed larger barriers in the corrected PMFs when the dihedral CV was omitted. This implies an energetic contribution from the conformational change during the reaction, which is overlooked in the absence of this pertinent CV. The conformational change can be mapped to a specific step by comparison of the PMFs and the dihedral progression. The PMF profiles delineate a two-step acylation process with a metastable intermediate state, which could be erroneously categorised as a one-step mechanism due to its minimal energy disparity with the transition states [182–184, 186–188, 191, 192]. The most pronounced alterations in plane and dihedral angles commence with the formation of the tetrahedral intermediate, thus occurring concertedly with the acylation process (Fig. 5.2). In conclusion, the reorientation of the PET benzene ring is evident even when it is not incorporated into the CVs. When this dihedral is utilised as a CV, a smooth, concerted transition with reduced energy barriers is manifested, emphasising the significance of this conformational alteration for the reaction and its representation as a CV. Consequently, the final QM/MM simulations for all four enzymes were executed using the settings that incorporates the dihedral CV.

Comparing the uncorrected DFTB3 PMF profiles with their DFT-corrected counterparts reveals lower energy barriers for DFTB3. This discrepancy is likely attributed to the underestimation of proton transfer energies with DFTB3, rather resembling a one-step mechanism rather than a two-step mechanism for three out of the four enzymes analysed (Figs. A12, 5.3, and 5.4). Upon correction to the DFT level using the M06-2X functional [300], a distinct two-step mechanism is delineated for all enzymes. This correction also elevates the energy barriers to values consistent with those reported in the literature [182, 183, 185, 187–189, 191]. Consequently, the selection of the QM methodology significantly influences both the profile shape and barrier height. This may account for the observed discrepancies in prior QM/MM investigations of PET hydrolases. For instance, studies proposing a one-step mechanism and lower energy barriers utilised DFTB3 [189, 302] or the Perdew–Burke–Ernzerhof (PBE) functional [185, 332–335], both underestimating proton transfer energies. In contrast, studies suggesting a two-step mechanism and higher barriers used e.g. Austin Model 1 (AM1) [182, 301], which often tends to overestimate proton transfers. Thus, we recommend to compare at least two different methods or to correct for a higher level of theory using a complementary functional. Comparing the WT enzymes, LCC and PES-H1, with their highly active variants, LCC^{IG} and $PES\text{-}H1^{FY}$, our findings indicate that both variants display reduced activation free en-

ergy barriers for acylation (Figs. 5.3 and 5.4). Moreover, the MC exhibits equivalent or higher energy levels compared to the AE, which contrasts with the WT profiles where the MC displays lower energy levels than the AE. Consequently, we posit that the stabilisation of both the AE and the Transition State (TS) underpins the alterations observed in the PMF profiles and the height of the activation free energy barriers. This stabilisation likely promotes the acylation and potentially enhances the PET-degradation activity of the variants.

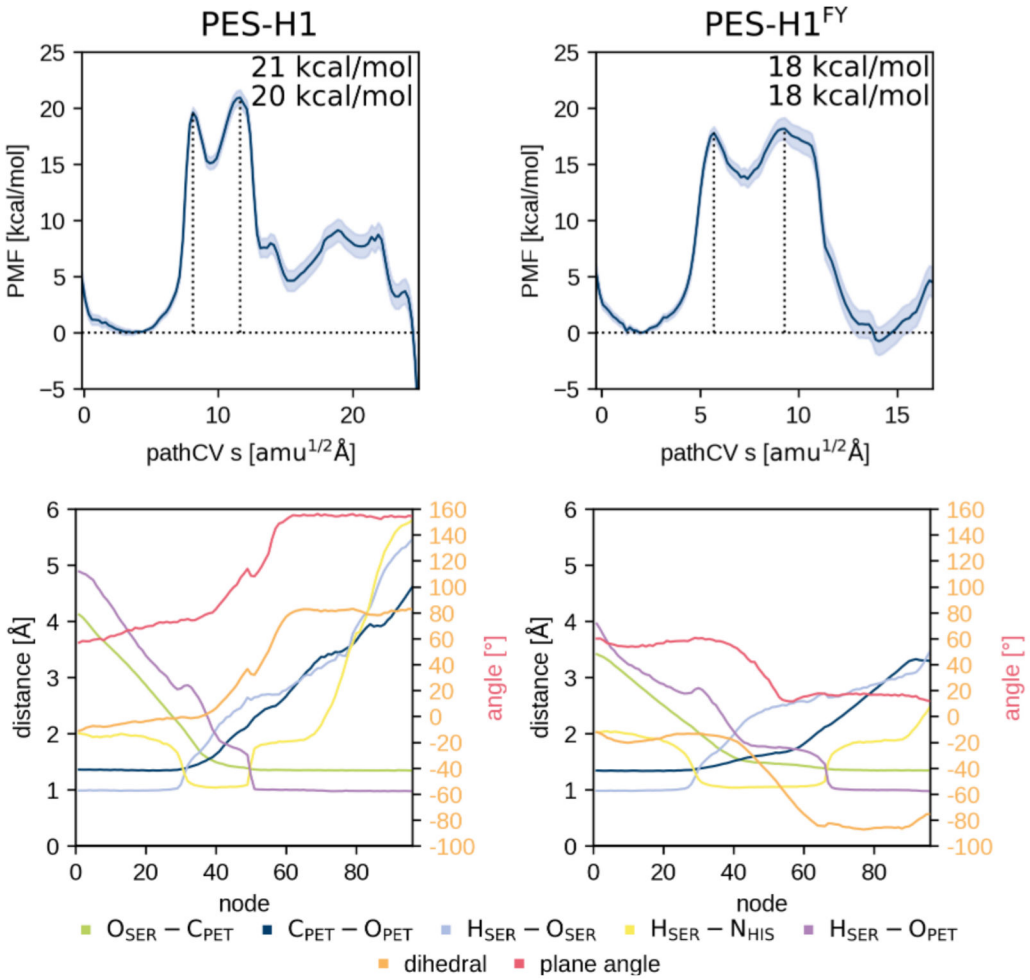


Fig. 5.3.: PMFs and CV progression of PES-H1 and PES-H1^{FY}. PMF of the PET acylation of PES-H1 (left) and its highly active variant PES-H1^{FY} (right) are shown including the height of the two barriers. The lower plots show the corresponding averaged distance CV values per node during the USMD stage and, thus, depict the CV progression along the reaction. Additionally, the angle between the ring planes of the 'wobbling' tryptophan and the PET benzene moiety is plotted in red to highlight the correlation with the dihedral angle change in orange. Adapted from manuscript I (Sec. A.2).

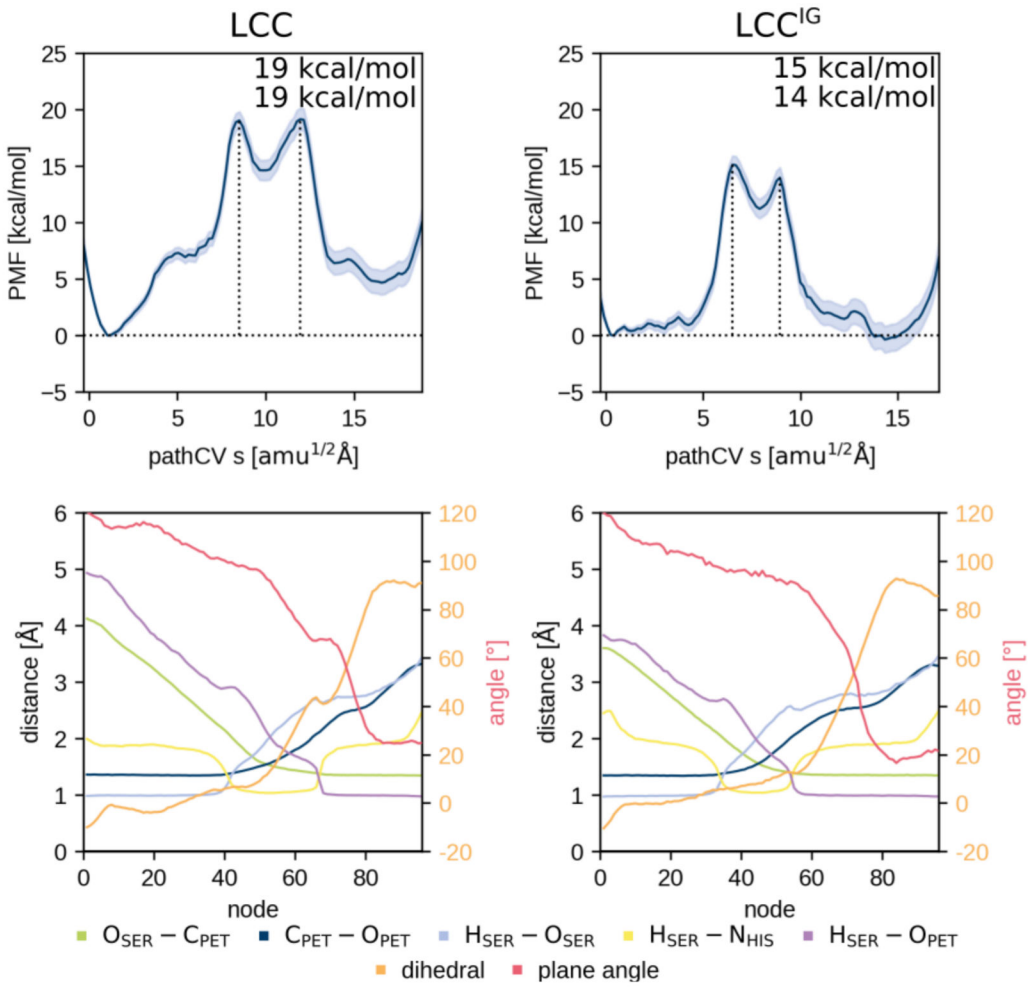


Fig. 5.4.: PMFs and CV progression of LCC and LCC^{IG}. PMF of the PET acylation of LCC (left) and its highly active variant LCC^{IG} (right). The height of the two barriers is provided as well. The lower plots show the corresponding averaged distance CV values per node during the USMD stage and, thus, depict the CV progression along the reaction. Additionally, the angle between the ring planes of the 'wobbling' tryptophan and the PET benzene moiety is plotted in red to highlight the correlation with the dihedral angle change in orange. Adapted from manuscript I (Sec. A.2).

5.2 Conclusion of manuscript I

This study offers crucial insights into the acylation mechanism of two PET hydrolases and its highly active variants and highlights methodological challenges in obtaining consistent results. Our findings can be summarised as follows: (1) We successfully simulated the PET acylation of LCC, PES-H1, and their LCC^{ICCG} (represented by LCC^{IG}) and PES-H1^{FY} variants using QM/MM in conjunction with ASM. (2) We identified a shift from T-stacked to parallel π–π interactions between the 'wobbling' tryptophan and the benzene ring of PET, resulting from a rotation of the latter. (3) It is essential to account for this conformational alteration when characterising acylation in QM/MM investigations – a factor overlooked in the CV selection of previous studies. We pinpointed a dihedral angle closely associated with the change in ring

orientation, utilising it as a CV. Moreover, the choice of QM methodology significantly impacts the resultant PMF shape and energy barrier heights, especially when applying QM methods underestimating proton transfer energies in the underlying acylation mechanism. Adjusting for a higher theoretical level using the M06-2X functional [300] corrected the energy barriers to plausible values, facilitating distinction between a 1-step and the 2-step mechanisms involving a metastable intermediate proposed in this research. (4) The reduction in acylation energy barrier, aided by the stabilisation of the TS with additional stabilisation of the AE, contributes to the enhanced activity of LCC^{ICCG} and PES-$H1^{FY}$ upon mutation.

Our computational analyses elucidate the reduced acylation energy barrier as one mediator underlying the activity enhancement in two PET hydrolases and highlight the significant conformational change in the PET benzene ring associated with acylation, hitherto overlooked. This revelation, coupled with our understanding of the QM method's influence, promises to be instrumental for future QM/MM investigations of PET hydrolases.

Conclusion

6

In this investigation, we meticulously examined the entire binding pathway of two thermophilic PET hydrolases, LCC and PES-H1, along with their highly active LCC^{ICCG} and $PES\text{-}H1^{FY}$ variants. This marks the first comprehensive analysis encompassing adsorption to a large, amorphous PET bulk and progressing to productive binding within the active site. Additionally, we scrutinised the initial stage of the catalysed PET degradation, known as acylation. Our methodology employed extensive conventional MD simulations, as well as enhanced sampling using HREMD simulations. These were complemented by QM/MM simulations utilising the ASM, alongside *in vitro* PET weight loss and kinetic assessments conducted in collaboration with the University of Greifswald. Collectively, these efforts yielded approximately 55 μs of MM MD simulation data, rendering this project one of the most exhaustive computational investigations of PET hydrolases to date.

As a first step, we examined the binding orientation of a PET analogue within the active site of PES-H1. Our analysis unveiled a predominant hydrophobic and aromatic character in the interatomic interactions, particularly with the centrally located PET unit that is bound in a productive manner. This observation is corroborated by our comprehensive HREMD simulations, which indicate tightly bound units in proximity to the catalytic centre and flexible termini. A comparative analysis with LCC^{ICCG} revealed that both enzymes possess a mutation at an identical position. However, the presence of a tyrosine residue at this specific location exerts divergent effects on enzymatic activity. Specifically, the activity of WT LCC is enhanced upon the removal of the tyrosine through the Y127G mutation, whereas the activity of PES-H1 is augmented when a tyrosine is substituted for a glutamine at the position yielding Q94Y, along with other mutations [105, 130]. We propose that these mutations modulate distinct processes involved in enzymatic activity. This underscores the significance of our research, which aims to elucidate the processes of substrate adsorption, entry, and conversion in addition to productive binding.

To address these aspects comprehensively, we conducted extensive MD simulations, successfully capturing the adsorption process of LCC and PES-H1 onto a large, amorphous PET substrate. Through this analysis, we pinpointed specific surface characteristics that impede PET binding while facilitating contact progression. Informed by these findings, we proposed modifications to LCC^{IG}, which serves as a computational proxy for LCC^{ICCG}, and the $PES\text{-}H1^{FY}$ by suggesting triple mutants. The objective was to diminish distal contacts in favour of proximal interactions, thereby promoting productive adsorption. *In silico*, this was accomplished by enhancing the negative surface potential to attenuate distal PET binding and incorporating small hydrophobic residues, notably alanine in LCC to emulate the surface profile of PES-

H1 and enhance contact progression. However, upon experimental evaluation, only one of the two assessed variants could be successfully expressed, which exhibited markedly reduced activity. Notably, the three mutations introduced in distal regions primarily impact adsorption rather than enzymatic activity directly. Our findings underscore the critical importance of considering PET adsorption mechanisms and comprehensively investigating the entire binding pathway. However, despite the prolonged duration of our simulations, we were unable to sample the entry process into the binding site in this part of the thesis project, emphasising the complexity and intricacy of the system under study.

In our subsequent HREMD simulations, transitioning to higher-energy replicas facilitated entry of a PET-5mer into the binding site. We demonstrated that the conformational flexibility of PET and in particular PET–PET interactions can hinder this process, which can be overcome at elevated temperatures. Utilising a free-energy approach and identifying specific FES characteristics, we identified specific residues that obstruct PET entry. Subsequently, we engineered PES-H1^{FY} and LCC^{IG} single mutants to facilitate PET entry. This was achieved by destabilising the unbound state, stabilising the bound states, and facilitating a seamless transition between these states without the stabilisation of off-pathway states. Despite observing comparable or reduced activity in terms of PET weight loss experiments, kinetic analyses corroborated the efficacy of our strategy, unveiling enhanced catalytic efficiency and improved K_m values. Among the evaluated variants, LCC^{ICCG} T211G and PES-H1^{FY} S68A emerged as the most promising ones. Notably, the latter mutation may sterically influence the entry process, a hypothesis supported by PCA, which identified three primary entry pathways. Our innovative approach, leveraging HREMD simulations in conjunction with FES and PCA, enabled us to sample PET entry for the first time. This methodology facilitated a comprehensive exploration of key factors modulating the energy barrier during the entry process, thereby advancing our understanding of the underlying mechanisms.

In our final investigations, we delved into the PET acylation processes of LCC, LCC^{IG}, PES-H1, and PES-H1^{FY} using QM/MM simulations, shedding light on methodological challenges that may account for inconsistent findings in prior studies [182, 186, 189, 191]. Firstly, we determined that the choice of the QM method significantly impacts both the energy barrier height and the shape of the PMF. Specifically, methods such as DFTB3, which underestimate the energy associated with proton transfers, hinder the identification of metastable intermediate states and obscure the 2-step nature of the acylation mechanism [189]. Secondly, we identified a conformational transition in the benzene ring of PET, altering its π–π interactions with the 'wobbling' tryptophan from a T-stacked to a parallel orientation. Surprisingly, this aspect has been overlooked in prior QM/MM studies, despite having been previously proposed by Han *et al.* [162]. Given its concurrent occurrence with acylation and its impact on energy barriers, we advocate for the inclusion of this motion as a CV, for which we propose a dihedral angle that correlates well with this conformational change.

Additionally, we observed that the highly active variants exhibited reduced energy barriers compared to their WT counterparts, implicating the mutated residues being involved in catalytic processes.

In summary, this computational study has made significant progress in elucidating previously unexplored aspects of enzymatic PET degradation in atomistic detail:

1. Investigation of PET hydrolase adsorption onto a large amorphous PET bulk.
2. Examination of PET entry into the active binding site.
3. The first QM/MM investigations of PES-H1 and PES-H1^{FY}.
4. Identification of a concerted conformational shift in the PET benzene ring during the acylation process.

Moreover, our research has led to the discovery of novel LCC^{ICCG} and PES-H1^{FY} variants exhibiting enhanced kinetic properties. This synthesis of atomistic detail from computational methodologies with the empirical precision of experimental data offers a more holistic understanding of PET hydrolases, particularly the novel PES-H1, and broader implications for polymer biocatalysis. We suggest methodologies and configurations to facilitate a holistic approach exploring previously elusive processes and fostering coherence in subsequent research endeavours:

1. Utilisation of HREMD simulations to sample polymer entry into the active site, complemented by subsequent analysis through FES and PCA.
2. Recognition of the substantial impact of QM/MM configurations on the resultant PMF, particularly when pivotal CVs are overlooked or when QM methods that underestimate proton transfer energies are employed.

Addressing these methodological and knowledge gaps is pivotal for advancing future engineering initiatives aimed at enhancing the activity of PET hydrolases. It is imperative for subsequent studies to incorporate additional processes, such as the subsequent PET degradation step involving the catalysed hydrolysis, as well as the mechanisms of product liberation and inhibition. Furthermore, transferring the insights gained from PET biocatalysis can facilitate the optimisation of other polymer hydrolases. This knowledge transfer holds the potential to catalyse large-scale industrial applications, paving the way for efficient and environmentally-friendly recycling of plastic waste.

Bibliography

1. Krause, D. & Thörnig, P. JURECA: Modular Supercomputer at Jülich Supercomputing Centre. *JLSRF* **4** (2018) (cit. on p. viii).
2. Geyer, R., Jambeck, J. R. & Law, K. L. Production, use, and fate of all plastics ever made. *Sci Adv* **3,** e1700782 (2017) (cit. on p. 1).
3. PlasticsEurope. Plastics - the Facts 2022. *PlasticsEurope* (2022) (cit. on pp. 1, 2, 4).
4. Emblem, A. in *Packaging technology* (eds Emblem, A. & Emblem, H.) 287–309 (Woodhead Publishing, 2012) (cit. on p. 1).
5. Bajt, O. From plastics to microplastics and organisms. *FEBS Open Bio* **11,** 954–966 (2021) (cit. on p. 1).
6. Welden, N. A. in *Plastic waste and recycling* (ed Letcher, T. M.) 195–222 (Academic Press, 2020) (cit. on p. 1).
7. Mato, Y., Isobe, T., Takada, H., *et al.* Plastic resin pellets as a transport medium for toxic chemicals in the marine environment. *Environ Sci Technol* **35,** 318–324 (2001) (cit. on p. 1).
8. Mao, X., Xu, Y., Cheng, Z., *et al.* The impact of microplastic pollution on ecological environment: a review. *Front Biosci (Landmark Ed)* **27,** 46 (2022) (cit. on p. 1).
9. Nielsen, T. D., Hasselbalch, J., Holmberg, K. & Stripple, J. Politics and the plastic crisis: A review throughout the plastic life cycle. *WIREs Energy Environ* **9,** e360 (2020) (cit. on p. 1).
10. Amadei, A. M., Sanyé-Mengual, E. & Sala, S. Modeling the EU plastic footprint: Exploring data sources and littering potential. *Resour Conserv Recy* **178,** 106086 (2022) (cit. on p. 1).
11. Commission, E. & for Environment, D.-G. *Turning the tide on single-use plastics* (Publications Office, 2021) (cit. on pp. 1, 2).
12. Nisticò, R. Polyethylene terephthalate (PET) in the packaging industry. *Polym Test* **90,** 106707 (2020) (cit. on p. 1).
13. Shafiee, S. & Topal, E. When will fossil fuel reserves be diminished? *Energ Policy* **37,** 181–189 (2009) (cit. on p. 2).
14. Cabernard, L., Pfister, S., Oberschelp, C. & Hellweg, S. Growing environmental footprint of plastics driven by coal combustion. *Nat Sustain* **5,** 139–148 (2022) (cit. on p. 2).
15. Grant, A. & Lahme, V. PET market in Europe: State of play 2022. *EUNOMIA* (2022) (cit. on pp. 2, 4).

16. Merrington, A. in *Applied plastics engineering handbook (second edition)* (ed Kutz, M.) Second Edition, 167–189 (William Andrew Publishing, 2017) (cit. on p. 2).

17. Goodship, V. Plastic recycling. *Sci Prog* **90,** 245–268 (2007) (cit. on p. 2).

18. Maris, J., Bourdon, S., Brossard, J.-M., *et al.* Mechanical recycling: Compatibilization of mixed thermoplastic wastes. *Polym Degrad Stabil* **147,** 245–266 (2018) (cit. on p. 2).

19. Schyns, Z. O. G. & Shaver, M. P. Mechanical recycling of packaging plastics: A review. *Macromol Rapid Comm* **42,** 2000415 (2021) (cit. on pp. 2, 3).

20. Hong, M. & Chen, E. Y.-X. Chemically recyclable polymers: A circular economy approach to sustainability. *Green Chem* **19,** 3692–3706 (16 2017) (cit. on p. 2).

21. Scalenghe, R. Resource or waste? A perspective of plastics degradation in soil with a focus on end-of-life options. *Heliyon* **4,** e00941 (2018) (cit. on p. 2).

22. La Mantia, F. P. & Vinci, M. Recycling poly(ethyleneterephthalate). *Polym Degrad Stabil* **45,** 121–125 (1994) (cit. on p. 2).

23. Quicker, P., Seitz, M. & Vogel, J. Chemical recycling: A critical assessment of potential process approaches. *Waste Manage Res* **40,** 1494–1504 (2022) (cit. on p. 2).

24. Shirazimoghaddam, S., Amin, I., Faria Albanese, J. A. & Shiju, N. R. Chemical recycling of used PET by glycolysis using niobia-based catalysts. *ACS Eng Au* **3,** 37–44 (2023) (cit. on p. 2).

25. Damayanti & Wu, H. Strategic possibility routes of recycled PET. *Polymers (Basel)* **13,** 1475 (2021) (cit. on p. 2).

26. Volmajer Valh, J., Stopar, D., Selaya Berodia, I., *et al.* Economical chemical recycling of complex PET waste in the form of active packaging material. *Polymers (Basel)* **14,** 3244 (2022) (cit. on p. 2).

27. Meys, R., Frick, F., Westhues, S., *et al.* Towards a circular economy for plastic packaging wastes – the environmental potential of chemical recycling. *Resour Conserv Recy* **162,** 105010 (2020) (cit. on p. 2).

28. Shojaei, B., Abtahi, M. & Najafi, M. Chemical recycling of PET: A stepping-stone toward sustainability. *Polym Advan Technol* **31,** 2912–2938 (2020) (cit. on p. 2).

29. Vollmer, I., Jenks, M. J. F., Roelands, M. C. P., *et al.* Beyond mechanical recycling: Giving new life to plastic waste. *Angew Chem Int Edit* **59,** 15402–15423 (2020) (cit. on p. 2).

30. Grigore, M. E. Methods of recycling, properties and applications of recycled thermoplastic polymers. *Recycling* **2** (2017) (cit. on p. 2).

31. Al-Sabagh, A., Yehia, F., Eshaq, G., Rabie, A. & ElMetwally, A. Greener routes for recycling of polyethylene terephthalate. *Egypt J Petrol* **25,** 53–64 (2016) (cit. on p. 2).

32. Sinha, V., Patel, M. & Patel, J. PET waste management by chemical recycling: A review. *J Polym Environ* **18,** 8–25 (2018) (cit. on p. 2).

33. McKay, G. Dioxin characterisation, formation and minimisation during municipal solid waste (MSW) incineration: Review. *Chem Eng J* **86,** 343–368 (2002) (cit. on p. 2).

34. Li, C.-T., Zhuang, H.-K., Hsieh, L.-T., Lee, W.-J. & Tsao, M.-C. PAH emission from the incineration of three plastic wastes. *Environ Int* **27,** 61–67 (2001) (cit. on p. 2).

35. Rossi, V., Cleeve-Edwards, N., Lundquist, L., *et al.* Life cycle assessment of end-of-life options for two biodegradable packaging materials: Sound application of the European waste hierarchy. *J Clean Prod* **86,** 132–145 (2015) (cit. on p. 3).

36. Wojnowska-Baryła, I., Bernat, K. & Zaborowska, M. Plastic waste degradation in landfill conditions: The problem with microplastics, and their direct and indirect environmental effects. *Int J Environ Res Public Health* **19,** 13223 (2022) (cit. on p. 3).

37. Huysman, S., Debaveye, S., Schaubroeck, T., *et al.* The recyclability benefit rate of closed-loop and open-loop systems: A case study on plastic recycling in Flanders. *Resour Conserv Recy* **101,** 53–60 (2015) (cit. on p. 3).

38. Geueke, B., Groh, K. & Muncke, J. Food packaging in the circular economy: Overview of chemical safety aspects for commonly used materials. *J Clean Prod* **193,** 491–505 (2018) (cit. on p. 3).

39. Eriksen, M. K., Pivnenko, K., Faraca, G., Boldrin, A. & Astrup, T. F. Dynamic material flow analysis of PET, PE, and PP flows in europe: evaluation of the potential for circular economy. *Environ Sci Technol* **54,** 16166–16175 (2020) (cit. on p. 3).

40. Curtzwiler, G. W., Schweitzer, M., Li, Y., Jiang, S. & Vorst, K. L. Mixed post-consumer recycled polyolefins as a property tuning material for virgin polypropylene. *J Clean Prod* **239,** 117978 (2019) (cit. on p. 3).

41. Eriksen, M., Christiansen, J., Daugaard, A. & Astrup, T. Closing the loop for PET, PE and PP waste from households: Influence of material properties and product design for plastic recycling. *Waste Manage* **96,** 75–85 (2019) (cit. on p. 3).

42. Sadeghi, B., Marfavi, Y., AliAkbari, R., *et al.* Recent studies on recycled PET fibers: production and applications: A Review. *Mater Circ Econ* **3** (2021) (cit. on p. 3).

43. Ragaert, K., Delva, L. & Van Geem, K. Mechanical and chemical recycling of solid plastic waste. *Waste Manage* **69,** 24–58 (2017) (cit. on p. 3).

44. Foti, D. Use of recycled waste pet bottles fibers for the reinforcement of concrete. *Compos Struct* **96,** 396–404 (2013) (cit. on p. 3).

45. Mudondo, J., Lee, H. S., Jeong, Y., *et al.* Recent advances in the chemobiological upcycling of polyethylene terephthalate (PET) into value-added chemicals. *J Microbiol Biotechnol* **33,** 1–14 (2023) (cit. on p. 3).

46. Gaduan, A. N., Singkronart, K., Bell, C., *et al.* Mechanical upcycling immiscible polyethylene terephthalate-polypropylene blends with carbon fiber reinforcement. *ACS Appl Polym Mater* **4,** 3294–3303 (2022) (cit. on p. 3).

47. Sadler, J. C. & Wallace, S. Microbial synthesis of vanillin from waste poly(ethylene terephthalate). *Green Chem* **23,** 4665–4672 (2021) (cit. on p. 3).

48. Zhou, H., Ren, Y., Li, Z., *et al.* Electrocatalytic upcycling of polyethylene terephthalate to commodity chemicals and H2 fuel. *Nat Commun* **12,** 4679 (2021) (cit. on p. 3).

49. Roosen, M., Mys, N., Kusenberg, M., *et al.* Detailed analysis of the composition of selected plastic packaging waste products and its implications for mechanical and thermochemical recycling. *Environ Sci Technol* **54,** 13282–13293 (2020) (cit. on p. 3).

50. Ügdüler, S., Van Geem, K. M., Roosen, M., Delbeke, E. I. & De Meester, S. Challenges and opportunities of solvent-based additive extraction methods for plastic recycling. *Waste Manage* **104,** 148–182 (2020) (cit. on p. 3).

51. Schuch, D., Lederer, J., Fellner, J. & Scharff, C. Separate collection rates for plastic packaging in Austria – A regional analysis taking collection systems and urbanization into account. *Waste Manage* **155,** 211–219 (2023) (cit. on p. 3).

52. Lange, J.-P. Managing plastic waste-sorting, recycling, disposal, and product redesign. *ACS Sustain Chem Eng* **9,** 15722–15738 (2021) (cit. on p. 3).

53. Dijkgraaf, E. & Gradus, R. Post-collection separation of plastic waste: Better for the environment and lower collection costs? *Environ Resource Econ* **77,** 127–142 (2020) (cit. on p. 3).

54. Roosen, M., De Somer, T., Demets, R., *et al.* Towards a better understanding of odor removal from post-consumer plastic film waste: A kinetic study on deodorization efficiencies with different washing media. *Waste Manage* **120,** 564–575 (2021) (cit. on p. 3).

55. Eriksen, M., Pivnenko, K., Olsson, M. & Astrup, T. Contamination in plastic recycling: Influence of metals on the quality of reprocessed plastic. *Waste Manage* **79,** 595–606 (2018) (cit. on p. 3).

56. Hopewell, J., Dvorak, R. & Kosior, E. Plastics recycling: Challenges and opportunities. *Philos T R Soc B* **364,** 2115–2126 (2009) (cit. on p. 3).

57. Arvanitoyannis, I. S. & Bosnea, L. A. Recycling of polymeric materials used for food packaging: Current status and perspectives. *Food Rev Int* **17,** 291–346 (2001) (cit. on p. 3).

58. Carr, C. M., Clarke, D. J. & Dobson, A. D. W. Microbial polyethylene terephthalate hydrolases: Current and future perspectives. *Front Microbiol* **11,** 571265 (2020) (cit. on p. 4).

59. Sheldon, R. A. & Brady, D. Green chemistry, biocatalysis, and the chemical industry of the future. *ChemSusChem* **15,** e202102628 (2022) (cit. on p. 4).

60. Pleissner, D. & Kümmerer, K. in *Sustainability and Life Cycle Assessment in Industrial Biotechnology* (eds Fröhling, M. & Hiete, M.) 281–298 (Springer International Publishing, Cham, 2020) (cit. on p. 4).

61. Fryszkowska, A. & Devine, P. N. Biocatalysis in drug discovery and development. *Curr Opin Chem Biol* **55,** 151–160 (2020) (cit. on p. 4).

62. Yushkova, E. D., Nazarova, E. A., Matyuhina, A. V., *et al.* Application of immobilized enzymes in food industry. *J Agr Food Chem* **67,** 11553–11567 (2019) (cit. on p. 4).

63. Vojcic, L., Pitzler, C., Körfer, G., *et al.* Advances in protease engineering for laundry detergents. *New Biotechnol* **32.** European Congress of Biotechnology - ECB 16, 629–634 (2015) (cit. on p. 4).

64. Arnold, F. H. The nature of chemical innovation: New enzymes by evolution. *Q Rev Biophys* **48,** 404–410 (2015) (cit. on p. 4).

65. Intasian, P., Prakinee, K., Phintha, A., *et al.* Enzymes, *in vivo* biocatalysis, and metabolic engineering for enabling a circular economy and sustainability. *Chem Rev* **121,** 10367–10451 (2021) (cit. on p. 4).

66. Venkatesh, A., Posen, I. D., MacLean, H. L., *et al.* in *Sustainability and Life Cycle Assessment in Industrial Biotechnology* (eds Fröhling, M. & Hiete, M.) 77–119 (Springer International Publishing, Cham, 2020) (cit. on p. 4).

67. Zhang, Y.-H. P., Sun, J. & Ma, Y. Biomanufacturing: History and perspective. *J Ind Microbiol Biot* **44,** 773–784 (2017) (cit. on p. 4).

68. Rossino, G., Robescu, M. S., Licastro, E., *et al.* Biocatalysis: A smart and green tool for the preparation of chiral drugs. *Chirality* **34,** 1403–1418 (2022) (cit. on p. 4).

69. Li, Z., Jiang, Y., Guengerich, F. P., *et al.* Engineering cytochrome P450 enzyme systems for biomedical and biotechnological applications. *J Biol Chem* **295,** 833–849 (2020) (cit. on p. 4).

70. Huang, K., Zhang, S., Guan, X., *et al.* Thermostable arginase from *Sulfobacillus acidophilus* with neutral pH optimum applied for high-efficiency L-ornithine production. *Appl Microbiol Biotechnol* **104,** 6635–6646 (2020) (cit. on p. 4).

71. Nomura, T., Ogita, S. & Kato, Y. One-step enzymatic synthesis of 1-tuliposide a using tuliposide-converting enzyme. *Appl Biochem Biotechnol* **188,** 12–28 (2019) (cit. on p. 4).

72. Patel, R. N. Biocatalysis for synthesis of pharmaceuticals. *Bioorgan Med Chem* **26.** Enzyme Catalysis in the Synthesis of Pharmaceuticals, 1252–1274 (2018) (cit. on p. 4).

73. Benkovic, S. J. & Hammes-Schiffer, S. A perspective on enzyme catalysis. *Science* **301,** 1196–1202 (2003) (cit. on p. 4).

74. Alcántara, A. R., Domínguez de María, P., Littlechild, J. A., *et al.* Biocatalysis as key to sustainable industrial chemistry. *ChemSusChem* **15,** e202102709 (2022) (cit. on p. 4).

75. Gavrilescu, M. & Chisti, Y. Biotechnology – A sustainable alternative for chemical industry. *Biotechnol Adv* **23,** 471–499 (2005) (cit. on p. 4).

76. Jegannathan, K. R. & Nielsen, P. H. Environmental assessment of enzyme use in industrial production – A literature review. *J Clean Prod* **42,** 228–240 (2013) (cit. on p. 4).

77. Wu, S., Snajdrova, R., Moore, J. C., Baldenius, K. & Bornscheuer, U. T. Biocatalysis: Enzymatic synthesis for industrial applications. *Angew Chem Int Ed Engl* **60,** 88–119 (2021) (cit. on p. 4).

78. Aziz, N. S., Sofian-Seng, N.-S., Mohd Razali, N. S., Lim, S. J. & Mustapha, W. A. A review on conventional and biotechnological approaches in white pepper production. *J Sci Food Agr* **99,** 2665–2676 (2019) (cit. on p. 4).

79. Singh, R., Kumar, M., Mittal, A. & Mehta, P. K. Microbial enzymes: Industrial progress in 21st century. *3 Biotech* **6,** 174 (2016) (cit. on p. 4).

80. Rajakumara, E., Abhishek, S., Nitin, K., *et al.* Structure and cooperativity in substrate–enzyme interactions: Perspectives on enzyme engineering and inhibitor design. *ACS Chem Biol* **17,** 266–280 (2022) (cit. on p. 4).

81. Amobonye, A., Bhagwat, P., Singh, S. & Pillai, S. Plastic biodegradation: Frontline microbes and their enzymes. *Sci Total Environ* **759,** 143536 (2021) (cit. on p. 4).

82. Sulaiman, S., You, D.-J., Kanaya, E., Koga, Y. & Kanaya, S. Crystal structure and thermodynamic and kinetic stability of metagenome-derived LC-Cutinase. *Biochemistry* **53,** 1858–1869 (2014) (cit. on pp. 4, 9, 14).

83. Cheng, S., Tong, X., Woodard, R. W., *et al.* Identification and characterization of bacterial cutinase*. *J Biol Chem* **283,** 25854–25862 (2008) (cit. on p. 4).

84. Müller, R.-J., Schrader, H., Profe, J., Dresler, K. & Deckwer, W.-D. Enzymatic degradation of poly(ethylene terephthalate): Rapid hydrolyse using a hydrolase from *T. fusca*. *Macromol Rapid Comm* **26,** 1400–1405 (2005) (cit. on p. 4).

85. Yoshida, S., Hiraga, K., Takehana, T., *et al.* A bacterium that degrades and assimilates poly(ethylene terephthalate). *Science* **351,** 1196–1199 (2016) (cit. on p. 5).

86. Ollis, D. L. & Carr, P. D. α/β Hydrolase fold: An update. *Protein Pept Lett* **16,** 1137–1148 (2009) (cit. on p. 5).

87. Gao, R., Pan, H. & Lian, J. Recent advances in the discovery, characterization, and engineering of poly(ethylene terephthalate) (PET) hydrolases. *Enzyme Microb Tech* **150,** 109868 (2021) (cit. on p. 5).

88. Joo, S., Cho, I. J., Seo, H., *et al.* Structural insight into molecular mechanism of poly(ethylene terephthalate) degradation. *Nat Commun* **9,** 382 (2018) (cit. on pp. 5, 11, 51).

89. Richter, P. K., Blázquez-Sánchez, P., Zhao, Z., *et al.* Structure and function of the metagenomic plastic-degrading polyester hydrolase PHL7 bound to its product. *Nat Commun* **14,** 1905 (2023) (cit. on pp. 5, 11).

90. Wolfenden, R. & Snider, M. J. The depth of chemical time and the power of enzymes as catalysts. *Accounts Chem Res* **34,** 938–945 (2001) (cit. on p. 5).

91. Baker, D. An exciting but challenging road ahead for computational enzyme design. *Protein Sci* **19,** 1817–1819 (2010) (cit. on p. 5).

92. Wiltschi, B., Cernava, T., Dennig, A., *et al.* Enzymes revolutionize the bioproduction of value-added compounds: From enzyme discovery to special applications. *Biotechnol Adv* **40,** 107520 (2020) (cit. on p. 5).

93. Samak, N. A., Jia, Y., Sharshar, M. M., *et al.* Recent advances in biocatalysts engineering for polyethylene terephthalate plastic waste green recycling. *Environ Int* **145,** 106144 (2020) (cit. on p. 5).

94. Ahamed Kameel, N. I., Wan Daud, W. M. A., Abdul Patah, M. F. & Mohd Zulkifli, N. W. Influence of reaction parameters on thermal liquefaction of plastic wastes into oil: A review. *Energ Convers Manage* **14,** 100196 (2022) (cit. on p. 5).

95. Heidrich, D. & Gehde, M. The 3-phase structure of polyesters (PBT, PET) after isothermal and non-isothermal crystallization. *Polymers (Basel)* **14** (2022) (cit. on p. 5).

96. Thomsen, T. B., Hunt, C. J. & Meyer, A. S. Standardized method for controlled modification of poly (ethylene terephthalate) (PET) crystallinity for assaying PET degrading enzymes. *MethodsX* **9,** 101815 (2022) (cit. on p. 5).

97. Karagiannidis, P. G., Stergiou, A. C. & Karayannidis, G. P. Study of crystallinity and thermomechanical analysis of annealed poly(ethylene terephthalate) films. *Eur Polym J* **44,** 1475–1486 (2008) (cit. on p. 5).

98. Tarazona, N. A., Wei, R., Brott, S., *et al.* Rapid depolymerization of poly(ethylene terephthalate) thin films by a dual-enzyme system and its impact on material properties. *Chem Catal* **2,** 3573–3589 (2022) (cit. on pp. 6, 7, 14, 50, 53).

99. Taniguchi, I., Yoshida, S., Hiraga, K., *et al.* Biodegradation of PET: Current status and application aspects. *ACS Catal* **9,** 4089–4105 (2019) (cit. on pp. 6, 7).

100. Wei, R., Breite, D., Song, C., *et al.* Biocatalytic degradation efficiency of postconsumer polyethylene terephthalate packaging determined by their polymer microstructures. *Adv Sci (Weinh)* **6,** 1900491 (2019) (cit. on pp. 6, 7, 11).

101. Thomsen, T. B., Hunt, C. J. & Meyer, A. S. Influence of substrate crystallinity and glass transition temperature on enzymatic degradation of polyethylene terephthalate (PET). *New Biotechnol* **69,** 28–35 (2022) (cit. on pp. 6, 7, 14, 50).

102. Schubert, S. W., Thomsen, T. B., Clausen, K. S. R., *et al.* Relationships of crystallinity and reaction rates for enzymatic degradation of poly (ethylene terephthalate), PET. *ChemSusChem,* e202301752 (cit. on pp. 6, 50).

103. Sun, F., Dedong, H., Fei, L., *et al.* Molecular-level investigation of plasticization of polyethylene terephthalate (PET) in supercritical carbon dioxide via molecular dynamics simulation. *R Soc Open Sci* **9,** 220606 (2022) (cit. on p. 6).

104. Panowicz, R., Konarzewski, M., Durejko, T., *et al.* Properties of polyethylene terephthalate (PET) after thermo-oxidative aging. *Materials (Basel)* **14** (2021) (cit. on p. 6).

105. Tournier, V., Topham, C. M., Gilles, A., *et al.* An engineered PET depolymerase to break down and recycle plastic bottles. *Nature* **580,** 216–219 (2020) (cit. on pp. 7, 9, 11, 15, 39, 43, 49, 55, 59, 67).

106. Reetz, M. T. What are the limitations of enzymes in synthetic organic chemistry? *Chem Rec* **16,** 2449–2459 (2016) (cit. on p. 7).

107. Liszka, M. J., Clark, M. E., Schneider, E. & Clark, D. S. Nature versus nurture: Developing enzymes that function under extreme conditions. *Annu Rev Chem Biomol* **3,** 77–102 (2012) (cit. on p. 7).

108. Yeoman, C. J., Han, Y., Dodd, D., *et al.* in *Advances in applied microbiology* 1–55 (Academic Press, 2010) (cit. on p. 7).

109. Yazbeck, D. R., Martinez, C. A., Hu, S. & Tao, J. Challenges in the development of an efficient enzymatic process in the pharmaceutical industry. *Tetrahedron Asymmetr* **15,** 2757–2763 (2004) (cit. on p. 7).

110. Liu, Q., Xun, G. & Feng, Y. The state-of-the-art strategies of protein engineering for enzyme stabilization. *Biotechnol Adv* **37.** Biorefining: An indispensable solution for bioresource utilization and sustainable development, 530–537 (2019) (cit. on p. 7).

111. Durmoné, K., Córdova, D. C., Eló, M. & Renganathan, P. Extremozymes: A potential source for industrial applications. *J Microbiol Biotechnol* **27,** 649–659 (2017) (cit. on p. 7).

112. Suplatov, D., Voevodin, V. & Švedas, V. Robust enzyme design: Bioinformatic tools for improved protein stability. *Biotechnol J* **10,** 344–355 (2015) (cit. on p. 7).

113. Wei, R., von Haugwitz, G., Pfaff, L., *et al.* Mechanism-based design of efficient PET hydrolases. *ACS Catal* **12,** 3382–3396 (2022) (cit. on p. 7).

114. Wellen, R. & Rabello, M. The kinetics of isothermal cold crystallization and tensile properties of poly(ethylene terephthalate). *J Mater Sci,* 6099–6104 (40 2005) (cit. on p. 7).

115. Taylor, T. J. & Vaisman, I. I. Discrimination of thermophilic and mesophilic proteins. *BMC Struct Biol* **10 Suppl 1,** S5 (2010) (cit. on p. 7).

116. Carniel, A., de Abreu Waldow, V. & de Castro, A. M. A comprehensive and critical review on key elements to implement enzymatic PET depolymerization for recycling purposes. *Biotechnol Adv* **52,** 107811 (2021) (cit. on pp. 7, 14).

117. CARBIOS. *Enzymatic recycling* `https://www.carbios.com/en/enzymatic-recycling/` (May 23, 2023) (cit. on p. 7).

118. Samak, N. A., Jia, Y., Sharshar, M. M., *et al.* Recent advances in biocatalysts engineering for polyethylene terephthalate plastic waste green recycling. *Environ Int* **145,** 106144 (2020) (cit. on p. 7).

119. Victorino da Silva Amatto, I., Gonsales da Rosa-Garzon, N., Antônio de Oliveira Simões, F., *et al.* Enzyme engineering and its industrial applications. *Biotechnol and Appl Bioc* **69,** 389–409 (2022) (cit. on p. 7).

120. Kawai, F. Emerging strategies in polyethylene terephthalate hydrolase research for biorecycling. *ChemSusChem* **14,** 4115–4122 (2021) (cit. on p. 7).

121. Alves, N., Mano, J., Balaguer, E., Meseguer Dueñas, J. & Gómez Ribelles, J. Glass transition and structural relaxation in semi-crystalline poly(ethylene terephthalate): A DSC study. *Polymer* **43,** 4111–4122 (2002) (cit. on p. 7).

122. Thumarat, U., Nakamura, R., Kawabata, T., Suzuki, H. & Kawai, F. Biochemical and genetic analysis of a cutinase-type polyesterase from a thermophilic *Thermobifida alba* AHK119. *Appl Microbiol Biotechnol* **95,** 419–430 (2012) (cit. on pp. 9, 10, 47).

123. Miyakawa, T., Mizushima, H., Ohtsuka, J., *et al.* Structural basis for the Ca^{2+}-enhanced thermostability and activity of PET-degrading cutinase-like enzyme from *Saccharomonospora viridis* AHK190. *Appl Microbiol Biotechnol* **99,** 4297–4307 (2015) (cit. on pp. 9, 10, 47).

124. Numoto, N., Kamiya, N., Bekker, G.-J., *et al.* Structural dynamics of the PET-degrading cutinase-like enzyme from *Saccharomonospora viridis* AHK190 in substrate-bound states elucidates the Ca2+-driven catalytic cycle. *Biochemistry* **57,** 5289–5300 (2018) (cit. on p. 9).

125. Then, J., Wei, R., Oeser, T., *et al.* Ca^{2+} and Mg^{2+} binding site engineering increases the degradation of polyethylene terephthalate films by polyester hydrolases from *Thermobifida fusca*. *Biotechnol J* **10,** 592–598 (2015) (cit. on p. 9).

126. Then, J., Wei, R., Oeser, T., *et al.* A disulfide bridge in the calcium binding site of a polyester hydrolase increases its thermal stability and activity against polyethylene terephthalate. *FEBS Open Bio* **6,** 425–432 (2016) (cit. on p. 9).

127. Oda, M., Yamagami, Y., Inaba, S., *et al.* Functional role of three Ca^{2+}-ions bound to a cutinase-like enzyme, Cut190*, and its engineering for improved activity. *Appl Microbiol Biotechnol* **102,** 10067–10077 (2018) (cit. on p. 9).

128. Zhong-Johnson, E. Z. L., Voigt, C. A. & Sinskey, A. J. An absorbance method for analysis of enzymatic degradation kinetics of poly(ethylene terephthalate) films. *Sci Rep* **11,** 928 (2021) (cit. on p. 9).

129. Brott, S., Pfaff, L., Schuricht, J., *et al.* Engineering and evaluation of thermostable *Is*PETase variants for PET degradation. *Eng Life Sci* **22,** 192–203 (2022) (cit. on p. 9).

130. Pfaff, L., Gao, J., Li, Z., *et al.* Multiple substrate binding mode-guided engineering of a thermophilic PET hydrolase. *ACS Catal* **12,** 9790–9800 (2022) (cit. on pp. 9, 11, 14, 15, 39–41, 43, 49, 53, 55, 59, 67).

131. Kawai, F., Oda, M., Tamashiro, T., *et al.* A novel Ca^{2+}-activated, thermostabilized polyesterase capable of hydrolyzing polyethylene terephthalate from *Saccharomonospora viridis* AHK190. *Appl Microbiol Biotechnol* **98,** 10053–10064 (2014) (cit. on p. 9).

132. Son, H. F., Cho, I. J., Joo, S., *et al.* Rational protein engineering of thermo-stable PETase from *Ideonella sakaiensis* for highly efficient PET degradation. *ACS Catal* **9,** 3519–3526 (2019) (cit. on p. 9).

133. Zeng, W., Li, X., Yang, Y., *et al.* Substrate-binding mode of a thermophilic PET hydrolase and engineering the enzyme to enhance the hydrolytic efficacy. *ACS Catal* **12,** 3033–3040 (2022) (cit. on pp. 9, 11, 39, 40).

134. Arnold, F. H. Directed evolution: Bringing new chemistry to life. *Angew Chem Int Edit* **57,** 4143–4148 (2018) (cit. on p. 9).

135. Arnold, F. H. Design by directed evolution. *Accounts Chem Res* **31,** 125–131 (1998) (cit. on p. 9).

136. *The nobel prize in chemistry 2018* `nobelprize.org`. accessed: 2024-01-30 (cit. on p. 9).

137. Bell, E. L., Smithson, R., Kilbride, S., *et al.* Directed evolution of an efficient and thermostable PET depolymerase. *Nature Catalysis,* 673–681 (5 2022) (cit. on p. 9).

138. Cui, Y., Chen, Y., Liu, X., *et al.* Computational redesign of a PETase for plastic biodegradation under ambient condition by the GRAPE strategy. *ACS Catal* **11,** 1340–1350 (2021) (cit. on p. 9).

139. Lu, H., Diaz, D. J., Czarnecki, N. J., *et al.* Machine learning-aided engineering of hydrolases for PET depolymerization. *Nature* **604,** 662–667 (2022) (cit. on p. 9).

140. Li, Q., Zheng, Y., Su, T., *et al.* Computational design of a cutinase for plastic biodegradation by mining molecular dynamics simulations trajectories. *Comput Struct Biotechnol J* **20,** 459–470 (2022) (cit. on p. 9).

141. Badino, S. F., Bååth, J. A., Borch, K., Jensen, K. & Westh, P. Adsorption of enzymes with hydrolytic activity on polyethylene terephthalate. *Enzyme Microb Tech* **152,** 109937 (2021) (cit. on p. 9).

142. Weber, J., Petrović, D., Strodel, B., *et al.* Interaction of carbohydrate-binding modules with poly(ethylene terephthalate). *Appl Microbiol Biotechnol* **103,** 4801–4812 (2019) (cit. on pp. 9, 10).

143. Rennison, A. P., Westh, P. & Møller, M. S. Protein-plastic interactions: The driving forces behind the high affinity of a carbohydrate-binding module for polyethylene terephthalate. *Sci Total Environ* **870,** 161948 (2023) (cit. on p. 9).

144. Zhang, Y., Wang, L., Chen, J. & Wu, J. Enhanced activity toward PET by site-directed mutagenesis of *Thermobifida fusca* cutinase–CBM fusion protein. *Carbohyd Polym* **97,** 124–129 (2013) (cit. on p. 9).

145. Ribitsch, D., Yebra, A. O., Zitzenbacher, S., *et al.* Fusion of binding domains to *Thermobifida cellulosilytica* cutinase to tune sorption characteristics and enhancing PET hydrolysis. *Biomacromolecules* **14,** 1769–1776 (2013) (cit. on p. 9).

146. Xue, R., Chen, Y., Rong, H., *et al.* Fusion of chitin-binding domain from *Chitinolyticbacter meiyuanensis* SYBC-H1 to the leaf-branch compost cutinase for enhanced PET hydrolysis. *Front Bioeng Biotechnol* **9** (2021) (cit. on p. 9).

147. Dai, L., Qu, Y., Huang, J.-W., *et al.* Enhancing PET hydrolytic enzyme activity by fusion of the cellulose–binding domain of cellobiohydrolase I from *Trichoderma reesei*. *J Biotechnol* **334,** 47–50 (2021) (cit. on p. 9).

148. Wösten, H. A. & de Vocht, M. L. Hydrophobins, the fungal coat unravelled. *BBA - Rev Biomembranes* **1469,** 79–86 (2000) (cit. on p. 10).

149. Stanzione, I., Pitocchi, R., Pennacchio, A., *et al.* Innovative surface bio-functionalization by fungal hydrophobins and their engineered variants. *Front Mol Biosci* **9** (2022) (cit. on p. 10).

150. Ribitsch, D., Acero, E. H., Przylucka, A., *et al.* Enhanced cutinase-catalyzed hydrolysis of polyethylene terephthalate by covalent fusion to hydrophobins. *Appl Environ Microb* **81,** 3586–3592 (2015) (cit. on p. 10).

151. Espino-Rammer, L., Ribitsch, D., Przylucka, A., *et al.* Two novel class II hydrophobins from *Trichoderma spp.* stimulate enzymatic hydrolysis of poly(ethylene terephthalate) when expressed as fusion proteins. *Appl Environ Microbiol* **79,** 4230–4238 (2013) (cit. on p. 10).

152. Puspitasari, N., Tsai, S. L. & Lee, C. K. Fungal hydrophobin RolA enhanced PETase hydrolysis of polyethylene terephthalate. *Appl Biochem Biotechnol* **193,** 1284–1295 (2021) (cit. on p. 10).

153. Furukawa, M., Kawakami, N., Oda, K. & Miyamoto, K. Acceleration of enzymatic degradation of poly(ethylene terephthalate) by surface coating with anionic surfactants. *ChemSusChem* **11,** 4018–4025 (2018) (cit. on p. 10).

154. Furukawa, M., Kawakami, N., Tomizawa, A. & Miyamoto, K. Efficient degradation of poly(ethylene terephthalate) with *Thermobifida fusca* cutinase exhibiting improved catalytic activity generated using mutagenesis and additive-based approaches. *Sci Rep* **9,** 16038 (2019) (cit. on p. 10).

155. Nakamura, A., Kobayashi, N., Koga, N. & Iino, R. Positive charge introduction on the surface of thermostabilized PET hydrolase facilitates PET binding and degradation. *ACS Catal* **11,** 8550–8564 (2021) (cit. on pp. 10, 11, 47).

156. Sagong, H. Y., Son, H. F., Seo, H., *et al.* Implications for the PET decomposition mechanism through similarity and dissimilarity between PETases from *Rhizobacter gummiphilus* and *Ideonella sakaiensis*. *J Hazard Mater* **416,** 126075 (2021) (cit. on pp. 10, 47).

157. Thomsen, T. B., Schubert, S., Hunt, C. J., *et al.* Rate response of poly(ethylene terephthalate)-hydrolases to substrate crystallinity: Basis for understanding the lag phase. *ChemSusChem* **16,** e202300291 (2023) (cit. on pp. 10, 44, 47).

158. Herrero Acero, E., Ribitsch, D., Dellacher, A., *et al.* Surface engineering of a cutinase from *Thermobifida cellulosilytica* for improved polyester hydrolysis. *Biotechnol Bioeng* **110,** 2581–2590 (2013) (cit. on pp. 10, 47).

159. Bååth, J. A., Jensen, K., Borch, K., Westh, P. & Kari, J. Sabatier principle for rationalizing enzymatic hydrolysis of a synthetic polyester. *JACS Au* **2,** 1223–1231 (2022) (cit. on pp. 10, 48, 55).

160. Li, Z., Zhao, Y., Wu, P., *et al.* Structural insight and engineering of a plastic degrading hydrolase Ple629. *Biochem Bioph Res Co* **626,** 100–106 (2022) (cit. on p. 11).

161. Yang, Y., Min, J., Xue, T., *et al.* Complete bio-degradation of poly(butylene adipate-co-terephthalate) via engineered cutinases. *Nat Commun* **14,** 1645 (2023) (cit. on p. 11).

162. Han, X., Liu, W., Huang, J. W., *et al.* Structural insight into catalytic mechanism of PET hydrolase. *Nat Commun* **8,** 2106 (2017) (cit. on pp. 11–14, 40, 59, 61, 68).

163. Von Haugwitz, G., Han, X., Pfaff, L., *et al.* Structural insights into (tere)phthalate-ester hydrolysis by a carboxylesterase and its role in promoting PET depolymerization. *ACS Catal* **12,** 15259–15270 (2022) (cit. on p. 11).

164. Bollinger, A., Thies, S., Knieps-Grünhagen, E., *et al.* A novel polyester hydrolase from the marine bacterium *Pseudomonas aestusnigri* – Structural and functional insights. *Front Microbiol* **11** (2020) (cit. on pp. 11, 43, 50).

165. Kawabata, T., Oda, M. & Kawai, F. Mutational analysis of cutinase-like enzyme, Cut190, based on the 3D docking structure with model compounds of polyethylene terephthalate. *J Biosci Bioeng* **124,** 28–35 (2017) (cit. on p. 11).

166. Fecker, T., Galaz-Davison, P., Engelberger, F., *et al.* Active site flexibility as a hallmark for efficient PET degradation by *I.sakaiensis* PETase. *Biophys J* **114,** 1302–1312 (2018) (cit. on pp. 11, 39).

167. Charupanit, K., Tipmanee, V., Sutthibutpong, T. & Limsakul, P. Identification of potential sites for a plastic-degrading enzyme by a reverse screening through the protein sequence space and molecular dynamics simulations. *Molecules* **27** (2022) (cit. on p. 11).

168. Pirillo, V., Orlando, M., Tessaro, D., Pollegioni, L. & Molla, G. An efficient protein evolution workflow for the improvement of bacterial PET hydrolyzing enzymes. *Int J Mol Sci* **23** (2022) (cit. on pp. 11, 39).

169. Aristizábal-Lanza, L., Mankar, S. V., Tullberg, C., Zhang, B. & Linares-Pastén, J. A. Comparison of the enzymatic depolymerization of polyethylene terephthalate and AkestraTM using *Humicola insolens* cutinase. *Front Chem Eng* **4** (2022) (cit. on p. 11).

170. Austin, H. P., Allen, M. D., Donohoe, B. S., *et al.* Characterization and engineering of a plastic-degrading aromatic polyesterase. *Proc Natl Acad Sci USA* **115,** E4350–E4357 (2018) (cit. on pp. 11, 43).

171. Zumstein, M. T., Rechsteiner, D., Roduner, N., *et al.* Enzymatic hydrolysis of polyester thin films at the nanoscale: Effects of polyester structure and enzyme active-site accessibility. *Environ Sci Technol* **51,** 7476–7485 (2017) (cit. on pp. 11, 50).

172. Liu, B., He, L., Wang, L., *et al.* Protein crystallography and site-direct mutagenesis analysis of the poly(ethylene terephthalate) hydrolase PETase from *Ideonella sakaiensis*. *ChemBioChem* **19,** 1471–1475 (2018) (cit. on pp. 11, 43, 50).

173. Araújo, R., Silva, C., O'Neill, A., *et al.* Tailoring cutinase activity towards polyethylene terephthalate and polyamide 6,6 fibers. *J Biotechnol* **128,** 849–857 (2007) (cit. on pp. 11, 43, 50).

174. Silva, C., Da, S., Silva, N., *et al.* Engineered *Thermobifida fusca* cutinase with increased activity on polyester substrates. *Biotechnol J* **6,** 1230–1239 (2011) (cit. on pp. 11, 43, 50).

175. Ma, Y., Yao, M., Li, B., *et al.* Enhanced poly(ethylene terephthalate) hydrolase activity by protein engineering. *Engineering* **4,** 888–893 (2018) (cit. on p. 11).

176. Chen, C. C., Han, X., Ko, T. P., Liu, W. & Guo, R. T. Structural studies reveal the molecular mechanism of PETase. *FEBS J* **285,** 3717–3723 (2018) (cit. on pp. 11, 14, 59).

177. Chen, C.-C., Han, X., Li, X., *et al.* General features to enhance enzymatic activity of poly(ethylene terephthalate) hydrolysis. *Nat Catal,* 425–430 (4 2021) (cit. on pp. 11, 14, 59).

178. Crnjar, A., Griñen, A., Kamerlin, S. C. L. & Ramírez-Sarmiento, C. A. Conformational selection of a tryptophan side chain drives the generalized increase in activity of PET hydrolases through a Ser/Ile double mutation. *ACS Org Inorg Au* **3,** 109–119 (2023) (cit. on pp. 11, 14, 59).

179. Groß, C., Hamacher, K., Schmitz, K. & Jager, S. Cleavage product accumulation decreases the activity of cutinase during PET hydrolysis. *J Chem Inf Model* **57,** 243–255 (2017) (cit. on pp. 11, 14).

180. James, A. & De, S. Cation–π and hydrophobic interaction controlled PET recognition in double mutated cutinase – identification of a novel binding subsite for better catalytic activity. *RSC Adv* **12,** 20563–20577 (32 2022) (cit. on p. 11).

181. Falkenstein, P., Zhao, Z., Di Pede-Mattatelli, A., *et al.* On the binding mode and molecular mechanism of enzymatic polyethylene terephthalate degradation. *ACS Catal* **13,** 6919–6933 (2023) (cit. on pp. 11, 14, 50, 51, 55).

182. Boneta, S., Arafet, K. & Moliner, V. QM/MM study of the enzymatic biodegradation mechanism of polyethylene terephthalate. *J Chem Inf Model* **61,** 3041–3051 (2021) (cit. on pp. 12, 13, 39, 59, 63, 68).

183. Zheng, M., Li, Y., Dong, W., Zhang, Q. & Wang, W. Enantioselectivity and origin of enhanced efficiency in polyethylene terephthalate hydrolases catalyzed depolymerization. *J Hazard Mater* **452,** 131295 (2023) (cit. on pp. 12, 13, 39, 59, 63).

184. Feng, S., Yue, Y., Zheng, M., *et al. Is*PETase- and *Is*MHETase-catalyzed cascade degradation mechanism toward polyethylene terephthalate. *ACS Sustain Chem & Eng* **9,** 9823–9832 (2021) (cit. on pp. 12, 13, 59, 63).

185. Jerves, C., Neves, R. P. P., Ramos, M. J., da Silva, S. & Fernandes, P. A. Reaction mechanism of the PET degrading enzyme PETase studied with DFT/MM molecular dynamics simulations. *ACS Catal* **11,** 11626–11638 (2021) (cit. on pp. 12–14, 59, 63).

186. Magalhães, R. P., Fernandes, H. S. & Sousa, S. F. The critical role of Asp206 stabilizing residues on the catalytic mechanism of the *Ideonella sakaiensis* PETase. *Cata Sci Technol* **12,** 3474–3483 (11 2022) (cit. on pp. 12, 13, 59, 63, 68).

187. Zheng, M., Li, Y., Dong, W., *et al.* Computational biotransformation of polyethylene terephthalate by depolymerase: A QM/MM approach. *J Hazard Mater* **423,** 127017 (2022) (cit. on pp. 12, 13, 39, 59, 63).

188. Zheng, M., Li, Y., Dong, W., *et al.* Depolymerase-catalyzed polyethylene terephthalate hydrolysis: A unified mechanism revealed by quantum mechanics/molecular mechanics analysis. *ACS Sustain Chem & Eng* **10,** 7341–7348 (2022) (cit. on pp. 12, 13, 59, 63).

189. García-Meseguer, R., Ortí, E., Tuñón, I., Ruiz-Pernía, J. J. & Aragó, J. Insights into the enhancement of the poly(ethylene terephthalate) degradation by FAST-PETase from computational modeling. *J Am Chem Soc* **145,** 19243–19255 (2023) (cit. on pp. 12, 13, 59, 63, 68).

190. Shrimpton-Phoenix, E., Mitchell, J. B. O. & Bühl, M. Computational insights into the catalytic mechanism of *Is*-PETase: An enzyme capable of degrading poly(ethylene) terephthalate. *Chem–Eur J* **28,** e202201728 (2022) (cit. on pp. 13, 14, 59).

191. Zheng, M., Li, Y., Zhang, Q. & Wang, W. Impacts of QM region sizes and conformation numbers on modelling enzyme reactions: A case study of polyethylene terephthalate hydrolase. *Phys Chem Chem Phys* **25,** 31596–31603 (46 2023) (cit. on pp. 13, 59, 63, 68).

192. Świderek, K., Velasco-Lozano, S., Galmés, M. Á., *et al.* Mechanistic studies of a lipase unveil effect of pH on hydrolysis products of small PET modules. *Nat Commun* **14,** 3556 (2023) (cit. on pp. 13, 14, 59, 63).

193. Burschowsky, D., van Eerde, A., Ökvist, M., *et al.* Electrostatic transition state stabilization rather than reactant destabilization provides the chemical basis for efficient chorismate mutase catalysis. *P Natl A Sci* **111,** 17516–17521 (2014) (cit. on p. 13).

194. Pauling, L. Molecular architecture and biological reactions. *Chem Eng News* **24,** 1375–1377 (1946) (cit. on p. 13).

195. Horn, S. J., Sørbotten, A., Synstad, B., *et al.* Endo/exo mechanism and processivity of family 18 chitinases produced by *Serratia marcescens*. *FEBS J* **273,** 491–503 (2006) (cit. on p. 14).

196. Kawai, F., Kawabata, T. & Oda, M. Current knowledge on enzymatic PET degradation and its possible application to waste stream management and other fields. *Appl Microbiol Biotechnol* **103,** 4253–4268 (2019) (cit. on p. 14).

197. Sagong, H.-Y., Seo, H., Kim, T., *et al.* Decomposition of the PET film by MHETase using exo-PETase function. *ACS Catal* **10,** 4805–4812 (2020) (cit. on pp. 14, 50).

198. Wei, R., Breite, D., Song, C., *et al.* Biocatalytic degradation efficiency of postconsumer polyethylene terephthalate packaging determined by their polymer microstructures. *Adv Sci* **6,** 1900491 (2019) (cit. on pp. 14, 50).

199. Barth, M., Oeser, T., Wei, R., *et al.* Effect of hydrolysis products on the enzymatic degradation of polyethylene terephthalate nanoparticles by a polyester hydrolase from *Thermobifida fusca*. *Biochem Eng J* **93,** 222–228 (2015) (cit. on p. 14).

200. Knott, B. C., Erickson, E., Allen, M. D., *et al.* Characterization and engineering of a two-enzyme system for plastics depolymerization. *Proc Natl Acad Sci U S A* **117,** 25476–25485 (2020) (cit. on p. 14).

201. Wei, R., Oeser, T., Schmidt, J., *et al.* Engineered bacterial polyester hydrolases efficiently degrade polyethylene terephthalate due to relieved product inhibition. *Biotechnol Bioeng* **113,** 1658–1665 (2016) (cit. on pp. 14, 39).

202. Sonnendecker, C., Oeser, J., Richter, P. K., *et al.* Low carbon footprint recycling of post-consumer PET plastic with a metagenomic polyester hydrolase. *ChemSusChem* **15,** e202101062 (2022) (cit. on pp. 14, 39, 53, 55).

203. Williams, D. H., Stephens, E., O'Brien, D. P. & Zhou, M. Understanding noncovalent interactions: Ligand binding energy and catalytic efficiency from ligand-induced reductions in motion within receptors and enzymes. *Angew Chem Int Edit* **43,** 6596–6616 (2004) (cit. on p. 17).

204. Adcock, S. A. & McCammon, J. A. Molecular dynamics: Survey of methods for simulating the activity of proteins. *Chem Rev* **106,** 1589–1615 (2006) (cit. on p. 17).

205. Milardi, D. & Pappalardo, M. Molecular dynamics: New advances in drug discovery. *Eur J Med Chem* **91,** 1–3 (2015) (cit. on p. 17).

206. Hospital, A., Goni, J. R., Orozco, M. & Gelpi, J. L. Molecular dynamics simulations: Advances and applications. *Adv Appl Bioinform Chem* **8,** 37–47 (2015) (cit. on pp. 17, 18, 20).

207. Lindahl, E. R. *Molecular modeling of proteins* (ed Kukol, A.) chap. Molecular Dynamics Simulation (2008) (cit. on pp. 17, 18, 20, 22, 24).

208. Baig, K. Interaction of enzymes with lignocellulosic materials: Causes, mechanism and influencing factors. *Bioresour Bioprocess* **7,** 21 (2020) (cit. on p. 17).

209. Pietrucci, F. Strategies for the exploration of free energy landscapes: Unity in diversity and challenges ahead. *Rev Phys* **2,** 32–45 (2017) (cit. on pp. 17, 27).

210. Bussi, G. Hamiltonian replica exchange in GROMACS: A flexible implementation. *Mol Phys* **112,** 379–384 (2014) (cit. on pp. 17, 28).

211. Abraham, M., Murtola, T., Schulz, R., *et al.* GROMACS: High performance molecular simulations through multi-level parallelism from laptops to supercomputers. *SoftwareX* **1-2,** 19–25 (2015) (cit. on p. 17).

212. The PLUMED consortium. *Promoting transparency and reproducibility in enhanced molecular simulations* 2019 (cit. on p. 17).

213. Tribello, G. A., Bonomi, M., Branduardi, D., Camilloni, C. & Bussi, G. PLUMED 2: New feathers for an old bird. *Comput Phys Commun* **185,** 604–613 (2014) (cit. on p. 17).

214. Bussi, G. & Tribello, G. A. in *Methods in molecular biology* 529–578 (Springer New York, 2019) (cit. on p. 17).

215. Bonomi, M., Branduardi, D., Bussi, G., *et al.* PLUMED: A portable plugin for free-energy calculations with molecular dynamics. *Comput Phys Commun* **180,** 1961–1972 (2009) (cit. on p. 17).

216. Warshel, A. & Levitt, M. Theoretical studies of enzymic reactions: Dielectric, electrostatic and steric stabilization of the carbonium ion in the reaction of lysozyme. *J Mol Biol* **103,** 227–249 (1976) (cit. on pp. 18, 32).

217. Zinovjev, K. & Tuñón, I. Adaptive finite temperature string method in collective variables. *J Phys Chem A* **121,** 9764–9772 (2017) (cit. on pp. 18, 36, 38, 60).

218. Case, D., Ben-Shalom, I., Brozell, S., *et al. AMBER 2021* University of California, San Francisco, 2021 (cit. on p. 18).

219. Jäckering, A. *Computational analyses towards the mechanism behind resistance to organic solvent and sodium dodecyl sulfate of a novel esterase* 2020 (cit. on p. 18).

220. Schlick, T. *Molecular modeling and simulation: An interdisciplinary guide* (Springer New York, 2010) (cit. on pp. 18–20, 24, 25).

221. Daan Frenkel, B. S. *Understanding molecular simulation: From algorithms to applications* (Academic Press, 1996) (cit. on p. 18).

222. Abraham, M., Alekseenko, A., Bergh, C., *et al. GROMACS 2023.2 Manual* version 2023.2. 2023 (cit. on pp. 18, 21, 23).

223. Cauchy, M. A. Méthode généerale pour la résolution des systèmes d' éequations simultanéees. *CR Hebd Acad Sci* **25,** 536–538 (1847) (cit. on p. 18).

224. Bussi, G., Donadio, D. & Parrinello, M. Canonical sampling through velocity rescaling. *J Chem Phys* **126** (2007) (cit. on p. 20).

225. Berendsen, H. J. C., Postma, J. P. M., van Gunsteren, W. F., DiNola, A. & Haak, J. R. Molecular dynamics with coupling to an external bath. *J Chem Phys* **81,** 3684–3690 (1984) (cit. on p. 20).

226. Nosé, S. Molecular-dynamics method for simulations in the canonical ensemble. *Mol Phys* **52,** 255–268 (1984) (cit. on p. 20).

227. Hoover, W. Canonical dynamics - equilibrium phase-space distributions. *Phys Rev A* **31,** 1695–1697 (1985) (cit. on p. 20).

228. Parrinello, M. & Rahman, A. Crystal structure and pair potentials: A molecular-dynamics study. *Phys Rev Lett* **45,** 1196–1199 (14 1980) (cit. on p. 20).

229. Parrinello, M. & Rahman, A. Polymorphic transitions in single-crystals - a new molecular-dynamics method. *Mol Phys* **52,** 7182–7190 (1981) (cit. on p. 20).

230. Parrinello, M. & Rahman, A. Strain fluctuations and elastic constants. *J Chem Phys* **76,** 2662–2666 (1982) (cit. on p. 20).

231. P, L. *On the theory of brownian motion.* 1908 (cit. on p. 20).

232. Verlet, L. Computer "experiments" on classical fluids. II. Equilibrium correlation functions. *Phys Rev* **165,** 201–214 (1 1968) (cit. on p. 21).

233. Gunsteren, W. F. V. & Berendsen, H. J. C. A leap-frog algorithm for stochastic dynamics. *Mol Simulat* **1,** 173–185 (1988) (cit. on p. 21).

234. Swope, W. C., Andersen, H. C., Berens, P. H. & Wilson, K. R. A computer simulation method for the calculation of equilibrium constants for the formation of physical clusters of molecules: Application to small water clusters. *J Chem Phys* **76,** 637–649 (1982) (cit. on pp. 21, 22).

235. Hess, B., Bekker, H., Berendsen, H. & Fraaije, J. LINCS: A linear constraint solver for molecular simulations. *J Comput Chem* **18,** 1463–1472 (1997) (cit. on p. 22).

236. Ryckaert, J.-P., Ciccotti, G. & Berendsen, H. J. Numerical integration of the cartesian equations of motion of a system with constraints: Molecular dynamics of n-alkanes. *J Comput Phys* **23,** 327–341 (1977) (cit. on p. 22).

237. Darden, T., York, D. & Pedersen, L. Particle mesh Ewald - an $N \cdot log(N)$ method for Ewald sums in large systems. *J Chem Phys* **98,** 10089–10092 (1993) (cit. on p. 25).

238. Essmann, U., Perera, L. & Berkowitz, M. A smooth particle mesh Ewald method. *J Chem Phys* **103,** 8577–8593 (1995) (cit. on p. 25).

239. Perram, J. W., Petersen, H. G. & Leeuw, S. W. D. An algorithm for the simulation of condensed matter which grows as the 3/2 power of the number of particles. *Mol Phys* **65,** 875–893 (1988) (cit. on p. 25).

240. Fincham, D. Optimisation of the Ewald sum for large systems. *Mol Simulat* **13,** 1–9 (1994) (cit. on p. 25).

241. Lyubartsev, A. P. & Rabinovich, A. L. Force field development for lipid membrane simulations. *BBA - Biomembranes* **1858,** 2483–2497 (2016) (cit. on p. 25).

242. Liebl, K. & Zacharias, M. The development of nucleic acids force fields: From an unchallenged past to a competitive future. *Biophys J* **122,** 2841–2851 (2023) (cit. on p. 25).

243. Lopes, P. E. M., Guvench, O. & MacKerell, A. D. in *Molecular modeling of proteins* (ed Kukol, A.) 47–71 (Springer New York, New York, NY, 2015) (cit. on p. 25).

244. Bayly, C. I., Cieplak, P., Cornell, W. & Kollman, P. A. A well-behaved electrostatic potential based method using charge restraints for deriving atomic charges: The RESP model. *J Phys Chem* **97,** 10269–10280 (1993) (cit. on p. 25).

245. Cornell, W. D., Cieplak, P., Bayly, C. I. & Kollman, P. A. Application of RESP charges to calculate conformational energies, hydrogen bond energies, and free energies of solvation. *J Am Chem Soc* **115,** 9620–9631 (1993) (cit. on p. 25).

246. Woods, R. J. & Chappelle, R. Restrained electrostatic potential atomic partial charges for condensed-phase simulations of carbohydrates. *Theochem* **527,** 149–156 (2000) (cit. on p. 26).

247. Gelin, B. R. & Karplus, M. Side-chain torsional potentials: Effect of dipeptide, protein, and solvent environment. *Biochemistry* **18,** 1256–1268 (1979) (cit. on p. 26).

248. Blaney, J. M., Weiner, P. K., Dearing, A., *et al.* Molecular mechanics simulation of protein-ligand interactions: Binding of thyroid hormone analogs to prealbumin. *J Am Chem Soc* **104,** 6424–6434 (1982) (cit. on p. 26).

249. Wipff, G., Dearing, A., Weiner, P. K., Blaney, J. M. & Kollman, P. A. Molecular mechanics studies of enzyme-substrate interactions: The interaction of L- and D-N-acetyltryptophanamide with α-chymotrypsin. *J Am Chem Soc* **105,** 997–1005 (1983) (cit. on p. 26).

250. Weiner, S. J., Kollman, P. A., Nguyen, D. T. & Case, D. A. An all atom force field for simulations of proteins and nucleic acids. *J Comput Chem* **7,** 230–252 (1986) (cit. on p. 26).

251. Maier, J. A., Martinez, C., Kasavajhala, K., *et al.* ff14SB: Improving the accuracy of protein side chain and backbone parameters from ff99SB. *J Chem Theory Comput* **11,** 3696–3713 (2015) (cit. on p. 26).

252. Hornak, V., Abel, R., Okur, A., *et al.* Comparison of multiple Amber force fields and development of improved protein backbone parameters. *Proteins* **65,** 712–725 (2006) (cit. on p. 26).

253. Jorgensen, W. L. Quantum and statistical mechanical studies of liquids. 10. Transferable intermolecular potential functions for water, alcohols, and ethers. Application to liquid water. *J Am Chem Soc* **103,** 335–340 (1981) (cit. on p. 26).

254. Jorgensen, W., Chandrasekhar, J., Madura, J., Impey, R. & Klein, M. Comparison of simple potential functions for simulating liquid water. *J Chem Theory Comput* **79,** 926–935 (1983) (cit. on p. 26).

255. Liao, Q. in *Computational approaches for understanding dynamical systems: Protein folding and assembly* (eds Strodel, B. & Barz, B.) 177–213 (Academic Press, 2020) (cit. on p. 27).

256. Sugita, Y. & Okamoto, Y. Replica-exchange molecular dynamics method for protein folding. *Chem Phys Lett* **314,** 141–151 (1999) (cit. on p. 27).

257. Sugita, Y. & Okamoto, Y. Replica-exchange multicanonical algorithm and multicanonical replica-exchange method for simulating systems with rough energy landscape. *Chem Phys Lett* **329,** 261–270 (2000) (cit. on p. 27).

258. Metropolis, N., Rosenbluth, A. W., Rosenbluth, M. N., Teller, A. H. & Teller, E. Equation of state calculations by fast computing machines. *J Chem Phys* **21,** 1087–1092 (2004) (cit. on p. 27).

259. Hastings, W. K. Monte Carlo sampling methods using Markov chains and their applications. *Biometrika* **57,** 97–109 (1970) (cit. on p. 27).

260. Moors, S. L. C., Michielssens, S. & Ceulemans, A. Improved replica exchange method for native-state protein sampling. *J Chem Theory Comput* **7,** 231–237 (2011) (cit. on p. 28).

261. Wang, L., Friesner, R. A. & Berne, B. J. Replica exchange with solute scaling: A more efficient version of replica exchange with solute tempering (REST2). *J Phys Chem B* **115,** 9431–9438 (2011) (cit. on p. 28).

262. Matsunaga, Y., Kamiya, M., Oshima, H., *et al.* Use of multistate Bennett acceptance ratio method for free-energy calculations from enhanced sampling and free-energy perturbation. *Biophys Rev* **14,** 1503–1512 (2022) (cit. on pp. 28, 29).

263. Shirts, M. R. & Ferguson, A. L. Statistically optimal continuous free energy surfaces from biased simulations and multistate reweighting. *J Chem Theory Comput* **16,** 4107–4125 (2020) (cit. on p. 28).

264. Chodera, J. D. A simple method for automated equilibration detection in molecular simulations. *J Chem Theory Comput* **12,** 1799–1805 (2016) (cit. on p. 28).

265. Shirts, M. R. & Chodera, J. D. Statistically optimal analysis of samples from multiple equilibrium states. *J Chem Phys* **129,** 124105 (2008) (cit. on p. 28).

266. Hotelling, H. Relations between two sets of variates. *Biometrika* **28,** 321–377 (1936) (cit. on p. 29).

267. Pearson, K. LIII. On lines and planes of closest fit to systems of points in space. *London Edinburgh Dublin Philos Mag J Sci* **2,** 559–572 (1901) (cit. on p. 29).

268. Jolliffe, I. T. *Principal component analysis* (Springer New York, NY, 2006) (cit. on p. 29).

269. Jolliffe, I. T. & Cadima, J. Principal component analysis: A review and recent developments. *Philos T R Soc A* **374,** 20150202 (2016) (cit. on p. 29).

270. Cossio-Pérez, R., Palma, J. & Pierdominici-Sottile, G. Consistent principal component modes from molecular dynamics simulations of proteins. *J Chem Inf Model* **57,** 826–834 (2017) (cit. on p. 29).

271. Amadei, A., Linssen, A. B. M. & Berendsen, H. J. C. Essential dynamics of proteins. *Proteins* **17,** 412–425 (1993) (cit. on p. 29).

272. Berendsen, H. J. & Hayward, S. Collective protein dynamics in relation to function. *Curr Opin Struc Biol* **10,** 165–169 (2000) (cit. on p. 29).

273. Hess, B. Convergence of sampling in protein simulations. *Phys Rev E* **65,** 031910 (2002) (cit. on p. 30).

274. Palma, J. & Pierdominici-Sottile, G. On the uses of PCA to characterise molecular dynamics simulations of biological macromolecules: Basics and tips for an effective use. *ChemPhysChem* **24,** e202200491 (2023) (cit. on p. 30).

275. Torrie, G. & Valleau, J. Nonphysical sampling distributions in Monte Carlo free-energy estimation: Umbrella sampling. *J Comput Phys* **23,** 187–199 (1977) (cit. on p. 30).

276. Kästner, J. Umbrella sampling. *WIREs Comput Mol Sci* **1,** 932–942 (2011) (cit. on p. 30).

277. Kästner, J. & Thiel, W. Bridging the gap between thermodynamic integration and umbrella sampling provides a novel analysis method: "Umbrella integration". *J Chem Phys* **123,** 144104 (2005) (cit. on p. 32).

278. Kästner, J. & Thiel, W. Analysis of the statistical error in umbrella sampling simulations by umbrella integration. *J Chem Phys* **124,** 234106 (2006) (cit. on p. 32).

279. Kästner, J. Umbrella integration in two or more reaction coordinates. *J Chem Phys* **131,** 034109 (2009) (cit. on p. 32).

280. Kumar, S., Rosenberg, J. M., Bouzida, D., Swendsen, R. H. & Kollman, P. A. THE weighted histogram analysis method for free-energy calculations on biomolecules. I. The method. *J Comput Chem* **13,** 1011–1021 (1992) (cit. on p. 32).

281. Groenhof, G. Introduction to QM/MM simulations. *Methods Mol Biol* **924,** 43–66 (2013) (cit. on p. 32).

282. Clemente, C. M., Capece, L. & Martí, M. A. Best practices on QM/MM Simulations of biological systems. *J Chem Inf Model* **63,** 2609–2627 (2023) (cit. on p. 32).

283. Jensen, F. *Introduction to computational chemistry* (John Wiley & Sons, Inc., Hoboken, NJ, USA, 2006) (cit. on p. 32).

284. Gaunt, J. A. A theory of Hartree's atomic fields. *Math Proc Cambridge* **24,** 328–342 (1928) (cit. on p. 34).

285. Hartree, D. R. The wave mechanics of an atom with a non-coulomb central field. Part II. Some results and discussion. *Math Proc Cambridge* **24,** 111–132 (1928) (cit. on p. 34).

286. Slater, J. C. The self consistent field and the structure of atoms. *Physical Review* **32,** 339–348 (1928) (cit. on p. 34).

287. Fock, V. Näherungsmethode zur Lösung des quantenmechanischen Mehrkörperproblems. *Zeitschrift fur Physik* **61,** 126–148 (1930) (cit. on p. 34).

288. Hartree, D. R. & Hartree, W. Self-consistent field, with exchange, for beryllium. *Proc R Soc Lond A - Mat* **150,** 9–33 (1935) (cit. on p. 34).

289. Slater, J. C. Note on Hartree's method. *Phys Rev* **35,** 210–211 (2 1930) (cit. on p. 34).

290. Ditchfield, R., Hehre, W. J. & Pople, J. A. Self-consistent molecular-orbital methods. IX. An extended Gaussian-type basis for molecular-orbital studies of organic molecules. *J Chem Phys* **54,** 724–728 (1971) (cit. on p. 35).

291. Hehre, W. J., Ditchfield, R. & Pople, J. A. Self-consistent molecular orbital methods. XII. Further extensions of Gaussian-type basis sets for use in molecular orbital studies of organic molecules. *J Chem Phys* **56,** 2257–2261 (Sept. 1972) (cit. on p. 35).

292. Hariharan, P. & Pople, J. The influence of polarization functions on molecular orbital hydrogenation energies. *Theoret Chim Acta* **28,** 213–222 (1973) (cit. on p. 35).

293. Francl, M. M., Pietro, W. J., Hehre, W. J., *et al.* Self-consistent molecular orbital methods. XXIII. A polarization-type basis set for second-row elements. *J Chem Phys* **77,** 3654–3665 (1982) (cit. on p. 35).

294. Frisch, M. J., Pople, J. A. & Binkley, J. S. Self-consistent molecular orbital methods 25. Supplementary functions for Gaussian basis sets. *J Chem Phys* **80,** 3265–3269 (1984) (cit. on p. 35).

295. Mardirossian, N. & Head-Gordon, M. Thirty years of density functional theory in computational chemistry: an overview and extensive assessment of 200 density functionals. *Mol Phys* **115,** 2315–2372 (2017) (cit. on p. 35).

296. Burke, K. Perspective on density functional theory. *J Chem Phys* **136,** 150901 (2012) (cit. on p. 35).

297. Becke, A. D. Perspective: Fifty years of density-functional theory in chemical physics. *J Chem Phys* **140,** 18A301 (2014) (cit. on p. 35).

298. Hohenberg, P. & Kohn, W. Inhomogeneous electron gas. *Phys Rev* **136,** B864–B871 (3B 1964) (cit. on p. 35).

299. Kohn, W. & Sham, L. J. Self-consistent equations including exchange and correlation effects. *Phys Rev* **140,** A1133–A1138 (4A 1965) (cit. on p. 35).

300. Zhao, Y. & Ruhlar, D. The M06 suite of density functionals for main group thermochemistry, thermochemical kinetics, noncovalent interactions, excited states, and transition elements: two new functionals and systematic testing of four M06-class functionals and 12 other functionals. *Theor Chem Account* **120,** 215–241 (2008) (cit. on pp. 36, 60, 63, 66).

301. Dewar, M. J. S., Zoebisch, E. G., Healy, E. F. & Stewart, J. J. P. Development and use of quantum mechanical molecular models. 76. AM1: a new general purpose quantum mechanical molecular model. *J Am Chem Soc* **107,** 3902–3909 (1985) (cit. on pp. 36, 63).

302. Gaus, M., Cui, Q. & Elstner, M. DFTB3: Extension of the self-consistent-charge density-functional tight-binding method (SCC-DFTB). *J Chem Theory Comput* **7,** 931–948 (2011) (cit. on pp. 36, 60, 63).

303. Maragliano, L. & Vanden-Eijnden, E. On-the-fly string method for minimum free energy paths calculation. *Chem Phys Lett* **446,** 182–190 (2007) (cit. on p. 36).

304. Maragliano, L., Fischer, A., Vanden-Eijnden, E. & Ciccotti, G. String method in collective variables: Minimum free energy paths and isocommittor surfaces. *J Chem Phys* **125,** 024106 (2006) (cit. on p. 36).

305. Fritzsche, S., Tischer, F., Peukert, W. & Castiglione, K. You get what you screen for: a benchmark analysis of leaf branch compost cutinase variants for polyethylene terephthalate (PET) degradation. *React Chem Eng* **8,** 2156–2169 (9 2023) (cit. on p. 39).

306. Ding, Z., Xu, G., Miao, R., *et al.* Rational redesign of thermophilic PET hydrolase LCCICCG to enhance hydrolysis of high crystallinity polyethylene terephthalates. *Journal of Hazardous Materials* **453,** 131386 (2023) (cit. on p. 39).

307. Mrigwani, A., Thakur, B. & Guptasarma, P. Counter-intuitive enhancement of degradation of polyethylene terephthalate through engineering of lowered enzyme binding to solid plastic. *Proteins* **91,** 807–821 (2023) (cit. on pp. 39, 53).

308. Ronkvist, Å. M., Xie, W., Lu, W. & Gross, R. A. Cutinase-catalyzed hydrolysis of poly(ethylene terephthalate). *Macromolecules* **42,** 5128–5138 (2009) (cit. on pp. 40, 55).

309. Roth, C., Wei, R., Oeser, T., *et al.* Structural and functional studies on a thermostable polyethylene terephthalate degrading hydrolase from *Thermobifida fusca*. *Appl Microbiol Biotechnol* **98,** 7815–7823 (2014) (cit. on p. 41).

310. Rabe, M., Verdes, D. & Seeger, S. Understanding protein adsorption phenomena at solid surfaces. *Adv Colloid Interfac* **162,** 87–106 (2011) (cit. on p. 44).

311. Secundo, F. Conformational changes of enzymes upon immobilisation. *Chem Soc Rev* **42,** 6250–6261 (15 2013) (cit. on p. 44).

312. Bourassin, N., Barbault, F., Baaden, M. & Sacquin-Mora, S. Between two walls: Modeling the adsorption behavior of β-glucosidase A on bare and SAM-functionalised gold surfaces. *bioRxiv* (2021) (cit. on p. 44).

313. Thomsen, T. B., Almdal, K. & Meyer, A. S. Significance of poly(ethylene terephthalate) (PET) substrate crystallinity on enzymatic degradation. *New Biotechnol* **78,** 162–172 (2023) (cit. on p. 44).

314. Sabatier, P. *La Catalyse en chimie organique* (Nouveau Monde, 2013) (cit. on p. 47).

315. Wei, R., Song, C., sing, D., *et al.* Conformational fitting of a flexible oligomeric substrate does not explain the enzymatic PET degradation. *Nat Commun* **10,** 5581 (2019) (cit. on p. 50).

316. Guo, B., Vanga, S. R., Lopez-Lorenzo, X., *et al.* Conformational selection in biocatalytic plastic degradation by PETase. *ACS Catal* **12,** 3397–3409 (2022) (cit. on p. 50).

317. Giraldo-Narcizo, S., Guenani, N., Sánchez-Pérez, A. M. & Guerrero, A. Accelerated polyethylene terephthalate (PET) enzymatic degradation by room temperature alkali pre-treatment for reduced polymer crystallinity. *ChemBioChem* **24,** e202200503 (2023) (cit. on p. 50).

318. Kawai, F., Kawabata, T. & Oda, M. Current ctate and perspectives related to the polyethylene terephthalate hydrolases available for biorecycling. *ACS Sustain Chem Eng* **8,** 8894–8908 (2020) (cit. on p. 50).

319. Bai, C., Spontak, R., Koch, C., Saw, C. & Balik, C. Structural changes in poly(ethylene terephthalate) induced by mechanical milling. *Polymer* **41,** 7147–7157 (2000) (cit. on p. 50).

320. Brizendine, R. K., Erickson, E., Haugen, S. J., *et al.* Particle size reduction of poly(ethylene terephthalate) increases the rate of enzymatic depolymerization but does not increase the overall conversion extent. *ACS Sustain Chem Eng* **10,** 9131–9140 (2022) (cit. on p. 50).

321. Schubert, S., Schaller, K., Bååth, J. A., *et al.* Reaction pathways for the enzymatic degradation of poly(ethylene terephthalate): What characterizes an efficient PET-hydrolase? *ChemBioChem* **24,** e202200516 (2023) (cit. on pp. 50, 55).

322. Kawai, F., Furushima, Y., Mochizuki, N., *et al.* Efficient depolymerization of polyethylene terephthalate (PET) and polyethylene furanoate by engineered PET hydrolase Cut190. *AMB Express* **12,** 134 (2022) (cit. on p. 50).

323. Bussi, G. & Laio, A. Using metadynamics to explore complex free-energy landscapes. *Nat Rev Phys* **2,** 200–212 (2020) (cit. on pp. 50, 56).

324. Pfaff, L., Breite, D., Badenhorst, C. P., Bornscheuer, U. T. & Wei, R. in *Enzymatic Plastic Degradation* (eds Weber, G., Bornscheuer, U. T. & Wei, R.) 253–270 (Academic Press, 2021) (cit. on p. 55).

325. Belisário-Ferrari, M. R., Wei, R., Schneider, T., Honak, A. & Zimmermann, W. Fast turbidimetric assay for analyzing the enzymatic hydrolysis of polyethylene terephthalate model substrates. *Biotechnol J* **14,** 1800272 (2019) (cit. on p. 55).

326. Bååth, J. A., Borch, K., Jensen, K., Brask, J. & Westh, P. Comparative biochemistry of four polyester (PET) hydrolases**. *ChemBioChem* **22,** 1627–1637 (2021) (cit. on p. 55).

327. Scandola, M., Focarete, M. L. & Frisoni, G. Simple kinetic model for the heterogeneous enzymatic hydrolysis of natural poly(3-hydroxybutyrate). *Macromolecules* **31,** 3846–3851 (1998) (cit. on p. 55).

328. Kari, J., Andersen, M., Borch, K. & Westh, P. An inverse Michaelis–Menten approach for interfacial enzyme kinetics. *ACS Catal* **7,** 4904–4914 (2017) (cit. on p. 55).

329. Cui, Y., Chen, Y., Sun, J., *et al.* Computational redesign of a hydrolase for nearly complete PET depolymerization at industrially relevant high-solids loading. *Nat Commun* **15,** 1417 (2024) (cit. on p. 55).

330. Selvaraj, C., Rudhra, O., Alothaim, A. S., Alkhanani, M. & Singh, S. K. in *Protein Design and Structure* (ed Donev, R.) 59–83 (Academic Press, 2022) (cit. on p. 59).

331. Schrödinger, LLC. *The PyMOL molecular graphics system, Version 1.8* 2015 (cit. on p. 61).

332. Perdew, J. P., Burke, K. & Ernzerhof, M. Generalized gradient approximation made simple. *Phys Rev Lett* **77,** 3865–3868 (18 1996) (cit. on p. 63).

333. Zhang, Y. & Yang, W. Comment on "Generalized gradient approximation made simple". *Phys Rev Lett* **80,** 890–890 (4 1998) (cit. on p. 63).

334. Fischer, S. A., Dunlap, B. I. & Gunlycke, D. Correlated dynamics in aqueous proton diffusion. *Chem Sci* **9,** 7126–7132 (35 2018) (cit. on p. 63).

335. Mangiatordi, G. F., Brémond, E. & Adamo, C. DFT and proton transfer reactions: A benchmark study on structure and kinetics. *J Chem Theory Comput* **8,** 3082–3088 (2012) (cit. on p. 63).

Appendix

A

A.1 Supplementary Figures

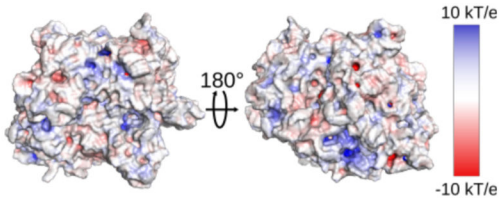


Fig. A1.: The EPS of an amorphous PET bulk. The EPS of the PET bulk starting structure used in this study is shown from two perspectives with a positive EPS coloured in blue and a negative coloured in red, while hydrophobic areas are shown in white. Adapted from publication II (Sec. A.2).

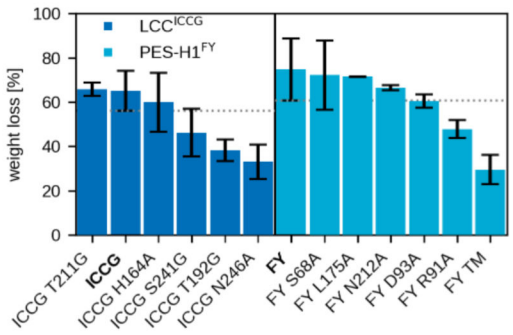


Fig. A2.: PET film weight loss of the original and variants of LCC^{ICCG} and PES-H1^{FY}. The LCC^{ICCG} (ICCG, left, blue) and PES-H1^{FY} (FY, right, lightblue) variants include five single-point mutations per enzyme, given as axis labels, and the PES-H1^{FY} triple mutant (TM) T11V/S13A/S14A. Variants are ordered according to the percentage weight loss of PET films upon degradation, which serves as a measure for the PET degradation activity. Depolymerisation of 60 mg PET film was conducted for 24 h at 70 °C in 1 M potassium phosphate buffer (pH 8) adding the respective enzyme variants in a 1 mg enzyme/g PET ratio. Reactions were performed in duplicate for PES-H1^{FY} L175A and LCC^{ICCG} T211G and for all others at least in triplicate. Adapted from publication II (Sec. A.2).

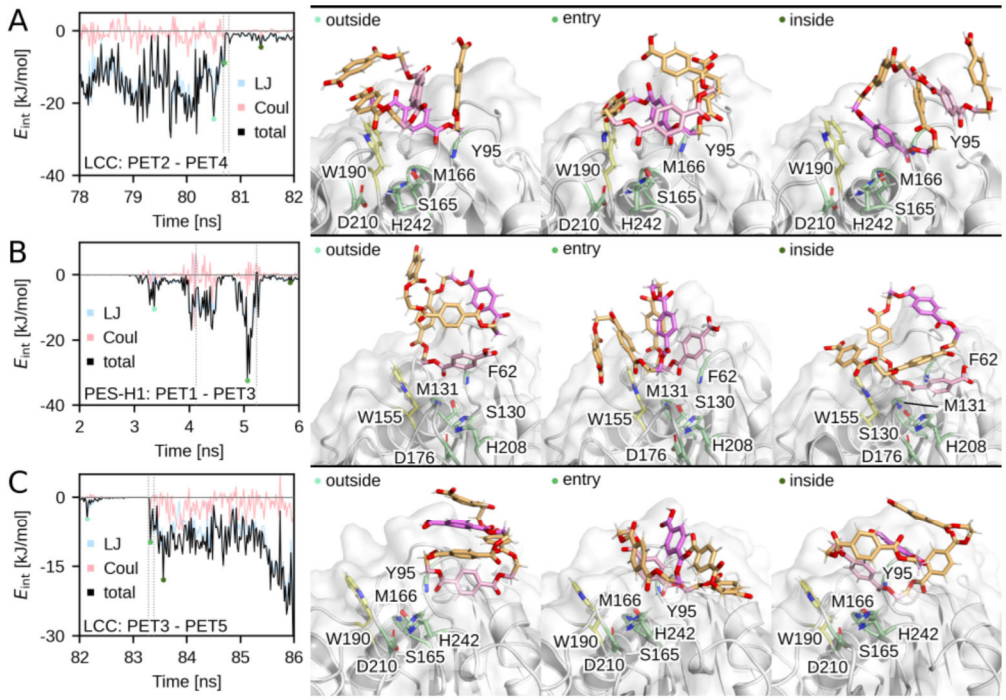


Fig. A3.: Examples of intramolecular PET–PET interactions. The examples comprise interactions exclusively before entry (A, LCC PET2–PET4), during entry (B, PES-H1 PET1–PET3), or after entry (C, LCC PET3–PET5). The left plot depicts the total interaction energy E_{int}, comprising polar Coul and hydrophobic LJ interactions during a 4 ns snippet around the entry. Catalytic triad and oxyanion hole are depicted in green, the 'wobbling' tryptophan in yellow, PET in orange, and the two interacting PET units in light pink (lower residue ID) and dark pink (higher residue ID). The time of the entry phase is indicated by dotted lines. Three snapshots from each phase (outside, entry, inside) are presented on the right, with exact timestamps highlighted in shades of green in the plot. Adapted from publication II (Sec. A.2).

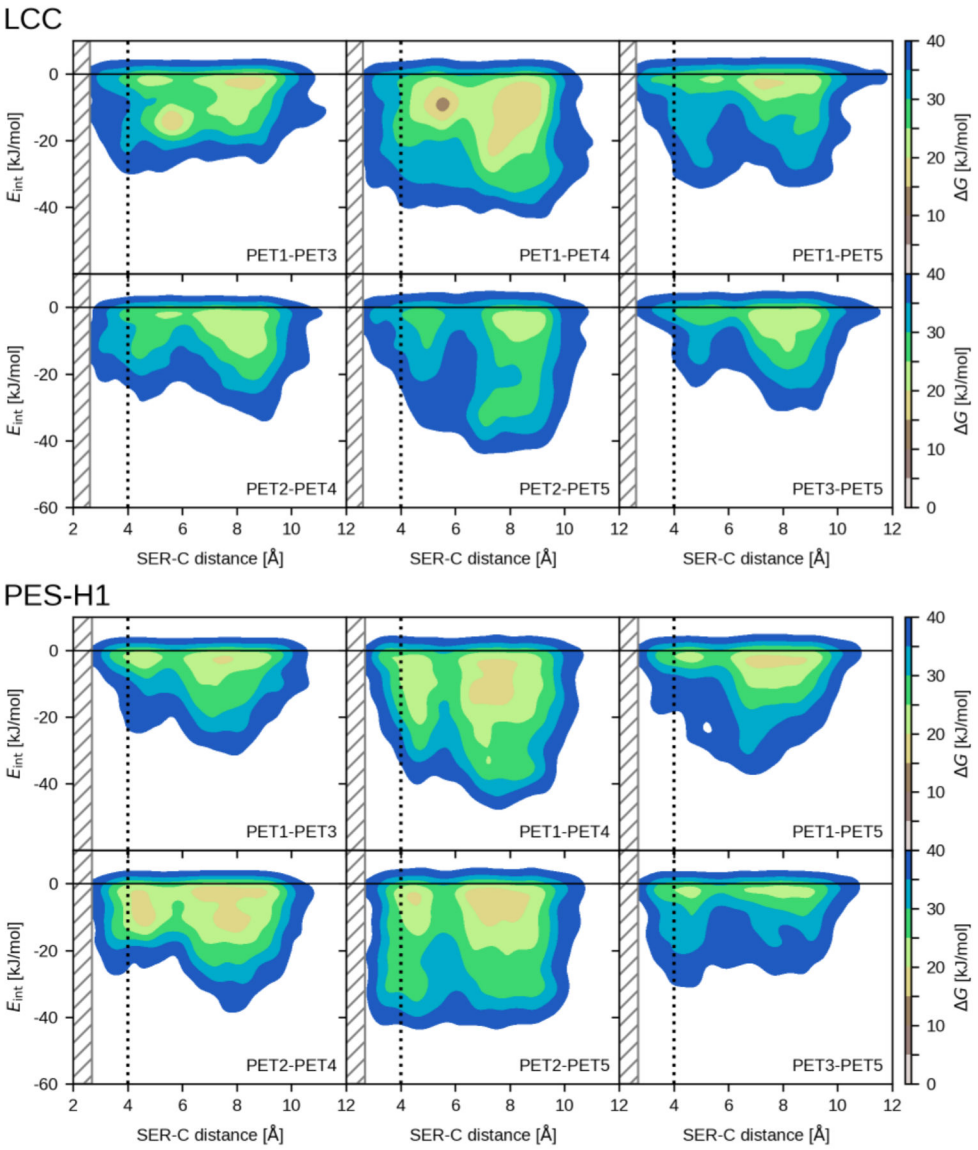


Fig. A4.: Free energy surfaces of PET–PET interactions over the SER–C distance. The FESs are shown for LCC (top) and PES-H1 (bottom) simulations. The area with a minimum SER–C distance <4 Å harbours productive poses. The grey hatched area indicates distances that were not sampled, resulting in a truncated FES. Adapted from publication II (Sec. A.2).

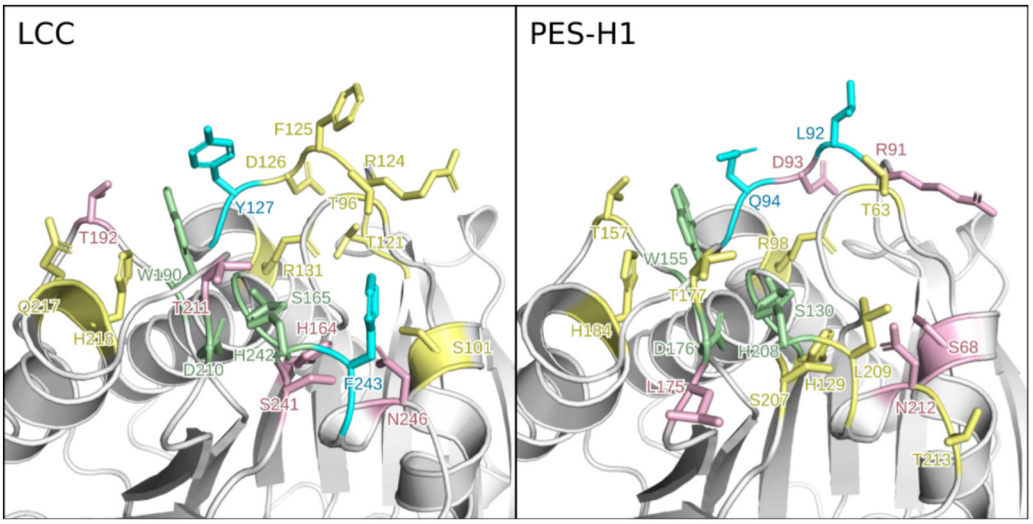


Fig. A5.: Mutation sites of variants addressed using FES. The catalytic triad residues as well as the 'wobbling' tryptophan are shown in green, the LCC^{IG} and PES-H1^{FY} mutation sites in cyan, the experimentally evaluated mutation sites in red and all other mutation sites addressed in yellow. Adapted from publication II (Sec. A.2).

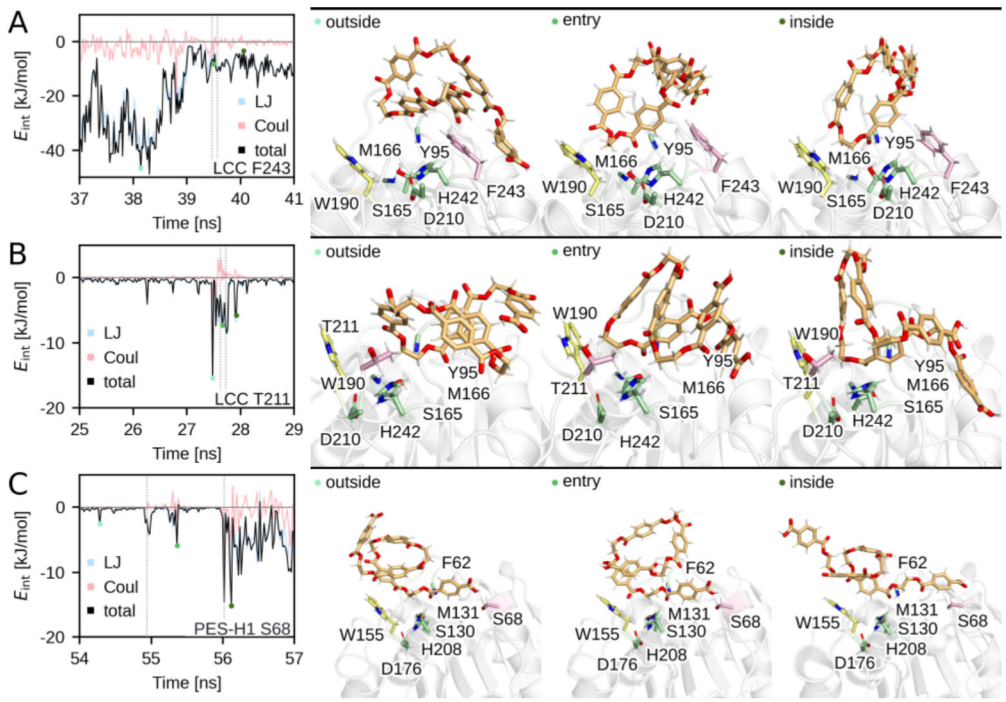


Fig. A6.: Examples of intermolecular PET–residue interactions. Instances of residues interacting with PET exclusively before entry (A, LCC F243), during entry (B, LCC T211), or after entry (C, PES-H1 S68). The left plot depicts the total interaction energy E_{int}, comprising polar Coul and hydrophobic LJ interactions during a 4 ns snippet around the entry. The catalytic triad and oxyanion hole are depicted in green, the 'wobbling' tryptophan in yellow, PET in orange, and the interacting residue in pink. Dotted lines indicate the entry phase's duration. Three snapshots from each phase (outside, entry, inside) are displayed on the right, with exact timestamps highlighted in shades of green in the plot. Adapted from publication II (Sec. A.2).

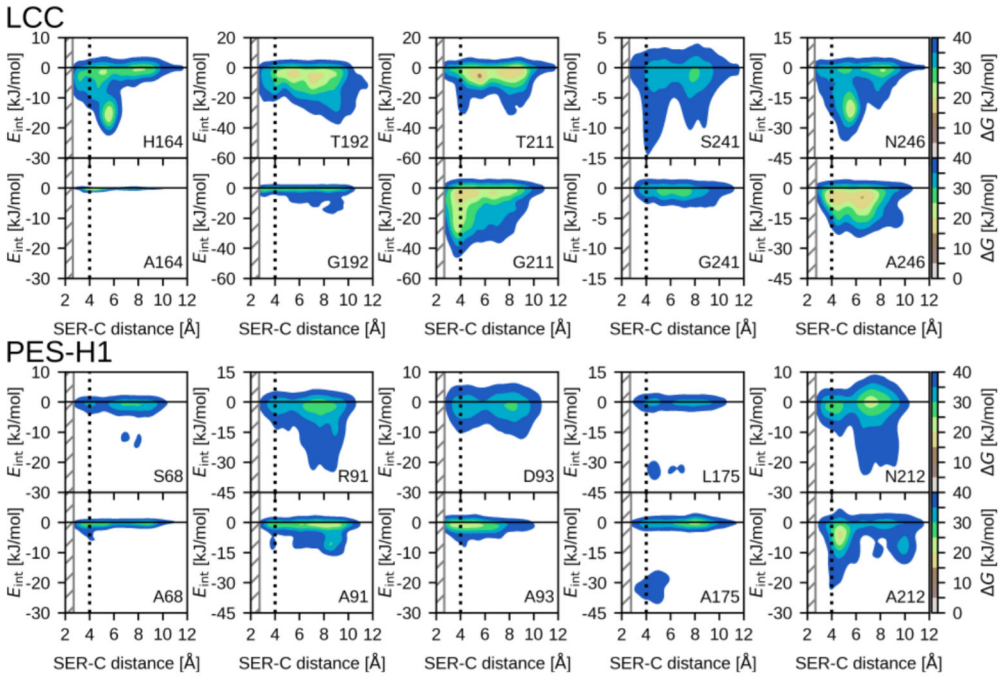


Fig. A7.: FESs of PET–residue interactions over the SER–C distance. The FESs are shown for LCC and PES-H1 residues (top) and mutated residues of the corresponding variants (bottom). The area with a minimum SER–C distance <4 Å harbours productive poses. The grey hatched area indicates distances that were not sampled, resulting in a truncated FES. Adapted from publication II (Sec. A.2).

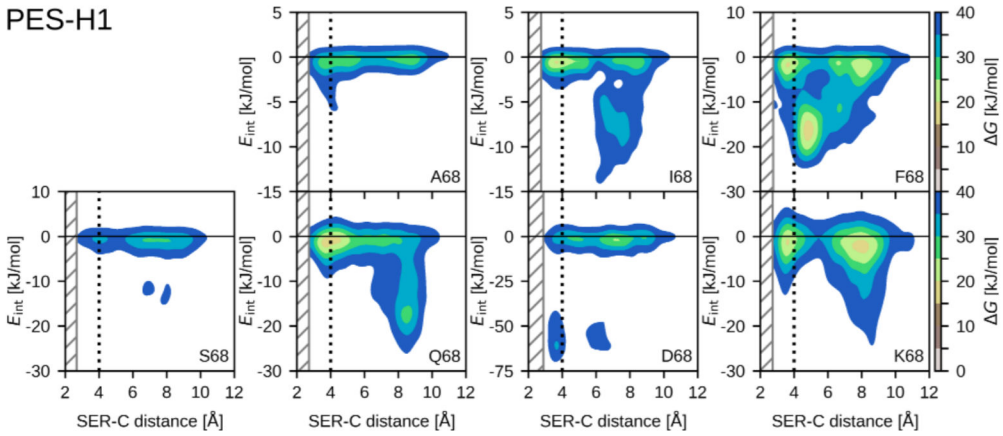


Fig. A8.: FESs of PET–residue interactions at position 68 of PES-H1^{FY} variants over the SER–C distance. The left FES shows the interaction of the WT S68 and the remaining ones of PES-H1^{FY} variants. The area with a minimum SER–C distance <4 Å harbours productive poses. The grey hatched area indicates distances that were not sampled, resulting in a truncated FES. Adapted from publication II (Sec. A.2).

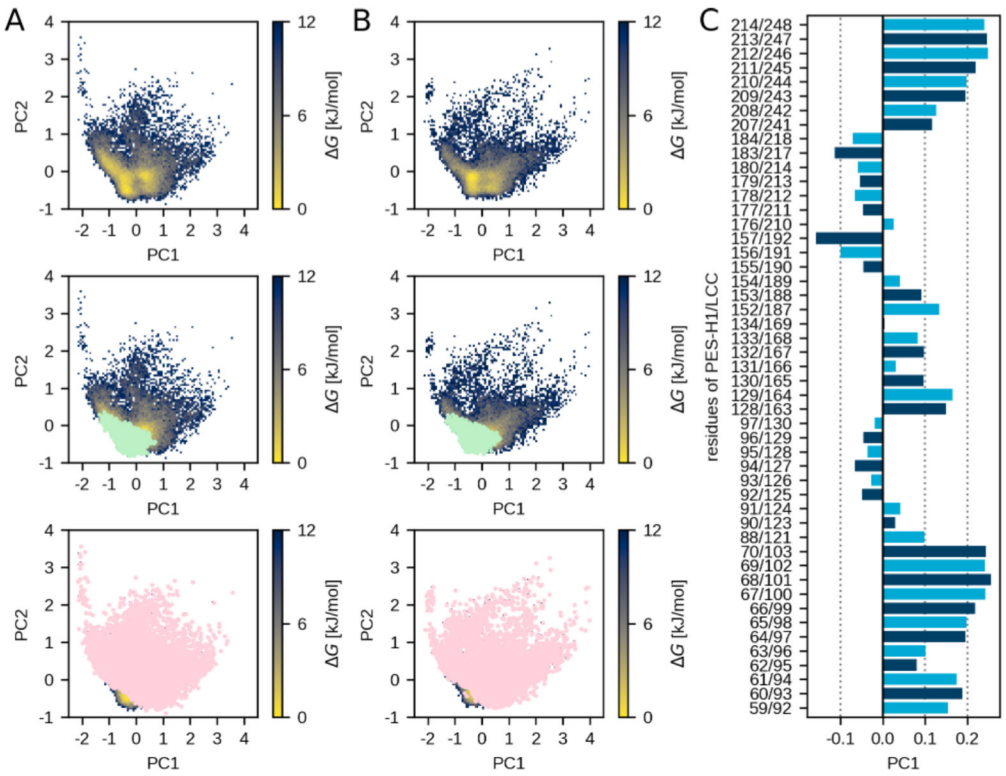


Fig. A9.: FESs over PC1 and PC2 and the contribution profile of amino acid positions to PC1. In the central figure of A and B, productive states of PET in the active site of LCC (A) and PES-H1 (B) are highlighted in green, while the lower figure depicts unproductive states in red. The contribution profile of amino acid positions to PC1 is shown in C. Adapted from publication II (Sec. A.2).

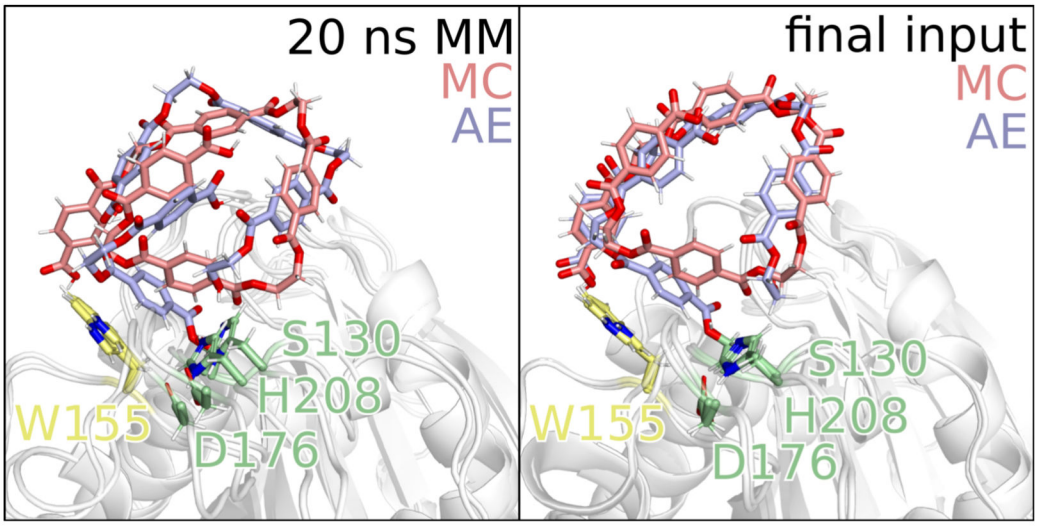


Fig. A10.: Comparison of the PET conformations after thorough relaxation with the input structures for PES-H1. PET conformations of the MC (red) and AE (blue) for PES-H1 after 20 ns MM production run (left) with prior two-step equilibration and the final structures used as input for the ASM run (right). Here, an additional QM/MM optimisation and 50 ps relaxation followed the 20 ns production run for the MC. The AE was generated from the RC structure after 20 ns MM production run and subjected to MM minimisation, QM/MM optimisation and two 50 ps QM/MM simulations, of which the first included restraints to set the dihedral angle to that observed during the 20 ns MM production run while the second was performed without restraints to relax the structures prior to ASM. Adapted from manuscript I (Sec. A.2).

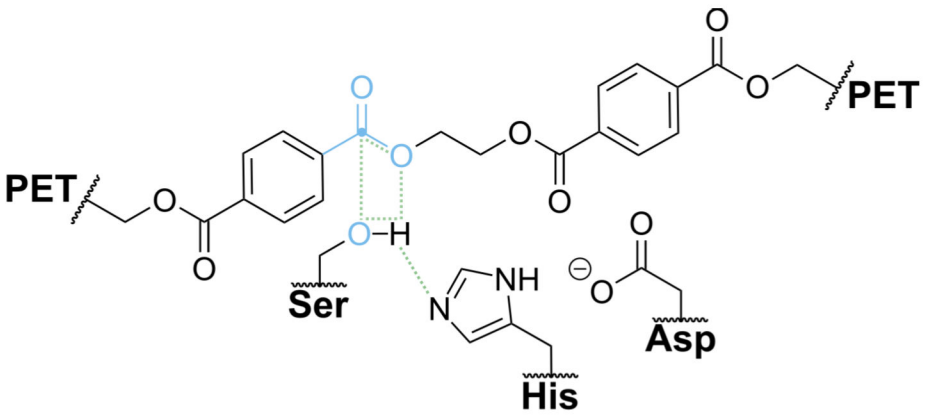


Fig. A11.: QM region and CVs employed in this study. The QM region includes two PET units connected via the ester bond to be broken and the side chains of the three catalytic triad residues (PES-H1: S130, D176, H208; LCC: S165, D210, H242). The distance CVs are highlighted in green, and the point-to-plane CVs are in blue, with the PET ester's carbon corresponding to the point marked by a blue circle. The remaining atoms forming the plane include those in the ester between the PET units in the MC and the ester between PET and the catalytic serine in the AE, respectively. An additional dihedral CV is included, which is highlighted in figure 5.1. Adapted from manuscript I (Sec. A.2).

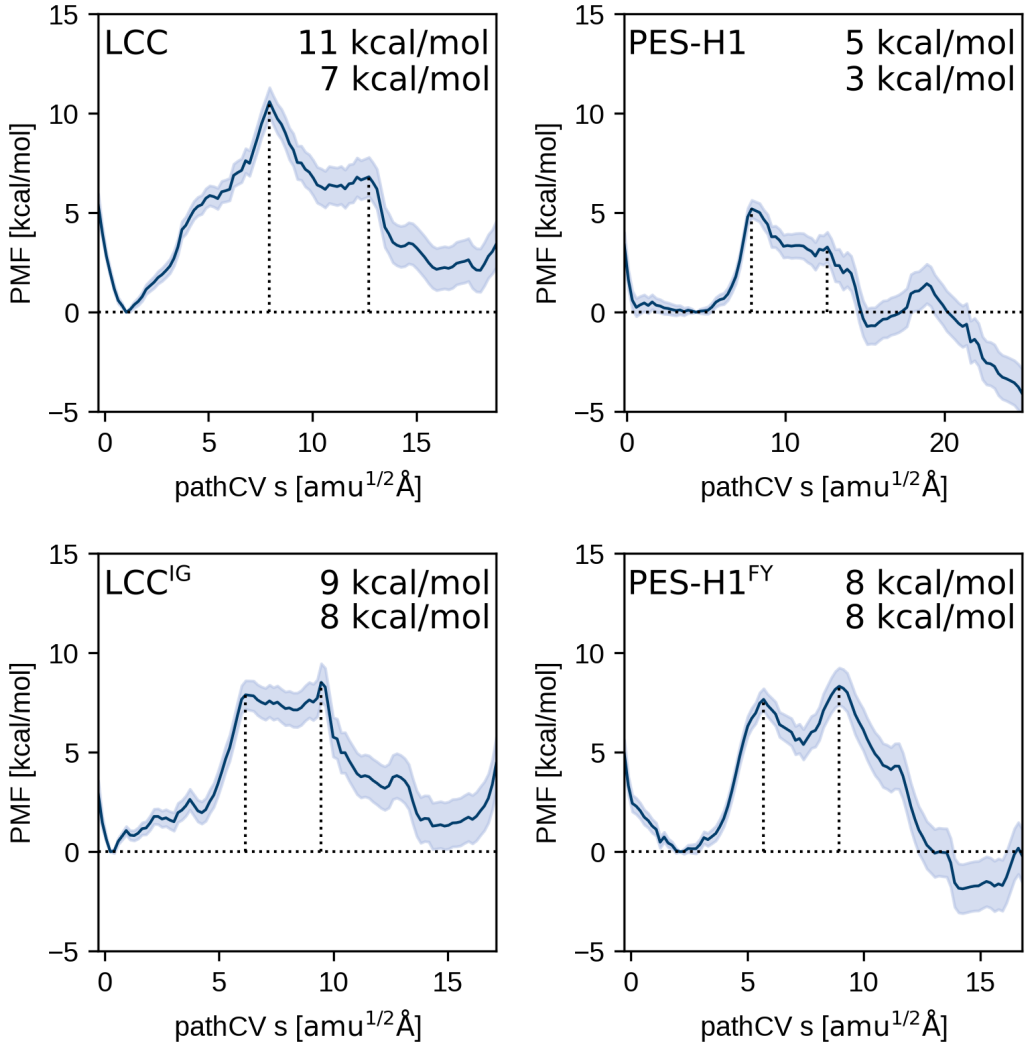


Fig. A12.: Uncorrected PMFs of the final acylation simulations. PMF of the PET deacylation of LCC (top, left) and PES-H1 (bottom, right) and their highly active variants LCC^{IG} (top, right) and $PES\text{-}H1^{FY}$ (bottom, right). The height of the two barriers is provided as well. Adapted from manuscript I (Sec. A.2).

A.2 Supplementary Tables

Tab. A1.: Kinetic parameters obtained from conventional and inverse Michaelis–Menten approaches. The Michaelis–Menten constants K_{m} were derived from the nonlinear fit to experimental data for both settings, $^{\mathrm{conv}}$MM and $^{\mathrm{inv}}$MM, and both enzymes, PES-H1$^{\mathrm{FY}}$ (FY) and LCC$^{\mathrm{ICCG}}$ (ICCG), and corresponding variants. Additional secondary parameters k_{cat}, $^{\mathrm{molar}}K_{\mathrm{m}}$ and $^{molar}\eta$ are provided.

	$^{\mathrm{conv}}\mathbf{K_m}\left[\frac{\mathrm{g}}{\mathrm{L}}\right]$	$^{\mathrm{inv}}\mathbf{K_m}[\mu\mathrm{M}]$	$\mathbf{k_{cat}}\left[\frac{1}{\mathrm{min}\cdot\mu\mathrm{M}}\right]$	$^{\mathrm{molar}}\mathbf{K_M}\,[\mu\mathrm{M}]$	$^{\mathrm{molar}}\eta\left[\frac{1}{\mathrm{min}\cdot\mu\mathrm{M}^2}\right]$
PES-H1$^{\mathrm{FY}}$	0.391 ±0.109	0.892 ±0.105	0.088	1.036	0.085
FY S68A	0.357 ±0.117	0.278 ±0.053	0.084	0.728	0.115
FY D93A	0.501 ±0.180	2.017 ±0.481	0.040	2.434	0.016
FY N212A	0.481 ±0.174	1.767 ±0.318	0.068	1.564	0.043
LCC$^{\mathrm{ICCG}}$	0.215 ±0.059	0.365 ±0.061	0.047	0.357	0.132
ICCG H164A	0.095 ±0.063	0.861 ±0.164	0.032	0.278	0.114
ICCG T211G	0.091 ±0.068	0.430 ±0.130	0.042	0.223	0.189
ICCG S241G	0.250 ±0.068	0.234 ±0.070	0.054	0.357	0.151

ACS Catalysis

pubs.acs.org/acscatalysis

Research Article

Multiple Substrate Binding Mode-Guided Engineering of a Thermophilic PET Hydrolase

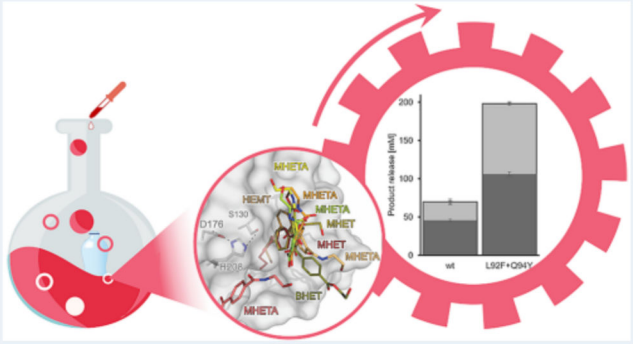
Lara Pfaff, Jian Gao, Zhishuai Li, Anna Jäckering, Gert Weber, Jan Mican, Yinping Chen, Weiliang Dong, Xu Han, Christian G. Feiler, Yu-Fei Ao, Christoffel P. S. Badenhorst, David Bednar, Gottfried J. Palm, Michael Lammers, Jiri Damborsky, Birgit Strodel, Weidong Liu,* Uwe T. Bornscheuer,* and Ren Wei*

Cite This: *ACS Catal.* 2022, 12, 9790−9800

Read Online

ACCESS | Metrics & More | Article Recommendations | Supporting Information

ABSTRACT: Thermophilic polyester hydrolases (PES-H) have recently enabled biocatalytic recycling of the mass-produced synthetic polyester polyethylene terephthalate (PET), which has found widespread use in the packaging and textile industries. The growing demand for efficient PET hydrolases prompted us to solve high-resolution crystal structures of two metagenome-derived enzymes (PES-H1 and PES-H2) and notably also in complex with various PET substrate analogues. Structural analyses and computational modeling using molecular dynamics simulations provided an understanding of how product inhibition and multiple substrate binding modes influence key mechanistic steps of enzymatic PET hydrolysis. Key residues involved in substrate-binding and those identified previously as mutational hotspots in homologous enzymes were subjected to mutagenesis. At 72 °C, the L92F/Q94Y variant of PES-H1 exhibited 2.3-fold and 3.4-fold improved hydrolytic activity against amorphous PET films and pretreated real-world PET waste, respectively. The R204C/S250C variant of PES-H1 had a 6.4 °C higher melting temperature than the wild-type enzyme but retained similar hydrolytic activity. Under optimal reaction conditions, the L92F/Q94Y variant of PES-H1 hydrolyzed low-crystallinity PET materials 2.2-fold more efficiently than LCC ICCG, which was previously the most active PET hydrolase reported in the literature. This property makes the L92F/Q94Y variant of PES-H1 a good candidate for future applications in industrial plastic recycling processes.



KEYWORDS: *polyethylene terephthalate (PET), PET hydrolysis, thermophilic polyester hydrolase, enzyme engineering, crystallization, molecular dynamics, binding modes, kinetics*

Downloaded via 92.192.222.111 on July 17, 2023 at 21:22:41 (UTC).
See https://pubs.acs.org/sharingguidelines for options on how to legitimately share published articles.

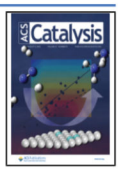
INTRODUCTION

Polyethylene terephthalate (PET), the most abundant synthetic polyester, is widely used in the packaging and textile industries. The global production of PET recently reached 82 million metric tons per year.[1] This contributes significantly to the global solid waste stream and environmental plastic pollution. Biocatalytic recycling of PET has emerged as a promising technology that allows the recovery of monomeric building blocks at both laboratory and pilot plant scales.[2−5] Although PET hydrolases from a wide range of microorganisms have been identified, only a handful of benchmark enzymes have been extensively engineered for industrial applications.[6]

As an interfacial biocatalytic reaction, the efficiency of PET degradation is limited by the number of accessible ester bonds at the polymer surface. Amorphous PET polymer chains become more accessible to enzymatic hydrolysis at temperatures approaching the glass transition temperature of PET (T_g, 65−71 °C).[6] In aqueous environments, water serves as a plasticizer that lowers the T_g of PET by up to 16 °C.[6−8] This effect increases the flexibility of polymer chains at the PET surface layer, allowing degradation at ambient temperatures by mesophilic PET hydrolases, like *Is*PETase from *Ideonella sakaiensis*, which have optimal operating temperatures (T_{opt}) of approximately 40 °C.[9] Nonetheless, thermophilic and thermostable PET hydrolases have superior degradation activity because of increased substrate accessibility at elevated temperatures.[10−12]

LCC, a cutinase isolated from a leaf-branch compost metagenome library, is one of the most extensively investigated thermophilic PET hydrolases.[13−15] Structure-based protein engineering of LCC has resulted in an F243I/D238C/S283C/

Received: May 8, 2022
Revised: July 6, 2022
Published: July 27, 2022



ACS Publications

© 2022 The Authors. Published by American Chemical Society

Y127G variant (LCC ICCG) that can efficiently depolymerize pretreated postconsumer PET bottles within 10 h at 72 °C. This enables the biocatalytic recycling of PET waste at industrially relevant scales.[5] Calcium ions (Ca^{2+}) can boost the thermostability of many bacterial PET hydrolases (changes in T_m (ΔT_m) = 10−16 °C and $\Delta T_{opt} \geq 10$ °C).[13,16−18] Engineering of residues in the Ca^{2+} binding sites has proven to be a useful approach for increasing the T_m of several PET hydrolases by up to 26 °C.[5,11,17,19−22] Introduction of a disulfide bridge at this site (D238C/S283C) markedly increased the melting point (T_m) of LCC from 84.7 to 94.5 °C. In a recent study, LCC ICCG was further engineered to obtain an A59K/V63I/N248P variant with a T_m of 98.9 °C.[23] Nonetheless, the T_{opt} of this variant for degrading low-crystallinity PET (lcPET, <15% crystallinity) was 74 °C, only 2 °C higher than that for the precursor LCC ICCG.[5] At reaction temperatures above 70 °C, water-plasticized lcPET rapidly crystallizes to high-crystallinity PET (hcPET), which is much harder to hydrolyze.[6,24,25] The 20% crystallinity threshold for enzymatic hydrolysis can be reached within 3 h at 75 °C.[5] This competitive physical aging process of amorphous polymers can therefore considerably reduce the efficiency of enzymatic PET depolymerization, which limits the maximum extent of degradation that can be achieved.[25] Therefore, biocatalysts with T_{opt} in the range 72−74 °C, rather than with extremely high T_m values, are desired.[6] The mesophilic *Is*PETase (T_m of 48.7 °C) has also been subjected to protein engineering to improve its thermostability. For example, Cui et al. used a computational strategy to design DuraPETase, a variant with a 31 °C higher T_m and considerably improved PET hydrolysis activity than the wild-type enzyme.[26] More recently, a machine-learning-aided approach was used to engineer *Is*PETase to produce Fast-PETase, a variant with a T_m of 67.1 °C and increased depolymerization efficiency.[27]

In-depth understanding of the binding mechanisms and noncovalent interactions of insoluble polymeric substrates with biocatalysts can contribute to the design of more efficient PET hydrolases. So far, only two studies have reported structures of crystals soaked with PET analogues. Han et al. reported a structure of the inactive R103G/S131A *Is*PETase mutant complexed with 1-(2-hydroxyethyl) 4-methyl terephthalate (HEMT).[28] Zeng et al. reported the structure of an inactive S165A mutant of LCC ICCG complexed with mono-(2-hydroxyethyl) terephthalate (MHET).[23] Consequently, more structures of PET hydrolases with bound substrate analogues are needed. This would enable more precise computational simulations for elucidating the mechanisms of enzymatic depolymerization and predicting more efficient mutants. So far, studies mostly relied on computationally modeled PET substrate conformations.[15,29−32] Therefore, we solved crystal structures of two PET hydrolases in complex with PET analogues.

Two highly similar thermophilic PET hydrolases (PES-H1 and PES-H2), derived from a compost metagenome library, were recently disclosed in a patent application.[33] PES-H1 demonstrated exceptional hydrolytic activity on amorphous PET films, outperforming wild-type LCC under identical conditions.[13,15] Nearly complete depolymerization was achieved after incubation at 70 °C for 24 h.[33] We first solved high-resolution structures of both enzymes in their apo form (PDB codes: 7CUV for PES-H1 and 7W69 for PES-H1). While this work was in progress, another crystal structure of PES-H1 (called PHL7 in the publication, PDB code: 7NEI) was solved.[34] By soaking with various PET substrate analogues, structures of both PES-H1 and PES-H2 in complex with these ligands were obtained by us. These structures were used for exploring substrate binding modes by molecular dynamics (MD) simulations. Finally, we generated PES-H1 variants with significantly improved activity on both amorphous Goodfellow PET (Gf-PET) films and pretreated postconsumer ('real-world') PET waste. These variants outperformed both the wild-type PES-H1 and LCC ICCG.[5]

RESULTS AND DISCUSSION

Structures of PES-H1 and PES-H2. The crystal structures of PES-H1 and PES-H2 were solved at atomic resolutions of 1.45 Å (PDB code: 7CUV) and 1.56 Å (PDB code: 7W69), in the space groups $P2_1$ and $C2$, respectively (Figure S1; Tables S1 and S2). PES-H1 and PES-H2 differ in only four residues (A/E1, L/F209, D/N232, and S/A254), of which only the L/F209 residues are in close vicinity to the catalytic triad (Figure 1). The two hydrolases have similar structures that adopt the canonical α/β-hydrolase fold with a core consisting of nine β-sheets and ten α-helices (Figure S1). Comparison of the apo structure of PES-H1 with the structures of other bacterial PET hydrolases resulted in low root-mean-square deviation (RMSD) values for the protein backbone (Table S3). These highly conserved structures form a distinct subclass of the α/β-hydrolase superfamily.[6] PES-H1 has a catalytic triad consisting of S130, H208, and D176 (Figure 1). The nucleophile S130 is located within hydrogen bond distance to be polarized by the base H208, which is in turn stabilized by the acid D176. PES-H1 forms an intramolecular disulfide bridge like structurally similar homologous enzymes (e.g., PDB codes: 5XH3, 3VIS, 4CGI, 4EB0, 4WFJ, and 1JFR). This conserved disulfide bridge (C241/C256) connects two loops between the last β-sheet (Figure S1).

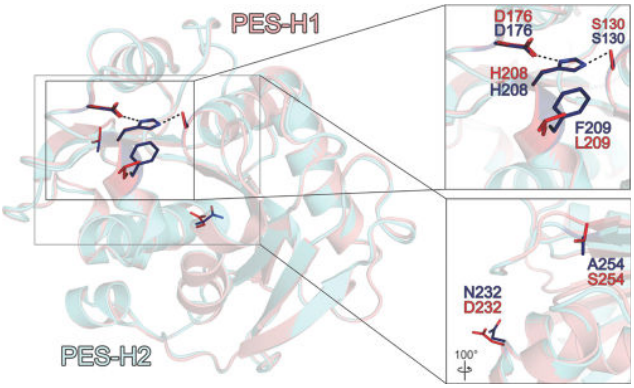


Figure 1. Structural comparison of PES-H1 (salmon, PDB code: 7CUV) and PES-H2 (light blue, PDB code: 7W69). The locations of the variable residues L/F209, D/N232, and S/A254 are indicated. The variable position A/E1 is located at the flexible N-terminal ends of PES-H1 and PES-H2 and are therefore not visible. The S130−H208−D176 catalytic triad is also shown. The amino acid residues are shown as sticks in red for PES-H1 and in dark blue for PES-H2. The inset in the right upper panel demonstrates the close vicinity of the variable position L/F209 to the catalytic triad.

Binding Modes of Substrate Analogues and Degradation Intermediates. Although more than 70 crystal structures of bacterial PET-degrading enzymes are available in the PDB database, the majority of them are apo structures

https://doi.org/10.1021/acscatal.2c02275
ACS Catal. 2022, 12, 9790−9800

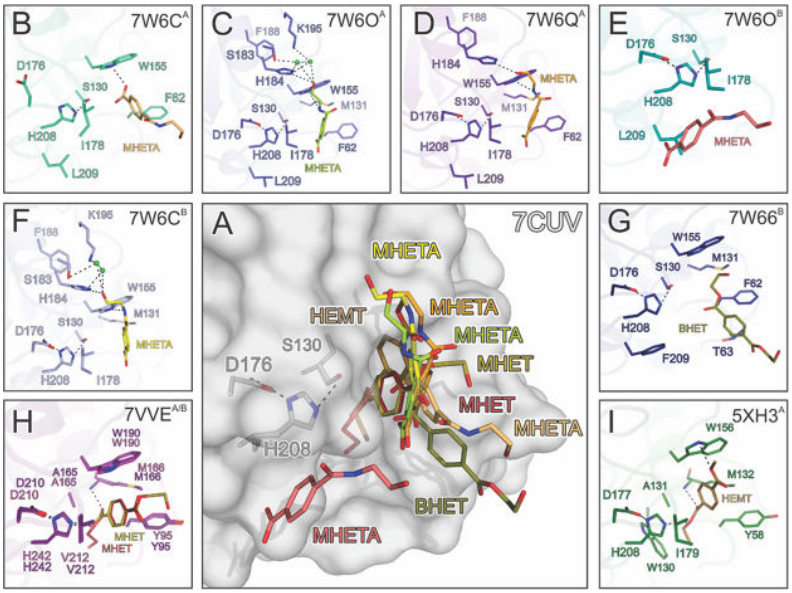


Figure 2. Comparison of the PET substrate analogue binding modes in the structures of PES-H1, PES-H2, LCC ICCG S165A, and *Is*PETase R103G/S131A. Single chains (superscripts for chain A or chain B) were extracted from the deposited structures in the PDB database to identify individual binding modes of the soaked ligands within an asymmetric unit. Dashed lines indicate hydrogen bonds (H-bond cut off of 3.5 Å). Interacting residues are shown as sticks and are colored by element: carbon, as for the respective molecule; nitrogen, blue; oxygen, red; sulfur, yellow. Green spheres represent water oxygens. (A) Superimposed structures show the overlapping binding modes of the substrate analogues with the apo structure of PES-H1 (PDB code: 7CUV). (B–F) PES-H1 in complex with MHETA: (B) 7W6C^A; (C) 7W6O^A; (D) 7W6Q^A; (E) 7W6O^B; and (F) 7W6C^B. (G) PES-H2 in complex with BHET (7W66). (H) LCC ICCG S165A in complex with MHET (7VVE^A, 7VVE^B). (I) *Is*PETase R103G/S131A in complex with HEMT (5XH3).

with no substrate bound.[6] In order to investigate the mechanism of PET hydrolysis, we solved the structures of PES-H1 in complex with citrate (PDB code: 7E30) and also in complex with the nonhydrolyzable substrate analogue 4-(2-hydroxyethylcarbamoyl) benzoic acid (MHETA) (PDB codes: 7W6C, 7W6O, and 7W6Q; Figure 2B–F), to better understand changes in the protein structure upon binding a PET substrate based on this analogue. We also solved the structures of PES-H2 in complex with polyethylene glycol (PEG) 6000 (PDB code: 7E31) and in complex with bis(2-hydroxyethyl) terephthalate (BHET) (PDB code: 7W66; Figure 2G) (Tables S1 and S2). Based on the structures of PES-H1 (with bound MHETA) and PES-H2 (with bound BHET), six ligand-binding modes were identified. The orientations of the ligands in the substrate binding cavities are distinct but similar to those observed for HEMT bound to *Is*PETase R103G/S131A[28] (PDB code: 5XH3; Figure 2I) and MHET bound to the S165A variant of LCC ICCG[23] (PDB code: 7VVE; Figure 2H).

While the structures of LCC ICCG S165A (PDB code: 7VVE; Figure 2H) and *Is*PETase R103G/S131A (PDB code: 5XH3; Figure 2I) exhibited productive ligand conformations with the ester carbonyl carbons interacting with the oxygen of the catalytic serine residue, the PES-H structures revealed multiple noncatalytic intermediate binding modes (IBMs) with the ester bonds (or amide bond in MHETA) positioned too far from S130 for nucleophilic attack. This supports the previous hypothesis that PET hydrolysis may involve dynamic reorientation of polymer chains in the active sites of PET hydrolases.[15,35] MHET and BHET have frequently been found to inhibit enzymatic PET depolymerization.[36,37] The multiple IBMs suggest an enhanced residence likelihood of these inhibitory degradation intermediates in the substrate-binding groove, where they may prevent productive binding of polyester segments.

The conformational flexibility of predominantly hydrophobic residues surrounding the active site may help to recognize and bind bulky PET substrates during biocatalysis. In the enzyme–substrate complex structures of LCC ICCG S165A (Figure 2H) and *Is*PETase R103G/S131A (Figure 2I), the aromatic rings of the substrate analogues are T-stacked to W190 and W156, respectively. This effect has been proposed to be very important for PET binding.[38] Similar π-stacking interactions with the equivalent W155 were discovered in the PES-H1 structures 7W6C (Figure 2B, F), 7W6O^A (Figure 2C), and 7W6Q^A (Figure 2D). In most IBMs of MHETA ligands (Figure 2B–F), the hydroxyl end of the ethanolamine moiety points away from the catalytic triad. This is partly in agreement with the MHET conformation shown in 7VVE (Figure 2H), which is different from the position of the ethylene glycol (EG) moiety of HEMT bound to *Is*PETase R103G/S131A (5XH3; Figure 2I). MHETA ligands also interacted with other hydrophobic residues like F62, I178, and L209 in the binding groove of PES-H1. The backbone amide NH groups of M131 and F62 form an oxyanion hole, which is a characteristic shared by many α/β-hydrolases. Terephthalate (TPA) moieties in our structures are found in close vicinity to F62 (equivalent to Y95 in LCC ICCG S165A and Y58 in *Is*PETase R103G/S131A), rather than close to the catalytic triads as in *Is*PETase R103G/S131A (Figure 2I) and LCC ICCG S165A (7VVE^A; Figure 2H). Furthermore, the hydroxyl end of the ethanolamine moiety forms a hydrogen bond with H184 (Figure 2C,D). The only distinct MHETA binding mode in PES-H1 was observed in 7W6O^B (Figure 2E), in which MHETA is bound at the surface of PES-H1, slightly outside the catalytic cavity. This binding mode suggests that

https://doi.org/10.1021/acscatal.2c02275
ACS Catal. 2022, 12, 9790–9800

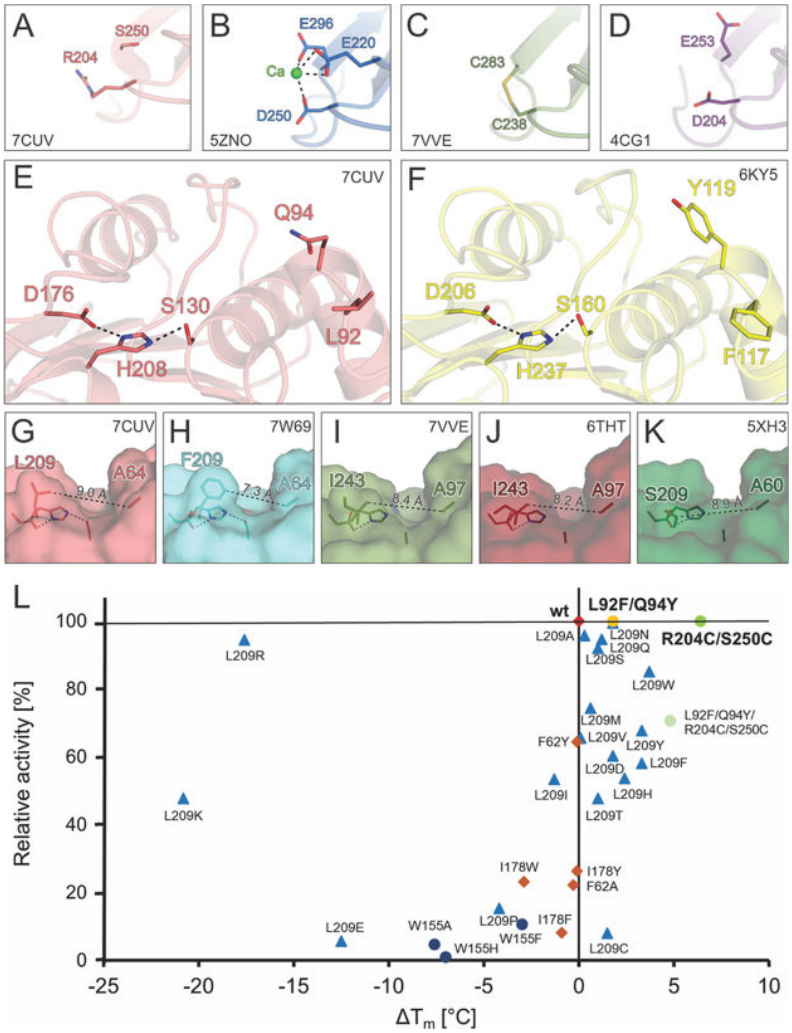


Figure 3. Overview of selected engineering hotspots in PES-H1 for enhancing PET hydrolysis activity and thermostability. (A) A disulfide bridge (R204/S250) is introduced into PES-H1 (PDB code: 7CUV) where a putative Ca^{2+} binding site (D250/E296) is found in (B) the homologous Cut190. (C) Similarly engineered disulfide bridges in LCC ICCG (C238/C283; PDB codes: 7VVE and 6THT) and (D) TfCut2 (D204/E253; PDB code: 4CG1). (E) The L92F and Q94Y substitutions of PES-H1 were based on the corresponding residues in (F) DuraPETase (F117 and Y119; PDB code: 6KY5). (G–K) Variable amino acid residues were found at the site equivalent to L209 in PES-H1: (G) PES-H1, PDB code 7CUV; (H) PES-H2, PDB code 7W69; (I, J) LCC ICCG S165A, PDB codes 7VVE and 6THT; and (K) *Is*PETase R103G/S131A, PDB code 5XH3. These residues influence the width of the substrate-binding groove. (L) A number of PES-H1 variants had different PET hydrolyzing activities and thermostabilities. Changes in T_m compared to the wild-type enzyme (ΔT_m (°C)) are shown. The percentage relative activity compared to the wild-type enzyme was calculated based on the weight loss of Gf-PET film after 24 h at 72 °C. Red square: wild-type PES-H1. Blue triangles: L209 variants. Orange squares: I178 and F62 variants. Dark blue dots: W155 variants. Light green dot: L92F/Q94Y/R204C/S250C variant. Green dot: R204C/S250C variant with a disulfide bond introduced. Yellow dot: L92F/Q94Y variant.

substrates can bind at the surface prior to entering deeper into the active site cavity. BHET is more loosely bound to PES-H2 (7W66[B]; Figure 2G). It is embedded in a groove consisting of S130, H207, W155, I178, H129, F62, and M131. The ester bond between the TPA and EG moieties is closer to S130 but is still outside the catalytic distance, in contrast to the positioning of MHETA in PES-H1. The TPA moiety is close to F62 but far from W155. The second EG moiety is completely exposed to the solvent and has no obvious interactions with any residue.

MD Simulations to Study the Interactions of PES-H1 with a PET Oligomer. To better understand the mechanism of PET hydrolysis, we performed MD simulations of PES-H1 in complex with a modeled oligomer consisting of three repeating PET units (3PET) (Figure S3C) to resemble the binding of a longer polymer segment. PES-H1 remained stable in MD simulations at a time scale of 100 ns as indicated by the steady low backbone RMSD of less than 1 Å compared to the crystal structure (Figure S2). The modeled PES-H1-3PET complex corresponds to a productive state with short distances between the oxyanion hole amides and the central 3PET carbonyl oxygen atom (2.32 and 1.80 Å), and between the carbonyl carbon of an ester in 3PET and the side chain oxygen of the catalytic S130 (2.32 Å). Unfluctuating distances of the 3PET carbonyl carbons to the catalytic S130 verified the productive state of the modeled oligomer during three independent 100 ns MD simulations (Figure S3). Nonetheless, 3PET was slightly flexible in the PES-H1 binding site (Figure S3A). To identify the most favorable 3PET binding modes, we concatenated the trajectories and clustered the 3PET

https://doi.org/10.1021/acscatal.2c02275
ACS Catal. 2022, 12, 9790−9800

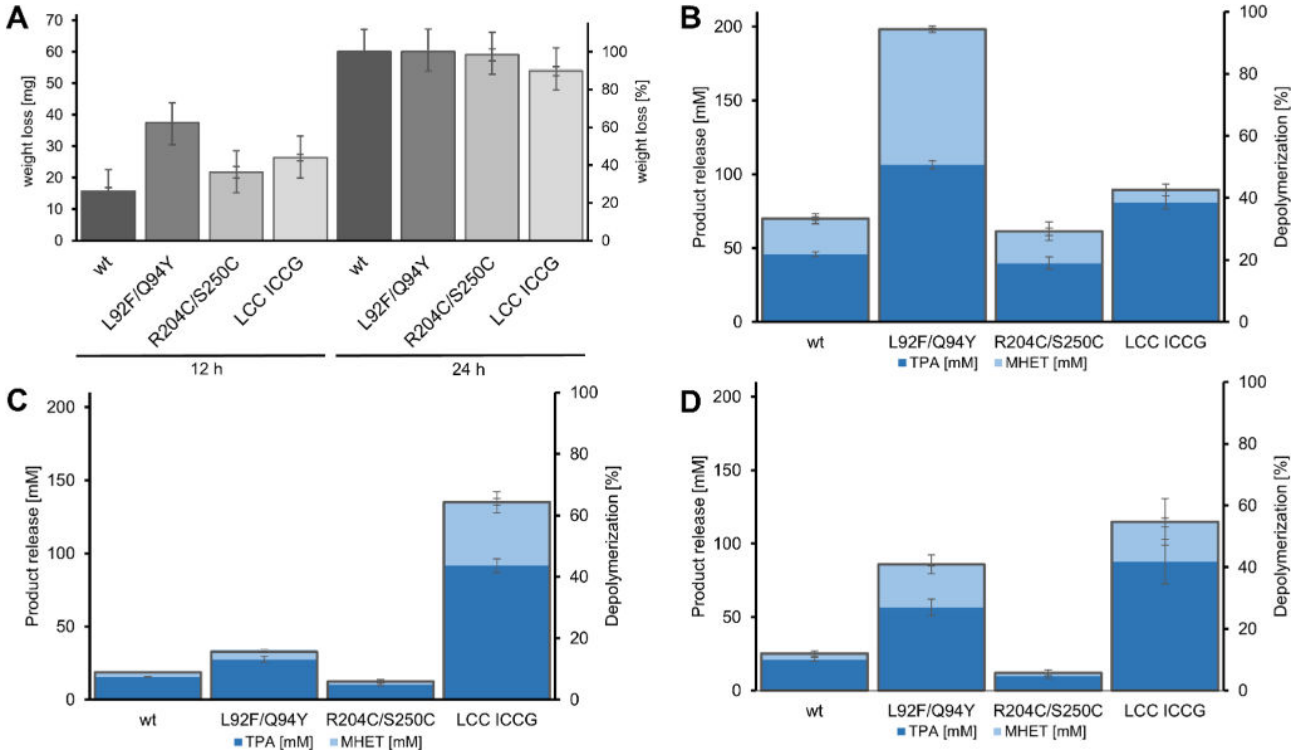


Figure 4. Characterization of PET-hydrolyzing activity of PES-H1 (wt), the L92F/Q94Y and R204C/S250C variants, and LCC ICCG. (A) Weight loss (in [mg] and [%]) of Gf-PET film determined after enzymatic hydrolysis at 72 °C for 12 and 24 h in 1 M potassium phosphate buffer (pH 8.0). (B–D) Total product release [mM] is shown and used to calculate the depolymerization efficiency [%] with (B) lcPET powder (13%), (C) ball-milled hcPET powder (26%), and (D) grinder-crushed hcPET powder (33%) after 24 h at 72 °C. The total product was defined as the sum of TPA (dark blue), MHET (light blue), and BHET (light gray). Error bars indicate the standard deviation calculated from at least three replicates.

conformations. The four most populated clusters correspond to the four preferred binding modes, each including >5% of all ligand conformations (Figure S4). Cluster 1 represents the 3PET binding mode adopted in about 28% of the conformations (Table S4, Figure S4C). After superimposing the PES-H1 (PDB code: 7CUV) and LCC ICCG S165A structures (PDB code: 7VVE), the central PET unit of cluster 1 and the MHET overlap well with an RMSD of 2.95 Å, while the binding mode of cluster 3 (found in about 8% of all conformations) deviates the most from that of MHET, with an RMSD of 4.01 Å (Figure S4D). This suggests that being adjacent to S130 results in multiple beneficial interactions between PET and the surrounding residues. Evaluating the interaction energies of the four binding poses demonstrated that hydrophobic Lennard-Jones (LJ) interactions between the side chains and the central 3PET unit had a predominant influence on binding. F62, W155, and I178 formed strong LJ interactions (<−10 kJ mol^{-1}), in agreement with their close interactions with soaked MHETA ligands (Figure 2B–D,F,G). H208 and M131 also formed strong LJ interactions (<−7 kJ mol^{-1}) (Figures 1 and 3; Figure S4C). Additionally, T63, A64, and L209 mediate strong LJ interactions (<−7 kJ mol^{-1}) with all three units of 3PET. The side chains of F62 and W155 form stable aromatic interactions with the aromatic rings of 3PET. The orientation of the TPA moieties suggest T-stacking interactions with W155, in agreement with the orientation of MHETA bound to PES-H1 (PDB codes: 7W6C^{A}, 7W6C^{b} 7W6O^{A}, and 7W6Q^{A}) and with earlier studies on other PET hydrolases.[12,23] Furthermore, the strong LJ interactions with F62 are in agreement with the close proximity between MHETA and F62. The Coulomb interactions involve fewer residues and are often mediated by backbone atoms of residues, like F62 and M131 from the oxyanion hole, and L92, but can also involve side chains of residues like Q94, H208, N212, and the catalytic S130 (<−7 kJ mol^{-1}). It should be emphasized that the significant contributions by L92 and Q94 are the result of hydrogen bonding with the terminal carboxyl group of the first PET unit, which should only occur when exoscission of polymeric PET substrates takes place. When the total interaction energy is considered, G61, H129, and T157 are also identified as strong PET-binding residues (<−7 kJ mol^{-1}).

Engineering PES-H1 for Improved Thermostability and Activity on Amorphous PET Film. Elevated reaction temperatures of up to 75 °C increase polymer chain mobility, making the amorphous fractions of PET more accessible to enzymatic hydrolysis. We investigated enzymatic PET degradation at 72 °C because it is the optimal temperature for the hydrolysis of amorphized PET waste by the reference enzyme LCC ICCG.[5] Empirical data have shown that the T_m of a PET hydrolase is usually at least 12 °C higher than its T_{opt}.[5,11,13,17] Hence, biocatalysts with a T_m over 85 °C are preferred for efficient PET degradation. When determined in buffers with low ionic strengths (Table S5), PES-H1 had a T_m of 77.1 °C, as determined by nano differential scanning fluorimetry (NanoDSF) and differential scanning calorimetry (DSC). This is in agreement with previously published data.[34] In the 1 M potassium phosphate buffer demonstrated by previous studies to be optimal for PET degradation by selected enzymes,[33,34,39] the T_m of PES-H1 was increased to 85 °C

https://doi.org/10.1021/acscatal.2c02275
ACS Catal. 2022, 12, 9790−9800

(Table S5), thereby enabling its application at 72 °C (Figure S5). Because high salt concentrations are not ideal for industrial processes, we investigated the degradation of Gf-PET film by PES-H1 in the presence of lower phosphate buffer concentrations (Figure S6). The results demonstrated a positive correlation between the buffer concentration and the PET degradation performance of wild-type PES-H1 at 72 °C. This is most likely due to the decreased thermostability of PES-H1 at lower buffer concentrations (Table S5).

Many homologous PET hydrolases, including PES-H1 itself, have been found to be stabilized in the presence of Ca^{2+} ions, as indicated by increased T_m, improved PET-hydrolyzing activity, or both.[13,17,18] Ca^{2+} binding can be mediated by several negatively charged residues. For example, D250 and E296 in the homologous Cut190 from *Saccharomonospora viridis* were identified by crystallographic investigations to be involved in Ca^{2+} binding (Figure 3B).[40] Ca^{2+} can be precipitated by buffer ions like phosphate and also by the PET hydrolysis product terephthalate,[6,41] making the dependence of PET hydrolase stability on Ca^{2+} undesirable. This dependence can be significantly mitigated by replacing the Ca^{2+} binding residues by a disulfide bridge to generate variants that are thermostable in the absence of Ca^{2+}.[5,19,11,17,20−22] Accordingly, we generated an R204C/S250C variant of PES-H1 and confirmed disulfide bond formation using Ellman's reagent (Figure S7). The T_m of this variant was increased by 6.4 °C (Figure 3L, Table S5). Previous studies reported that introducing disulfide bridges at equivalent positions of homologous PET hydrolases resulted in higher increases in T_m (TfCut2, ΔT_m = 24.9 °C; *Is*PETase, ΔT_m = 22.3 °C; LCC, ΔT_m = 9.8 °C; Cut190, ΔT_m = 23.1 °C).[5,17,19,21] While more negatively charged amino acids like D250 and E296 in Cut190 (Figure 3B), D238 and S283 in LCC (Figure 3C), and D204 and E253 in TfCut2 (Figure 3D) are frequently observed at these sites, wild-type *Is*PETase (N204 and S253) and PES-H1 (R204 and S250, Figure 3A) lack these negatively charged residues. This suggests that the generic thermostabilizing effect of an engineered disulfide bridge at this position might be due to a variety of interactions rather than just replacing the Ca^{2+} binding site. After 24 h at 72 °C, both the wild-type and the R204C/S250C variant of PES-H1 hydrolyzed Gf-PET film (98% depolymerization) almost completely (Figure 4A).

Recently, Nakamura et al. reported an R47C/G89C variant of the homologous hydrolase PET2 and validated the formation of a disulfide bridge by X-ray crystallography.[22] Compared to wild-type PET2, the T_m of the R47C/G89C variant of PET2 was increased by 3.1 °C, and its PET hydrolysis activity was 1.3-fold higher. We created a R6C/S49C variant in an attempt to form an equivalent disulfide bridge in PES-H1. This variant was inactive and was therefore not further investigated.

The PES-H1 structure (PDB code: 7CUV, Figure 3E) was compared to the thermostabilized DuraPETase (PDB code: 6KYS, Figure 3F) for identifying additional mutation hotspots. Using Rosetta energy calculations, an L92F/Q94Y variant of PES-H1 was constructed based on the L117F/Q119Y mutations present in DuraPETase. The L92F/Q94Y variant of PES-H1 had a 1.8 °C higher T_m and could almost completely depolymerize Gf-PET film after 24 h at 72 °C (Figures 3L and 4A). Interestingly, the aromatic amino acids that we introduced (L92F/Q94Y) correspond to equivalent residues (F125 and Y127) in LCC ICC.[5] Interestingly, LCC ICC was converted to the more active LCC ICCG by removal of the tyrosine residue (Y127G), while introduction of the equivalent tyrosine into PES-H1 (Q94Y) in combination with L92F resulted in increased activity. The L92F/Q94Y variant of PES-H1 outperformed LCC ICCG in the hydrolysis of various PET materials under conditions optimal for PES-H1 (Figure 4A,B). Cui et al. also observed synergistic effects between the equivalent L117F (L92F in PES-H1) and Q119Y (Q94Y in PES-H1) substitutions.[26] They argued that these aromatic residues interact with other residues (S214, W185, and Y87) to form an "aromatic tunnel" that facilitates the binding of PET chains to the active site. The hydrophobic nature of the mutations enhances noncovalent interactions with the substrate and improves the overall hydrophobic packing and stability of DuraPETase. The same effect could explain the increased activity and stability of the L92F/Q94Y variant of PES-H1. We introduced the previously discussed disulfide bridge (R204C/S250C) to the L92F/Q94Y variant to generate the L92F/Q94Y/R204C/S250C variant of PES-H1. Although the T_m of this variant was increased by 4.8 °C, it was not further characterized because it hydrolyzed Gf-PET film less efficiently than wild-type PES-H1 (Figure 3L).

Of the four residues that differ between PES-H1 and PES-H2, only L209 is located close to the active site (Figures 1 and 3G). This site has repeatedly been recognized as an engineering hotspot in other homologous PET hydrolases due to its potential interactions with polymeric substrates. Variants with increased specific activity on PET have been created by replacing F at this position with A (TfCut2: F208A), W (LCC WCCG: F243W), or I (LCC ICCG: F243I; Figure 3I,J).[5,42] The equivalent S of *Is*PETase (Figure 3K) has also been replaced with F, but an additional W159H substitution was required for improved PET hydrolysis activity.[43] It was recently shown that exchanging L209 in PES-H1 (called PHL7 by Sonnendecker et al.[34]) to the F found in PES-H2 (Fig 3G,H) reduced PET hydrolysis activity by half. We obtained similar results for the hydrolysis of Gf-PET film by the L209F variant of PES-H1 (Figure 3L). We subjected position L209 to saturation mutagenesis and found that most variants (except L209K, L209R, L209E, L209P, and L209I) resulted in enhanced thermostability. For the L209W, L209F, and L209Y variants, the highest ΔT_m in 50 mM phosphate buffer ranged from 3.3 to 3.7 °C (Figure 3L). However, the PET hydrolysis activities of these variants were decreased by more than 15%. Several earlier studies[43,44] suggested that the S238F substitution (equivalent to L209F in PES-H1) in the W159H/S238F variant of *Is*PETase narrowed the active site cleft, potentially enhancing π-stacking between PET and F238. In contrast, Furukawa et al.[42] suggested that the corresponding F of TfCut2 restricts access to lcPET, attributing the influence of this residue on catalytic activity to side-chain volume rather than hydrophobicity. Therefore, the role of this important residue is still not fully understood, and it may play different roles in different PET hydrolases.

In addition, we engineered several key residues potentially involved in strong interactions with PET as indicated by structures of PES-H1 and PES-H2 in complex with PET analogues (Figure 2) and MD simulations (Figure S4). These include F62 (Figure 2B−D,G), W155 (Figure 2B−D,F,G), and I178 (Figure 2E). F62 is part of the oxyanion hole. Except for PES-H1, Cut190,[18] and Tcur1278,[45] other known homologous PET hydrolases have a tyrosine at this position. Introducing this tyrosine into PES-H1 (F62Y) lowered the hydrolytic

https://doi.org/10.1021/acscatal.2c02275
ACS Catal. 2022, 12, 9790−9800

activity drastically but had no influence on T_m (Figure 3L). The same effects were observed for the F62A variant.

The W155 residue of PES-H1 is equivalent to the W185 residue of *Is*PETase. The W185 of *Is*PETase (W130 in Figure 2I due to different residue numbering in the 5XH3 crystal structure) is flexible and can move to open or close access to the active site.[43] This wobbling is beneficial for mesophilic PET hydrolases because the PET polymer chain has lower chain mobility at ambient temperatures, and a flexible W185 may facilitate substrate binding.[15] This dynamic tryptophan is conserved in many homologous PET hydrolases and is involved in strong interactions with the aromatic rings of PET. We replaced the W155 of PES-H1 to A, F or H, resulting in almost complete loss of activity and considerably reduced stability (Figure 3L). Austin et al. reported similarly reduced activity for the equivalent W185A variant of *Is*PETase.[43] In contrast, the conformation of the corresponding W190 (Figure 2H) in the thermophilic LCC ICCG is fixed by interactions with H218 and F222 (H184 and F188 in PES-H1, Figure 2C,D,F). As a result, LCC ICCG has a more rigid substrate-binding groove, yet it still allows PET binding at elevated temperatures as a result of increased polymer chain mobility.[23]

The I178 residue is located near the catalytic triad of PES-H1 (Figure 2B−D,F). Previous studies have reported substitutions of this I178 residue in homologous *Thermobifida fusca* cutinases to smaller residues like S or A, which resulted in PET hydrolyzing activities comparable to that of the wild-type enzyme.[46,47] Therefore, we instead substituted I178 to large aromatic residues. However, the I178W, I178F, and I178Y variants lost significant PET hydrolysis activity, and their T_m decreased slightly, suggesting that additional aromatic interactions may hinder productive binding of PET chains. Therefore, we did not further investigate the I178 residue of PES-H1.

Comparing the Hydrolytic Activity of Selected PES-H1 Variants on Different PET Materials. The L92F/Q94Y and R204C/S250C variants of PES-H1 were further investigated using different PET materials. The crystallinity of real-world postconsumer PET waste depends on its thermal history and life cycle.[6] Therefore, for biocatalytic recycling at the industrial scale, pretreatment by thermomechanical amorphization and micronization is essential to provide uniformly degradable substrates (in terms of comparable crystallinity, particle size, etc.).[5,48] In this study, we used a melt-quenching technique to amorphize postconsumer PET bottles, which were then micronized by various methods. Crystallinity of the PET bottle waste was decreased from 27% to 19% after melt-quenching and increased again to 33% and 26%, respectively, after crushing or ball milling (Table S6). The crystallinity values determined with differently micronized PET powders are in good agreement with two previous studies.[48,49] However, the crystallinities of our samples were markedly higher than that reported by Tournier et al., who used other techniques.[5] We determined the average molecular masses of selected PET samples by gel permeation chromatography (GPC) and found that values decreased after melt-quenching and micronization (Table S6). Since the particle size can influence the biocatalytic degradability of PET powders, it was important to use similarly sized particles for all assays. Therefore, we sieved all micronized PET samples using a 177 μm mesh to obtain more homogeneous powders.

LCC ICCG and the wild-type PES-H1 were used as reference enzymes. The distinct distribution of charged amino acids at the surfaces of these two enzymes may explain the differences in their buffer requirements (Figure S8). Compared to PES-H1, LCC ICCG does not lose its thermostability and PET degrading activity at a low phosphate buffer concentration (100 mM).[5] However, higher phosphate concentrations (up to 1 M) do not reduce the PET hydrolysis activity of wild-type LCC.[15,39,50] Since 1 M phosphate buffer is optimal for the activity and stability of PES-H1 while not negatively influencing LCC, we used this buffer for all subsequent PET degradation experiments. As shown in Figure 4A, wild-type PES-H1 and the L92F/Q94Y variant completely depolymerized Gf-PET film in 24 h at 72 °C. Therefore, we also determined the weight loss after 12 h of incubation. The highest weight loss of 37.1 mg (62.4%) was obtained with the L92F/Q94Y variant, and this was 2.3-fold higher than with wild-type PES-H1. The L92F/Q94Y variant also significantly outperformed both the R204C/S250C variant and LCC ICCG in the hydrolysis of Gf-PET film (Figure 4A). Averaged conversion rates of 2.5 mg_{PET} h^{-1} and 2.3 mg_{PET} h^{-1} were obtained using wild-type PES-H1 and LCC ICCG, respectively. While the value for PES-H1 is similar to that previously determined by Sonnendecker et al.,[34] the value for LCC ICCG is markedly lower than that reported by Tournier et al.[5] As explained above, this may in part be due to differences between the PET materials used in different studies. Based on the information provided by the manufacturer, Gf-PET films differ considerably in terms of crystallinity, thickness, molecular mass, and many other polymer parameters, making a direct comparison of data generated in different studies impossible.[6]

After 24 h at 72 °C, the degradation performance of PES-H1, L92F/Q94Y, R204C/S250C, and LCC ICCG on low-crystallinity (13%) micronized waste PET powder was comparable to that on Gf-PET film. The L92F/Q94Y variant yielded 2.9-fold and 2.2-fold more degradation products than wild-type PES-H1 and LCC ICCG, respectively (Figure 4B). This indicated that, under the applied degradation conditions, the L92F/Q94Y variant was the most active lcPET hydrolase. The R204C/S250C variant was as active as the wild-type PES-H1 in hydrolyzing lcPET materials (Figure 4A,B). However, the R204C/S250C variant was significantly less active than the wild-type against hcPET materials (Figure 4C,D). In contrast, the L92F/Q94Y variant was more active than the wild-type PES-H1 against hcPET powders, forming up to 3.4-fold more degradation products (Figure 4D). For hydrolyzing hcPET powders (Figure 4C,D) generated by different pretreatment methods, LCC ICCG outperformed all PES-H1 variants and yielded up to 4.0-fold more degradation products than the L92F/Q94Y variant (Figure 4C,D). While the crystallinities of the crushed and ball-milled PET powders were clearly higher than the degradable threshold value of approximately 20% suggested by Wei et al.[25] and Thomsen et al.,[24] LCC ICCG surprisingly released more degradation products from these substrates than from lcPET powder (13% crystallinity) (Figure 4B−D). By comparison with PES-H1 and its variants, the extent of degradation was inversely correlated to the material crystallinity, which is in agreement with previous research on using hydrolases to degrade PET with varying crystallinities.[6]

In addition to the crystallinity values obtained by DSC, we also determined the number-average (M_n) and weight-average (M_w) molecular masses of the PET powders used for the enzymatic degradation experiments (Table S6). The lower M_n values determined for the hcPET powders derived from ball-milled and grinder-crushed PET bottle waste than that with

https://doi.org/10.1021/acscatal.2c02275
ACS Catal. 2022, 12, 9790−9800

the grinder-crushed PET film means that the PET bottle powders contained significantly shorter polymers (or even oligomers). When the degradation by PES-H1, its variants, and LCC ICCG (Figure 4B–D) is interpreted in terms of the molecular masses of the PET powders, it appears that M_n had a larger influence on the degradation by LCC ICCG than by PES-H1 and its variants. LCC ICCG seems to hydrolyze shorter polymers more efficiently, while the degradation by PES-H1 and its variants seems to be more influenced by crystallinity. Tournier et al.[5] found that LCC ICCG could not efficiently depolymerize the hcPET obtained by their pretreatment methods, but they did not report the molecular masses of their materials. Therefore, a direct comparison of our data to that reported by Tournier et al.[5] cannot be made, but our data suggest that not only crystallinity but also average polymer length may influence the enzymatic degradation of PET. This suggests that crystallinity might be only one of several important polymer characteristics that influence enzymatic degradation and that polymer properties should be more extensively characterized in future studies. The superiority of the L92F/Q94Y variant of PES-H1 in degrading lcPET is important since industrially amorphized PET waste has crystallinities below 15%.[5] The L92F/Q94Y variant of PES-H1 could therefore be investigated as an alternative to LCC ICCG for PET hydrolysis.

A heterogeneous kinetic model described by the following equation has been widely used for evaluating enzymatic PET hydrolysis.[12,45,46,51−53]

$$v_0 = k_h[S_0]\frac{K_A[E_0]}{1 + K_A[E_0]} \quad (1)$$

In this equation, v_0 describes the initial reaction rate, k_h the hydrolysis rate constant, $[S_0]$ the initial substrate concentration, $[E_0]$ the enzyme concentration, and K_A the adsorption equilibrium constant. We used PET nanoparticles (PET-NP) prepared using previously published protocols[51,54] as the substrate to characterize the hydrolysis kinetics catalyzed by PES-H1, its variants, and LCC ICCG. The rates of turbidity change measured at 600 nm as a result of PET-NP degradation were determined in a microplate reader at 70 °C (Figures S9 and S10). The kinetic constants determined according to eq 1 are summarized in Table 1. The initial reaction velocity v_0 was defined as the turbidity decrease over a reaction time of 40 min using 0.5 mg mL^{-1} PET-NP (Figure S9). The L92F/Q94Y variant resulted in the highest hydrolysis rate constant (k_h) of 0.065 mL mg^{-1} min^{-1}, followed by R204C/S250C (0.064 mL mg^{-1} min^{-1}), wild-type PES-H1 (0.054 mL mg^{-1} min^{-1}), and LCC ICCG (0.048 mL mg^{-1} min^{-1}). The adsorption equilibrium constant K_A is a parameter to evaluate the enzyme affinity to PET-NP. The R204C/S250C variant had the lowest affinity to PET, while the L92F/Q94Y variant had the highest affinity, which was 1.8-fold higher than that of wild-type PES-H1 and 1.4-fold higher than that of LCC ICCG. The high affinity of the L92F/Q94Y variant to PET nanoparticles demonstrates the importance of the adsorption of enzymes to the surface of PET-NP for efficient hydrolysis. The K_A values determined in this study fall in the same range as those determined for many homologous PET hydrolases by other procedures.[12,45,46,51,52] In general, the kinetic data, depicted in Table 1 and Table S7 support the observations made using other PET materials (Figure 4A,B). Additionally, we measured the initial hydrolysis rate as a function of the substrate concentration in the range 0–0.5 mg mL^{-1} using a constant enzyme concentration of 0.7 μM. This enzyme concentration was selected to ensure substrate-saturated conditions (Figure S9). The experimental data fit well to the kinetic model (Figures S9 and S10), demonstrating that under these conditions the model describes the experimental data accurately.

Table 1. Kinetic Parameters for PET-NP Hydrolysis by PES-H1, Its Variants, and LCC ICCG

	K_A [μM^{-1}]	k_h [mL mg^{-1} min^{-1}]
PES-H1 wild-type	4.710 ± 0.087	0.054 ± 0.001
L92F/Q94Y	8.259 ± 0.028	0.065 ± 0.002
R204C/S250C	4.063 ± 0.191	0.064 ± 0.001
LCC ICCG	5.953 ± 0.032	0.048 ± 0.001

CONCLUSIONS

In this study, we solved crystal structures of the thermophilic enzymes PES-H1 and PES-H2 in apo form and notably also in complexes with the PET monomer analogues MHETA and BHET. This enabled the identification of six intermediate binding modes and several key residues involved in binding to PET. MD simulations supported the involvement of these residues in PET binding. Structural analyses and previously identified mutational hotspots were used to select PES-H1 residues for mutagenesis. Several PES-H1 variants with improved thermostability and PET hydrolysis activity were identified. The most active L92F/Q94Y variant outperformed the reference enzyme LCC ICCG in hydrolyzing lcPET materials (<15% crystallinity). Its superior activity over wild-type PES-H1 was also evident with other hcPET materials derived from real-world PET bottle waste. Our detailed structural analyses provide a better understanding of the mechanisms of interfacial biocatalysis, and our engineered variants hold promise for future applications in biocatalytic plastic recycling.

ASSOCIATED CONTENT

Supporting Information

The Supporting Information is available free of charge at https://pubs.acs.org/doi/10.1021/acscatal.2c02275.

Materials and methods; data collection of crystal structures of PES-H1 and PES-H2 in apo form and in complex with MHETA and BHET; RMSD of selected PET hydrolases; MD simulations; changes in T_m; crystallinities and molecular masses of PET substrates; kinetic parameters of PET-NP hydrolysis; oligonucleotides; structure of PES-H1; stability of PES-H1 in MD simulations; RMSD of 3PET during MD simulations; binding positions of 3PET clusters; degradation of PET at 70 and 72 °C; phosphate dependence; cysteine calibration curve; electrostatic surface display; hydrolysis of PET-NP with varying enzyme concentrations; and hydrolysis of PET-NP with varying substrate concentrations (PDF)

GAFF parameters for each PET unit in 3PET (TXT)

AUTHOR INFORMATION

Corresponding Authors

Weidong Liu − *Tianjin Institute of Industrial Biotechnology, Chinese Academy of Sciences, Tianjin 300308, China;*

https://doi.org/10.1021/acscatal.2c02275
ACS Catal. 2022, 12, 9790−9800

National Technology Innovation Center of Synthetic Biology, Tianjin 300308, China; University of Chinese Academy of Sciences, Beijing 100049, China; orcid.org/0000-0001-7954-7700; Email: liu_wd@tib.cas.cn

Uwe T. Bornscheuer − *Department of Biotechnology & Enzyme Catalysis, Institute of Biochemistry, University of Greifswald, 17487 Greifswald, Germany;* orcid.org/0000-0003-0685-2696; Email: uwe.bornscheuer@uni-greifswald.de

Ren Wei − *Department of Biotechnology & Enzyme Catalysis, Institute of Biochemistry, University of Greifswald, 17487 Greifswald, Germany;* orcid.org/0000-0003-3876-1350; Email: ren.wei@uni-greifswald.de

Authors

Lara Pfaff − *Department of Biotechnology & Enzyme Catalysis, Institute of Biochemistry, University of Greifswald, 17487 Greifswald, Germany;* orcid.org/0000-0002-1529-8917

Jian Gao − *Tianjin Institute of Industrial Biotechnology, Chinese Academy of Sciences, Tianjin 300308, China; National Technology Innovation Center of Synthetic Biology, Tianjin 300308, China*

Zhishuai Li − *Tianjin Institute of Industrial Biotechnology, Chinese Academy of Sciences, Tianjin 300308, China; University of Chinese Academy of Sciences, Beijing 100049, China*

Anna Jäckering − *Institute of Biological Information Processing: Structural Biochemistry (IBI-7), Forschungszentrum Jülich, 52428 Jülich, Germany; Institute of Theoretical and Computational Chemistry, Heinrich Heine University, 40225 Düsseldorf, Germany;* orcid.org/0000-0003-0031-159X

Gert Weber − *Helmholtz-Zentrum Berlin für Materialien und Energie, 14109 Berlin, Germany;* orcid.org/0000-0003-3624-1060

Jan Mican − *Loschmidt Laboratories, Department of Experimental Biology and RECETOX, Faculty of Science, Masaryk University, 625 00 Brno, Czech Republic;* orcid.org/0000-0002-8877-163X

Yinping Chen − *State Key Laboratory of Materials-Oriented Chemical Engineering, College of Biotechnology and Pharmaceutical Engineering, Nanjing Tech University, Nanjing 211816, China*

Weiliang Dong − *State Key Laboratory of Materials-Oriented Chemical Engineering, College of Biotechnology and Pharmaceutical Engineering, Nanjing Tech University, Nanjing 211816, China;* orcid.org/0000-0002-8556-5689

Xu Han − *Tianjin Institute of Industrial Biotechnology, Chinese Academy of Sciences, Tianjin 300308, China; National Technology Innovation Center of Synthetic Biology, Tianjin 300308, China*

Christian G. Feiler − *Helmholtz-Zentrum Berlin für Materialien und Energie, 14109 Berlin, Germany*

Yu-Fei Ao − *Department of Biotechnology & Enzyme Catalysis, Institute of Biochemistry, University of Greifswald, 17487 Greifswald, Germany; CAS Key Laboratory of Molecular Recognition and Function, Institute of Chemistry, Chinese Academy of Sciences, Beijing 100190, China*

Christoffel P. S. Badenhorst − *Department of Biotechnology & Enzyme Catalysis, Institute of Biochemistry, University of Greifswald, 17487 Greifswald, Germany;* orcid.org/0000-0002-5874-4577

David Bednar − *Loschmidt Laboratories, Department of Experimental Biology and RECETOX, Faculty of Science, Masaryk University, 625 00 Brno, Czech Republic; International Clinical Research Center, St. Anne's University Hospital, 656 91 Brno, Czech Republic*

Gottfried J. Palm − *Department Synthetic and Structural Biochemistry, Institute of Biochemistry, University of Greifswald, 17487 Greifswald, Germany;* orcid.org/0000-0003-0329-0413

Michael Lammers − *Department Synthetic and Structural Biochemistry, Institute of Biochemistry, University of Greifswald, 17487 Greifswald, Germany*

Jiri Damborsky − *Loschmidt Laboratories, Department of Experimental Biology and RECETOX, Faculty of Science, Masaryk University, 625 00 Brno, Czech Republic; International Clinical Research Center, St. Anne's University Hospital, 656 91 Brno, Czech Republic*

Birgit Strodel − *Institute of Biological Information Processing: Structural Biochemistry (IBI-7), Forschungszentrum Jülich, 52428 Jülich, Germany; Institute of Theoretical and Computational Chemistry, Heinrich Heine University, 40225 Düsseldorf, Germany;* orcid.org/0000-0002-8734-7765

Complete contact information is available at: https://pubs.acs.org/10.1021/acscatal.2c02275

Author Contributions

Conceptualization: R.W., W.L., and U.T.B. Protein crystallographic studies: J.G., Z.L., X.H., C.G.F., G.J.P., M.L., and W.L. Computational simulations: A.J., G.W., J.M., Y.-F.A., D.B., J.D., B.S., and W.L. Protein engineering and characterization: L.P., J.G., and Z.L. Polymer treatment and characterization: Y.C. and W.D. Writing—original draft: L.P., A.J., G.W., C.P.S.B., W.L., and R.W. Writing—review and editing: all authors. Supervision and funding acquisition: W.D., J.D., B.S., W.L., U.T.B., and R.W.

Funding

The authors W.L., J.G., Z.L., X.H., and W.D. acknowledge the financial support provided by the National Key Research and Development Program of China (2021YFC2103600 and 2021YFA0910200). The authors U.T.B., R.W., L.P., D.B., J.M., and J.D. gratefully acknowledge the financial support received from the European Union's Horizon 2020 research and innovation program (MIX-UP, grant 870294; upPE-T, grant 953214; CETOCOEN Excellence, grant 857560) and from the Czech Ministry of Education (CZ.02.1.01/0.0/0.0/16_026/0008451). A.J. is financially supported by the German Federal Environmental Foundation. The authors J.G., X.H., and W.L. also thank the Tianjin Synthetic Biotechnology Innovation Capacity Improvement Project (TSBICIP-PTJJ-008, TSBICIP-IJCP-003, TSBICIP-KJGG-009-01, and TSBICIP-KJGG-002-06), the Youth Innovation Promotion Association CAS, and the China Scholarship Council for financial support. The authors W.D. and Y.C. acknowledge the financial support provided by the National Natural Science Foundation of China (31961133017).

Notes

The authors declare no competing financial interest.

■ ACKNOWLEDGMENTS

A.J. and B.S. gratefully acknowledge the computing time granted through JARA-HPC (project PETaseMD) on the supercomputer JURECA at Forschungszentrum Jülich,[55] the hybrid computer cluster purchased from funding by the Deutsche Forschungsgemeinschaft (DFG, German Research Foundation) project number INST 208/704-1 FUGG, and the Centre for Information and Media Technology at Heinrich Heine University Düsseldorf. Furthermore, we thank the staff from BL10U2/BL17B/BL17B/BL18U1/BL19U1 beamline of the National Facility for Protein Science in Shanghai (NFPS) at Shanghai Synchrotron Radiation Facility (SSRF) and staff from Beamline 14.1 at BESSY, for assistance during data collection.

■ REFERENCES

(1) Singh, A.; Rorrer, N. A.; Nicholson, S. R.; Erickson, E.; DesVeaux, J. S.; Avelino, A. F. T.; Lamers, P.; Bhatt, A.; Zhang, Y.; Avery, G.; Tao, L.; Pickford, A. R.; Carpenter, A. C.; McGeehan, J. E.; Beckham, G. T. Techno-Economic, Life-Cycle, and Socioeconomic Impact Analysis of Enzymatic Recycling of Poly(Ethylene Terephthalate). *Joule* **2021**, *5* (9), 2479−2503.

(2) Wei, R.; Tiso, T.; Bertling, J.; O'Connor, K.; Blank, L. M.; Bornscheuer, U. T. Possibilities and Limitations of Biotechnological Plastic Degradation and Recycling. *Nat. Catal.* **2020**, *3* (11), 867−871.

(3) Tiso, T.; Winter, B.; Wei, R.; Hee, J.; de Witt, J.; Wierckx, N.; Quicker, P.; Bornscheuer, U. T.; Bardow, A.; Nogales, J.; Blank, L. M. The Metabolic Potential of Plastics as Biotechnological Carbon Sources − Review and Targets for the Future. *Metab. Engin.* **2022**, *71*, 77−98.

(4) Jönsson, C.; Wei, R.; Biundo, A.; Landberg, J.; Schwarz Bour, L.; Pezzotti, F.; Toca, A.; Jacques, L. M.; Bornscheuer, U. T.; Syrén, P. Biocatalysis in the Recycling Landscape for Synthetic Polymers and Plastics towards Circular Textiles. *ChemSusChem* **2021**, *14* (19), 4028−4040.

(5) Tournier, V.; Topham, C. M.; Gilles, A.; David, B.; Folgoas, C.; Moya-Leclair, E.; Kamionka, E.; Desrousseaux, M.-L.; Texier, H.; Gavalda, S.; Cot, M.; Guémard, E.; Dalibey, M.; Nomme, J.; Cioci, G.; Barbe, S.; Chateau, M.; André, I.; Duquesne, S.; Marty, A. An Engineered PET Depolymerase to Break down and Recycle Plastic Bottles. *Nature* **2020**, *580* (7802), 216−219.

(6) Wei, R.; von Haugwitz, G.; Pfaff, L.; Mican, J.; Badenhorst, C. P. S.; Liu, W.; Weber, G.; Austin, H. P.; Bednar, D.; Damborsky, J.; Bornscheuer, U. T. Mechanism-Based Design of Efficient PET Hydrolases. *ACS Catal.* **2022**, *12* (6), 3382−3396.

(7) Bianchi, R.; Chiavacci, P.; Vosa, R.; Guerra, G. Effect of Moisture on the Crystallization Behavior of PET from the Quenched Amorphous Phase. *J. Appl. Polym. Sci.* **1991**, *43* (6), 1087−1089.

(8) Langevin, D.; Grenet, J.; Saiter, J. M. Moisture Sorption in PET Influence on the Thermokinetic Parameters. *Eur. Polym. J.* **1994**, *30* (3), 339−345.

(9) Yoshida, S.; Hiraga, K.; Takehana, T.; Taniguchi, I.; Yamaji, H.; Maeda, Y.; Toyohara, K.; Miyamoto, K.; Kimura, Y.; Oda, K. A Bacterium That Degrades and Assimilates Poly(Ethylene Terephthalate). *Science* **2016**, *351* (6278), 1196−1199.

(10) Kawai, F. The Current State of Research on PET Hydrolyzing Enzymes Available for Biorecycling. *Catalysts* **2021**, *11* (2), 206.

(11) Brott, S.; Pfaff, L.; Schuricht, J.; Schwarz, J.; Böttcher, D.; Badenhorst, C. P. S.; Wei, R.; Bornscheuer, U. T. Engineering and Evaluation of Thermostable *Is*PETase Variants for PET Degradation. *Eng. Life Sci.* **2022**, *22* (3−4), 192−203.

(12) Ronkvist, Å. M.; Xie, W.; Lu, W.; Gross, R. A. Cutinase-Catalyzed Hydrolysis of Poly(Ethylene Terephthalate). *Macromolecules* **2009**, *42* (14), 5128−5138.

(13) Sulaiman, S.; You, D.-J.; Kanaya, E.; Koga, Y.; Kanaya, S. Crystal Structure and Thermodynamic and Kinetic Stability of Metagenome-Derived LC-Cutinase. *Biochemistry* **2014**, *53* (11), 1858−1869.

(14) Sulaiman, S.; Yamato, S.; Kanaya, E.; Kim, J.-J.; Koga, Y.; Takano, K.; Kanaya, S. Isolation of a Novel Cutinase Homolog with Polyethylene Terephthalate-Degrading Activity from Leaf-Branch Compost by Using a Metagenomic Approach. *Appl. Environ. Microbiol.* **2012**, *78* (5), 1556−1562.

(15) Wei, R.; Song, C.; Gräsing, D.; Schneider, T.; Bielytskyi, P.; Böttcher, D.; Matysik, J.; Bornscheuer, U. T.; Zimmermann, W. Conformational Fitting of a Flexible Oligomeric Substrate Does Not Explain the Enzymatic PET Degradation. *Nat. Commun.* **2019**, *10* (1), 5581.

(16) Miyakawa, T.; Mizushima, H.; Ohtsuka, J.; Oda, M.; Kawai, F.; Tanokura, M. Structural Basis for the Ca2+-Enhanced Thermostability and Activity of PET-Degrading Cutinase-like Enzyme from *Saccharomonospora viridis* AHK190. *Appl. Microbiol. Biotechnol.* **2015**, *99* (10), 4297−4307.

(17) Then, J.; Wei, R.; Oeser, T.; Gerdts, A.; Schmidt, J.; Barth, M.; Zimmermann, W. A Disulfide Bridge in the Calcium Binding Site of a Polyester Hydrolase Increases Its Thermal Stability and Activity against Polyethylene Terephthalate. *FEBS Open Bio* **2016**, *6* (5), 425−432.

(18) Oda, M.; Yamagami, Y.; Inaba, S.; Oida, T.; Yamamoto, M.; Kitajima, S.; Kawai, F. Enzymatic Hydrolysis of PET: Functional Roles of Three Ca^{2+} Ions Bound to a Cutinase-like Enzyme, Cut190*, and Its Engineering for Improved Activity. *Appl. Microbiol. Biotechnol.* **2018**, *102* (23), 10067−10077.

(19) Zhong-Johnson, E. Z. L.; Voigt, C. A.; Sinskey, A. J. An Absorbance Method for Analysis of Enzymatic Degradation Kinetics of Poly(Ethylene Terephthalate) Films. *Sci. Rep.* **2021**, *11* (1), 928.

(20) Then, J.; Wei, R.; Oeser, T.; Barth, M.; Belisário-Ferrari, M. R.; Schmidt, J.; Zimmermann, W. Ca $^{2+}$ and Mg $^{2+}$ Binding Site Engineering Increases the Degradation of Polyethylene Terephthalate Films by Polyester Hydrolases from *Thermobifida fusca*. *Biotechnol. J.* **2015**, *10* (4), 592−598.

(21) Emori, M.; Numoto, N.; Senga, A.; Bekker, G.; Kamiya, N.; Kobayashi, Y.; Ito, N.; Kawai, F.; Oda, M. Structural Basis of Mutants of PET -degrading Enzyme from *Saccharomonospora viridis* AHK190 with High Activity and Thermal Stability. *Proteins* **2021**, *89* (5), 502−511.

(22) Nakamura, A.; Kobayashi, N.; Koga, N.; Iino, R. Positive Charge Introduction on the Surface of Thermostabilized PET Hydrolase Facilitates PET Binding and Degradation. *ACS Catal.* **2021**, *11* (14), 8550−8564.

(23) Zeng, W.; Li, X.; Yang, Y.; Min, J.; Huang, J.-W.; Liu, W.; Niu, D.; Yang, X.; Han, X.; Zhang, L.; Dai, L.; Chen, C.-C.; Guo, R.-T. Substrate-Binding Mode of a Thermophilic PET Hydrolase and Engineering the Enzyme to Enhance the Hydrolytic Efficacy. *ACS Catal.* **2022**, *12* (5), 3033−3040.

(24) Thomsen, T. B.; Hunt, C. J.; Meyer, A. S. Influence of Substrate Crystallinity and Glass Transition Temperature on Enzymatic Degradation of Polyethylene Terephthalate (PET). *N. Biotechnol.* **2022**, *69*, 28−35.

(25) Wei, R.; Breite, D.; Song, C.; Gräsing, D.; Ploss, T.; Hille, P.; Schwerdtfeger, R.; Matysik, J.; Schulze, A.; Zimmermann, W. Biocatalytic Degradation Efficiency of Postconsumer Polyethylene Terephthalate Packaging Determined by Their Polymer Microstructures. *Adv. Sci.* **2019**, *6* (14), 1900491.

(26) Cui, Y.; Chen, Y.; Liu, X.; Dong, S.; Tian, Y.; Qiao, Y.; Mitra, R.; Han, J.; Li, C.; Han, X.; Liu, W.; Chen, Q.; Wei, W.; Wang, X.; Du, W.; Tang, S.; Xiang, H.; Liu, H.; Liang, Y.; Houk, K. N.; Wu, B. Computational Redesign of a PETase for Plastic Biodegradation under Ambient Condition by the GRAPE Strategy. *ACS Catal.* **2021**, *11* (3), 1340−1350.

(27) Lu, H.; Diaz, D. J.; Czarnecki, N. J.; Zhu, C.; Kim, W.; Shroff, R.; Acosta, D. J.; Alexander, B. R.; Cole, H. O.; Zhang, Y.; Lynd, N. A.; Ellington, A. D.; Alper, H. S. Machine Learning-Aided Engineering of Hydrolases for PET Depolymerization. *Nature* **2022**, *604* (7907), 662−667.

https://doi.org/10.1021/acscatal.2c02275
ACS Catal. 2022, 12, 9790−9800

(28) Han, X.; Liu, W.; Huang, J.-W.; Ma, J.; Zheng, Y.; Ko, T.-P.; Xu, L.; Cheng, Y.-S.; Chen, C.-C.; Guo, R.-T. Structural Insight into Catalytic Mechanism of PET Hydrolase. *Nat. Commun.* **2017**, *8* (1), 2106.
(29) Boneta, S.; Arafet, K.; Moliner, V. QM/MM Study of the Enzymatic Biodegradation Mechanism of Polyethylene Terephthalate. *J. Chem. Inf. Model.* **2021**, *61* (6), 3041−3051.
(30) Feng, S.; Yue, Y.; Zheng, M.; Li, Y.; Zhang, Q.; Wang, W. *Is* PETase- and *Is* MHETase-Catalyzed Cascade Degradation Mechanism toward Polyethylene Terephthalate. *ACS Sustain. Chem. Eng.* **2021**, *9* (29), 9823−9832.
(31) Jerves, C.; Neves, R. P. P.; Ramos, M. J.; da Silva, S.; Fernandes, P. A. Reaction Mechanism of the PET Degrading Enzyme PETase Studied with DFT/MM Molecular Dynamics Simulations. *ACS Catal.* **2021**, *11* (18), 11626−11638.
(32) Zheng, M.; Li, Y.; Dong, W.; Feng, S.; Zhang, Q.; Wang, W. Computational Biotransformation of Polyethylene Terephthalate by Depolymerase: A QM/MM Approach. *J. Hazard. Mater.* **2022**, *423*, 127017.
(33) Zimmermann, W.; Wei, R.; Hille, P.; Oeser, T.; Schmidt, J. New Polypeptides Having a Polyester Degrading Activity and Uses Thereof. EP3517608A1, July 31, 2019.
(34) Sonnendecker, C.; Oeser, J.; Richter, P. K.; Hille, P.; Zhao, Z.; Fischer, C.; Lippold, H.; Blázquez-Sánchez, P.; Engelberger, F.; Ramírez-Sarmiento, C. A.; Oeser, T.; Lihanova, Y.; Frank, R.; Jahnke, H.; Billig, S.; Abel, B.; Sträter, N.; Matysik, J.; Zimmermann, W. Low Carbon Footprint Recycling of Post-Consumer PET Plastic with a Metagenomic Polyester Hydrolase. *ChemSusChem* **2022**, *15* (9), No. e202101062.
(35) Falkenstein, P.; Wei, R.; Matysik, J.; Song, C. Mechanistic Investigation of Enzymatic Degradation of Polyethylene Terephthalate by Nuclear Magnetic Resonance. In *Methods in Enzymology*; Elsevier, 2021; Vol. *648*, pp 231−252.
(36) Barth, M.; Honak, A.; Oeser, T.; Wei, R.; Belisário-Ferrari, M. R.; Then, J.; Schmidt, J.; Zimmermann, W. A Dual Enzyme System Composed of a Polyester Hydrolase and a Carboxylesterase Enhances the Biocatalytic Degradation of Polyethylene Terephthalate Films. *J. Biotechnol.* **2016**, *11* (8), 1082−1087.
(37) Eugenio, E. de Q.; Campisano, I. S. P.; de Castro, A. M.; Coelho, M. A. Z.; Langone, M. A. P. Kinetic Modeling of the Post-Consumer Poly(Ethylene Terephthalate) Hydrolysis Catalyzed by Cutinase from *Humicola insolens*. *J. Polym. Environ.* **2022**, *30*, 1627−1637.
(38) Chen, C.; Han, X.; Ko, T.; Liu, W.; Guo, R. Structural Studies Reveal the Molecular Mechanism of PETase. *FEBS J.* **2018**, *285* (20), 3717−3723.
(39) Schmidt, J.; Wei, R.; Oeser, T.; Belisário-Ferrari, M. R.; Barth, M.; Then, J.; Zimmermann, W. Effect of Tris, MOPS, and Phosphate Buffers on the Hydrolysis of Polyethylene Terephthalate Films by Polyester Hydrolases. *FEBS Open Bio* **2016**, *6* (9), 919−927.
(40) Numoto, N.; Kamiya, N.; Bekker, G.-J.; Yamagami, Y.; Inaba, S.; Ishii, K.; Uchiyama, S.; Kawai, F.; Ito, N.; Oda, M. Structural Dynamics of the PET-Degrading Cutinase-like Enzyme from *Saccharomonospora viridis* AHK190 in Substrate-Bound States Elucidates the Ca^{2+} -Driven Catalytic Cycle. *Biochemistry* **2018**, *57* (36), 5289−5300.
(41) Baker, P. J.; Poultney, C.; Liu, Z.; Gross, R.; Montclare, J. K. Identification and Comparison of Cutinases for Synthetic Polyester Degradation. *Appl. Microbiol. Biotechnol.* **2012**, *93* (1), 229−240.
(42) Furukawa, M.; Kawakami, N.; Tomizawa, A.; Miyamoto, K. Efficient Degradation of Poly(Ethylene Terephthalate) with *Thermobifida fusca* Cutinase Exhibiting Improved Catalytic Activity Generated Using Mutagenesis and Additive-Based Approaches. *Sci. Rep.* **2019**, *9* (1), 16038.
(43) Austin, H. P.; Allen, M. D.; Donohoe, B. S.; Rorrer, N. A.; Kearns, F. L.; Silveira, R. L.; Pollard, B. C.; Dominick, G.; Duman, R.; El Omari, K.; Mykhaylyk, V.; Wagner, A.; Michener, W. E.; Amore, A.; Skaf, M. S.; Crowley, M. F.; Thorne, A. W.; Johnson, C. W.; Woodcock, H. L.; McGeehan, J. E.; Beckham, G. T. Characterization and Engineering of a Plastic-Degrading Aromatic Polyesterase. *Proc. Natl. Acad. Sci. U.S.A.* **2018**, *115* (19), E4350−E4357.
(44) Erickson, E.; Shakespeare, T. J.; Bratti, F.; Buss, B. L.; Graham, R.; Hawkins, M. A.; König, G.; Michener, W. E.; Miscall, J.; Ramirez, K. J.; Rorrer, N. A.; Zahn, M.; Pickford, A. R.; McGeehan, J. E.; Beckham, G. T. Comparative Performance of PETase as a Function of Reaction Conditions, Substrate Properties, and Product Accumulation. *ChemSusChem* **2022**, *15* (1), No. e202101932.
(45) Wei, R.; Oeser, T.; Then, J.; Kühn, N.; Barth, M.; Schmidt, J.; Zimmermann, W. Functional Characterization and Structural Modeling of Synthetic Polyester-Degrading Hydrolases from *Thermomonospora curvata*. *AMB Expr.* **2014**, *4* (1), 44.
(46) Wei, R.; Oeser, T.; Schmidt, J.; Meier, R.; Barth, M.; Then, J.; Zimmermann, W. Engineered Bacterial Polyester Hydrolases Efficiently Degrade Polyethylene Terephthalate Due to Relieved Product Inhibition: Engineered Polyester Hydrolases. *Biotechnol. Bioeng.* **2016**, *113* (8), 1658−1665.
(47) Silva, C.; Da, S.; Silva, N.; Matamá, T.; Araújo, R.; Martins, M.; Chen, S.; Chen, J.; Wu, J.; Casal, M.; Cavaco-Paulo, A. Engineered *Thermobifida fusca* Cutinase with Increased Activity on Polyester Substrates. *J. Biotechnol.* **2011**, *6* (10), 1230−1239.
(48) Gamerith, C.; Zartl, B.; Pellis, A.; Guillamot, F.; Marty, A.; Acero, E. H.; Guebitz, G. M. Enzymatic Recovery of Polyester Building Blocks from Polymer Blends. *Process. Biochem.* **2017**, *59*, 58−64.
(49) Bai, C. Structural Changes in Poly(Ethylene Terephthalate) Induced by Mechanical Milling. *Polymer* **2000**, *41* (19), 7147−7157.
(50) Falkenstein, P.; Gräsing, D.; Bielytskyi, P.; Zimmermann, W.; Matysik, J.; Wei, R.; Song, C. UV Pretreatment Impairs the Enzymatic Degradation of Polyethylene Terephthalate. *Front. Microbiol.* **2020**, *11*, 689.
(51) Vogel, K.; Wei, R.; Pfaff, L.; Breite, D.; Al-Fathi, H.; Ortmann, C.; Estrela-Lopis, I.; Venus, T.; Schulze, A.; Harms, H.; Bornscheuer, U. T.; Maskow, T. Enzymatic Degradation of Polyethylene Terephthalate Nanoplastics Analyzed in Real Time by Isothermal Titration Calorimetry. *Sci. Total Environ.* **2021**, *773*, 145111.
(52) Wei, R.; Oeser, T.; Barth, M.; Weigl, N.; Lübs, A.; Schulz-Siegmund, M.; Hacker, M. C.; Zimmermann, W. Turbidimetric Analysis of the Enzymatic Hydrolysis of Polyethylene Terephthalate Nanoparticles. *J. Mol. Catal. B: Enzym.* **2014**, *103*, 72−78.
(53) Scandola, M.; Focarete, M. L.; Frisoni, G. Simple Kinetic Model for the Heterogeneous Enzymatic Hydrolysis of Natural Poly(3-Hydroxybutyrate). *Macromolecules* **1998**, *31* (12), 3846−3851.
(54) Pfaff, L.; Breite, D.; Badenhorst, C. P. S.; Bornscheuer, U. T.; Wei, R. Fluorimetric High-Throughput Screening Method for Polyester Hydrolase Activity Using Polyethylene Terephthalate Nanoparticles. In *Methods in Enzymology*; Elsevier, 2021; Vol. *648*, pp 253−270.
(55) Krause, D.; Thörnig, P. JURECA: Modular Supercomputer at Jülich Supercomputing Centre. *JLSRF* **2018**, *4*, A132.

https://doi.org/10.1021/acscatal.2c02275
ACS Catal. 2022, 12, 9790−9800

Supporting Information

Multiple Substrate Binding Mode-Guided Engineering of a Thermophilic PET Hydrolase

Lara Pfaff[1], Jian Gao[2,3], Zhishuai Li[2,4], Anna Jäckering[5,6], Gert Weber[7], Jan Mican[8], Yinping Chen[9], Weiliang Dong[9], Xu Han[2,3], Christian G. Feiler[7], Yu-Fei Ao[1,10], Christoffel P.S. Badenhorst[1], David Bednar[8,11], Gottfried J. Palm[12], Michael Lammers[12], Jiri Damborsky[8,11], Birgit Strodel[5,6], Weidong Liu[2,3,4], Uwe T. Bornscheuer[1*], Ren Wei[1*]*

[1]Department of Biotechnology & Enzyme Catalysis, Institute of Biochemistry, University of Greifswald, Felix-Hausdorff-Str. 4, 17487 Greifswald, Germany

[2]Tianjin Institute of Industrial Biotechnology, Chinese Academy of Sciences, 32 West 7th Avenue, Tianjin Airport Economic Area, Tianjin 300308, China

[3]National Technology Innovation Center of Synthetic Biology, 32 West 7th Avenue, Tianjin Airport Economic Area, Tianjin 300308, China

[4]University of Chinese Academy of Sciences, 19A Yuquan Road, Beijing, 100049 China

[5]Institute of Biological Information Processing: Structural Biochemistry (IBI-7), Forschungszentrum Jülich, Wilhelm-Johnen-Straße, 52428 Jülich, Germany

[6]Institute of Theoretical and Computational Chemistry, Heinrich Heine University, Düsseldorf, Universitätsstr. 1, 40225 Düsseldorf, Germany

[7]Helmholtz-Zentrum Berlin für Materialien und Energie, Hahn-Meitner-Platz 1, 14109 Berlin, Germany

[8]Loschmidt Laboratories, Department of Experimental Biology and RECETOX, Faculty of Science, Masaryk University, Kamenice 5/C13, 625 00 Brno, Czech Republic

[9]State Key Laboratory of Materials-Oriented Chemical Engineering, College of Biotechnology and Pharmaceutical Engineering, Nanjing Tech University, Nanjing, China

[10]CAS Key Laboratory of Molecular Recognition and Function, Institute of Chemistry, Chinese Academy of Sciences, Zhongguancun North First Street 2, 100190 Beijing, China

[11]International Clinical Research Center, St. Anne's University Hospital, Pekarska 53, 656 91 Brno, Czech Republic

[12]Department Synthetic and Structural Biochemistry, Institute of Biochemistry, University of Greifswald, Felix-Hausdorff-Str. 4, 17487 Greifswald, Germany

[*]Email: liu_wd@tib.cas.cn; uwe.bornscheuer@uni-greifswald.de; ren.wei@uni-greifswald.de

Materials and Methods

Materials

Chemicals and consumables were purchased from Merck KGaA (Darmstadt, Germany), Sigma-Aldrich (Steinheim, Germany), Carl Roth (Karlsruhe, Germany), TCI (Tokyo, Japan), Thermo Fisher Scientific (Waltham, MA, USA) and New England Biolabs GmbH (Frankfurt am Main, Germany). Oligonucleotides (Table S8) were ordered from Thermo Fisher Scientific (Waltham, MA, USA) and Eurofins (Ebersberg, Germany). Amorphous PET film (250 μm thickness, product number ES301445) was purchased from Goodfellow GmbH (Bad Nauheim, Germany).

Protein production for crystallization, structure determination, and refinement

The genes encoding PES-H1 and PES-H2 were synthesized by GENE ray Biotech Co. (Shanghai, China) and cloned into the pET-32a vector between the EcoRI and NotI restriction sites. Detailed nucleotide sequences encoding the enzymes are given after the Material and Methods. The pET-32a-*pes-h1* and pET-32a-*pes-h2* plasmids were transformed into *Escherichia coli* BL21trxB (DE3). Cells from single colonies were used to inoculate 5 mL lysogeny broth (LB) medium and grown at 37 °C to an optical density at 600 nm (OD_{600}) of approximately 0.8 before induction using 0.5 mM isopropyl β-D-thiogalactopyranoside (IPTG) at 16 °C for 18 h. Cells were harvested by centrifugation at 5,000 *g* for 15 min and then resuspended in lysis buffer consisting of 25 mM Tris-HCl (pH 7.5), 150 mM sodium chloride (NaCl), and 20 mM imidazole, followed by disruption using a French Press (800-1200 bar, 2-5 cycles). Cell debris were removed by centrifugation at 17,000 *g* for 1 h at 4 °C. The supernatant was then applied to a 5 mL Ni-NTA column on an FPLC system (GE Healthcare, Chicago, USA) for protein purification. Target proteins were eluted at 100 mM imidazole when a 20-250 mM imidazole

gradient was applied. Each protein was dialyzed against 25 mM Tris-HCl (pH 7.5) containing 150 mM NaCl, and subjected to tobacco etch virus (TEV) protease digestion overnight to remove the hexahistidine (His_6)-tag. The solutions were then passed through an Ni-NTA column again. The untagged target protein was eluted with 25 mM Tris-HCl (pH 7.5) containing 150 mM NaCl. The purity of each protein (>95%) was confirmed by sodium dodecyl sulfate polyacrylamide gel electrophoresis (SDS-PAGE) analysis. The purified proteins were concentrated to ~20 mg mL^{-1} for screening crystallization conditions.

Crystallization, data collection, structure determination, and refinement

All crystallization experiments were conducted at 25 °C using the sitting-drop vapor-diffusion method. In general, 1 μL of a PES-H1 or PES-H2 containing solution (15 mg mL^{-1} in 25 mM Tris-HCl (pH 7.5) containing 150 mM NaCl) were mixed with 1 μL of reservoir solution in 48-well Cryschem plates and equilibrated against 100 μL of the reservoir solution. The two optimized crystallization conditions for PES-H1 were: 17% w/v polyethylene glycol (PEG) 6000, 0.1 M citric acid (cit) (pH 5.0), 30% 2-methylpentane-2,4-diol (MPD) and 8% Tacsimate (pH 4.0), 0.1 M citric acid (pH 5.0), 20% PEG3350.

The two optimized crystallization conditions for PES-H2 were: 32% PEG 2000 MME, 0.1 M KBr and 24% PEG4000, 0.1 M citric acid (pH 5.6), and 9% isopropanol. Within one week, the crystals reached sizes suitable for X-ray diffraction. The crystals in complex with 4-(2-hydroxyethylcarbamoyl) benzoic acid (MHETA) or bis(2-hydroxyethyl) terephthalate (BHET) were obtained by soaking them with their respective mother liquor containing substrate powder for 72 h. All X-ray diffraction data sets were collected at the Beamlines BL10U2(BL17U1)/BL17B/BL18U1/BL19U1 of the National Facility for Protein Science in

Shanghai (NFPS) at the Shanghai Synchrotron Radiation Facility (SSRF), and Beamline 14.1 at Berlin using the third-generation synchrotron radiation source (BESSY). The crystals were mounted in a CryoLoop and soaked with cryoprotectant solution prior to data collection at 100 K. The diffraction images were processed by using HKL2000.[1] All crystal structures were solved by the molecular replacement (MR) method with the Phaser program[2] from the Phenix[3] suite using the structure of the *Is*PETase from *Ideonella sakaiensis* 201-F6 (PDB code: 5XG0) as the search model.[4] Further refinement was carried out using the programs phenix.refine[5] and Coot.[6] Prior to the structural refinements, 5% randomly selected reflections were set aside for calculating R_{free}[7] as a monitor. Data collection and refinement statistics are summarized in Tables S1 and S2. All figures were prepared using PyMOL (http://pymol.sourceforge.net).

Molecular dynamics simulations

To model and analyze the PET-PES-H1 interactions, we used a PET trimer (3PET) to mimic the polymeric substrate of PES-H1. For correctly placing 3PET into the binding cleft, PyMOL[8] was used to superimpose the central 3PET unit with the position of 1-2(-hydroxyethyl) 4-methyl terephthalate (HEMT) in complex with *Is*PETase (PDB code 5XH3).[4] Generalized AMBER force field (GAFF) parameters[9] were derived for 3PET by performing quantum mechanics calculations at the HF6-31G* level using Gaussian 09[10]. The partial charges were determined by restrained electrostatic potential (RESP) calculations[11,12] using the antechamber tool of the Antechamber package[9,13,14] available in AmberTools 21[15] and redistributed to yield a net charge of zero for each 3PET unit using the Antechamber tool Prepgen (see GAFF parameters). All molecular dynamics (MD) simulations were carried out using GROMACS 2020.4[16] using the AMBER14SB[17] protein force field with Parmbsc1 parameters[18] and the newly derived PET parameters to determine the

potential energy and forces. After determining the pKa of titratable residues using Propka3 3.4.0, hydrogens were added to or removed from the PES-H1 crystal structure to mimic a protonation state at pH 7. The PES-H1-3PET complex was centered in a periodic dodecahedron box with at least 1 nm distance to the box edges, solvated with water described by the TIP3P water model[19] and neutralized by adding Na^+ ions, resulting in a system containing 32,990 atoms in total. Energy minimization of the system was conducted using the steepest descent algorithm[20] prior to a two-step equilibration, first in the NVT ensemble for 0.2 ns, followed by a 1 ns equilibration simulation in the NpT ensemble to set the temperature to 303 K (30 °C, Nosé-Hoover thermostat)[21,22] and the pressure at 1.0 bar (Parrinello-Rahman barostat).[23] The final 100 ns production run was performed in triplicates using different randomly generated initial velocities. The electrostatic interactions were calculated using the particle-mesh Ewald method[24,25] and a cutoff of 8 Å was applied to both the electrostatic and Lennard-Jones (LJ) interactions. The bonds were constrained using the LINCS algorithm[26], which allows for a time step of 2 fs. Coordinates were saved every 20 ps.

The three trajectories were concatenated and the 3PET conformations were clustered using the algorithm described by Daura et al.[27] together with a cutoff of 2 Å applied to the root-mean-square deviation (RMSD) to assign the cluster membership. This resulted in the identification of four particularly stable binding poses corresponding to the four most populated clusters (Figure S3C). All MD snapshots belonging to each of the four clusters were retrieved and submitted to further analysis per binding pose. The protein residues putatively interacting with 3PET were identified using the Visual Molecular Dynamics (VMD)[28] software and the strength of these residue-3PET interactions was energetically quantified.

Enzyme production and purification for the enzymatic hydrolysis of PET substrates

The genes encoding PES-H1 and the reference enzyme LCC ICCG were codon-optimized for expression in *E. coli*, synthesized and cloned into the pET-28a(+) vector and the pET-26b(+) vector by BioCat GmbH (Heidelberg, Germany) between the NcoI (for PES-H1) or NdeI (for LCC ICCG) and XhoI restriction sites. The plasmids (pET-28a(+)-*pes-h1* and variants) were used to transform competent *E. coli* SHuffle® T7 Express or *E. coli* BL21 (DE3). For the expression in *E. coli* SHuffle® T7 Express, the cells were grown in LB medium supplemented with kanamycin (50 μg mL^{-1}) at 30 °C to OD_{600} of ~1 and then induced using 1 mM IPTG at 16 °C for 12 h. LCC ICCG and PES-H1 variants were expressed in autoinduction medium (ZYM-5052) supplemented with kanamycin (50 μg mL^{-1}) at 21 °C for 23 h and 20 h, respectively, as described previously.[29] Cells were harvested by centrifugation at 10,000 *g* for 30 min, resuspended in lysis buffer (50 mM sodium phosphate (pH 8.0), 300 mM NaCl) and lysed by ultrasonication (2×3 min, 50% power, 50% amplitude). Cell debris were removed by centrifugation at 10,000 *g* for 30 min and the enzymes were purified using cobalt-ion affinity chromatography (ROTI®Garose-His/Co Beads, Carl Roth, Karlsruhe, Germany). Unbound proteins were removed using lysis buffer (pH 8.0) supplemented with 20 mM or 50 mM imidazole. PES-H1 and LCC ICCG were eluted with elution buffer (50 mM sodium phosphate (pH 8.0), 300 mM NaCl, and 100 mM or 250 mM imidazole, respectively). The target proteins were desalted with 50 mM sodium phosphate buffer (pH 8.0) and concentrated using Vivaspin™ ultrafiltration devices (10 kDa MWCO, Cytiva, Freiburg, Germany). Enzyme purities were verified by SDS-PAGE analysis.

Site-directed mutagenesis

Enzyme variants were generated using the Q5® Site-Directed Mutagenesis Kit (New England Biolabs GmbH, Frankfurt am Main, Germany). The sequences of the mutagenesis oligonucleotides are listed in Table S8. Mutagenesis was verified by Sanger sequencing (Eurofins Genomics Germany GmbH, Ebersberg, Germany).

Melting temperature measurements

The T_m values of the PES-H1 variants were determined by nano differential scanning fluorimetry (NanoDSF) using the Prometheus NT.48 (NanoTemper Technologies, Munich, Germany) and differential scanning calorimetry (DSC; TA Instruments, Newcastle, USA). The measurements were conducted using protein concentrations of 0.5 mg mL^{-1} or 0.3 mg mL^{-1} to determine temperature profiles from 20 °C to 95 °C and 20 °C to 100°C at 1 °C per minute, respectively. The nanoDSF instrument has a fixed excitation wavelength of 285 nm and records emitted light at 330 nm and 350 nm.

Enzymatic hydrolysis of PET film and PET powder

The degradation of amorphous Gf-PET PET film (7% crystallinity) was performed using an enzyme concentration of 0.5 mg_{enzyme} g_{PET}^{-1}, 1 mg_{enzyme} g_{PET}^{-1}, or 2 mg_{enzyme} g_{PET}^{-1} in 1.5 mL potassium phosphate buffer (1 M, pH 8.0) by shaking at 1,000 rpm and 72 °C on a ThermoMixer C (Eppendorf, Hamburg, Germany) for 12 h or 24 h. The reaction conditions were adapted from a published patent application.[30] The hydrolysis reactions were performed in triplicate. Gf-PET films were cut into small pieces of ~2 cm × 1 cm and washed with 0.1% SDS solution, ultrapure H_2O and absolute ethanol before drying at room temperature for 24 h. Weight loss as a result of

enzymatic degradation was determined gravimetrically. The degradation of PET powder (13%, 26%, or 33% crystallinity) was conducted in the same way with an enzyme concentration of 1 mg_{enzyme} g_{PET}^{-1} for 24 h. The degradation products were analyzed by reversed-phase high-performance liquid chromatography (HPLC) on a VWR Hitachi LaChrom Elite system (VWR International, Radnor, USA) equipped with a Kinetex® column (5 µM EVO C18 100 Å, 150x4.6 mm; Phenomenex®, Aschaffenburg, Germany).[31] Samples (10 µl) were injected and separated at 30 °C with a gradient of acetonitrile in water containing 0.1% (v/v) formic acid. Acetonitrile was increased from 5% to 44% over 12 min and then to 70% over 3 min, after which the ratio remained constant for a further 3 min, using a flow rate of 0.8 mL min^{-1}. Terephthalate (TPA), mono-(2-hydroxyethyl) terephthalate (MHET), and BHET were detected by UV absorbance at 240 nm and quantified based on a calibration curve obtained with commercially available TPA in the concentration range from 0 to 1 mM.

Kinetic analysis

For the kinetic analysis of PET nanoparticle (PET-NP) degradation by PES-H1 and its variants, PET-NPs were produced as previously described.[32–34] For determining the kinetic parameters, a turbidimetric assay was applied as described before.[35] A mixture of 3 mL ROTIPHORESE® gel 40, 3 mL potassium phosphate buffer (1 M, pH 8.0), 120 µL tetramethylethylenediamine and PET-NP suspension (1.7 mg mL^{-1}) was prepared and filled up to a final volume of 15 mL with ultrapure H_2O. Ammonium persulfate (2 µL of a 40% (w/v) solution) and the enzyme solution were added to a total volume of 50 µL and mixed with 150 µL of the substrate- and acrylamide-containing mixture. The turbidimetric assay monitoring the enzymatic hydrolysis of PET-NP was performed at 600 nm in a microtiter plate at 70 °C for 40 min with 0.5 mg mL^{-1} PET-NP and varying enzyme

concentrations in the range of 0-2 μM. In addition, the degradation of PET-NP was also carried out with a constant enzyme concentration of 0.7 μM and substrate concentrations ranging from 0 to 0.5 mg mL^{-1}. All determinations were performed in triplicate.

A kinetic model (equation 1) based on previous studies,[36–38] was used to analyze the heterogenous kinetics of the PET-NP degradation, where v_0 is the initial reaction rate; k_h, the hydrolysis rate constant; $[S_0]$, the initial substrate concentration; $[E_0]$, enzyme concentration, and K_A the adsorption equilibrium constant.

$$v_0 = k_h [S_0] \frac{K_A [E_0]}{1 + K_A [E_0]} \quad (1)$$

PET powder production and analysis

Pretreatment of waste PET bottles

The bottle wall part of collected post-consumer PET plastic bottles was cut into small flakes of about 5 cm × 5 cm for more even melting and crushing processes. PET flakes were washed with ultrapure water and then dried in the drying oven. Before the melting experiment, the dried PET flakes were placed in an aluminum tray and sealed with tin foil to prevent oxidation. Then, the temperature was set to 280 °C in the high-temperature reactor for 40 min. This temperature exceeds the T_m of PET (250-260 °C) and can thus result in homogeneous melts of PET. Low-crystallinity PET (lcPET) can be obtained by rapidly cooling the molten PET with ice-cold water within 10 s (quenching step). The melt quenched PET was crushed into powders using a portable herb grinder (Model 800Y, Yongkang Boou Hardware Products Co., Ltd., Yongkang, China) for 5 min or a planetary ball mill (Model PM2L, Shanghai Droide Instruments Ltd., Shanghai, China) for 30 min. The herb grinder uses a rotating blade to mechanically grind the melt-quenched PET. The temperature of the portable herb grinder could not be controlled and increased above room

temperature during grinding. In the ball milling process, the melt-quenched PET is mixed with steel milling balls, followed by continuous rotation at a speed of 400 rpm to grind the plastics through the collision of the beads. The temperature of the ball mill was constantly maintained at room temperature. Finally, PET powders with different particle sizes were collected and sieved with different mesh sizes. Similarly, Gf-PET films were crushed using the herb grinder and sieved in the same manner to produce lcPET powders for enzymatic degradation.

Characterization of PET samples

The crystallinity of PET was measured by differential scanning calorimetry (DSC) on an TAQ2000 instrument (TA instruments, Newcastle, USA). Thermograms were monitored from the first heating process from 50 to 300 °C at a rate of 10 °C min^{-1} under a nitrogen atmosphere. Under these conditions, the crystallinity of virgin PET (waste PET bottles and commercial PET films), melt-quenched PET, and PET powders obtained by different pulverization methods were determined as described in a previous publication.[39]

Additionally, gel permeation chromatography (GPC) measurements were performed using an Agilent PL-GPC50 (Agilent, California, USA) device to detect the molecular weight distributions of various PET samples dissolved in hexafluoro-2-propanol.

The crystallinity, the number average molecular weight (Mn), and the weight average molecular weight (Mw) of the PET samples are summarized in Table S6.

Using Ellman's reagent to determine the presence of a disulfide bond

To quantify the number of free cysteine residues, Ellman's reagent (5,5'-dithiobis-(2-nitrobenzoic acid, DNTB) was used. 25 μL of 1 mg mL^{-1} R204C/S250C were incubated with 255 μL of freshly prepared Ellman's reaction solution (2 mg mL^{-1} DTNB in 0.1 M sodium phosphate buffer, pH 8.0) and 250 μL 0.1 M sodium phosphate buffer (pH 8.0) containing 0.1 M EDTA and incubated for 15 min. The absorption of TBN^{2-} was measured at 412 nm. To calculate the concentration of free cysteine residues, a calibration curve prepared with cysteine solutions at concentrations from 0 to 1.5 mM was used.

Nucleotide sequences

PES-H1

Codon-optimized nucleotide sequence of PES-H1 cloned between the NcoI and XhoI restriction sites of the pET-28b(+) bacterial expression plasmid and between the EcoRI and NotI restriction sites of the pET-32a bacterial expression plasmid.

ATGGCTAACCCGTATGAACGCGGCCCGGATCCGACCGAAAGCAGCATTGAAGCGGT
GCGCGGCCCGTTTGCGGTGGCGCAGACCACCGTCAGCCGTCTGCAGGCGGATGGCT
TTGGCGGCGGCACCATTTATTATCCGACCGATACCAGCCAGGGCACCTTTGGCGCGG
TGGCGATCAGCCCGGGCTTTACCGCCGGTCAGGAAAGCATTGCCTGGCTGGGCCCG
CGTATTGCCAGCCAGGGCTTTGTGGTGATTACCATTGATACCATCACCCGTCTGGAT
CAGCCGGACAGCCGCGGTCGTCAGTTGCAGGCGGCGCTGGATCATCTGCGTACCAA
CAGCGTGGTGCGTAACCGTATTGATCCGAACCGTATGGCGGTGATGGGTCACAGCAT
GGGCGGCGGCGGCGCGCTGTCGGCGGCGGCGAATAACACCAGCCTGGAAGCGGCG
ATTCCGCTGCAGGGCTGGCATACCCGCAAAAACTGGAGCAGCGTGCGCACGCCGAC
GCTGGTGGTTGGCGCGCAGCTGGATACCATTGCGCCGGTTTCCAGCCACAGCGAAG
CGTTTTATAACAGCCTGCCGAGCGATCTGGATAAAGCCTATATGGAACTGCGCGGTG
CCAGCCATCTGGTCAGCAATACGCCGGATACCACCACCGCCAAATACAGCATTGCCT
GGCTGAAACGCTTTGTCGATGATGATCTGCGTTATGAACAGTTCCTGTGCCCGGCGC
CGGATGATTTTGCCATCAGCGAATATCGCAGCACCTGCCCGTTTTAA

PES-H2

Codon-optimized nucleotide sequence of PES-H2 cloned between the EcoRI and NotI restriction sites of the pET-32a bacterial expression plasmid.

ATGGAAAACCCGTATGAACGTGGCCCGGATCCGACCGAAAGCAGCATTGAAGCAGT
TCGCGGCCCGTTTGCAGTGGCCCAGACCACCGTGAGTCGCTTACAGGCAGATGGTTT
TGGTGGCGGCACTATTTATTATCCGACCGATACCTCTCAGGGGACGTTTGGTGCCGT
GGCCATTTCTCCGGGCTTTACCGCAGGCCAGGAAAGTATTGCCTGGTTAGGTCCGCG
TATTGCCTCTCAGGGCTTTGTTGTGATTACCATTGATACCATTACCCGCTTAGATCAG
CCGGATTCACGCGGTCGTCAGTTACAGGCAGCACTGGATCATCTGCGCACCAATTCT
GTTGTTCGTAATCGTATTGATCCGAATCGCATGGCAGTTATGGGTCATAGCATGGGT
GGCGGCGGCGCCTTAAGTGCAGCCGCCAATAATACCTCTTTAGAAGCCGCAATTCCG
TTACAGGGCTGGCATACCCGTAAAAATTGGAGTAGCGTTCGCACCCCGACCTTAGTT
GTGGGCGCCCAGCTGGATACCATTGCTCCCGTGTCAAGTCATAGTGAAGCATTTTAT
AATTCACTGCCGAGCGATTTAGATAAAGCCTATATGGAACTGCGTGGTGCATCACAT
TTTGTGTCTAATACCCCGGATACCACCACCGCCAAATATAGTATTGCCTGGCTGAAA
CGCTTTGTTGATAATGATCTGCGCTATGAACAGTTTCTGTGTCCGGCCCCGGATGATT
TTGCAATTAGCGAATATCGTGCAACCTGTCCGTTTTAA

Table S1. Data collection and refinement statistics of PES-H1-apo, PES-H1-cit, PES-H2-apo and PES-H2-PEG crystals.

	PES-H1-apo	**PES-H1-cit**	**PES-H2-apo**	**PES-H2-PEG**
PDB code	7CUV	7E30	7W69	7E31
Data collection				
space group	$P2_1$	$P2_12_12_1$	C2	$P2_12_12_1$
-cell				
a [Å]	52.01	55.97	105.52	55.34
b [Å]	69.54	97.08	55.34	94.86
c [Å]	74.85	99.11	51.15	105.5
α /β /γ (°)	90/90/90	90/90/90	90/93.36/90	90/90/90
resolution [Å]	25.0-1.45 (1.50-1.45)	25.0-1.56 (1.62-1.56)	22.9-1.56 (1.62-1.56)	24.3-1.38 (1.43-1.38)
unique reflections	89271 (8550)	77551 (7586)	41976 (4156)	114425 (11157)
redundancy	6.8 (3.8)	5.0 (3.2)	9.4 (6.4)	7.5 (4.3)
completeness [%]	96.9 (93.5)	99.9 (99.6)	99.86 (99.43)	99.78 (98.39)
average I/σ(I)	15.1 (2.5)	18.5 (3.02)	22.4 (2.80)	49.3 (2.64)
Rmeans	0.18 (0.53)	0.084 (0.48)	0.12 (0.65)	0.056 (0.52)
CC 1/2	0.994 (0.872)	0.993 (0.838)	0.993 (0.853)	0.992 (0.829)
Refinement				
no. of reflections	89157 (8383)	77449 (7581)	41964 (4156)	114421 (11157)
	4457(419)	3866 (373)	2101 (210)	5721 (557)
Rwork[a] (95 % of data)	0.163 (0.214)	0.152 (0.203)	0.1838 (0.2487)	0.1672 (0.2244)

Rfree[a] (5 % of data)	0.180 (0.246)	0.172 (0.225)	0.1928 (0.2475)	0.1772 (0.2426)
RMSD bonds [Å]	0.009	0.013	0.013	0.008
RMSD angles [°]	1.534	1.649	1.64	1.41
dihedral angles				
most favored [%]	98.2	97.8	97.66	98.24
allowed [%]	1.8	2.2	2.34	1.76
disallowed [%]	0	0	0	0
Average B-factor/ Number of non-hydrogen atoms				
Protein	16.25/3912	18.29/3924	20.37/3936	14.61/1968
Ion/ligands		32.35/47	43.23/20	29.84/10
solvent	31.10/653	32.03/555	33.86/773	29.75/313

Values in parentheses are for the highest resolution shell.

Table S2. Data collection and refinement statistics of PES-H1-MHETA, PES-H1-MHETA2, PES-H2-MHETA3 and PES-H2-BHET crystals.

	PES-H1-MHETA1	**PES-H1-MHETA2**	**PES-H1-MHETA3**	**PES-H2-BHET**
PDB code	7W6C	7W6O	7W6Q	7W66
Data collection				
space group	$P2_1$	$P2_1$	$P2_1$	$P2_12_12_1$
-cell				
a [Å]	52.51	52.67	52.71	105.84
b [Å]	56.01	56.19	56.22	55.62
c [Å]	102.31	100.03	108.62	95.88
α /β /γ (°)	90/94.41/90	90/93.91/90	90/93.78/90	90/90/90
resolution [Å]	29.5-2.3 (2.382-2.3)	25.8-2.2 (2.279-2.2)	27.1-2.2 (2.279-2.2)	49.2-1.96 (2.03-1.96)
unique reflections	26497 (2642)	29919 (2947)	30069 (2951)	39103 (4057)
redundancy	5.6 (5.4)	6.4 (6.7)	6.3 (6.3)	6.2 (5.2)
completeness [%]	99.45 (98.80)	99.84 (100.00)	99.83 (99.97)	94.36 (99.78)
average I/σ(I)	9.2 (6.0)	22.2 (18.6)	22.7 (17.6)	13.0 (2.5)
Rmeans	0.19 (0.35)	0.09 (0.12)	0.083 (0.105)	0.109 (0.75)
CC 1/2	0.979 (0.911)	0.995 (0.985)	0.996 (0.987)	0.998 (0.797)
Refinement				
no. of reflections	26482 (2642)	29906 (2947)	30051 (2952)	39072 (4056)
	1352 (122)	1479 (144)	1517 (147)	1954 (202)
Rwork[a] (95 % of data)	0.2487 (0.2789)	0.2224 (0.2575)	0.2250 (0.2567)	0.1976 (0.2879)

Rfree[a] (5 % of data)	0.2791 (0.2733)	0.2657 (0.3247)	0.2550 (0.2916)	0.2281 (0.3240)
RMSD bonds [Å]	0.013	0.006	0.006	0.005
RMSD. angles [°]	1.82	0.90	0.96	0.81
dihedral angles				
most favored [%]	94.71	95.49	94.51	97.65
allowed [%]	5.29	4.51	5.49	2.35
disallowed [%]	0.00	0.00	0.00	0.00
Average B-factor/ Number of non-hydrogen atoms				
Protein	18.35/3912	15.09/3912	16.21/3912	24.89/3916
Ion/ligands	38.57/30	30.84/15	31.07/15	36.50/18
solvent	17.78/169	21.14/347	22.78/382	32.81/363

Values in parentheses are for the highest resolution shell.

Table S3. Backbone RMSD values calculated based on the crystal structures of selected homologous PET hydrolases to that of PES-H1 (PDB code: 7CUV). *Bur*PL: *Is*PETase-like enzyme from *Burkholderiales bacterium* RIFCSPLOWO2_02_ FULL_57_36. *Rg*PETase: PETase from *Rhizobacter gummiphilus*.

Enzyme	**PDB ID**	**Main chain RMSD (Å)**
PES-H1	7CUV	0.000
PES-H1-cit	7E30	0.259
PES-H1-MHETA1	7W6C	0.358
PES-H1-MHETA2	7W6O	0.209
PES-H1-MHETA3	7W6Q	0.232
PES-H2	7W69	0.207
PES-H2-PEG	7E31	0.208
PES-H2-BHET	7W66	0.258
lipase	1JFR	0.388
Est119	3VIS	0.541
TfCut2	4CG1	0.457
LC-cutinase	6THT	0.644
Cut190^{S226P}	4WFI	0.471
Thermobifida fusca cutinase	5ZOA	0.459
*Is*PETase	5XG0	0.512
*Bur*PL	7CWQ	0.578
LCC cutinase from Biortus	7DS7	0.655
PE-H	6SBN	0.732
PET2 F105R/E110K	7EC8	0.766
*Rg*PETase	7DZT	0.605
PHL-7	7NEI	0.285

Table S4. Characteristics of the four binding positions observed by clustering. In total, 252 clusters were found. The distance between the catalytic S130 and the carbonyl carbon of the central PET unit was averaged over all frames belonging to the respective cluster.

	Total / 1-4	**Cluster 1**	**Cluster 2**	**Cluster 3**	**Cluster 4**
frames	15003 / 8765	4253	2592	1136	784
	100% / 58.40%	28.35%	17.28%	7.57%	5.23%
Fraction 1st	5001 / 3746	2074	101	1133	438
	100% / 42.74%	48.77%	3.90%	99.74%	55.87%
Fraction 2nd	5001 / 2836	2041	790	3	2
	100% / 32.36%	47.99%	30.48%	0.26%	0.26%
Fraction 3rd	5001 / 2183	138	1701	0	344
	100% / 24.91%	3.24%	65.63%	0%	43.88%
Distance [Å]					
Ser130-O - PET-C		3.27 ± 0.30	4.12 ± 0.31	4.48 ± 0.34	3.58 ± 0.26

Table S5. Melting temperatures of PES-H1 and variants in potassium phosphate buffer. Values which were not determined are abbreviated with "n.d.".

Buffer	T_m [°C]		
	PES-H1	L92F/Q94Y	R204C/S250C
0.05 M potassium phosphate	77.1	78.2	76.8
0.1 M potassium phosphate	n.d.	n.d.	79.6
0.5 M potassium phosphate	n.d.	n.d.	88.2
1 M potassium phosphate	84.9	86.7	91.3

Table S6. Crystallinity and molecular mass of PET materials before and after pretreatments determined by DSC and GPC, respectively. Values which were not determined are abbreviated with "n.d." M_w: weight average molecular mass, M_n: number average molecular mass.

Sample name	Crystallinity (%) by DSC	Molecular mass by GPC
Goodfellow PET film untreated	7%	M_w:39872 M_n:19652
PET nanoparticles prepared with Gf PET film	n.d.	M_w:8864 M_n:5770
Crushed PET film powder (particle size: 177 µM mesh)	13%	M_w:26197 M_n:20874
Post-consumer PET bottle (untreated)	27%	M_w:32304 M_n:14885
PET bottle after melt-quenching	19%	M_w:30214 M_n:14542
crushed PET bottle powder (particle size: 177 µM mesh)	33%	M_w:26667 M_n:13290
ball-milled PET bottle powder (particle size: 177 µM mesh)	26%	M_w:22266 M_n:16224

Table S7. Kinetic parameters for PET-NP hydrolysis by PES-H1, its variants, and LCC ICCG. K_A= adsorption equilibrium constant. k_h= hydrolysis rate constant, $k_h \times K_A$= pseudo-catalytic efficiency.

	K_A [μM^{-1}]	k_h [mL mg^{-1} min^{-1}]	$k_h \times K_A$ [mL μM^{-1} mg^{-1} min^{-1}]*
PES-H1 wild-type	4.710 ± 0.087	0.054 ± 0.001	0.254
L92F/Q94Y	8.259 ± 0.028	0.065 ± 0.002	0.537
R204C/S250C	4.063 ± 0.191	0.064 ± 0.001	0.260
LCC ICCG	5.953 ± 0.032	0.048 ± 0.001	0.286

*We can clearly show a 2.1-fold higher "pseudo-catalytic efficiency" value (mathematically equivalent to the catalytic efficiency described by k_{cat}/K_M based on the conventional Michaelis-Menten kinetics) with L92F/Q94Y compared to the wild-type enzyme. In addition, the ranking of the enzymes in terms of this value is remarkably consistent with that determined in the hydrolysis of amorphous PET materials as shown in Figures 4A and 4B. However, this pseudo-catalytic efficiency parameter based on the Langmuir-isotherm-based model is not yet properly defined and fully understood, which does not allow us to give a clear statement in the main text.

Table S8. Oligonucleotide primers used for the generation of PES-H1 variants.

Variant	**Sequence (5' → 3')**
L92F/Q94Y_fw	TTATCCGGACAGCCGCGGTCGT
L92F/Q94Y_rv	TCAAAACGGGTGATGGTATCAATGGTAATCACCAC
S204C_fw	TATGGAACTGTGCGGTGCCAGCC
S204C_rv	TAGGCTTTATCCAGATCGCTCGG
S250C_fw	TTTTGCCATCTGCGAATATCGCAGCACCTGC
S250C_rv	TCATCCGGCGCCGGGCAC

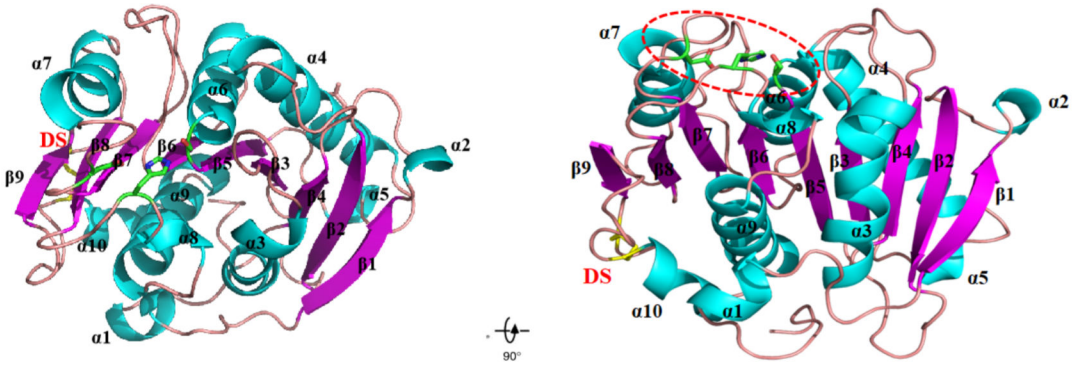


Figure S1. Structure of PES-H1. The structure of PES-H1 is represented as a cartoon. The catalytic triad (red dashed circle, top left) and disulfide bridge (red labels) are shown as sticks. The α-helices, β-sheets and loops are shown in light blue, purple, and cyan, respectively.

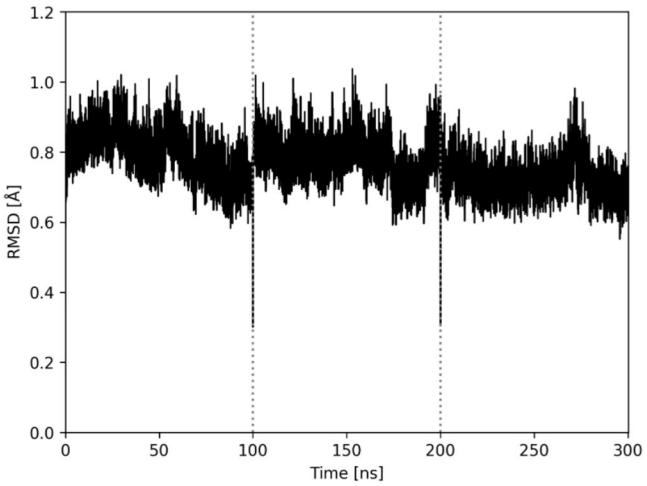


Figure S2. RMSD of the PES-H1 calculated against its crystal structure during the 3 × 100 ns MD simulations. The protein backbone atoms were used for this calculation. The three simulations were concatenated for this analysis and the start of the second and third simulation is indicated by vertical dotted lines. The RMSD values below 1 Å confirm the stability of the protein in the simulations.

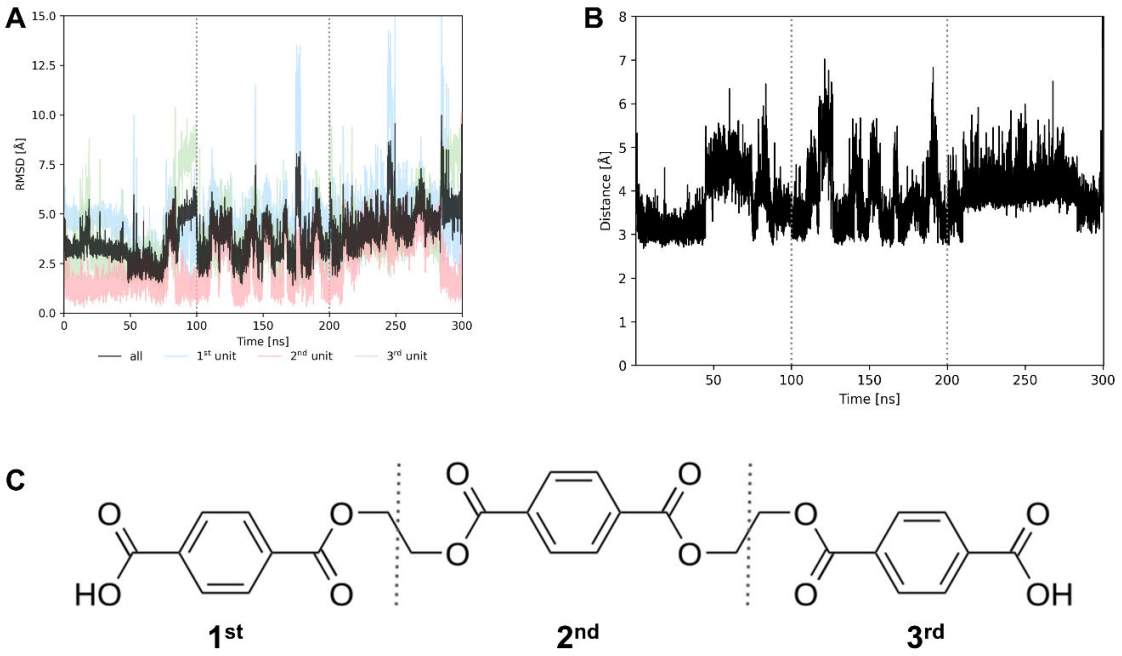


Figure S3. RMSD of 3PET from its starting structure and the minimum distance between the catalytic S130 and the second carbonyl carbon of the 2nd repeating unit during the 3 × 100 ns MD simulations. (A) The RMSD values were determined for the whole 3PET substrate (black: all) as well as each 3PET unit (blue: 1st, red: 2nd and green: 3rd unit), respectively, after alignment of the protein structures. This provides a measure for the change in binding position of 3PET. (B) The evolution of the minimum distance between the γ-O atom of the catalytic S130 and the closest carbonyl carbon atom of the central repeating unit in 3PET was calculated. This analysis revealed that 3PET adopted a hydrolysis-competent orientation. Three simulations were concatenated for this analysis and the start of the second and third simulation is indicated by vertical dotted lines. (C) 3PET oligomer structure with the 1st, 2nd, and 3rd PET repeating units labeled from left to right and divided by dotted lines

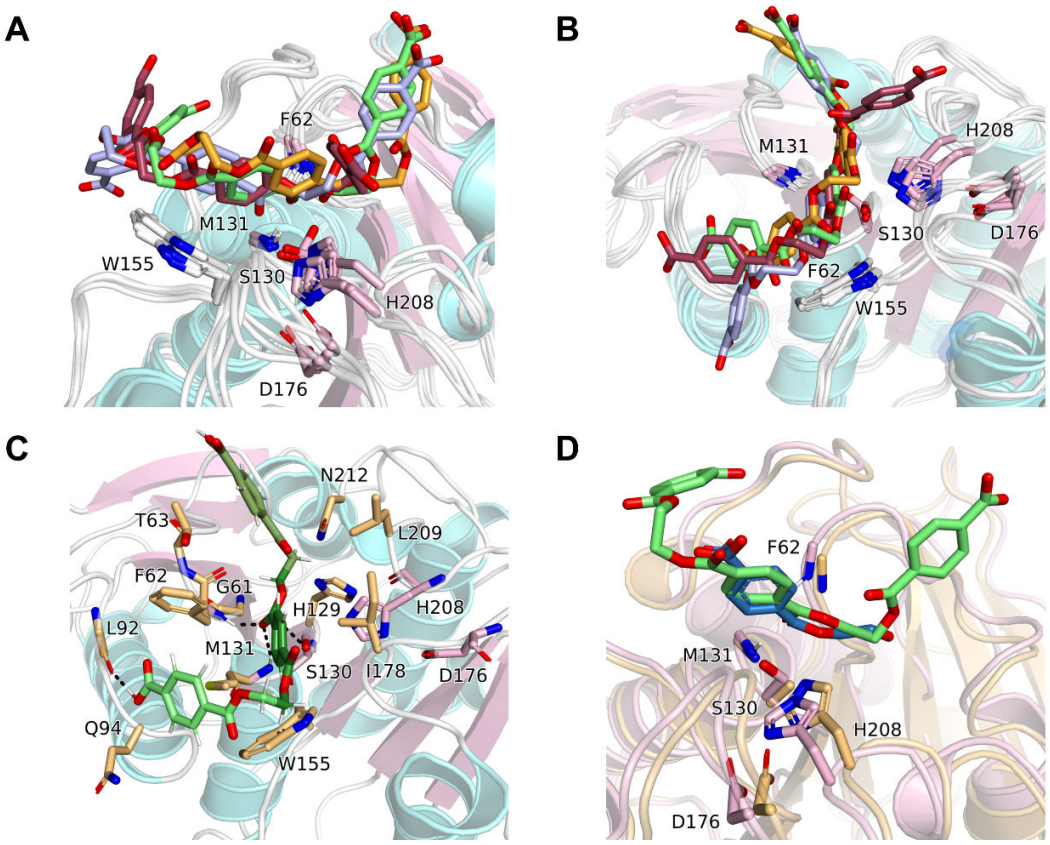


Figure S4. Binding positions of the 3PET clusters. Binding positions of all four clusters are given from a side view (A) and top view (B). The 3PET ligands are shown in green (cluster 1), orange (cluster 2), blue (cluster 3) and red (cluster 4). As an orientation marker, W155 is additionally shown as white sticks. The binding mode of cluster 1 (C) is colored from light green (1st unit) to dark green (3rd unit) and the most prominent interacting residues (sidechain/ backbone) are shown as orange sticks. (D) Superposition of the PES-H1 (light pink) and LCC ICCG with bound MHET (light orange, PDB code: 7VVE) structures. The 3PET ligand in the binding pose of cluster 1 is shown in light green, while MHET is colored in deep teal. For all images, the catalytic triad residues (S130, D176, and H208) and the oxyanion hole (F62 and M131) of PES-H1 are shown in light magenta. Nitrogen atoms are colored blue and oxygen atoms are colored red. The images were generated using PyMOL.

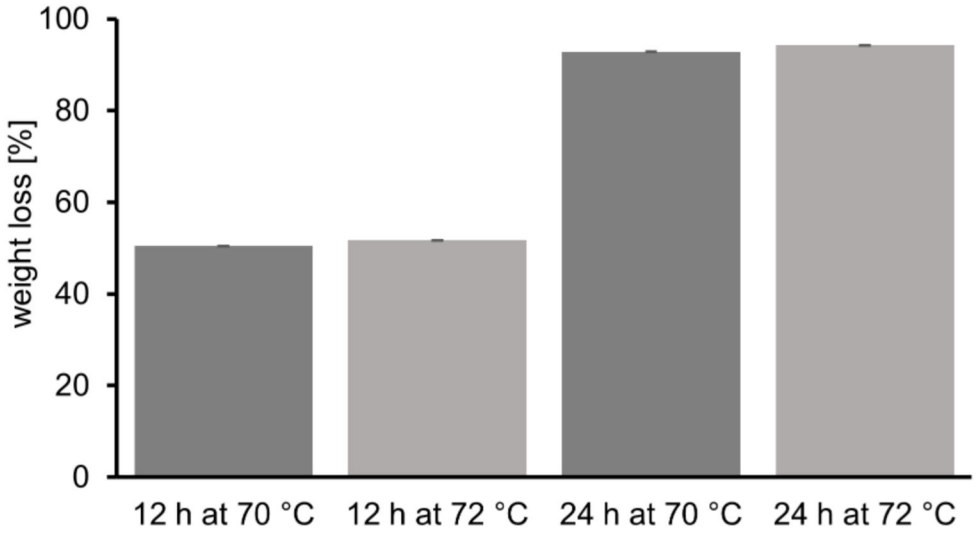


Figure S5. PET film degradation catalyzed by PES-H1 at 70 °C and 72 °C. Error bars indicate the standard deviations calculated from three replicates

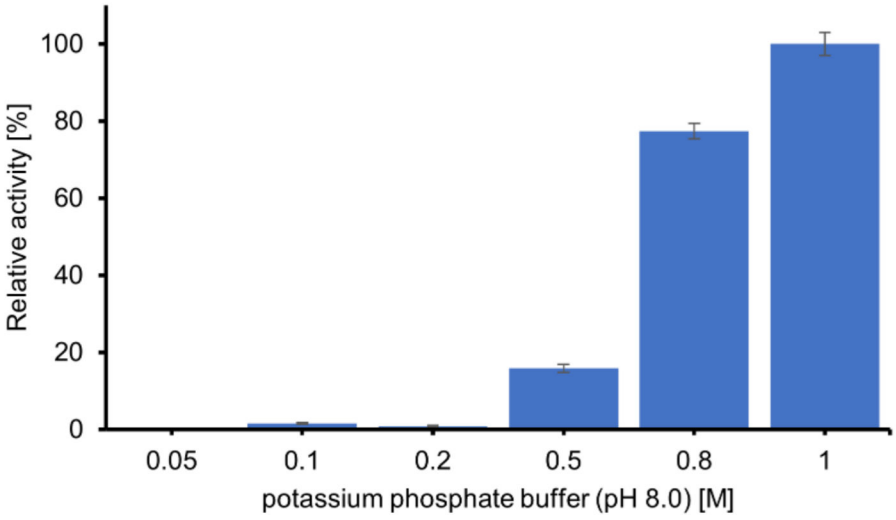


Figure S6. Phosphate dependence of PES-H1. PES-H1 was used to catalyze hydrolysis of Gf-PET film at 72 °C for 24 h in potassium phosphate buffer (pH 8.0). Phosphate concentrations ranged from 0.05 M to 1 M. Error bars indicate the standard deviations calculated from three replicates..

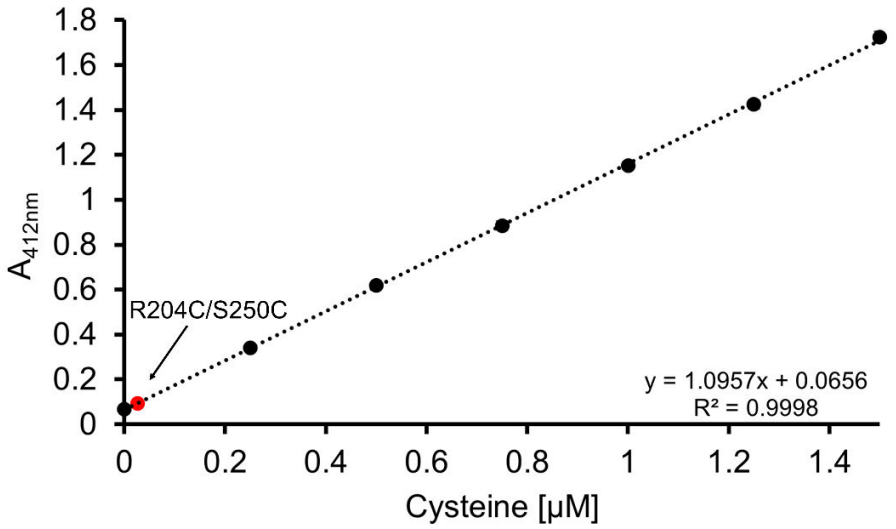


Figure S7. Cysteine calibration curve to determine the amount of free sulfhydryl-groups and confirm the disulfide bond formation. The concentration of free cysteines in the R204C/S250C variant of PES-H1 (0.02 ±0 μM; red dot) was calculated based on the dotted calibration line obtained with linearly fitted absorbance data according to the experimentally determined absorbance values at 412 nm. No absorbance was measured for the R204C/S250C variant, demonstrating the formation of a new disulfide bond.

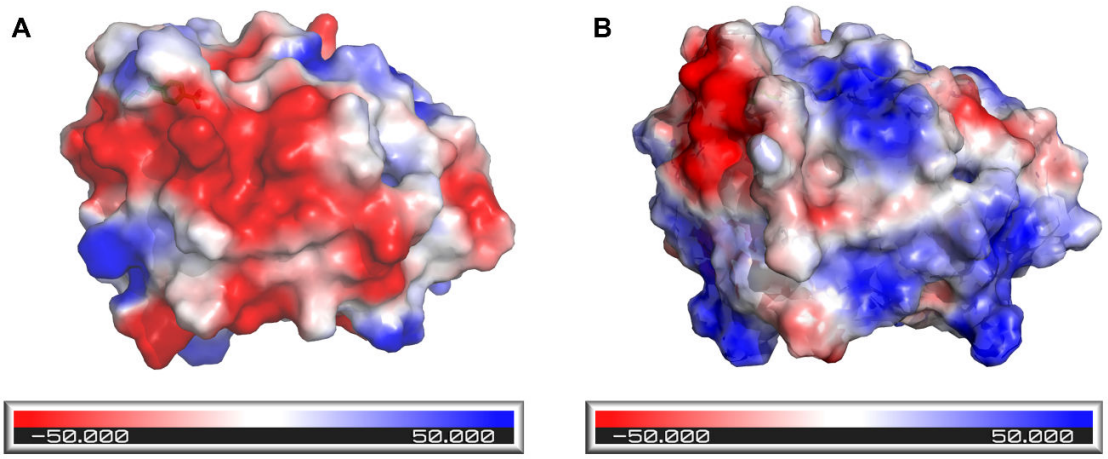


Figure S8. Electrostatic surfaces of PES-H1 (A) and LCC ICCG (B). Red areas indicate negatively charged residues whereas blue areas represent positively charged residues (-50 kT/e to +50 kT/e). The images were generated using PyMOL.

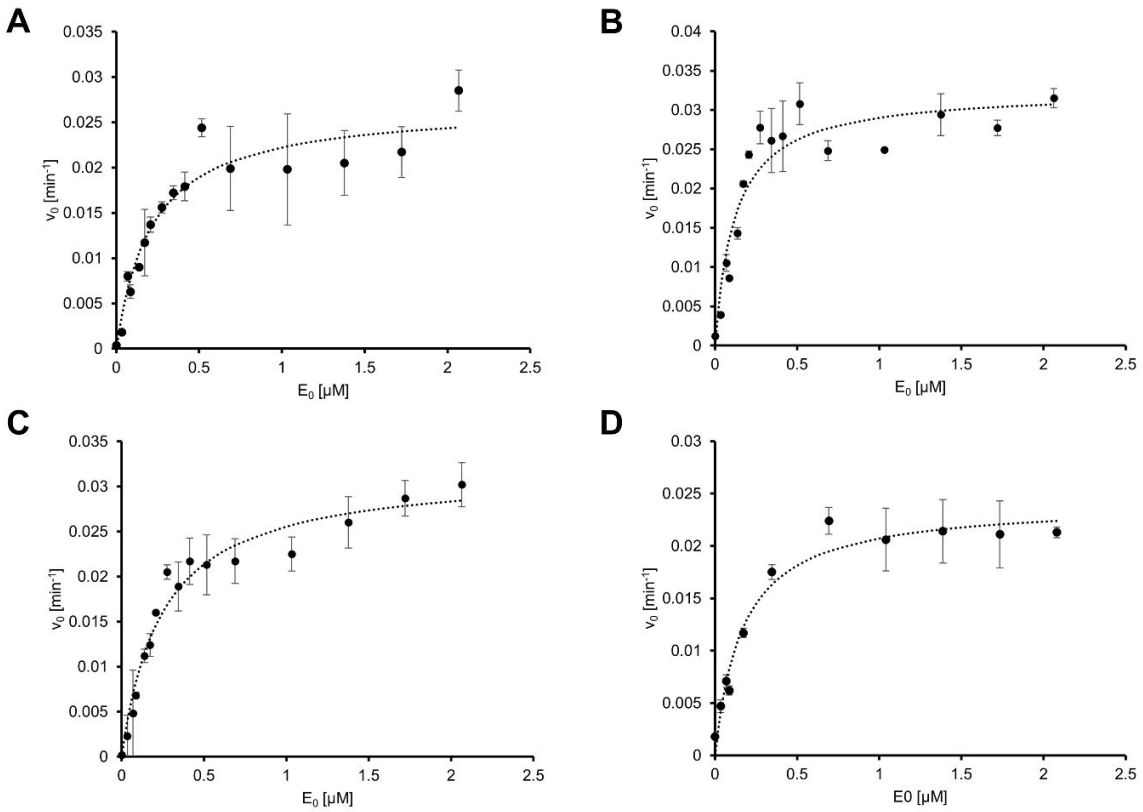


Figure S9. Hydrolysis of PET-NP by (A) PES-H1, (B) the L92F/Q94Y variant, (C) the R204C/S250C variant, and (D) LCC ICCG. The initial PET hydrolysis rates were determined by a turbidimetric assay by measuring apparent absorbance of light at 600 nm in a microtiter plate reader. Reactions in 1 M potassium phosphate buffer (pH 8.0) contained 0.5 mg mL^{-1} PET-NP and 0-2 μM enzyme and were incubated at 70 °C. Data points represent the averages and error bars the standard deviations calculated from three replicates. The fitted data are shown as dotted curves.

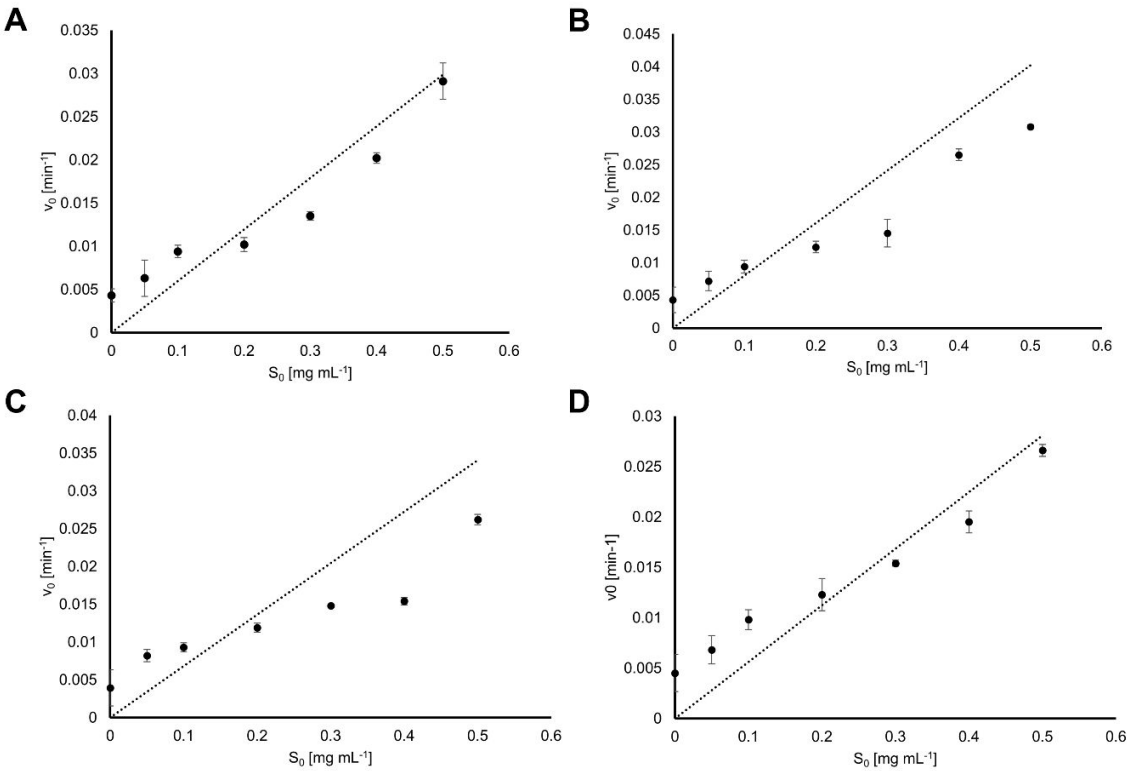


Figure S10. Hydrolysis of PET-NP by (A) PES-H1, (B) the L92F/Q94Y variant, (C) the R204C/S250C variant, and (D) LCC ICCG. The initial PET hydrolysis rates were determined by a turbidimetric assay by measuring apparent absorbance of light at 600 nm in a microtiter plate reader. Reactions in 1 M potassium phosphate buffer (pH 8.0) contained 0.7 μM enzyme and 0-0.5 mg mL^{-1} PET-NP and were incubated at 70 °C. Data points represent the averages and error bars the standard deviations calculated from three replicates. The fitted data are shown as dotted lines.

REFERENCES

(1) Otwinowski, Z.; Minor, W. [20] Processing of X-Ray Diffraction Data Collected in Oscillation Mode. In *Methods in Enzymology*; Elsevier, **1997**; Vol. 276, pp 307–326.

(2) McCoy, A. J.; Grosse-Kunstleve, R. W.; Adams, P. D.; Winn, M. D.; Storoni, L. C.; Read, R. J. *Phaser* Crystallographic Software. *J. Appl. Crystallogr.* **2007**, *40* (4), 658–674.

(3) Liebschner, D.; Afonine, P. V.; Baker, M. L.; Bunkóczi, G.; Chen, V. B.; Croll, T. I.; Hintze, B.; Hung, L.-W.; Jain, S.; McCoy, A. J.; Moriarty, N. W.; Oeffner, R. D.; Poon, B. K.; Prisant, M. G.; Read, R. J.; Richardson, J. S.; Richardson, D. C.; Sammito, M. D.; Sobolev, O. V.; Stockwell, D. H.; Terwilliger, T. C.; Urzhumtsev, A. G.; Videau, L. L.; Williams, C. J.; Adams, P. D. Macromolecular Structure Determination Using X-Rays, Neutrons and Electrons: Recent Developments in *Phenix*. *Acta Crystallogr. D. Struct. Biol.* **2019**, *75* (10), 861–877.

(4) Han, X.; Liu, W.; Huang, J.-W.; Ma, J.; Zheng, Y.; Ko, T.-P.; Xu, L.; Cheng, Y.-S.; Chen, C.-C.; Guo, R.-T. Structural Insight into Catalytic Mechanism of PET Hydrolase. *Nat. Commun.* **2017**, *8* (1), 2106.

(5) Afonine, P. V.; Grosse-Kunstleve, R. W.; Echols, N.; Headd, J. J.; Moriarty, N. W.; Mustyakimov, M.; Terwilliger, T. C.; Urzhumtsev, A.; Zwart, P. H.; Adams, P. D. Towards Automated Crystallographic Structure Refinement with *Phenix.Refine*. *Acta Crystallogr. D. Biol. Crystallogr.* **2012**, *68* (4), 352–367.

(6) Emsley, P.; Cowtan, K. *Coot*: Model-Building Tools for Molecular Graphics. *Acta Crystallogr. D. Biol. Crystallogr.* **2004**, *60* (12), 2126–2132.

(7) Brünger, A. T.; Adams, P. D.; Clore, G. M.; DeLano, W. L.; Gros, P.; Grosse-Kunstleve, R. W.; Jiang, J. S.; Kuszewski, J.; Nilges, M.; Pannu, N. S.; Read, R. J.; Rice, L. M.; Simonson,

T.; Warren, G. L. Crystallography & NMR System: A New Software Suite for Macromolecular Structure Determination. *Acta Crystallogr. D. Biol. Crystallogr.* **1998**, *54* (5), 905–921.

(8) *The PyMOL Molecular Graphics System, Version 1.8,* **2015**. *Schrödinger, LLC.*

(9) Wang, J.; Wolf, R. M.; Caldwell, J. W.; Kollman, P. A.; Case, D. A. Development and Testing of a General Amber Force Field. *J. Comput. Chem.* **2004**, *25* (9), 1157–1174.

(10) M.J. Frisch, G.W. Trucks, H.B. Schlegel, G.E. Scuseria, M.A. Robb, J.R. Cheeseman, G. Scalmani, V. Barone, B. Mennucci, G.A. Petersson, H. Nakatsuji, M. Caricato, X. Li, H.P. Hratchian, A.F. Izmaylov, J. Bloino, G. Zheng, J.L. Sonnenberg, M. Hada, M. Ehara, K. Toyota, R. Fukuda, J. Hasegawa, M. Ishida, T. Nakajima, Y. Honda, O. Kitao, H. Nakai, T. Vreven, J.A. Montgomery, J.E. Peralta, F. Ogliaro, M. Bearpark, J.J. Heyd, E. Brothers, K.N. Kudin, V.N. Staroverov, R. Kobayashi, J. Normand, K. Raghavachari, A. Rendell, J.C. Burant, S.S. Iyengar, J. Tomasi, M. Cossi, N. Rega, J.M. Millam, M. Klene, J.E. Knox, J.B. Cross, V. Bakken, C. Adamo, J. Jaramillo, R. Gomperts, R.E. Stratmann, O. Yazyev, A.J. Austin, R. Cammi, C. Pomelli, J.W. Ochterski, R.L. Martin, K. Morokuma, V.G. Zakrzewski, G.A. Voth, P. Salvador, J.J. Dannenberg, S. Dapprich, A.D. Daniels, Ö. Farkas, J.B. Foresman, J.V. Ortiz, J. Cioslowski, and D.J. Fox. Gaussian 09. Revision E.01, Gaussian Inc., Wallingford CT. **2009**.

(11) Bayly, C. I.; Cieplak, P.; Cornell, W.; Kollman, P. A. A Well-Behaved Electrostatic Potential Based Method Using Charge Restraints for Deriving Atomic Charges: The RESP Model. *J. Phys. Chem.* **1993**, *97* (40), 10269–10280.

(12) Cornell, W. D.; Cieplak, P.; Bayly, C. I.; Kollman, P. A. Application of RESP Charges to Calculate Conformational Energies, Hydrogen Bond Energies, and Free Energies of Solvation. *J. Am. Chem. Soc.* **1993**, *115* (21), 9620–9631.

(13) Wang, J.; Wang, W.; Kollman, P. A.; Case, D. A. Antechamber, An Accessory Software Package For Molecular Mechanical Calculations. *J. Am. Chem. Soc.* **2001**, 222.

(14) Wang, J.; Wang, W.; Kollman, P. A.; Case, D. A. Automatic Atom Type and Bond Type Perception in Molecular Mechanical Calculations. *J. Mol. Graph. Model.* **2006**, *25* (2), 247–260.

(15) K. Belfon, I.Y. Ben-Shalom, S.R. Brozell, D.S. Cerutti, T.E. Cheatham III, G.A. Cisneros, V.W.D. Cruzeiro, T.A. Darden, R.E. Duke, G. Giambasu, M.K. Gilson, H. Gohlke, A.W. Goetz, R. Harris, S. Izadi, S.A. Izmailov ,C. Jin K. Kasavajhala, M.C. Kaymak ,E. King, A. Kovalenko, T. Kurtzman, T.S. Lee, S. LeGrand, P. Li, C. Lin, J. Liu, T. Luchko, R. Luo, M. Machado, V. Man, M. Manathunga, K.M. Merz ,Y. Miao, O. Mikhailovskii, G. Monard, H. Nguyen, K.A. O'Hearn, A. Onufriev, F. Pan, S. Pantano, R. Qi A. Rahnamoun, D.R. Roe, A. Roitberg, C. Sagui, S. Schott- Verdugo, J. Shen ,C.L. Simmerling, N.R. Skrynnikov, J. Smith, J. Swails, R.C. Walker, J. Wang, H. Wei, R.M. Wolf, X. Wu, Y. Xue, D.M. York, S. Zhao, P.A. Kollman, D.A. Case, H.M. Aktulga. *Amber 2021*; University of California, San Francisco, **2021**.

(16) Abraham, M. J.; Murtola, T.; Schulz, R.; Páll, S.; Smith, J. C.; Hess, B.; Lindahl, E. GROMACS: High Performance Molecular Simulations through Multi-Level Parallelism from Laptops to Supercomputers. *SoftwareX* **2015**, *1–2*, 19–25.

(17) Maier, J. A.; Martinez, C.; Kasavajhala, K.; Wickstrom, L.; Hauser, K. E.; Simmerling, C. Ff14SB: Improving the Accuracy of Protein Side Chain and Backbone Parameters from Ff99SB. *J. Chem. Theory Comput.* **2015**, *11* (8), 3696–3713.

(18) Ivani, I.; Dans, P. D.; Noy, A.; Pérez, A.; Faustino, I.; Hospital, A.; Walther, J.; Andrio, P.; Goñi, R.; Balaceanu, A.; Portella, G.; Battistini, F.; Gelpí, J. L.; González, C.; Vendruscolo, M.; Laughton, C. A.; Harris, S. A.; Case, D. A.; Orozco, M. Parmbsc1: A Refined Force Field for DNA Simulations. *Nat. Methods* **2016**, *13* (1), 55–58.

(19) Jorgensen, W. L.; Chandrasekhar, J.; Madura, J. D.; Impey, R. W.; Klein, M. L. Comparison of Simple Potential Functions for Simulating Liquid Water. *J. Chem. Phys* **1983**, *79* (2), 926–935.

(20) Cauchy, M. A. Méthode Générale Pour La Résolution Des Systemes d'équations Simultanées. *CR Hebd. Acad. Sci.* **1847**, No. 25, 536–538.

(21) Nosé, S. A Molecular Dynamics Method for Simulations in the Canonical Ensemble. *Mol. Phys.* **1984**, *52* (2), 255–268.

(22) Hoover, W. G. Canonical Dynamics: Equilibrium Phase-Space Distributions. *Phys. Rev. A* **1985**, *31* (3), 1695–1697.

(23) Parrinello, M.; Rahman, A. Polymorphic Transitions in Single Crystals: A New Molecular Dynamics Method. *J. Appl. Phys.* **1981**, *52* (12), 7182–7190.

(24) Darden, T.; York, D.; Pedersen, L. Particle Mesh Ewald: An $N \cdot \log(N)$ Method for Ewald Sums in Large Systems. *J. Chem. Phys.* **1993**, *98* (12), 10089–10092.

(25) Essmann, U.; Perera, L.; Berkowitz, M. L.; Darden, T.; Lee, H.; Pedersen, L. G. A Smooth Particle Mesh Ewald Method. *J. Chem. Phys.* **1995**, *103* (19), 8577–8593.

(26) Hess, B.; Bekker, H.; Berendsen, H. J. C.; Fraaije, J. G. E. M. LINCS: A Linear Constraint Solver for Molecular Simulations. *J. Comput. Chem.* **1997**, *18* (12), 1463–1472.

(27) Daura, X.; Gademann, K.; Jaun, B.; Seebach, D.; van Gunsteren, W. F.; Mark, A. E. Peptide Folding: When Simulation Meets Experiment. *Angew. Chem. Int. Ed.* **1999**, *38* (1–2), 236–240.

(28) Humphrey, W.; Dalke, A.; Schulten, K. VMD: Visual Molecular Dynamics. *J. Mol. Graph.* **1996**, *14* (1), 33–38.

(29) Studier, F. W. Protein Production by Auto-Induction in High-Density Shaking Cultures. *Protein Expression Purif.* **2005**, *41* (1), 207–234.

(30) Zimmermann, W.; Wei, R.; Hille, P.; Oeser, T.; Schmidt, J. New Polypeptides Having a Polyester Degrading Activity and Uses Thereof. EP3517608A1, July 31, **2019**.

(31) Palm, G. J.; Reisky, L.; Böttcher, D.; Müller, H.; Michels, E. A. P.; Walczak, M. C.; Berndt, L.; Weiss, M. S.; Bornscheuer, U. T.; Weber, G. Structure of the Plastic-Degrading *Ideonella sakaiensis* MHETase Bound to a Substrate. *Nat. Commun.* **2019**, *10* (1), 1717.

(32) Brott, S.; Pfaff, L.; Schuricht, J.; Schwarz, J.; Böttcher, D.; Badenhorst, C. P. S.; Wei, R.; Bornscheuer, U. T. Engineering and Evaluation of Thermostable *Is*PETase Variants for PET Degradation. *Eng. Life Sci.* **2021**, *22* (3-4), 192-203

(33) Pfaff, L.; Breite, D.; Badenhorst, C. P. S.; Bornscheuer, U. T.; Wei, R. Fluorimetric High-Throughput Screening Method for Polyester Hydrolase Activity Using Polyethylene Terephthalate Nanoparticles. In *Methods in Enzymology*; Elsevier, 2021; Vol. 648, pp 253–270.

(34) Vogel, K.; Wei, R.; Pfaff, L.; Breite, D.; Al-Fathi, H.; Ortmann, C.; Estrela-Lopis, I.; Venus, T.; Schulze, A.; Harms, H.; Bornscheuer, U. T.; Maskow, T. Enzymatic Degradation of

Polyethylene Terephthalate Nanoplastics Analyzed in Real Time by Isothermal Titration Calorimetry. *Sci. Total Environ.* **2021**, *773*, 145111.

(35) Belisário-Ferrari, M. R.; Wei, R.; Schneider, T.; Honak, A.; Zimmermann, W. Fast Turbidimetric Assay for Analyzing the Enzymatic Hydrolysis of Polyethylene Terephthalate Model Substrates. *Biotechnol. J.* **2019**, *14* (4), 1800272.

(36) Ronkvist, Å. M.; Xie, W.; Lu, W.; Gross, R. A. Cutinase-Catalyzed Hydrolysis of Poly(Ethylene Terephthalate). *Macromolecules* **2009**, *42* (14), 5128–5138.

(37) Scandola, M.; Focarete, M. L.; Frisoni, G. Simple Kinetic Model for the Heterogeneous Enzymatic Hydrolysis of Natural Poly(3-Hydroxybutyrate). *Macromolecules* **1998**, *31* (12), 3846–3851.

(38) Wei, R.; Oeser, T.; Barth, M.; Weigl, N.; Lübs, A.; Schulz-Siegmund, M.; Hacker, M. C.; Zimmermann, W. Turbidimetric Analysis of the Enzymatic Hydrolysis of Polyethylene Terephthalate Nanoparticles. *J. Mol. Catal., B-Enzym* **2014**, *103*, 72–78.

(39) Wei, R.; Breite, D.; Song, C.; Gräsing, D.; Ploss, T.; Hille, P.; Schwerdtfeger, R.; Matysik, J.; Schulze, A.; Zimmermann, W. Biocatalytic Degradation Efficiency of Postconsumer Polyethylene Terephthalate Packaging Determined by Their Polymer Microstructures. *Adv. Sci.* **2019**, *6* (14), 1900491.

bioRxiv preprint doi: https://doi.org/10.1101/2024.04.21.590457; this version posted April 21, 2024. The copyright holder for this preprint (which was not certified by peer review) is the author/funder. All rights reserved. No reuse allowed without permission.

From Bulk to Binding: Decoding the Entry of PET into Hydrolase Binding Pockets

Anna Jäckering,[†,‡] Frederike Göttsch,[¶] Moritz Schäffler,[†,‡] Mark Doerr,[¶] Uwe T. Bornscheuer,[¶] Ren Wei,[¶] and Birgit Strodel[*,†,‡]

†*Institute of Theoretical and Computational Chemistry, Heinrich Heine University, Düsseldorf, Universitätsstr. 1, 40225 Düsseldorf, Germany*

‡*Institute of Biological Information Processing: Structural Biochemistry (IBI-7), Forschungszentrum Jülich, Wilhelm-Johnen-Straße, 52428 Jülich, Germany*

¶*Department of Biotechnology & Enzyme Catalysis, Institute of Biochemistry, University of Greifswald, Felix-Hausdorff-Str. 4, 17487 Greifswald, Germany*

E-mail: b.strodel@fz-juelich.de

Abstract

Plastic-degrading enzymes hold promise for biocatalytic recycling of poly(ethylene terephthalate) (PET), a key synthetic polymer. Despite their potential, the current activity of PET hydrolases is not sufficient for industrial use. To unlock their full potential, a deep mechanistic understanding followed by protein engineering is required. Using cutting-edge molecular dynamics simulations and free energy analysis methods, we uncover the entire pathway from the initial binding of two PET hydrolases – the thermophilic leaf-branch compost cutinase (LCC) and polyester hydrolase 1 (PES-H1) – to an amorphous PET material to a PET chain entering the active site and adopting a hydrolyzable geometry. Our results reveal the initial PET binding and elucidate its non-specific nature driven by electrostatic and hydrophobic forces. Upon PET entry into the active site, we

bioRxiv preprint doi: https://doi.org/10.1101/2024.04.21.590457; this version posted April 21, 2024. The copyright holder for this preprint (which was not certified by peer review) is the author/funder. All rights reserved. No reuse allowed without permission.

uncover that this process can occur via one of three key pathways and detect barriers to it arising from both PET–PET and PET–enzyme interactions, with specific residues identified by *in silico* and *in vitro* mutagenesis. These insights not only advance our understanding of PET degradation mechanisms and pave the way for targeted enzyme enhancement strategies, but also offer an innovative approach applicable to enzyme studies across disciplines.

1 Introduction

The plastic consumption of our society exhibits an escalating trajectory with each passing year, accompanied by a commensurate escalation in the volume of plastic waste that necessitates recycling.[1] However, the efficiency of plastic recycling remains suboptimal, in particular for composite materials. But even when dealing with a high degree of homogeneity in a given plastic, the employed recycling methodologies are invariably accompanied by significant greenhouse gas emissions.[2] For this reason, the quest for an environmentally-friendly enzymatic depolymerization process of plastic waste that allow for the monomer recovery has attracted attention, especially for the widely used polymer poly(ethylene terephthalate) (PET).[3–6]

PET is an aromatic, semicrystalline thermoplastic that can be enzymatically degraded into monomeric and oligomeric building blocks including 2-hydroxyethylterephthalic acid (MHET), which can then be further hydrolyzed into its monomers terephthalic acid (TPA) and ethylene glycol (EG) by the same or different enzymes.[4,7–9] The monomers can be recovered to synthesize high quality virgin PET (Fig. 1).[3,10] In 2005, enzymatic degradation of low-crystallinity PET, which resulted in a significant mass loss, has been reported for the first time with a *Thermobifida fusca* hydrolase.[11] Afterwards, many other ester hydrolases (EC 3.1.1.x) were found to be capable of degrading PET, which were assigned to the novel subclass for PETases (EC 3.1.1.101).[12] A milestone in microbial PET degradation was achieved eleven years later with the discovery of *Ideonella sakaiensis*, which features a two-enzyme

bioRxiv preprint doi: https://doi.org/10.1101/2024.04.21.590457; this version posted April 21, 2024. The copyright holder for this preprint (which was not certified by peer review) is the author/funder. All rights reserved. No reuse allowed without permission.

system for the depolymerization of PET and its degradation products as the main source of carbon and energy for the bacterial growth.[13] However, the activity and thermostability of wild-type (WT) PET hydrolases are often insufficient for their industrial application. To this end, diverse PET hydrolases such as the leaf-branch-compost cutinase (LCC) and the polyester hydrolase 1 (PES-H1) have been recently engineering yielding two of the currently most active and thermostable PET hydrolases, the LCC F243I/D238C/S283C/Y127G (ICCG) variant[3] and the PES-H1 L92F/Q94Y (FY) variant.[14] In particular, the development of LCC^{ICCG} by the French company Carbios enabled the launch of a first enzymatic PET recycling demonstration plant, initiating the evaluation of its pre-industrial-scale recycling process, which involves 100 tons of pretreated PET waste per year.[3,15,16] The increased thermal stability of LCC^{ICCG} allowed for its application in the temperature range of 68-72°C, where the PET polymers gain high mobility and are easily accessible to the enzymes.[3,4,17–19] At the same time, amorphous PET can recrystallize quickly in the aqueous milieu at temperatures above 72°C, necessitating rapid kinetics of enzymatic PET degradation when used in this temperature range, which remains a significant challenge for enzyme engineering.[3]

To make further progress here, a deeper understanding of the entire PET degradation process is required. This process consists of initial adsorption of the enzyme to the PET bulk, followed by a single PET chain from this bulk entering the active site of the PET hydrolase and assuming a binding position productive for subsequent hydrolysis. It was suggested that the PET hydrolases adsorb non-specifically on the surface of the PET bulk, resulting in either a productive complex that enables PET degradation by binding close to the active site, or in an unproductive complex that cannot hydrolyze PET.[20,21] Therefore, previous engineering studies have focused on modifying general surface properties such as charge, polarity and hydrophobicity of the PET hydrolases to improve PET adsorption.[22] Increased PET adsorption was observed after the introduction of positive charges[23,24] and increased hydrophobicity of the enzyme surface.[25–28] However, according to the Sabatier principle, optimal catalysis occurs when interactions between catalyst and substrate are of

bioRxiv preprint doi: https://doi.org/10.1101/2024.04.21.590457; this version posted April 21, 2024. The copyright holder for this preprint (which was not certified by peer review) is the author/funder. All rights reserved. No reuse allowed without permission.

intermediary strength. For LCC it was demonstrated that its activity increased when its substrate affinity is weakened due to addition of a cationic surfactant.[29] Thus, the optimal balance between binding affinity and activity of PET hydrolases remains unclear, necessitating a thorough examination of the initial PET adsorption process and the transition from non-specific adsorption to a productive PET binding mode at the active site. Therefore, it is not yet clear how to optimize the relationship between binding affinity and activity of PET hydrolases, which requires a detailed analysis of the initial PET adsorption and transition from adsorption far from the active site to productive PET binding.

Most design approaches target the formation of the substrate–enzyme complex that takes place in the catalytic binding cleft to enhance the activity of PET hydrolases. Many studies have introduced substitutions inspired by comparing the amino acid composition of different PET hydrolases in the active site, resulting in the PES-H1^{FY} variant, which was motivated by the thermostable DuraPETase.[14,30] Computational methods offer insights into the importance of specific residues in the binding site, which complements the limited high-resolution crystal structures of PET hydrolase with small ligands reported recently.[9,14,23,31–35] Based on the analysis of these structural complexes, it was hypothesized that widening the binding cleft would increase the accessibility of the active site and consequently the enzyme's activity,[36–39] while narrowing the binding site could enable specific interactions with PET that promote substrate binding and enzyme activity.[40] Since PET is an aromatic, mostly hydrophobic polymer that can form hydrogen bonds, it has been shown that the introduction of aromatic, hydrophobic or hydrogen bond-forming residues also has a positive effect on the efficiency of PET hydrolases.[37,39,41,42] A highly conserved tryptophan that flanks the binding cleft and appears to be crucial for enabling PET degradation deserves special mention. Its flexibility diverges between mesophilic and thermophilic enzymes that harbor different amino acids in the neighborhood of the tryptophan, which influences its 'wobbling' capacity.[35,43–45] Nevertheless, not all results are consistent with respect to the factors that promote productive PET binding, indicating that further analysis is needed to identify con-

bioRxiv preprint doi: https://doi.org/10.1101/2024.04.21.590457; this version posted April 21, 2024. The copyright holder for this preprint (which was not certified by peer review) is the author/funder. All rights reserved. No reuse allowed without permission.

sistent characteristics that support productive binding. Furthermore, the computational methods in the previous studies comprise mainly docking[3,35,36,46,47] in combination with short molecular dynamics (MD) simulations.[14,40,48–51] However, the dynamics of the binding process, which is composed of the flexibility of the binding site itself and the PET as well as the process of PET entry into the active site, cannot be adequately described by these methods, yet they have been suggested to be important factors for PET complexation and thus degradation.[4,48,49,52–54]

To fill this knowledge gap, we performed thorough computational simulations in combination with experimental studies on two metagenome-derived thermophilic PET hydrolases, LCC (catalytic triad: S165, D210, H242) and PES-H1 (catalytic triad: S130, D176, H208). To be precise, we subjected both enzymes to extensive MD as well as Hamiltonian replica exchange MD (HREMD) simulations to elucidate their adsorption to a PET bulk, tracking PET entry into the active site until PET binds in a productive mode to allow for hydrolysis. PET entry is analyzed using a free energy surface-based approach to reveal residues that affect the energy barrier during the entry process, whereupon residue substitutions are predicted and then evaluated *in vitro*. Our approach is the first to show how PET reaches the active site, uncovering important information about the dynamics of both the enzyme and PET, as well as the interactions between polymer and enzyme.

2 Results and discussion

To investigate the entire interfacial biocatalysis process, starting with the enzymes LCC and PES-H1 binding to a PET bulk and ending with a PET chain in the active site ready for hydrolysis, we began our study by placing both LCC and PES-H1 in random orientations and at least 10 Å away from an amorphous PET bulk. The structure of the PET bulk was based on Cruz-Chu *et al.*[55] including 100 PET-9mers(Fig. 1). Subsequently, we conducted a total of 10.5 µs of MD simulations for each enzyme. In these simulations, we observed enzyme

bioRxiv preprint doi: https://doi.org/10.1101/2024.04.21.590457; this version posted April 21, 2024. The copyright holder for this preprint (which was not certified by peer review) is the author/funder. All rights reserved. No reuse allowed without permission.

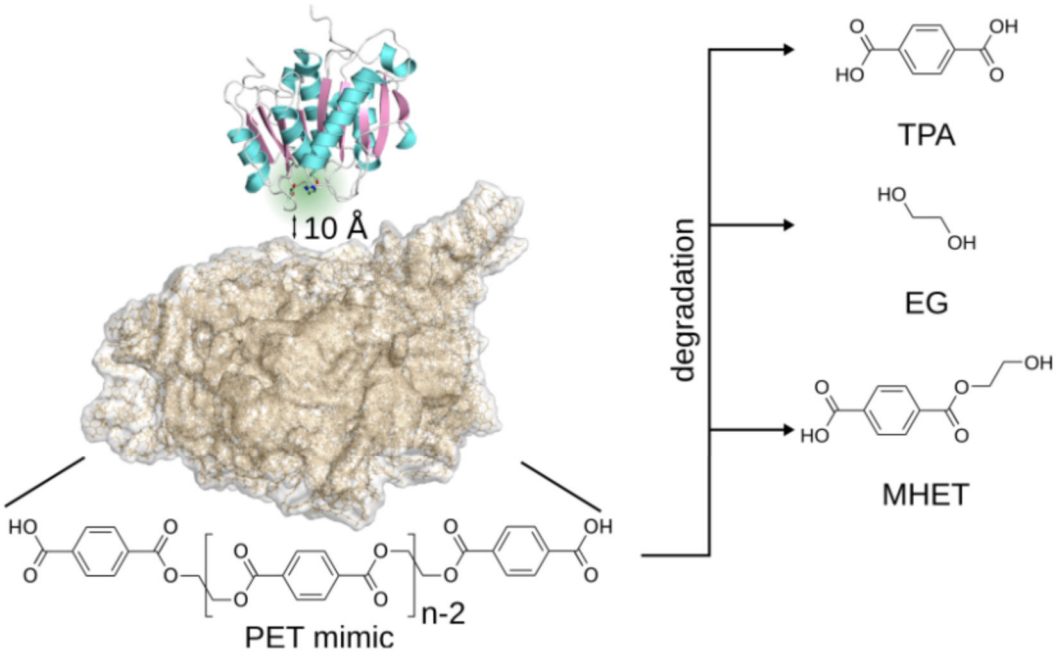


Figure 1: Representative starting structure for the MD simulations of enzyme adsorption on amorphous PET (without water and ions being shown). The system comprises one PET hydrolase, which is shown as cartoon and with the catalytic triad highlighted in green. The enzyme was randomly oriented and placed at least 10 Å away from the PET bulk, which is shown as brown surface and consists of 100 PET-9mers. The chemical structure of PET is shown at the bottom and the degradation products of PET, terephthalic acid (TPA), ethylene glycol (EG), and 2-hydroxyethyl terephthalic acid (MHET), are shown on the right.

adsorption on the PET surface at sites proximal and distal to the binding cleft during 75% of the simulation time, but the PET failed to enter into the active site. Therefore, we continued the simulations by applying the enhanced-sampling HREMD method (accumulating further 43.47 µs of sampling per enzyme). We used only one single PET chain closest to the binding cleft allowing PET to enter the active site and adopt productive binding poses. The results of these two sets of simulations are discussed in detail below along with the wet lab studies to consolidate our *in silico* findings.

2.1 PET adsorption to the surface of the enzyme

Both enzymes readily adsorb to PET, but without a strong preference for the binding cleft Adsorption to the PET bulk was sampled in all six of the 1.5 µs simulations

bioRxiv preprint doi: https://doi.org/10.1101/2024.04.21.590457; this version posted April 21, 2024. The copyright holder for this preprint (which was not certified by peer review) is the author/funder. All rights reserved. No reuse allowed without permission.

for both LCC and PES-H1. In addition, the initial enzyme–PET interactions of considerable strength with energies below $-10\,\mathrm{kcal{\cdot}mol^{-1}}$ were established early in the simulations (PES-H1: 2.0–40.2 ns; LCC: 0.8–15.0 ns) and abundant contacts (defined based on the residue–PET distance requirement ≤ 3 Å) were observed at the surfaces of LCC and PES-H1, suggesting that initial binding is based on general features such as charge and polarity rather than specific recognition sites.[56–58] These initial contacts occurred almost everywhere on the surface of both enzymes and can be divided into proximal and distal binding, depending on whether PET was located within 12 Å of the catalytic serine or not. These contact areas are colored blue and red in Fig. 2A, respectively, and the regions where distal and proximal areas overlap are indicated in purple. To follow the progression of the contacts during the simulations, we compared the contact areas during the first 50 ns and the remaining simulation time. However, only limited reorientations of the enzymes on the PET surface were observed (shown in yellow for newly explored surface and in brown for overlaps with only distal or proximal in Fig. 2A); most contacts remained unchanged for 75% or more of the simulation time. In the case of proximal binding at the end of the simulations, we extended the corresponding simulations to 2 µs to see if further PET progression towards the active site would occur. The general findings for both, simulations lasting for 1.5 µs and the elongated simulations lasting for 2 µs, are that when the initial contacts were established in proximal regions, the PET contact area remained close to the active site (PES-H1: 2 of 6; LCC: 4 of 6 simulations). In cases where the initial contacts were in distal areas, negligible progression towards the active site was observed. Only in one of the PES-H1 simulations, proximal contacts could be established starting from distal ones (highlighted in yellow and overlaps with regions establishing distal or proximal contact only in orange in Fig. 2A). The observed contact progression towards proximal binding in one of the PES-H1 simulations might contribute to the high activity of this enzyme.

If this is the case, a promising way to achieve accelerated and productive PET binding could be to facilitate enhanced proximal binding while attenuating PET interactions at distal

bioRxiv preprint doi: https://doi.org/10.1101/2024.04.21.590457; this version posted April 21, 2024. The copyright holder for this preprint (which was not certified by peer review) is the author/funder. All rights reserved. No reuse allowed without permission.

sites of the enzyme surfaces. To test this hypothesis, we first analyzed the physicochemical nature of the initial enzyme–PET contacts and then made rationally motivated mutations, which are studied *in silico* and *in vitro*.

Negative surface charges impede PET adsorption LCC has a net charge of +5, while PES-H1 has a net charge of −5, which is reflected in their electrostatic potential surface (EPS, shown in Fig. 2B). The EPS of LCC is mostly neutral and positive (shown in white and blue, respectively), while PES-H1 features large surface patches that are strongly negative (shown in red). For PES-H1 in particular, the negative regions overlap with those that do not have pronounced PET contacts. In addition, we visualized the EPS of the PET bulk used to construct the initial enzyme–PET systems. A mostly hydrophobic surface is revealed, with predominantly convex and exposed areas being partially negatively charged, while stronger positive or negative potentials can be found in concave and buried regions (Fig. S2). We therefore assume that negative charges at the surface discourage PET binding, which could open up the possibility of preventing distal binding to PET by introducing negatively charged residues there. This idea is consistent with the results of Nakamura *et al.*, who demonstrated accelerated binding to PET surfaces with higher positive charge density at the enzyme surface of PET2.[23] In addition, Sagong *et al.* found that changes in the electrostatic potential surface of a loop close to the active site increases PET degradation activity of *Rhizobacter gummiphilus* PETase (*Rg*PETase), especially when increasing the negative surface charge.[59] In order to transfer this finding from proximal regions to distal ones, they mutated four distal surface-exposed arginine to alanine and glutamate, which also increases the PET degradation activity.

bioRxiv preprint doi: https://doi.org/10.1101/2024.04.21.590457; this version posted April 21, 2024. The copyright holder for this preprint (which was not certified by peer review) is the author/funder. All rights reserved. No reuse allowed without permission.

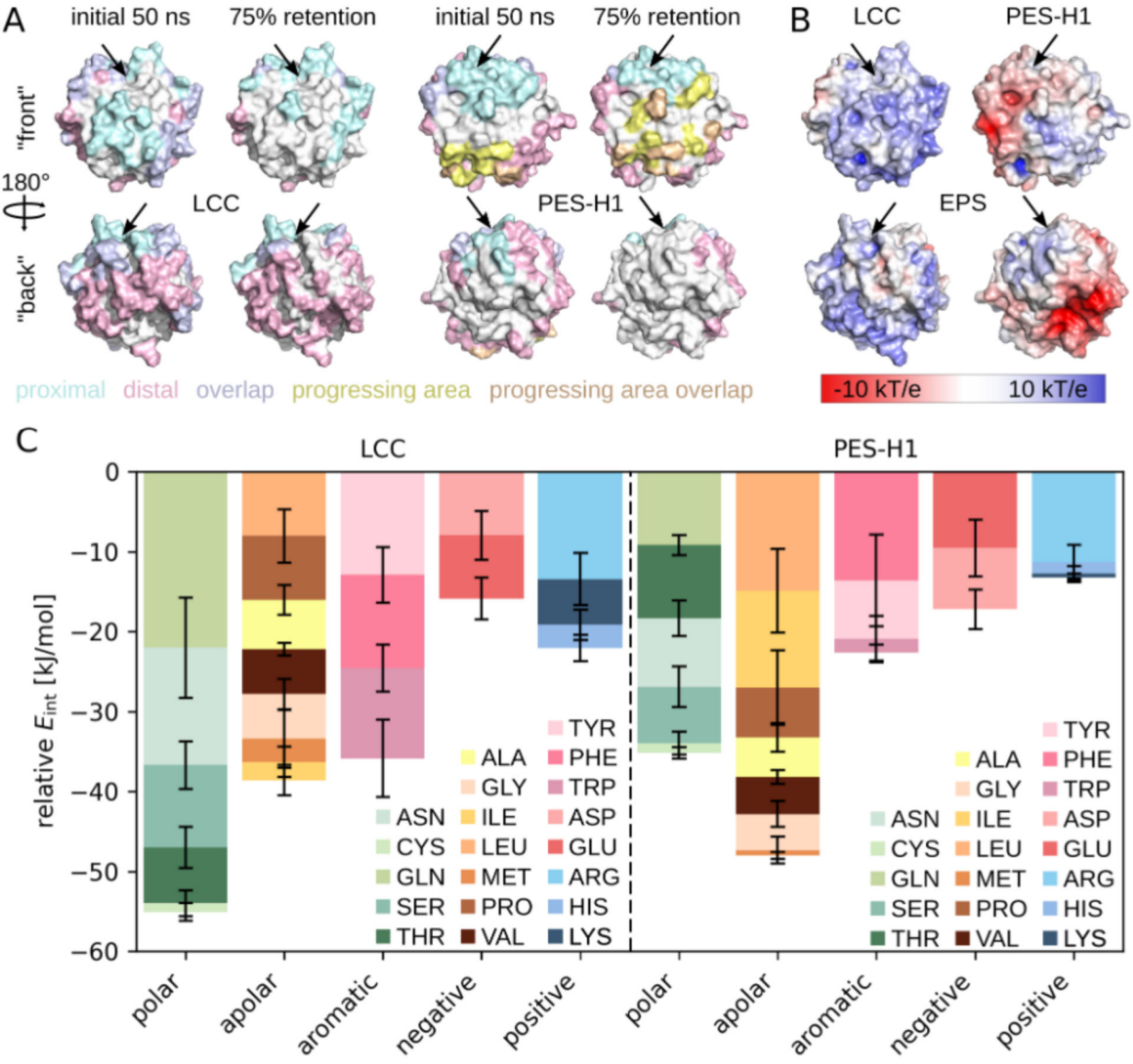


Figure 2: Analysis of LCC (left) and PES-H1 (right) adsorption on amorphous PET. (A) Residues contacting PET are highlighted on enzyme surfaces, using all six simulations per enzyme with a 3 Å PET–residue distance cutoff. Contacts during initial 50 ns (left) and stable contacts present for at least 75% of the full duration (right) are distinguished, with proximal (blue) and distal (rose) binding sites. Overlapping areas are colored violet. Some simulations show enzyme reorientation on PET bulk, with limited progression from distal to proximal binding, except in one PES-H1 simulation (highlighted in yellow). Overlaps with proximal or distal contact areas highlighted in brown. The position of the catalytic triad is denoted by an arrow. (B) Electrostatic potential surface (EPS) for LCC (left, net charge: +5) and PES-H1 (right, net charge: −5). (C) PET interaction energies E_{int} with amino acid types in LCC and PES-H1 are shown relative to the number of the corresponding residues within 3 Å, averaged over all simulations. Energies for amino acid types with the same physicochemical characteristics are summed up, with standard error of the mean (SEM) shown as error bars.

bioRxiv preprint doi: https://doi.org/10.1101/2024.04.21.590457; this version posted April 21, 2024. The copyright holder for this preprint (which was not certified by peer review) is the author/funder. All rights reserved. No reuse allowed without permission.

This effect was more pronounced when introducing glutamate, from which they conclude that a negative surface charge is favorable for the PET degradation activity of *Rg*PETase. Moreover, Thomsen *et al.* observed that PES-H1 creates craters on the PET surface, unlike other enzymes such as LCC exhibiting a uniform degradation.[21] They ascribe this distinct behavior in PES-H1 to its the distal negative surface patch influencing enzyme positioning and processivity after the initial contact due to repulsion with the negatively charged PET termini. We thus conclude that positive regions enhance overall PET adsorption and lead to prolonged PET retention in distal regions when present there, which in turn hinders the process of PET binding in a productive conformation at the active site.

Apolar residues contribute most to PET adsorption of PES-H1 To identify the amino acids most favored by PET, we calculated the interaction energy E_{int} between PET and each amino-acid type for all six simulations of both enzymes. We then scaled the resulting energy values by the number of residues of the corresponding amino-acid type that were in contact with PET during each simulation and took the average of the six values. These results are shown in Fig. 2C, where we grouped the amino acids according to their physicochemical property. The scaling by the contact residues accounts for the fact that more polar than apolar residues are exposed in both enzymes, making them more accessible to PET than apolar residues. The overall interaction with PET (i.e., the sum of all scaled E_{int} values) is stronger for LCC than for PES-H1, with polar residues contributing most to LCC binding and apolar contributing most to PES-H1 binding. Charged amino acids contribute the least to PET binding for both enzymes, followed by the aromatic ones. Given the progression from distal to proximal binding observed for PES-H1 but not for LCC in this study, we propose that modification of the surface of LCC to make it more similar to that of PES-H1 could increase proximal PET binding for LCC and thus its enzymatic activity. Based on our research findings, it appears that the PET binding is excessively strong, which leads to extended retention in unproductive adsorption orientations. Consequently, our mutation

bioRxiv preprint doi: https://doi.org/10.1101/2024.04.21.590457; this version posted April 21, 2024. The copyright holder for this preprint (which was not certified by peer review) is the author/funder. All rights reserved. No reuse allowed without permission.

strategy aims to diminish the interactions between PET and LCC. This adjustment should facilitate the enzyme's reorientation following its initial attachment to the PET surface. The goal is to promote closer and more favorable binding without excessively compromising the overall adsorption capability. This should be achieved by eliminating strong PET interactions with polar LCC residues and by promoting weaker interactions with apolar residues. This design strategy gains support from previous studies that revealed that enhanced activity of PET hydrolases is associated with increased enzyme hydrophobicity.[25–27] In addition, a reduction in the hydrophobicity of LCC in proximal areas has been demonstrated to reduce the binding to a PET surface, resulting in increased enzyme activity due to increased conversion of degradation intermediates and consequently elevated TPA production.[60]

Distal introduction of alanine and negative charge reduces local interaction with PET To verify this assumption, we generated three *in silico* variants per enzyme, each containing three mutations. The mutations were incorporated into the highly active variants LCC F243I/Y127G (IG) (from $LCC^{ICCG\,3}$) and PES-H1 L92F/Q94Y (FY),[14] which replace the WT enzymes investigated up to this point. In LCC^{ICCG} there are two other mutations which we do not consider in this part of the study. The reason for this is that removing the negative charge by replacing D238 with cysteine for one of the mutations would change the surface charge so much that it would be difficult to assess the influence of the other mutations. Before proceeding with the mutations, we analyzed the behavior of the LCC^{ICCG} (studied further below), LCC^{IG} and PES-$H1^{FY}$ variants in solution through 100 ns MD simulation each. Comparison of their root mean square deviation and fluctuation (RMSD and RMSF) to the corresponding WT enzyme confirms their stability and similar dynamics (Fig. S1).

The mutations we selected mainly involved polar and positively charged residues, which we replaced by apolar and negatively charged residues of similar size. The aim is to increase the overall mobility on the PET surface so that proximal binding becomes more likely. Hence, by replacing positively charged residues, we intend to avoid stabilizing electrostatic interac-

bioRxiv preprint doi: https://doi.org/10.1101/2024.04.21.590457; this version posted April 21, 2024. The copyright holder for this preprint (which was not certified by peer review) is the author/funder. All rights reserved. No reuse allowed without permission.

tions with negative charges at the PET chain ends and the negatively charged regions on the PET bulk surface, as can be seen in the EPS of PET in Fig. S2. Moreover, to induce a strong local effect, three mutation sites in close proximity to each other were selected, where preference was given to residues that were in contact with PET in distal areas for at least 75% in one or more of our initial simulations (Fig. 2A). For each enzyme, two triple mutants were designed to change the E_{int} ratio of polar and apolar residues (PES-H1$^{\text{FY}}$: T11V/S13A/S14A, Q26L/T27V/T28V; LCC$^{\text{IG}}$: L66A/S67A/S69A, T211V/S216A/N239L) and a third triple mutant was created with the aim to to specifically influence the enzyme's EPS (PES-H1$^{\text{FY}}$: S13A/R19E/R75E, LCC$^{\text{IG}}$: R143E/S145A/R151E). The LCC$^{\text{IG}}$ T211V/S216A/N239L mutations are the only ones located near the active site. We have observed a dominant PET residency in this region, which may impede PET progression from this site to the biding cleft. For the modification of the EPS in PES-H1$^{\text{FY}}$, it was not possible to identify at least two positively charged residues that i) are in close proximity to each other, ii) were in lasting contact with PET in the simulations of PES-H1 and iii) whose replacement would not affect protein stability due to their involvement in intra-protein salt bridges. Therefore, R75 was included in the corresponding variant, PES-H1$^{\text{FY}}$ S13A/R19E/R75E, even though it did not make contact with PET for more than 75% of the simulation time. For LCC$^{\text{IG}}$ L66A/S67A/S69A, we deviated from the strategy of mutating polar and positive residues, as L66 appeared to favor PET binding, with more than 75% retention time in two of the six simulations. It should be mentioned that among the hydrophobic residues, leucine was always the strongest mediator for PET interactions. For LCC, L66 had the strongest effect in this regard, and due to its proximity to S67 and S69, we included it in the corresponding mutation.

For each of the LCC$^{\text{IG}}$ and PES-H1$^{\text{FY}}$ variants, we performed 100 ns MD simulations in triplicate starting from the snapshot of previous simulations where LCC or PES-H1 had the lowest distance between the PET bulk and the three mutation sites.

bioRxiv preprint doi: https://doi.org/10.1101/2024.04.21.590457; this version posted April 21, 2024. The copyright holder for this preprint (which was not certified by peer review) is the author/funder. All rights reserved. No reuse allowed without permission.

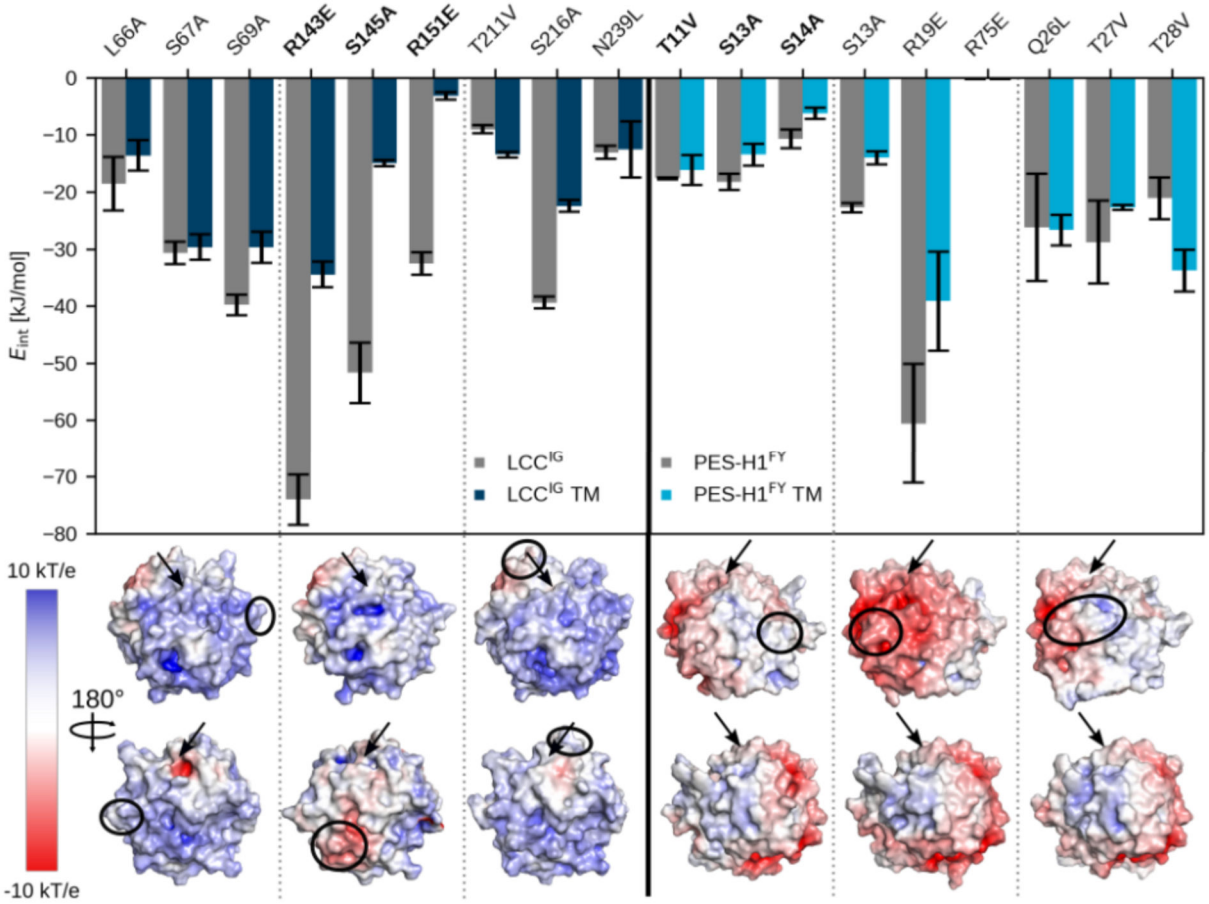


Figure 3: Results for the *in silico* mutation of surface residues for LCC^{IG} (left) and PES-H1^{FY} (right). (Top) The interaction energies (E_{int}) between PET and the residues at mutation sites are shown for the parent enzyme IG or FY (gray) and the three triple mutants (TMs) per enzyme (dark blue for LCC^{IG}, light blue for PES-H1^{FY}). The mutations are given at the top, the TMs are separated by vertical dotted lines and the TMs, which were evaluated experimentally are highlighted in bold. The E_{int} values are averages over three simulations with the SEM given by error bars. (Bottom) The EPS of the TMs are shown. The locations of the mutations are denoted by black circles and the catalytic site is indicated by an arrow.

The simulations were analyzed with respect to E_{int} and the possible reorientation of the enzyme at the PET surface. While the latter could not be observed in the simulations, we were able to alter E_{int} and also the EPS (Fig. 3). For both enzymes a reduction in their interaction with PET was achieved, i.e., the E_{int} values have become less negative. The most significant E_{int} changes occurred for the LCC^{IG} variants, which is consistent with our design strategy of making the LCC (IG) surface more similar to that of PES-H1 (FY) to facilitate

bioRxiv preprint doi: https://doi.org/10.1101/2024.04.21.590457; this version posted April 21, 2024. The copyright holder for this preprint (which was not certified by peer review) is the author/funder. All rights reserved. No reuse allowed without permission.

the reorientation of the enzyme on the PET surface. The introduction of negatively charged residues successfully changed the EPS in this region from positive or neutral to negative and significantly increased E_{int} for the corresponding LCC$^{\text{IG}}$ mutations (R143E, R151E) and to a lesser extent for the PES-H1$^{\text{FY}}$ mutation R19E. The latter can be explained by the fact that the PES-H1$^{\text{FY}}$ surface was already rather negative before this mutation, which reduces the mutation effect. PET did not interact with position 75 in any of the simulations with PES-H1$^{\text{FY}}$ and PES-H1$^{\text{FY}}$ S13A/R19E/R75E. This is probably because the starting structure chosen for the simulations had the residue 75 farthest from PET among the three mutation sites. Therefore, the effect of the R75E mutation cannot be quantified. The implementation of apolar residues, especially alanine, at the expense of polar residues also significantly increased E_{int} (e.g., S145A in LCC$^{\text{IG}}$, S13A in PES-H1$^{\text{FY}}$), while larger apolar residues such as valine or leucine yielded no significant changes or even made the interaction at these sites more favorable (e.g., T211V and N239L in LCC$^{\text{IG}}$; Q26L and T28V in PES-H1$^{\text{FY}}$). In conclusion, local PET binding was successfully reduced in our simulations by introducing small apolar alanine or negatively charged residues. This is hypothesized to promote the progression of the enzyme–PET contact area towards the binding cleft, thereby enhancing PET binding and hydrolysis.

Distal mutations have a major influence on PET degradation activity To test our hypotheses derived from the *in silico* studies, two of the triple mutants were subjected to *in vitro* analysis: PES-H1$^{\text{FY}}$ T11V/S13A/S14A with increased hydrophobicity and LCC$^{\text{IG}}$ R143E/S145A/R151E with increased negative charge. PES-H1$^{\text{FY}}$ and the LCC$^{\text{ICCG}}$ variant were used as reference enzymes. The latter was used instead of LCC$^{\text{IG}}$ to allow for a better comparison to published results.[3,14] The PET degradation activity was determined with amorphous PET films under specific reaction conditions favored for each enzyme.[14] For PES-H1$^{\text{FY}}$, 1 M potassium phosphate buffer has ensured the most efficient hydrolysis rates, which was presumably attributed to its stabilizing effect.[14,61,62] For an optimal comparison with

bioRxiv preprint doi: https://doi.org/10.1101/2024.04.21.590457; this version posted April 21, 2024. The copyright holder for this preprint (which was not certified by peer review) is the author/funder. All rights reserved. No reuse allowed without permission.

FY, LCC^{ICCG}, which is not as salt-dependent as PES-H1^{FY},[3] was also investigated in 1 M reaction buffer. Unfortunately, the LCC^{ICCG} triple mutant could not be expressed, possibly due to the altered surface charge, which could introduce repulsive forces that interfere with native folding.

The percentage weight loss of the PET films after 24 h was determined to evaluate the enzymatic PET degrading activity. As shown in Fig. 4 the substitution of three residues in PES-H1^{FY} far away from the binding site led to greatly reduced activity. This observation does not fully agree with our hypothesis that decreasing the surface polarity far away from the PET binding site should encourage proximal PET binding and thus increase the PET degrading activity. On the other hand, the *in vitro* results confirmed our hypothesis that the initial binding to the PET surface plays an important role for the enzymatic activity. This binding occurs far away from the active site, ruling out any direct interference with the hydrolysis reaction, as shown with the current PES-H1^{FY} variant T11V/S13A/S14A (Fig. 3). Therefore, future studies should thoroughly investigate mutations on the LCC and PES-H1 surface that enhance PET degradation.

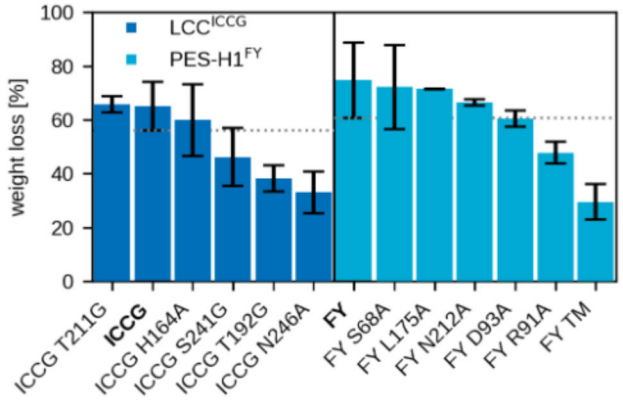


Figure 4: Results from the *in vitro* testing of the original and variants of LCC^{ICCG} (ICCG, left, blue) and PES-H1^{FY} (FY, right, light blue). The variants include five single-point mutations per enzyme, given as axis labels, and the PES-H1^{FY} triple mutant (TM) T11V/S13A/S14A. Variants are ordered according to the percentage weight loss of PET films upon degradation, which serves as a measure for the PET degradation activity. Depolymerization of 60 mg PET film was conducted for 24 h at 70 °C in 1 M potassium phosphate buffer (pH 8) with 60 µg of respective purified enzyme variants. Reactions were performed in duplicate for PES-H1^{FY} L175A and LCC^{ICCG} T211G and for all others at least in triplicate.

bioRxiv preprint doi: https://doi.org/10.1101/2024.04.21.590457; this version posted April 21, 2024. The copyright holder for this preprint (which was not certified by peer review) is the author/funder. All rights reserved. No reuse allowed without permission.

2.2 Entry of PET into the binding site

The energy barrier associated with PET entry can be overcome by enhanced sampling, leading to productive binding poses Since the entry of PET into the binding cleft was not observed with conventional MD simulations, our hypothesis is that a considerable energy barrier must be overcome for this to occur. Therefore, we performed HREMD simulations to increase the sampling of the conformational space of PET. In these simulations, the energy function of PET is changed in a way that the energy barriers for its conformational changes become smaller. We applied these changes to five of the six replicas we considered per HREMD simulation, with the height of the barriers decreasing with increasing replica number. The changes applied to the energy function correspond to increased simulation temperatures, which we will use in the following discussion. For the starting structures of these HREMD simulations, we extracted three conformations from the previous 2 µs MD simulations, in which the binding of the enzyme to a PET bulk was investigated, with the selection criterion of a distance between the catalytic serine and PET of at most 5 Å. In addition, we retained only the PET-9mer closest to the enzyme and removed four units from it, leaving a PET-5mer closest to the catalytic serine (Fig. 5A). This resulted in different starting structures for both enzymes, which were submitted to HREMD simulations with 115 ns per replica. For LCC we performed five HREMD simulations and four for PES-H1 (Tab. S1). In these simulations, and later in the simulations for LCC^{IG} and $PES\text{-}H1^{FY}$, we found that one of these three starting structures (designated 4thL) had the highest number of PET-5mer entry events. Therefore, for the later HREMD simulations of the enzyme variants, this particular starting structure was preferentially used, unless the mutation site was significantly closer to the PET-5mer in another starting structure, which was then used instead. These HREMD simulations enabled to observe several entry events of the PET-5mer into the active site and how this led to the formation of productive binding states, which we distinguish into pro-S and pro-R states (Fig. 5B). A productive state is

bioRxiv preprint doi: https://doi.org/10.1101/2024.04.21.590457; this version posted April 21, 2024. The copyright holder for this preprint (which was not certified by peer review) is the author/funder. All rights reserved. No reuse allowed without permission.

present when the distances between the carbon of the nearest PET-5mer ester and the γ-oxygen of the catalytic serine (SER–C distance) and between the carbonyl oxygen of the same ester and the two amino hydrogens of the oxyanion hole scaffold are sufficiently small to allow hydrolysis. As distance cutoff we defined $\leq$4 Å here. Pro-S and pro-R are defined as PET poses that promote the formation of an S- and R-type tetrahedral intermediate, respectively.[63] An example of the PET-5mer entry into the binding cleft is shown in Fig. 5C. Here, 12 ns of one of the HREMD simulations of LCC can be seen, where the SER–C distance is initially above 6 Å (the outer phase) and drops to below 4 Å (inner phase) within ≈2 ns (entry phase).

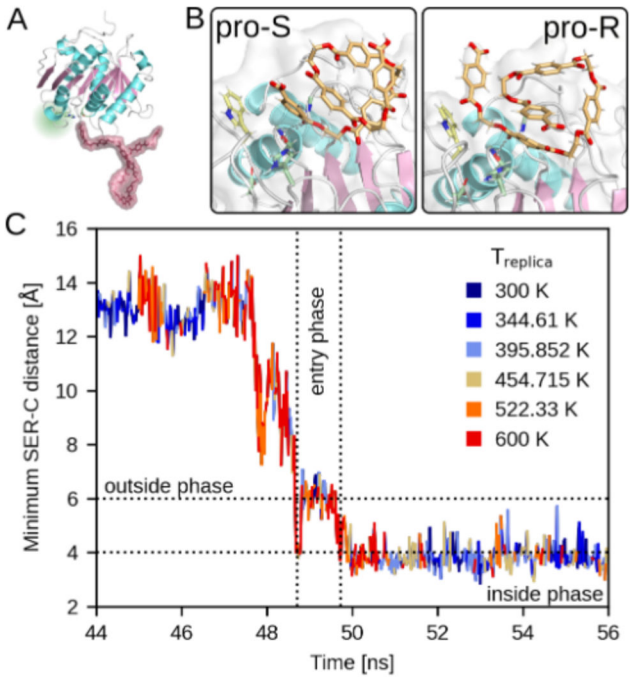


Figure 5: Setup for HREMD simulations and PET-5mer entry results. (A) An exemplary HREMD starting structure is shown to demonstrate the initial distance between the PET-9mer and the enzyme. (B) PET-5mer entry into the active site resulted in pro-S and pro-R poses, for which representative snapshots are shown. (C) The entry of the PET-5mer to the active site was monitored by the evolution of the SER–C distance. Here, a representative entry is shown for LCC. The entry was facilitated by the replicas at high energies/temperatures (colored in orange to red), while conformations from replicas simulated at low energies/temperatures are colored in shades of blue (see color key for exact values). The dotted lines indicate the boundaries for the outside, entry, and inside phases, which are defined by the distance criteria (horizontal lines) and resulting times (vertical lines).

bioRxiv preprint doi: https://doi.org/10.1101/2024.04.21.590457; this version posted April 21, 2024. The copyright holder for this preprint (which was not certified by peer review) is the author/funder. All rights reserved. No reuse allowed without permission.

Importantly, entry is enabled by exchanging low-energy replicas (corresponding to low temperatures, shown in blue) for high energy replicas (corresponding to high-temperatures, shown in red) immediately before and during entry. Once the entry is complete, the system remains in low-energy replicas. This observation explains why PET entry did not occur in the earlier conventional MD simulations and confirms our assumption that this process involves a significant energy barrier that must be overcome. Since the current results could be due to the changes we made to the system, i.e., removing the PET bulk, we performed conventional 115 ns MD simulations for the three HREMD starting structures (two LCC and one PES-H1 simulations) to see if PET-5mer entry still occurs. However, this was not the case and no productive PET state were sampled. Additional MD simulations were conducted at 343 K, a temperature recently proposed as optimal for enzymatic PET hydrolysis.[4,64] These simulations are crucial for surpassing the energy barrier for PET entry. The simulations resulted in pro-R and pro-S states for PES-H1 and LCC when simulated with a single PET-5mer. One of the LCC simulations that encompassed the entire PET bulk yielded a pro-S state.

In order to decipher the source of this energy barrier, we conducted further analyses and defined specific criteria for the identification of productive PET-5mer entries and their corresponding outside, entry, and inside phases: (1) An entry leading to the adoption of a productive state, either pro-S or pro-R, must have taken place and involve a decrease in the SER–C distance from >6 Å (outside phase) to <4 Å (inside phase). (2) The entry phase must last at least 100 ps and a maximum of 5 ns to minimize noise through in and out movements. (3) The inside and outside phases must each last at least 1 ns. The inside phase ends when the SER–C distance exceeds 6 Å and the outside phase ends when this distance falls below 4 Å, or, in the case of more gradual changes, when the SER–C distance exceeds 4 Å on average over the entire inside phase and falls below 6 Å on average over the entire outer phase. Based on these criteria, we identified 29 productive entries for LCC and 15 for PES-H1, corresponding to 4.35% and 6.49% of the corresponding MD frames. Of these entries, 13 and 7 resulted in pro-S poses for LCC and PES-H1, respectively, while the others

bioRxiv preprint doi: https://doi.org/10.1101/2024.04.21.590457; this version posted April 21, 2024. The copyright holder for this preprint (which was not certified by peer review) is the author/funder. All rights reserved. No reuse allowed without permission.

led to pro-R poses. The pro-R pose was identified via docking studies performed by Tournier *et al.*,[3] but others later found in QM/MM studies that the pro-S pose is energetically more favorable[63,65] and that robust binding of a state unfavorable for hydrolysis could inhibit PET degradation activity.[66] Thus, although several pro-R poses were sampled in our study, hydrolysis is expected to occur mainly via pro-S poses. Our analysis of the PET-5mer binding events further shows that the two units that share the ester bond to be hydrolyzed are tightly bound to the enzyme, which is required for the reaction to proceed, while the other PET units interact rather loosely with the enzyme and remain flexible. This finding is evidenced by the different snapshots in Figs. 5B, S3 and S5, which show the conformational freedom of PET units that do not interact directly with the active site. This finding is in contrast to earlier assumptions about a long binding cleft that has several subsites to bind several PET units simultaneously.[46,67]

From the analysis thus far it can be concluded that PET has to overcome an energy barrier for entry into the active site to adopt productive conformations. This energy barrier could be driven by conformational changes of PET to fit into the binding cleft. This is supported by recent studies suggesting that a 'wrapped' PET conformation is energetically favored in solution, while a 'W-shaped' extended conformation, which is crucial for productive binding poses, is observed in association with the enzyme at elevated temperatures.[68] Such conformational changes, and thus the associated energy barrier, could be influenced by PET–PET and residue–PET interactions, which is investigated next by analyzing intramolecular PET interactions and intermolecular PET–enzyme interactions during productive PET entries.

Intramolecular PET interactions hinder necessary conformational changes for entry into the binding cleft For successful PET binding in the active site of the enzyme, a polymer chain or a part of it has to detach from the amorphous or crystalline PET bulk, which means that nonbonded interactions such as hydrogen bonds and π-interactions within the same chain and with other PET chains must be resolved, in addition to meeting sterical

bioRxiv preprint doi: https://doi.org/10.1101/2024.04.21.590457; this version posted April 21, 2024. The copyright holder for this preprint (which was not certified by peer review) is the author/funder. All rights reserved. No reuse allowed without permission.

requirements. To assess the impact of the intramolecular PET-5mer interactions on the energy barrier during entry to the binding cleft, we calculated E_{int} between PET units during productive entries. In several instances, we observed robust interactions between multiple PET units prior to entry, suggesting an inhibitory effect (Fig. S3A). Conversely, individual energy peaks corresponding to favorable intramolecular interactions were detected shortly before or during entry, which probably facilitate the necessary structural rearrangements and interrupt the inhibitory interactions (Fig. S3B). In addition, in some cases, entry-promoting effects were found due to newly formed interactions between two units during and/or after entry (Fig. S3C).

To more comprehensively assess the predominant interactions throughout all simulations of both LCC and PES-H1, as opposed to focusing on individual entry events, we concatenated the HREMD data using all replicas, with the higher replicas weighted, for either enzyme and calculated 2D free energy surfaces (FESs) (Fig. S4). One coordinate in these FESs are the interaction energies between two PET units that are not directly adjacent, which allows us to monitor the intramolecular PET-5mer interactions. To correlate this with the PET-5mer entry, we used the SER–C distance as a second coordinate and distinguish between productive and non-productive regions with a cut-off value of 4 Å. All FESs indicate that non-productive PET-5mer states and also those during entry with SER–C distances below 6 Å but above 4 Å are energetically stabilized, which suggests that PET–PET interactions hinder rather than promote PET-5mer entry into the active site.

In our opinion, the most promising approach to overcome this inhibitory effect is to improve the preprocessing of PET waste. Tarazona *et al.* studied the surface erosion process of PET to differentiate between the PET surface and the bulk properties, which might enable to find a sweet spot between increased PET surface mobility and the increased bulk crystallization.[19] They found that enlarging the PET surface, e.g. by using micronized PET particles, increasing the surface amorphization and lowering the surface glass transition temperature due to the plasticization effect of water promotes the degradation activity by

bioRxiv preprint doi: https://doi.org/10.1101/2024.04.21.590457; this version posted April 21, 2024. The copyright holder for this preprint (which was not certified by peer review) is the author/funder. All rights reserved. No reuse allowed without permission.

increasing the PET accessibility and mobility to overcome intramolecular constraints. This is also consistent with a recent study by Schubert *et al.*, in which chain mobility and the number of available sites for endo-type chain scission, which depend on the degree of crystallinity, are postulated as the activity-limiting factor causing the initial lag phase for the release of the soluble product.[7] Another biotechnological approach to mitigate this hindering effect could be to design enzymes to introduce residues that enhance enzyme–PET interactions, which would promote and counterbalance the loss of PET–PET interactions upon entry into the binding cleft.

PET–enzyme interactions can also hinder PET entry Next, we analyzed the contribution of intermolecular interactions between the PET-5mer and enzyme to the observed overall energy barrier during PET-5mer entry. To this end, we first examined individual entry histories and identified effects that promote or inhibit entry by calculating E_{int} between the PET-5mer and residues within 3 Å during entry. PET-5mer entry can be hindered by strong PET–enzyme interactions prior to entry or by repulsion of PET-5mer within the binding cleft, so that PET-5mer states outside the cleft are favored (Fig. S5A). Conversely, an entry-promoting effect has favorable interactions during entry, which facilitate structural PET-5mer rearrangements that overcome PET–PET interactions (Fig. S5B). Furthermore, PET-5mer entry gets supported through stabilizing interactions for productive PET5-mer poses, which compensate for the loss of PET–PET interactions (Fig. S5C).

To obtain a more general overview, FESs were created using a similar approach as before, but this time for the PET–enzyme interactions. The SER–C distance was again used as a coordinate to monitor the entry process, while E_{int} between the PET-5mer and selected residues was used as another coordinate. The selection and mutation of certain residues allow us to investigate the specific, and sometimes different effects of amino acids in both enzymes. For instance, depletion of tyrosine in the LCC$^{\text{ICCG}}$ variant (Y127G) increased activity compared to WT-LCC, while introduction of tyrosine in the PES-H1$^{\text{FY}}$ variant

bioRxiv preprint doi: https://doi.org/10.1101/2024.04.21.590457; this version posted April 21, 2024. The copyright holder for this preprint (which was not certified by peer review) is the author/funder. All rights reserved. No reuse allowed without permission.

(Q94Y) at the corresponding position resulted in increased activity compared to WT-PES-H1.[3,14] Two more positions are relevant for the improved activity of LCC^{ICCG} and PES-H1^{FY}: the L92F mutation in PES-H1^{FY} and the F243I mutation in LCC^{ICCG}.[3,14] The F125L mutation in the LCC, corresponding to position L92F of PES-H1^{FY}, has been shown to reduce LCC binding to PET surfaces, increasing its availability for targeting degradation intermediates and enhancing overall activity, so it is also analyzed here.[60] Additionally, we studied L209 of PES-H1 corresponding to position F243I of LCC^{ICCG}, for which a mutation to alanine was chosen instead of isoleucine based on studies reporting alanine as the only variant exhibiting activity close to that of the WT.[14,32]

To investigate the effects of these mutations, we performed HREMD simulations for the LCC^{IG} and PES-H1^{FY} variants as well as for LCC^{IG} F125L and PES-H1^{FY} L209A, and calculated the FES from the HREMD data as described above. The resulting FESs reveals distinctive PET–enzyme interaction patterns for WT and mutated residues (Fig. 6). Mutations at positions PES-H1^{FY} 209/LCC^{IG} 243 stabilize productive states in both enzymes, which can be inferred from new free energy minima (in yellow/brown colors in Fig. 6) at SER–C distances below 4 Å and less pronounced minima for distances above 6 Å after mutation, suggesting weaker interactions with the PET-5mer in latter states. In contrast, the effects at positions PES-H1^{FY} 92/LCC^{IG} 125 and PES-H1^{FY} 94/LCC^{IG} 127 differ between the two enzymes. In the case of LCC^{IG}, entry of the PET-5mer after either mutation is promoted due to the elimination of non-productive energy minima resulting from weakened interaction with the PET-5mer for SER–C distances above 6 Å, whereas in PES-H1^{FY}, the entry of the PET-5mer after the mutation becomes more difficult due to increased interaction with the PET-5mer in non-productive states. We therefore conclude that the increase in PET degradation activity could result from a direct promotion of PET entry by the mutated residues for LCC^{ICCG}, but from different mechanism for PES-H1^{FY}.

bioRxiv preprint doi: https://doi.org/10.1101/2024.04.21.590457; this version posted April 21, 2024. The copyright holder for this preprint (which was not certified by peer review) is the author/funder. All rights reserved. No reuse allowed without permission.

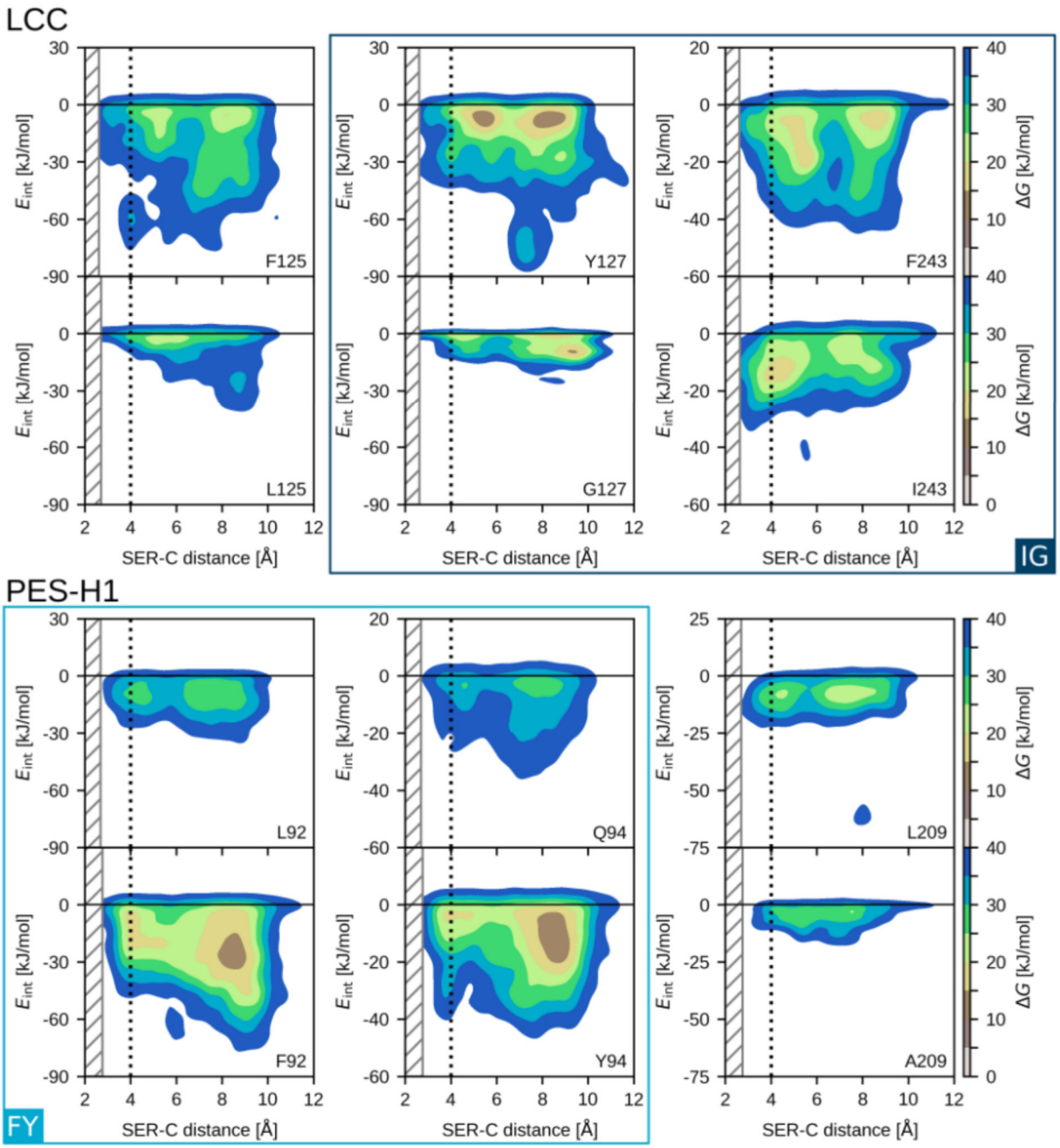


Figure 6: Free energy surfaces of the PET–residue interactions over the SER–C distance obtained from HREMD simulations of LCC and PES-H1 variants. The top row per enzyme presents the FESs for residues present in the WT and the bottom row for the mutated residues in the LCC^{IG}/PES-H1^{FY} variants (indicated by blue boxes) and for the LCC^{IG} F125L/PES-H1^{FY} L209A variants. The area for SER–C distance < 4 Å harbors productive poses. The gray hatched area indicates distances that were not sampled as the ester carbon atom would be too close to the catalytic serine. The free energies, ΔG are given in kJ/mol according to the color scale on the right.

bioRxiv preprint doi: https://doi.org/10.1101/2024.04.21.590457; this version posted April 21, 2024. The copyright holder for this preprint (which was not certified by peer review) is the author/funder. All rights reserved. No reuse allowed without permission.

To further explore our hypothesis that increased entry of PET into the active site contributes to increased activity as presumed for LCC^{ICCG}, we analyzed additional residues near the active site of both enzymes and then mutated them. Our aim was to identify residues that lack entry-promoting FES features and are therefore promising mutation targets to improve PET entry ability. FES features to be introduced include the creation of free energy minima in the productive region with a SER–C distance below 4 Å, indicating stabilized productive positions of PET-5mer, the elimination of free energy minima in the non-productive region, indicating reduced interactions with PET-5mer, and the facilitation of the transition from the non-productive to the productive region by avoiding energy barriers there. The residues that we identified as promising mutation sites were then mutated to glycine or alanine; larger amino acids were not introduced to avoid creating steric hindrances. In addition, the $PES\text{-}H1^{FY}$ H184S variant was simulated, in which the mutation site is located near a highly conserved tryptophan (PES-H1: W155, LCC: W190) adjacent to the binding cleft and whose 'wobbling' presumably increases catalytic activity.[45] Mutation of H184 to a serine is likely to increase the flexibility of this tryptophan due to the lower steric requirements of serine.

This resulted in a total of 14 mutation sites that were evaluated for each enzyme. For each mutant, an HREMD simulation was performed (see Table S1 for the list of HREMD simulations) and the FES calculated as described above. In many cases the overall goal of the *in silico* mutations to facilitate PET-5mer entry into the active site was achieved. For these cases the FES is shown in Fig. S7, and they include mutations with improved stabilization of productive states ($PES\text{-}H1^{FY}$: S68A, D93A; LCC^{IG}: T211G, N246A), reduced interaction in non-productive states ($PES\text{-}H1^{FY}$: S68A, R91A, D93A, N212A; LCC^{IG}: T192G, S241G), or smoother transitions towards productive states without intermediate states where the PET-5mer could get trapped ($PES\text{-}H1^{FY}$: S68A, D93A; LCC^{IG}: HIS164A, T211G, S241G, N246A). The $PES\text{-}H1^{FY}$ H184S variant could neither improve the interactions at position 184 nor the interactions of the 'wobbling' tryptophan with the PET-5mer. The five most promising *in silico* mutations per enzyme (i.e., the ones shown in Fig. S7) were then evalu-

bioRxiv preprint doi: https://doi.org/10.1101/2024.04.21.590457; this version posted April 21, 2024. The copyright holder for this preprint (which was not certified by peer review) is the author/funder. All rights reserved. No reuse allowed without permission.

ated experimentally, using the same protocol as employed for the previous PES-H1^{FY} triple mutant to determine the PET degradation activity. It should be noted that one of these mutants, PES-H1^{FY} L175A, is a borderline case, as a state slightly above the 4 Å criterion applied to the SER–C distance became stabilized; we nonetheless included it in our experimental evaluation, which is discussed below.

Kinetic experiments reveal an increase in activity for the PES-H1^{FY} S68A mutation In order to link simulation and experiment, the activity of the mentioned mutations introduced in the PES-H1^{FY} and LCC^{ICCG} enzymes was determined. The percentage weight loss of the PET films shown in Fig. 4 indicates that none of the variants resulted in a significant increase in the degradation activity. PES-H1^{FY} R91A, LCC^{ICCG} T192G, and LCC^{ICCG} N246A showed significantly lower degradation activity than PES-H1^{FY} and LCC^{ICCG}, respectively. Interestingly, these are also the three variants with the least promising FES profiles among the ten selected variants (Fig. S7). The FES improvements in these mutants were mainly related to the destabilization of the non-productive states, while the productive state did not gain in stability. In LCC^{IG} N246A, on the other hand, while the productive state was stabilized, also a non-productive state at SER–C distances of ≈6.5 Å became more stable, which could explain the reduction in activity for this variant. In addition, there is also the possibility that other factors may influence the experimental outcome and thus mask improvements due to mutations. It should also be mentioned that the reproducibility of the experiments was problematic despite uniform experimental conditions in all experiments, which we suggest can be attributed to influences of the inherent properties of the PET films such as crystallinity or molecular weight distribution.[16]

To reduce potential masking effects and identify subtle effects on individual steps in PET degradation, we analyzed the degradation kinetics using a previously described turbidimetric assay using PET nanoparticles (PET-NP) that measures turbidity changes at 600 nm over time.[14,69] Here, not only the substrate load $[S_0]$ was varied while maintaining

bioRxiv preprint doi: https://doi.org/10.1101/2024.04.21.590457; this version posted April 21, 2024. The copyright holder for this preprint (which was not certified by peer review) is the author/funder. All rights reserved. No reuse allowed without permission.

a fixed enzyme concentration $[E_0]$, as done in conventional Michaelis–Menten kinetics measurements ($^{\text{conv}}$MM), but also the reverse approach with varying enzyme concentration and fixed substrate load was followed, which is called inverse Michaelis–Menten ($^{\text{inv}}$MM) and is a commonly used approach for kinetic measurements with insoluble substrates such as PET.[20,29,70–76] To further ensure a more homogeneous distribution of the substrate, PET-NP were used instead of a PET film, which should lead to more uniform and reproducible results.[76] This approach was used to evaluate the three most interesting candidates per enzyme that showed the most improvement in their FES profiles upon mutation while exhibiting similar PET degradation activity to PES-H1$^{\text{FY}}$ and LCC$^{\text{ICCG}}$, respectively, namely PES-H1$^{\text{FY}}$ S68A, D93A, N212A and LCC$^{\text{ICCG}}$ H164A, T211G, S241G (Tab. 1 and Tab. S3).

Table 1: The Michaelis–Menten constants K_{m} were derived from the nonlinear fit to experimental data for both settings, $^{\text{conv}}$MM and $^{\text{inv}}$MM, and both enzymes, LCC$^{\text{ICCG}}$ (ICCG) and PES-H1$^{\text{FY}}$ (FY), and corresponding variants. Additional secondary parameters k_{cat}, $^{\text{molar}}K_{\text{m}}$ and $^{\text{molar}}\eta$ are provided.

	$^{\text{conv}}\mathbf{K}_{\text{m}}$ $\left[\frac{\mathbf{g}}{\mathbf{L}}\right]$	$^{\text{inv}}\mathbf{K}_{\text{m}}[\mu\mathbf{M}]$	$\mathbf{k}_{\text{cat}}$ $\left[\frac{\mathbf{1}}{\mathbf{min}\cdot\mu\mathbf{M}}\right]$	$^{\text{molar}}\mathbf{K}_{\mathbf{M}}$ $[\mu\mathbf{M}]$	$^{\text{molar}}\eta$ $\left[\frac{\mathbf{1}}{\mathbf{min}\cdot\mu\mathbf{M^2}}\right]$
LCC$^{\text{ICCG}}$	0.215 ±0.059	0.365 ±0.061	0.047	0.357	0.132
ICCG H164A	0.095 ±0.063	0.861 ±0.164	0.032	0.278	0.114
ICCG T211G	0.091 ±0.068	0.430 ±0.130	0.042	0.223	0.189
ICCG S241G	0.250 ±0.068	0.234 ±0.070	0.054	0.357	0.151
PES-H1$^{\text{FY}}$	0.391 ±0.109	0.892 ±0.105	0.088	1.036	0.085
FY S68A	0.357 ±0.117	0.278 ±0.053	0.084	0.728	0.115
FY D93A	0.501 ±0.180	2.017 ±0.481	0.040	2.434	0.016
FY N212A	0.481 ±0.174	1.767 ±0.318	0.068	1.564	0.043

It should be noted that the conventional measurements led to inconsistent results, especially for the LCC$^{\text{ICCG}}$ variants, which confirms that the conventional approach and the applied kinetic model meets experimental challenges when dealing with PET as substrate. Therefore, the following discussion is based on results obtained with the inverse Michaelis–Menten approach. For $^{\text{inv}}K_{\text{m}}$ significant differences are observed in enzyme–substrate affinity between some of the variants and the respective parent enzyme, LCC$^{\text{ICCG}}$ or PES-H1$^{\text{FY}}$. An approximate 3-fold decrease in $^{\text{inv}}K_{\text{m}}$ was detected for the PES-H1$^{\text{FY}}$ S68A variant compared

bioRxiv preprint doi: https://doi.org/10.1101/2024.04.21.590457; this version posted April 21, 2024. The copyright holder for this preprint (which was not certified by peer review) is the author/funder. All rights reserved. No reuse allowed without permission.

to PES-H1$^{\mathrm{FY}}$ (PES-H1$^{\mathrm{FY}}$ S68A: $^{\mathrm{inv}}K_{\mathrm{m}}$=0.273 µM; PES-H1$^{\mathrm{FY}}$: $^{\mathrm{inv}}K_{\mathrm{m}}$=0.892 µM), which indicates a higher enzyme–substrate affinity for PES-H1$^{\mathrm{FY}}$ S68A. For the other two PES-H1$^{\mathrm{FY}}$ variants, higher $^{\mathrm{inv}}K_{\mathrm{m}}$ values than for PES-H1$^{\mathrm{FY}}$ suggest a decreased affinity, which is supported by similar trends in the $^{\mathrm{molar}}K_{\mathrm{m}}$ values. For LCC$^{\mathrm{ICCG}}$ the results are less clear. The higher $^{\mathrm{inv}}K_{\mathrm{m}}$ values for LCC$^{\mathrm{ICCG}}$ H164A and LCC$^{\mathrm{ICCG}}$ T211G than for LCC$^{\mathrm{ICCG}}$ are not mirrored by the corresponding $^{\mathrm{molar}}K_{\mathrm{m}}$ results, which are lower, while the turnover rate constant k_{cat} could also not be improved. For the LCC$^{\mathrm{ICCG}}$ S241G variant a reduction in $^{\mathrm{molar}}K_{\mathrm{m}}$, a similar $^{\mathrm{molar}}K_{\mathrm{m}}$ value as for LCC$^{\mathrm{ICCG}}$ and an increase in k_{cat} were observed, but these improvements are not statistically significant (Tab. S3). Combining affinity and turnover rate into $^{\mathrm{molar}}\eta = k_{\mathrm{cat}}/^{\mathrm{molar}}K_{\mathrm{m}}$ yields the molar catalytic efficiency. First, it should be noted that a higher catalytic efficiency was observed for all LCC$^{\mathrm{ICCG}}$ variants than for the FY variants. A comparison of these figures per enzyme indicates that PES-H1$^{\mathrm{FY}}$ S68A and LCC$^{\mathrm{ICCG}}$ T211G outperform FY and LCC$^{\mathrm{ICCG}}$, respectively, while LCC$^{\mathrm{ICCG}}$ S241G shows a slight improvement. Thus, the most promising mutations revealed by experiments are also the mutations with the most promising FES changes (Fig. S7). In particular for the T211G mutation in LCC$^{\mathrm{ICCG}}$ we succeeded in creating a smooth free energy path leading to the productive state, which corresponds to the largest increase in $^{\mathrm{molar}}\eta$ with respect to the parent enzyme for all variants studied. With the S68A mutation in PES-H1$^{\mathrm{FY}}$ we were able to abolish the stabilization of unproductive states, while the productive state gained stability, yet not as much as with T211G in LCC$^{\mathrm{ICCG}}$.

In our *in silico* mutation strategy, we have restricted ourselves to alanine and glycine as target amino acids. Given the promising, yet not perfect results for the PES-H1$^{\mathrm{FY}}$ S68A variant, we decided to investigate the effects of side-chain size, polarity, charge and aromaticity at that position. To this end, we generated additional *in silico* variants (S68I, S68F, S68Q, S68D, S68K), run HREMD simulations per variant and analyzed the resulting FES (Fig. S8). The results reveal that our original strategy to mutate PES-H1$^{\mathrm{FY}}$ S68 to alanine was a good choice, as mutating this residue to any other residue stabilizes non-productive states and

bioRxiv preprint doi: https://doi.org/10.1101/2024.04.21.590457; this version posted April 21, 2024. The copyright holder for this preprint (which was not certified by peer review) is the author/funder. All rights reserved. No reuse allowed without permission.

isolated areas emerged in the FES, suggesting that the transition to the productive state to has become more difficult. We therefore conclude that interactions with this residue are generally not beneficial for PET entry, which is best avoided by removing steric hindrances as realized in the PES-H1^{FY} S68A mutant.

In conclusion, we were able to define PET entry features by comparing the FES of residues of the respective parent enzyme with their mutations, which allowed us to link the FES appearance with the enzymatic activity measured in experiments. The FES approach allowed us to identify residues that potentially hinder PET entry, and PES-H1^{FY} and LCC^{IG} variants were generated in which these residues were mutated and evaluated computationally and experimentally. This analysis confirmed our idea that changing the FES so that PET can more easily enter the active site by removing energy traps before reaching the productive state and stabilizing the latter, which was best realized in PES-H1^{FY} S68A and LCC^{ICCG} T211G and resulted in higher catalytic activity. With respect to the experimental results it should be noted that $^{inv}K_M$, in contrast to $^{conv}K_M$, reflects how effectively the enzyme can operate at different enzyme concentrations for a given substrate load. Considering the results of both approaches, it seems conceivable that the efficiency of the enzymes has increased especially at low enzyme concentrations, while their PET affinity has not necessarily improved. This would be advantageous in industrial applications where the substrate concentration is high and the enzyme concentration is relatively low and adaptation is impractical for cost or feasibility reasons.

Principal component analysis reveals that PET can enter via three pathways To complete our comprehensive analysis of the PET entry into the binding cleft, we next present the complete pathway of how the PET-5mer reaches its final productive state in the active site. In doing so, we do not limit our analysis to the assumption that there can only be one such pathway, but attempt to identify all possible pathways. To this end, we compiled data of all entry events with phases inside the active site of 1 ns. Here, we included data from

bioRxiv preprint doi: https://doi.org/10.1101/2024.04.21.590457; this version posted April 21, 2024. The copyright holder for this preprint (which was not certified by peer review) is the author/funder. All rights reserved. No reuse allowed without permission.

all simulated variants per enzyme, LCC and PES-H1, assuming that the general pathways should not be affected by the mutations, but only the energies along the pathways (as shown in our previous FES analysis), which could shift the balance between pathway preferences in the case of multiple entry pathways. This generated a large dataset that is suitable for a meaningful principal component analysis (PCA). The PCA was applied to the distances of the PET-5mer ester carbon, which becomes productively bound after entry, to all C_α atoms of the corresponding enzyme within 10 Å. This allows to capture the dynamics during the PET-5mer entry without introducing bias by pre-selecting specific residues. The resulting principal components (PCs) are used to calculate the free energy (ΔG) along the first two PCs, which account for 86% of the variance and are shown as FESs in Fig. S9A,B.

To identify productive and non-productive states in these FES presentations, we projected them into the PC1–PC2 space (indicated by green and rose color in Fig. S9A,B). This shows that the productive states are clearly separated from non-productive states and that the productive states are localized in the ΔG minima regions. We further analyzed the contributions of amino acids mainly involved in the PET-5mer entry by their contributions to PC1, which reveals 49 relevant amino acid positions, which account for 62% of the data variance (Fig. S9C). The involvement of so many positions highlights how complicated the entry pathway of a polymer such as PET into the active enzyme site is. This complexity also challenges the applicability of collective variable-based methods, such as metadynamics,[77] for the targeted sampling of entry pathways. HREMD simulations, as used in this study, do not restrict the conformational PET space to be sampled, but simply increase the space that is generally sampled, thus providing a suitable approach. Inspection of the FES along the PCs of the enzyme–PET contacts also shows that the PET-5mer does not enter the active site via an exclusive pathway, but has three such preferential entry routes in both enzymes. For each of these three pathways, a representative trajectory is projected onto the FES and also structures of both enzymes (Fig. 7).

bioRxiv preprint doi: https://doi.org/10.1101/2024.04.21.590457; this version posted April 21, 2024. The copyright holder for this preprint (which was not certified by peer review) is the author/funder. All rights reserved. No reuse allowed without permission.

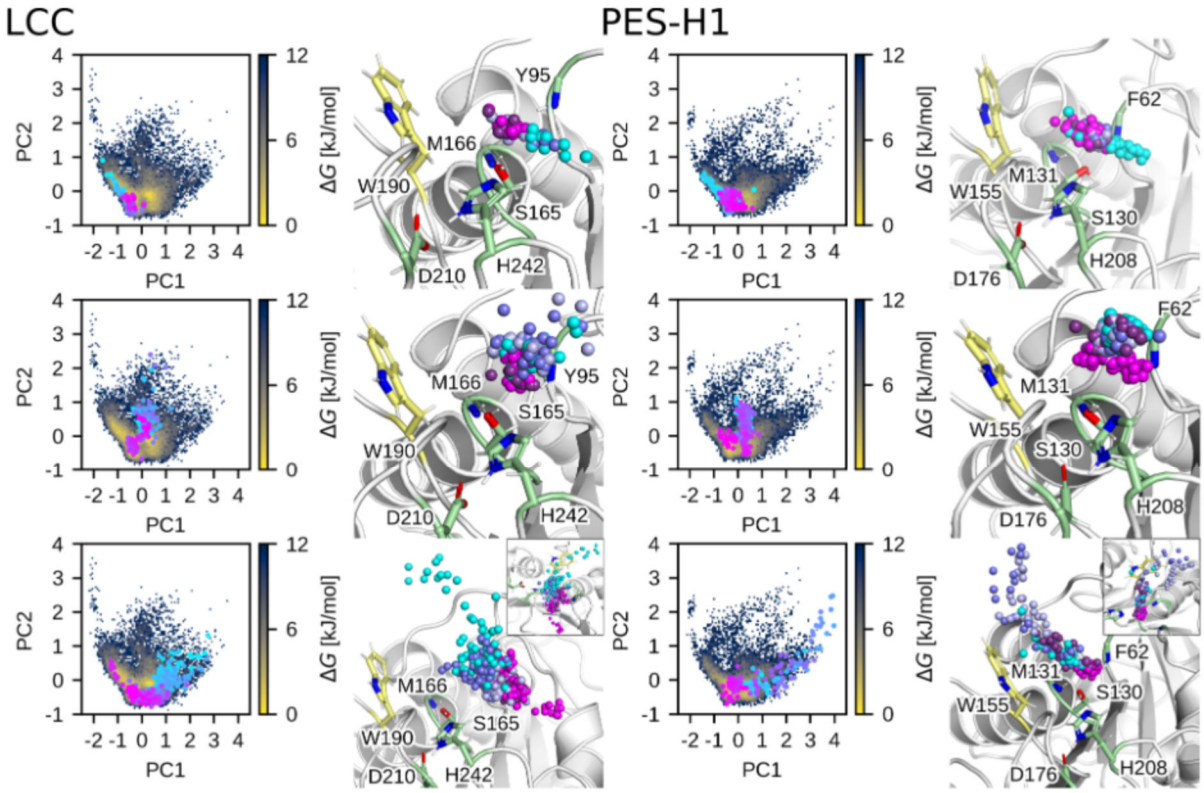


Figure 7: The three preferred entry pathways of the PET-5mer as revealed by PCA applied to the HREMD data involving the simulations of all LCC (left) and PES-H1 (right) variants performed in this work. For each pathway, a representative example is shown. The pathways are mapped as circles on the FES in the PC1,PC2 plane of either enzyme and are also shown (as spheres) together with the corresponding enzyme structure. The progress of each pathway is highlighted by the color change from cyan to magenta. In the structure plots, the spheres show the positions of the PET-5mer ester carbons that are finally productively bound.

These trajectories show how the position of the PET ester carbon evolves towards its productive pose, represented by the color change from cyan to magenta. The first pathway leads from the side opposite the 'wobbling' tryptophan to the active site (Fig. 7, top). The second pathway goes directly from the exterior to the catalytic serine (Fig. 7, middle), while in the third pathway, the ester bond slides over the benzene ring of the 'wobbling' tryptophan until it reaches its final position for hydrolysis (Fig. 7, bottom). Visual inspection of a number of entry pathways revealed a significant flexibility of the ester carbon position, involving multiple reorientations of the ester position, even when close to the active site, until a final productive conformation is attained. Both enzymes exhibit the same entry pathways, with

bioRxiv preprint doi: https://doi.org/10.1101/2024.04.21.590457; this version posted April 21, 2024. The copyright holder for this preprint (which was not certified by peer review) is the author/funder. All rights reserved. No reuse allowed without permission.

the first route being the most clearly defined and energetically favored in both cases. As for the second-preferred route, the LCC shows a preference for the direct entry of PET-5mer as found in the second pathway, which is also better defined than in PES-H1, while in the latter these arguments apply to the third pathway.

The pathway preference may be influenced by the interactions with certain residues and their contribution to PC1, the principal component that mainly distinguishes the three pathways from each other (Fig. S9C). Amino acids with a negative contribution predominantly influence the negative range of PC1, impacting the first pathway located at negative PC1 values. Conversely, amino acids with a positive contribution primarily affect the positive range of PC1, influencing the third pathway situated at positive PC1 values. The magnitude of the amino acid contributions reflects their respective strengths. The second pathway corresponds to PC1 ≈ 0 and therefore has no significant amino acid contributions along PC1. The positions mutated in PES-H1 and LCC correspond to amino acids that contribute to PC1. Among the three positions mutated in the more active IG and FY variants, two contribute negatively to PC1 (PES-H1$^{\mathrm{FY}}$: 94/LCC$^{\mathrm{ICCG}}$: 127 and PES-H1$^{\mathrm{FY}}$: 92) and thus primarily affect the first pathway, which has been identified as the most important for both enzymes. The other mutation in LCC$^{\mathrm{ICCG}}$ contributes to the positive PC1 direction and consequently to the third pathway (LCC$^{\mathrm{ICCG}}$: 243). For several of the positions that we previously analyzed in terms of the FES reflecting their interaction with the PET-5mer, we here find a strong contribution to PC1. In particular, position 68 of PES-H1 makes the largest contribution to PC1, which turned out to be the PES-H1$^{\mathrm{FY}}$ variant with the highest catalytic efficiency after its mutation from serine to alanine (Tab. 1). Together with position 209 in PES-H1 (which corresponds to position 243 in LCC and emerged as important for the LCC$^{\mathrm{ICCG}}$'s activity[3]), position 68 lines one end of the catalytic binding cleft and might, thus, constitute a sterical hindrance when the predominant entry pathway is attempted (Fig. S6) . For LCC, we had identified position 241 as a promising mutation site, which also contributes to the first entry pathway.

bioRxiv preprint doi: https://doi.org/10.1101/2024.04.21.590457; this version posted April 21, 2024. The copyright holder for this preprint (which was not certified by peer review) is the author/funder. All rights reserved. No reuse allowed without permission.

In summary, the PET entry process exhibits a certain degree of variability due to the considerable flexibility of the PET chain and persistent PET–PET interactions during entry as shown above, but also due to the possibility that the ester bond that is eventually cleaved can reach the active site by different routes. For both PES-H1 and LCC, we have identified one pathway as the predominant one, which is identical for both enzymes and is consistent with the findings by Falkenstein *et al.*, who proposed this pathway as the PET entry pathway.[52] However, the plausibility of stepwise PET degradation through 'hopping and sliding' and successive cleavage of PET ester bonds as the primary degradation mechanism appears less tenable.

3 Conclusion

In this study, we systematically investigated the binding trajectory of PET to LCC and PES-H1, aiming to deepen our understanding of the adsorption process and PET entry into the binding site. To this end, we designed the study approach summarized in Fig. 8. We started with examining the initial adsorption of the PET hydrolases at a large amorphous PET bulk using conventional atomistic MD simulations and explored the subsequent entry of PET into the catalytically active site using enhanced-sampling HREMD simulations. Each simulation step involved analyzing the energetics of the different binding phenomena to identify enzyme residues that either promoted or hindered these events. This analysis was complemented by amino acid mutations, initially evaluated through additional simulations and subsequently validated through experimental measurements in the wet lab.

Our primary finding regarding the PET surface binding is that heightened adsorption affinity, facilitated by the introduction of positive surface patches and polar residues, may not correlate with improved enzymatic activity. This conclusion aligns with the Sabatier principle, underscoring the importance of balancing binding affinity across enzyme regions, both proximal and distal to the active site, with enzymatic activity optimization. For the

bioRxiv preprint doi: https://doi.org/10.1101/2024.04.21.590457; this version posted April 21, 2024. The copyright holder for this preprint (which was not certified by peer review) is the author/funder. All rights reserved. No reuse allowed without permission.

next step, the entry of PET into the binding site, we have made the important observation that there is not just one such pathway, but three main ones. In each of these pathways, two critical sources of energy barriers may impede PET from accessing the active site and assuming a productive state. One arises from intra- and intermolecular PET-PET interactions, requiring resolution for the linear binding cleft to accommodate a long, flexible PET chain. The other potential hindrance stems from PET interactions with amino acid residues along the pathway. Our analysis, including free energy surface and principal component analysis of these interactions for wild-type and mutant LCC and PES-H1 enzymes, reveals that energy barriers may result from the stabilization of unproductive states. Conversely, facilitating a seamless energetic transition from unproductive to productive states and stabilizing the latter could enhance enzymatic activity. This theoretical deduction finds support in kinetic experiments involving the S68A mutant of PES-H1^{FY} and the T211G mutant of LCC^{ICCG}. However, it should be noted that the variants we identified to facilitate PET incorporation did not show a significant increase in PET degradation activity. This can be explained by the fact that we did not investigate the PET hydrolysis step itself and the subsequent product release, which are also of great importance for enzyme activity in addition to PET entry into the active site. Future studies should therefore investigate the effects of the mutations investigated here on the activation energy barrier of the hydrolysis reaction using QM/MM simulations and their influences on the resulting product complexes.

In summary, our pioneering methodology synergizes HREMD simulations and free energy analyses to dissect substrate entry pathways and pinpoint barriers. This approach unveils critical insights into the intricate pathways traversed by polymers during degradation, enabling the development of mutation strategies to enhance enzyme kinetics. Here, our computational simulations have significantly advanced the understanding of PET hydrolase mechanisms and offer invaluable guidance for future engineering endeavors aimed at maximizing PET hydrolase applicability. Moreover, this approach holds promise for application to a wide range of enzymes beyond PET hydrolases.

bioRxiv preprint doi: https://doi.org/10.1101/2024.04.21.590457; this version posted April 21, 2024. The copyright holder for this preprint (which was not certified by peer review) is the author/funder. All rights reserved. No reuse allowed without permission.

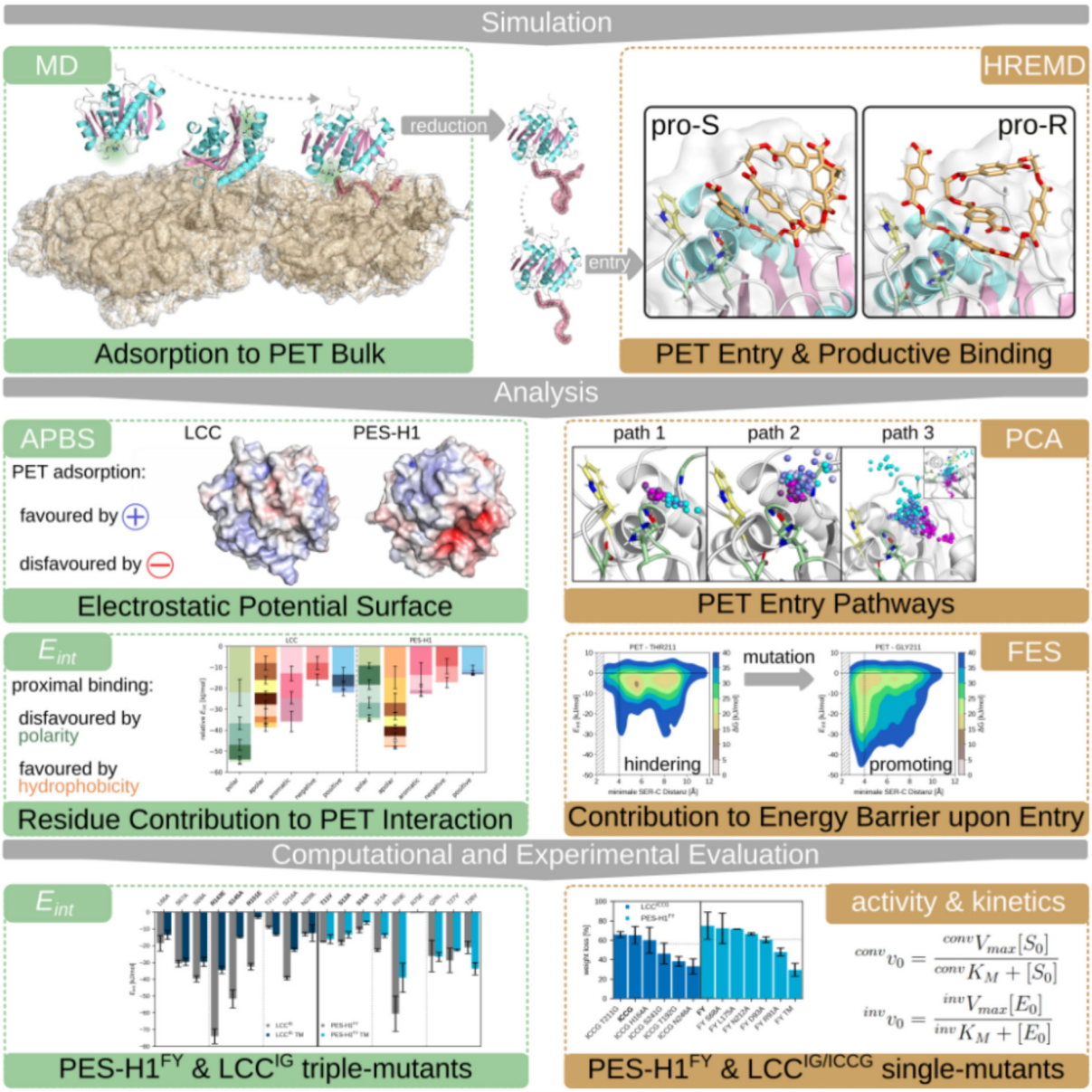


Figure 8: Summary of the workflow applied and results obtained in this study.

bioRxiv preprint doi: https://doi.org/10.1101/2024.04.21.590457; this version posted April 21, 2024. The copyright holder for this preprint (which was not certified by peer review) is the author/funder. All rights reserved. No reuse allowed without permission.

Acknowledgement

A.J. thanks the German Federal Environmental Foundation (Deutsche Bundesstiftung Umwelt) for the financial support by providing a PhD fellowship. A.J is furthermore grateful to her colleague Lara Scharbert for valuable suggestions in figure design. A.J. and B.S. gratefully acknowledge the computing time granted through JARA-HPC (project PETaseMD) on the supercomputer JURECA at Forschungszentrum Jülich,[78] the hybrid computer cluster purchased from funding by the Deutsche Forschungsgemeinschaft (DFG, German Research Foundation) project number INST 208/704-1 FUGG, the Center for Information and Media Technology at Heinrich Heine University Düsseldorf, and the Regional Computing Center of the University of Cologne (RRZK) for providing computing time on the DFG-funded (Funding number: INST 216/512/1FUGG) High Performance Computing (HPC) system CHEOPS. R.W. and U.T.B. acknowledge the funding received from the European Union's Horizon 2020 research and innovation program under grant agreement no. 870294 for the MIX-UP project and no. 953214 for the upPE-T project.

Supporting Information Available

The following files are available free of charge.

- Material and Methods Section
- RMSD and RMSF of PES-H1, PES-H1^{FY}, LCC, LCC^{ICCG} and LCC^{IG}
- EPS of PET
- exemplary PET–PET interaction plots during PET entry
- FES plots for PET–PET interaction for WT enzymes
- exemplary PET–residue interaction plots during PET entry

bioRxiv preprint doi: https://doi.org/10.1101/2024.04.21.590457; this version posted April 21, 2024. The copyright holder for this preprint (which was not certified by peer review) is the author/funder. All rights reserved. No reuse allowed without permission.

- Mutation sites highlighted in LCC and PES-H1 structures
- FES plots for PET–residue interaction for variants analyzed experimentally and additional PES-H1^{FY} S68 variants
- PC1 contribution profile and PC1/PC2 FES with projections of (non-)productive states
- additional kinetic parameters

References

(1) PlasticsEurope Plastics - the Facts 2022. *PlasticsEurope* **2022**,

(2) Wei, R.; Tiso, T.; Bertling, J.; O'Conner, K.; Blank, L. M.; Bornscheuer, U. T. Possibilities and limitations of biotechnological plastic degradation and recycling. *Nat Catal* **2020**, *3*, 867–871.

(3) Tournier, V. et al. An engineered PET depolymerase to break down and recycle plastic bottles. *Nature* **2020**, *580*, 216–219.

(4) Wei, R.; von Haugwitz, G.; Pfaff, L.; Mican, J.; Badenhorst, C. P. S.; Liu, W.; Weber, G.; Austin, H. P.; Bednar, D.; Damborsky, J.; Bornscheuer, U. T. Mechanism-based design of efficient PET hydrolases. *ACS Catal* **2022**, *12*, 3382–3396.

(5) Tournier, V.; Duquesne, S.; Guillamot, F.; Cramail, H.; Taton, D.; Marty, A.; André, I. Enzymes' power for plastics degradation. *Chem Rev* **2023**, *123*, 5612–5701.

(6) Mican, J.; Jaradat, D. M.; Liu, W.; Weber, G.; Mazurenko, S.; Bornscheuer, U. T.; Damborsky, J.; Wei, R.; Bednar, D. Exploring new galaxies: Perspectives on the discovery of novel PET-degrading enzymes. *Appl Catal B-Environ* **2024**, *342*, 123404.

(7) Schubert, S. W.; Thomsen, T. B.; Clausen, K. S. R.; Malmendal, A.; Hunt, C. J.; Borch, K.; Jensen, K.; Brask, J.; Meyer, A. S.; Westh, P. Relationships of crystallinity

bioRxiv preprint doi: https://doi.org/10.1101/2024.04.21.590457; this version posted April 21, 2024. The copyright holder for this preprint (which was not certified by peer review) is the author/funder. All rights reserved. No reuse allowed without permission.

and reaction rates for enzymatic degradation of poly (ethylene terephthalate), PET. *ChemSusChem* e202301752.

(8) Palm, G. J.; Reisky, L.; Böttcher, D.; Müller, H.; Michels, E. A. P.; Walczak, M. C.; Berndt, L.; Weiss, M. S.; Bornscheuer, U. T.; Weber, G. Structure of the plastic-degrading *Ideonella sakaiensis* MHETase bound to a substrate. *Nat Commun* **2019**, *10*, 1717.

(9) von Haugwitz, G. et al. Structural insights into (tere)phthalate-ester hydrolysis by a carboxylesterase and its role in promoting PET depolymerization. *ACS Catal* **2022**, *12*, 15259–15270.

(10) Wei, R.; Breite, D.; Song, C.; Gräsing, D.; Ploss, T.; Hille, P.; Schwerdtfeger, R.; Matysik, J.; Schulze, A.; Zimmermann, W. Biocatalytic degradation efficiency of postconsumer polyethylene terephthalate packaging determined by their polymer microstructures. *Adv Sci* **2019**, *6*, 1900491.

(11) Müller, R.-J.; Schrader, H.; Profe, J.; Dresler, K.; Deckwer, W.-D. Enzymatic degradation of poly(ethylene terephthalate): Rapid hydrolyse using a hydrolase from *T. fusca*. *Macromol Rapid Comm* **2005**, *26*, 1400–1405.

(12) Taniguchi, I.; Yoshida, S.; Hiraga, K.; Miyamoto, K.; Kimura, Y.; Oda, K. Biodegradation of PET: Current status and application aspects. *ACS Catal* **2019**, *9*, 4089–4105.

(13) Yoshida, S.; Hiraga, K.; Takehana, T.; Taniguchi, I.; Yamaji, H.; Maeda, Y.; Toyohara, K.; Miyamoto, K.; Kimura, Y.; Oda, K. A bacterium that degrades and assimilates poly(ethylene terephthalate). *Science* **2016**, *351*, 1196–1199.

(14) Pfaff, L. et al. Multiple substrate binding mode-guided engineering of a thermophilic PET hydrolase. *ACS Catal* **2022**, *12*, 9790–9800.

(15) CARBIOS `https://www.carbios.com/en/enzymatic-recycling/`.

bioRxiv preprint doi: https://doi.org/10.1101/2024.04.21.590457; this version posted April 21, 2024. The copyright holder for this preprint (which was not certified by peer review) is the author/funder. All rights reserved. No reuse allowed without permission.

(16) Arnal, G.; Anglade, J.; Gavalda, S.; Tournier, V.; Chabot, N.; Bornscheuer, U. T.; Weber, G.; Marty, A. Assessment of four engineered PET degrading enzymes considering large-scale industrial applications. *ACS Catalysis* **2023**, *13*, 13156–13166.

(17) Thomsen, T. B.; Hunt, C. J.; Meyer, A. S. Influence of substrate crystallinity and glass transition temperature on enzymatic degradation of polyethylene terephthalate (PET). *New Biotechnol* **2022**, *69*, 28–35.

(18) Wellen, R.; Rabello, M. The kinetics of isothermal cold crystallization and tensile properties of poly(ethylene terephthalate). *J Mater Sci* **2005**, 6099–6104.

(19) Tarazona, N. A.; Wei, R.; Brott, S.; Pfaff, L.; Bornscheuer, U. T.; Lendlein, A.; Machatschek, R. Rapid depolymerization of poly(ethylene terephthalate) thin films by a dual-enzyme system and its impact on material properties. *Chem Catalysis* **2022**, *2*, 3573–3589.

(20) Cui, Y.; Chen, Y.; Sun, J.; Zhu, T.; Li, H. P. C.; Geng, W.-C.; Wu, B. Computational redesign of a hydrolase for nearly complete PET depolymerization at industrially relevant high-solids loading. *Nat Commun* **2024**, *15*, 1417.

(21) Thomsen, T. B.; Schubert, S.; Hunt, C. J.; Borch, K.; Jensen, K.; Brask, J.; Westh, P.; Meyer, A. S. Rate response of poly(ethylene terephthalate)-hydrolases to substrate crystallinity: Basis for understanding the lag phase. *ChemSusChem* **2023**, *16*, e202300291.

(22) Badino, S. F.; Bååth, J. A.; Borch, K.; Jensen, K.; Westh, P. Adsorption of enzymes with hydrolytic activity on polyethylene terephthalate. *Enzyme Microb Tech* **2021**, *152*, 109937.

(23) Nakamura, A.; Kobayashi, N.; Koga, N.; Iino, R. Positive charge introduction on the surface of thermostabilized PET hydrolase facilitates PET binding and degradation. *ACS Catal* **2021**, *11*, 8550–8564.

bioRxiv preprint doi: https://doi.org/10.1101/2024.04.21.590457; this version posted April 21, 2024. The copyright holder for this preprint (which was not certified by peer review) is the author/funder. All rights reserved. No reuse allowed without permission.

(24) Fang, Y.; Chao, K.; He, J.; Wang, Z.; Chen, Z. High-efficiency depolymerization/degradation of polyethylene terephthalate plastic by a whole-cell biocatalyst. *3 Biotech* **2023**, *13*, 138.

(25) Thumarat, U.; Nakamura, R.; Kawabata, T.; Suzuki, H.; Kawai, F. Biochemical and genetic analysis of a cutinase-type polyesterase from a thermophilic *Thermobifida alba* AHK119. *Appl Microbiol Biotechnol* **2012**, *95*, 419–430.

(26) Herrero Acero, E.; Ribitsch, D.; Dellacher, A.; Zitzenbacher, S.; Marold, A.; Steinkellner, G.; Gruber, K.; Schwab, H.; Guebitz, G. M. Surface engineering of a cutinase from *Thermobifida cellulosilytica* for improved polyester hydrolysis. *Biotechnol Bioeng* **2013**, *110*, 2581–2590.

(27) Miyakawa, T.; Mizushima, H.; Ohtsuka, J.; Oda, M.; Kawai, F.; Tanokura, M. Structural basis for the Ca(2+)-enhanced thermostability and activity of PET-degrading cutinase-like enzyme from *Saccharomonospora viridis* AHK190. *Appl Microbiol Biotechnol* **2015**, *99*, 4297–4307.

(28) Ribitsch, D.; Hromic, A.; Zitzenbacher, S.; Zartl, B.; Gamerith, C.; Pellis, A.; Jungbauer, A.; Łyskowski, A.; Steinkellner, G.; Gruber, K.; Tscheliessnig, R.; Herrero Acero, E.; Guebitz, G. M. Small cause, large effect: Structural characterization of cutinases from *Thermobifida cellulosilytica*. *Biotechnol Bioeng* **2017**, *114*, 2481–2488.

(29) Bååth, J. A.; Jensen, K.; Borch, K.; Westh, P.; Kari, J. Sabatier principle for rationalizing enzymatic hydrolysis of a synthetic polyester. *JACS Au* **2022**, *2*, 1223–1231.

(30) Cui, Y. et al. Computational redesign of a PETase for plastic biodegradation under ambient condition by the GRAPE strategy. *ACS Catal* **2021**, *11*, 1340–1350.

(31) Li, Z.; Zhao, Y.; Wu, P.; Wang, H.; Li, Q.; Gao, J.; Qin, H.-M.; Wei, H.; Bornscheuer, U. T.; Han, X.; Wei, R.; Liu, W. Structural insight and engineering of a plastic degrading hydrolase Ple629. *Biochem Bioph Res Co* **2022**, *626*, 100–106.

bioRxiv preprint doi: https://doi.org/10.1101/2024.04.21.590457; this version posted April 21, 2024. The copyright holder for this preprint (which was not certified by peer review) is the author/funder. All rights reserved. No reuse allowed without permission.

(32) Richter, P. K.; Blázquez-Sánchez, P.; Zhao, Z.; Engelberger, F.; Wiebeler, C.; nze, G.; Frank, R.; Krinke, D.; Frezzotti, E.; Lihanova, Y.; Falkenstein, P.; Matysik, J.; Zimmermann, W.; Sträter, N.; Sonnendecker, C. Structure and function of the metagenomic plastic-degrading polyester hydrolase PHL7 bound to its product. *Nat Commun* **2023**, *14*, 1905.

(33) Zeng, W.; Li, X.; Yang, Y.; Min, J.; Huang, J.-W.; Liu, W.; Niu, D.; Yang, X.; Han, X.; Zhang, L.; Dai, L.; Chen, C.-C.; Guo, R.-T. Substrate-binding mode of a thermophilic PET hydrolase and engineering the enzyme to enhance the hydrolytic efficacy. *ACS Catal* **2022**, *12*, 3033–3040.

(34) Yang, Y. et al. Complete bio-degradation of poly(butylene adipate-co-terephthalate) via engineered cutinases. *Nat Commun* **2023**, *14*, 1645.

(35) Han, X.; Liu, W.; Huang, J. W.; Ma, J.; Zheng, Y.; Ko, T. P.; Xu, L.; Cheng, Y. S.; Chen, C. C.; Guo, R. T. Structural insight into catalytic mechanism of PET hydrolase. *Nat Commun* **2017**, *8*, 2106.

(36) Bollinger, A.; Thies, S.; Knieps-Grünhagen, E.; Gertzen, C.; Kobus, S.; Höppner, A.; Ferrer, M.; Gohlke, H.; Smits, S. H. J.; Jaeger, K.-E. A novel polyester hydrolase from the marine bacterium *Pseudomonas aestusnigri* – Structural and functional insights. *Front Microbiol* **2020**, *11*.

(37) Liu, B.; He, L.; Wang, L.; Li, T.; Li, C.; Liu, H.; Luo, Y.; Bao, R. Protein crystallography and site-direct mutagenesis analysis of the poly(ethylene terephthalate) hydrolase PETase from *Ideonella sakaiensis*. *ChemBioChem* **2018**, *19*, 1471–1475.

(38) Tailoring cutinase activity towards polyethylene terephthalate and polyamide 6,6 fibers. *J Biotechnol* **2007**, *128*, 849–857.

(39) Silva, C.; Da, S.; Silva, N.; Matamá, T.; Araújo, R.; Martins, M.; Chen, S.; Chen, J.;

bioRxiv preprint doi: https://doi.org/10.1101/2024.04.21.590457; this version posted April 21, 2024. The copyright holder for this preprint (which was not certified by peer review) is the author/funder. All rights reserved. No reuse allowed without permission.

Wu, J.; Casal, M.; Cavaco-Paulo, A. Engineered *Thermobifida fusca* cutinase with increased activity on polyester substrates. *Biotechnol J* **2011**, *6*, 1230–1239.

(40) Austin, H. P. et al. Characterization and engineering of a plastic-degrading aromatic polyesterase. *Proc Natl Acad Sci USA* **2018**, *115*, E4350–E4357.

(41) Ma, Y.; Yao, M.; Li, B.; Ding, M.; He, B.; Chen, S.; Zhou, X.; Yuan, Y. Enhanced poly(ethylene terephthalate) hydrolase activity by protein engineering. *Engineering* **2018**, *4*, 888–893.

(42) Mhashal, A. R.; Kumar T, N.; Kumar, N.; Singhal, A.; Ravandur, A.; Sokkar, P.; Kulkarni, N. The effect of double (S238F/W159H) mutations on the structure and dynamics of PET degrading enzyme. *J Biomol Struct Dyn* **2023**, *0*, 1–11.

(43) Chen, C. C.; Han, X.; Ko, T. P.; Liu, W.; Guo, R. T. Structural studies reveal the molecular mechanism of PETase. *FEBS J* **2018**, *285*, 3717–3723.

(44) Chen, C.-C. et al. General features to enhance enzymatic activity of poly(ethylene terephthalate) hydrolysis. *Nat Catal* **2021**, 425–430.

(45) Crnjar, A.; Griñen, A.; Kamerlin, S. C. L.; Ramírez-Sarmiento, C. A. Conformational selection of a tryptophan side chain drives the generalized increase in activity of PET hydrolases through a Ser/Ile double mutation. *ACS Org Inorg Au* **2023**, *3*, 109–119.

(46) Joo, S.; Cho, I. J.; Seo, H.; Son, H. F.; Sagong, H. Y.; Shin, T. J.; Choi, S. Y.; Lee, S. Y.; Kim, K. J. Structural insight into molecular mechanism of poly(ethylene terephthalate) degradation. *Nat Commun* **2018**, *9*, 382.

(47) Kawabata, T.; Oda, M.; Kawai, F. Mutational analysis of cutinase-like enzyme, Cut190, based on the 3D docking structure with model compounds of polyethylene terephthalate. *J Biosci Bioeng* **2017**, *124*, 28–35.

bioRxiv preprint doi: https://doi.org/10.1101/2024.04.21.590457; this version posted April 21, 2024. The copyright holder for this preprint (which was not certified by peer review) is the author/funder. All rights reserved. No reuse allowed without permission.

(48) Fecker, T.; Galaz-Davison, P.; Engelberger, F.; Narui, Y.; Sotomayor, M.; Parra, L. P.; Ramírez-Sarmiento, C. A. Active site flexibility as a hallmark for efficient PET degradation by *I.sakaiensis* PETase. *Biophys J* **2018**, *114*, 1302–1312.

(49) Charupanit, K.; Tipmanee, V.; Sutthibutpong, T.; Limsakul, P. Identification of potential sites for a plastic-degrading enzyme by a reverse screening through the protein sequence space and molecular dynamics simulations. *Molecules* **2022**, *27*, 3353.

(50) Pirillo, V.; Orlando, M.; Tessaro, D.; Pollegioni, L.; Molla, G. An efficient protein evolution workflow for the improvement of bacterial PET hydrolyzing enzymes. *Int J Mol Sci* **2022**, *23*, 264.

(51) Aristizábal-Lanza, L.; Mankar, S. V.; Tullberg, C.; Zhang, B.; Linares-Pastén, J. A. Comparison of the enzymatic depolymerization of polyethylene terephthalate and AkestraTM using *Humicola insolens* cutinase. *Front Chem Eng* **2022**, *4*.

(52) Falkenstein, P.; Zhao, Z.; Di Pede-Mattatelli, A.; Künze, G.; Sommer, M.; Sonnendecker, C.; Zimmermann, W.; Colizzi, F.; Matysik, J.; Song, C. On the binding mode and molecular mechanism of enzymatic polyethylene terephthalate degradation. *ACS Catal* **2023**, *13*, 6919–6933.

(53) James, A.; De, S. Cation–π and hydrophobic interaction controlled PET recognition in double mutated cutinase – identification of a novel binding subsite for better catalytic activity. *RSC Adv* **2022**, *12*, 20563–20577.

(54) Groß, C.; Hamacher, K.; Schmitz, K.; Jager, S. Cleavage product accumulation decreases the activity of cutinase during PET hydrolysis. *J Chem Inf Model* **2017**, *57*, 243–255.

(55) Cruz-Chu, E. R.; Ritz, T.; Siwy, Z. S.; Schulten, K. Molecular control of ionic conduction in polymer nanopores. *Faraday Discuss* **2009**, *143*, 47–62.

bioRxiv preprint doi: https://doi.org/10.1101/2024.04.21.590457; this version posted April 21, 2024. The copyright holder for this preprint (which was not certified by peer review) is the author/funder. All rights reserved. No reuse allowed without permission.

(56) Rabe, M.; Verdes, D.; Seeger, S. Understanding protein adsorption phenomena at solid surfaces. *Adv Colloid Interfac* **2011**, *162*, 87–106.

(57) Secundo, F. Conformational changes of enzymes upon immobilisation. *Chem Soc Rev* **2013**, *42*, 6250–6261.

(58) Bourassin, N.; Barbault, F.; Baaden, M.; Sacquin-Mora, S. Between two walls: Modeling the adsorption behavior of β-glucosidase A on bare and SAM-functionalised gold surfaces. *bioRxiv* **2021**,

(59) Sagong, H. Y.; Son, H. F.; Seo, H.; Hong, H.; Lee, D.; Kim, K. J. Implications for the PET decomposition mechanism through similarity and dissimilarity between PETases from *Rhizobacter gummiphilus* and *Ideonella sakaiensis*. *J Hazard Mater* **2021**, *416*, 126075.

(60) Mrigwani, A.; Thakur, B.; Guptasarma, P. Counter-intuitive enhancement of degradation of polyethylene terephthalate through engineering of lowered enzyme binding to solid plastic. *Proteins* **2023**, *91*, 807–821.

(61) Schmidt, J.; Wei, R.; Oeser, T.; Belisário-Ferrari, M. R.; Barth, M.; Then, J.; Zimmermann, W. Effect of Tris, MOPS, and phosphate buffers on the hydrolysis of polyethylene terephthalate films by polyester hydrolases. *FEBS Open Bio* **2016**, *6*, 919–927.

(62) Sonnendecker, C. et al. Low carbon footprint recycling of post-consumer PET plastic with a metagenomic polyester hydrolase. *ChemSusChem* **2022**, *15*, e202101062.

(63) Zheng, M.; Li, Y.; Dong, W.; Zhang, Q.; Wang, W. Enantioselectivity and origin of enhanced efficiency in polyethylene terephthalate hydrolases catalyzed depolymerization. *J Hazard Mater* **2023**, *452*, 131295.

(64) Akram, E.; Cao, Y.; Xing, H.; Ding, Y.; Luo, Y.; Wei, R.; Zhang, Y. On the temperature

bioRxiv preprint doi: https://doi.org/10.1101/2024.04.21.590457; this version posted April 21, 2024. The copyright holder for this preprint (which was not certified by peer review) is the author/funder. All rights reserved. No reuse allowed without permission.

dependence of enzymatic degradation of poly(ethylene terephthalate). *Chinese J Catal* **2024**,

(65) Boneta, S.; Arafet, K.; Moliner, V. QM/MM study of the enzymatic biodegradation mechanism of polyethylene terephthalate. *J Chem Inf Model* **2021**, *61*, 3041–3051.

(66) Ferrario, V.; Fischer, M.; Zhu, Y.; Pleiss, J. Modelling of substrate access and substrate binding to cephalosporin acylases. *Sci Rep* **2019**, *9*, 12402.

(67) Wei, R.; Song, C.; sing, D.; Schneider, T.; Bielytskyi, P.; ttcher, D.; Matysik, J.; Bornscheuer, U. T.; Zimmermann, W. Conformational fitting of a flexible oligomeric substrate does not explain the enzymatic PET degradation. *Nat Commun* **2019**, *10*.

(68) Orlando, C.; Prejanò, M.; Russo, N.; Marino, T. On the role of temperature in the depolymerization of PET by FAST-PETase: An atomistic point of view on possible active site pre-organization and substrate-destabilization effects. *ChemBioChem 24*, e202300412.

(69) Belisário-Ferrari, M. R.; Wei, R.; Schneider, T.; Honak, A.; Zimmermann, W. Fast turbidimetric assay for analyzing the enzymatic hydrolysis of polyethylene terephthalate model substrates. *Biotechnol J* **2019**, *14*, 1800272.

(70) Bååth, J. A.; Borch, K.; Jensen, K.; Brask, J.; Westh, P. Comparative biochemistry of four polyester (PET) hydrolases**. *ChemBioChem* **2021**, *22*, 1627–1637.

(71) Schubert, S.; Schaller, K.; Bååth, J. A.; Hunt, C.; Borch, K.; Jensen, K.; Brask, J.; Westh, P. Reaction pathways for the enzymatic degradation of poly(ethylene terephthalate): What characterizes an efficient PET-hydrolase? *ChemBioChem* **2023**, *24*, e202200516.

(72) Ronkvist, A. M.; Xie, W.; Lu, W.; Gross, R. A. Cutinase-catalyzed hydrolysis of poly(ethylene terephthalate). *Macromolecules* **2009**, *42*, 5128–5138.

bioRxiv preprint doi: https://doi.org/10.1101/2024.04.21.590457; this version posted April 21, 2024. The copyright holder for this preprint (which was not certified by peer review) is the author/funder. All rights reserved. No reuse allowed without permission.

(73) Scandola, M.; Focarete, M. L.; Frisoni, G. Simple kinetic model for the heterogeneous enzymatic hydrolysis of natural poly(3-hydroxybutyrate). *Macromolecules* **1998**, *31*, 3846–3851.

(74) Kari, J.; Andersen, M.; Borch, K.; Westh, P. An inverse Michaelis–Menten approach for interfacial enzyme kinetics. *ACS Catal* **2017**, *7*, 4904–4914.

(75) Wei, R.; Oeser, T.; Barth, M.; Weigl, N.; Lübs, A.; Schulz-Siegmund, M.; Hacker, M. C.; Zimmermann, W. Turbidimetric analysis of the enzymatic hydrolysis of polyethylene terephthalate nanoparticles. *J Mol Catal B-Enzym* **2014**, *103*, 72–78.

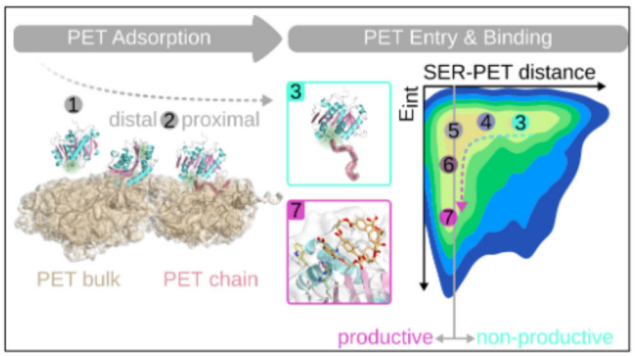
(76) Vogel, K.; Wei, R.; Pfaff, L.; Breite, D.; Al-Fathi, H.; Ortmann, C.; Estrela-Lopis, I.; Venus, T.; Schulze, A.; Harms, H.; Bornscheuer, U. T.; Maskow, T. Enzymatic degradation of polyethylene terephthalate nanoplastics analyzed in real time by isothermal titration calorimetry. *Sci Total Environ* **2021**, *773*, 145111.

(77) Bussi, G.; Laio, A. Using metadynamics to explore complex free-energy landscapes. *Nat Rev Phys* **2020**, *2*, 200–212.

(78) Krause, D.; Thörnig, P. JURECA: Modular Supercomputer at Jülich Supercomputing Centre. *JLSRF* **2018**, *4*.

bioRxiv preprint doi: https://doi.org/10.1101/2024.04.21.590457; this version posted April 21, 2024. The copyright holder for this preprint (which was not certified by peer review) is the author/funder. All rights reserved. No reuse allowed without permission.

TOC Graphic



Supplementary Information

From Bulk to Binding: Decoding the Entry of PET into Hydrolase Binding Pockets

Anna Jäckering,[†,‡] Frederike Göttsch,[¶] Moritz Schäffler,[†,‡] Mark Doerr,[¶] Uwe T. Bornscheuer,[¶] Ren Wei,[¶] and Birgit Strodel[*,†,‡]

[†]*Institute of Theoretical and Computational Chemistry, Heinrich Heine University, Düsseldorf, Universitätsstr. 1, 40225 Düsseldorf, Germany*

[‡]*Institute of Biological Information Processing: Structural Biochemistry (IBI-7), Forschungszentrum Jülich, Wilhelm-Johnen-Straße, 52428 Jülich, Germany*

[¶]*Department of Biotechnology & Enzyme Catalysis, Institute of Biochemistry, University of Greifswald, Felix-Hausdorff-Str. 4, 17487 Greifswald, Germany*

E-mail: b.strodel@fz-juelich.de

1 Methods

1.1 Parameterisation of PET

Quantum mechanics calculations were performed at the HF/6-31G* level for a small PET analogue consisting of three units using Gaussian 09[1] to develop generalized AMBER force field (GAFF)[2] parameters for the terminal and central units. Restrained electrostatic po-

tential (RESP) calculations[3,4] were performed using the antechamber tool[5,6] as available in AmberTools 21[7] to acquire the partial charges, which were redistributed using prepgen to obtain a zero net charge for each PET unit. The input files for the simulation software GROMACS[8] were retrieved using the ACPYPE tool[9] and were already published by Pfaff *et al.*[10]

1.2 MD simulations and analysis protocol

The following protocol was applied for all MD simulations performed in this study, using the software GROMACS version 2020.5.[8] The enzyme and/or PET was placed in a periodic dodecahedron box with at least 10 Å distance to the box edges, solvated using the TIP3P water model[11] and neutralized by addition of the respective amount of sodium or chloride ions matching a physiological concentration of 150 mM. Energy minimization was performed using the steepest descent algorithm[12] until the maximum force fell below 1,000 $kJ \cdot mol^{-1} \cdot nm^{-1}$. The solvent was relaxed in a two-step equilibration approach applying position restraints to enzyme and/or PET heavy atoms: First, a simulation in the NVT ensemble (i.e., with a constant number of atoms (N), constant volume (V), and constant temperature (T)) was followed by a second simulation in the NpT ensemble (i.e., with varying volume, but constant pressure (p)) to set the temperature at 303 K (30°C, v-rescale thermostat[13]) and the pressure at 1.0 bar using isotropic pressure scaling (Berendsen barostat[14]) before subjecting the system to the final production run in the NpT ensemble (303 K, Nosé-Hoover thermostat;[15,16] 1.0 bar, Parrinello-Rahman barostat[17]). During both, equilibration and production phase, the system was described by the AMBER14SB forcefield[18] supplemented with Parmbsc1[19] and PET parameters using periodic boundary conditions and bond lengths correction by the LINCS algorithm[20] allowing to integrate the equations of motion according to Newton's 2nd law of motion every 2 fs using the leap-frog stochastic dynamics integrator.[21] Computational demand was reduced by utilization of the particle mesh Ewald method[22,23] for calculation of electrostatic interactions and by limiting the short-range non-bonded interactions to 12 Å.

Data was collected at least every 20 ps and analyzed using tools implemented in GROMACS[8] as well as visual molecular dynamics (VMD) software,[24] PyMOL[25] and Python 3.[26] Conformational clustering was performed using the Daura algorithm[27] with an RMSD cutoff of 2 Å. The EPS for the enzymes and PET was obtained using the Poisson-Boltzmann equation[28] as implemented in the adaptive Poisson-Boltzmann solver (APBS).[29]

1.3 Enzyme-only simulations

The initial structures of LCC (PDB: 4EB0[30]) and PES-H1 (PDB: 7CUV,[10] chain B) were prepared by removing water, additives and additional enzyme chains in dimeric structures. Mutations were introduced using PyMOL to obtain the starting structures for the LCC^{IG} variant (F243I and Y127G), the LCC^{ICCG} variant (LCC^{IG} including D238C and S283C mutations) and the $PES\text{-}H1^{FY}$ variant (L92F and Q94Y). The charge state at pH 7 of titratable amino acids was determined using Propka 3.4[31,32] yielding a net charge of +5 for LCC and LCC^{IG}, +6 for LCC^{ICCG} and −5 for PES-H1 and $PES\text{-}H1^{FY}$, respectively. After energy minimization and equilibration, the enzymes were shortly simulated at 300 K (26.85°C) to check their stability and further relax the structures. Conformational clustering with a cutoff of 1 Å was applied using the Daura algorithm[27] to obtain the most populated cluster structure as a starting structure for subsequent simulations.

1.4 Preparation of PET bulk

The initial *bulk.pdb* structure taken from Cruz-Chu *et al.*[33] consists of 245 PET chains, each including nine units with neutral carboxy termini. To decrease computational demand, the bulk was reduced to 100 PET chains and solvated, and this structure relaxed by MD simulations in three steps, which reduced the box size from 1680 nm^3 to 1040 nm^3. For each step, an MD simulation was conducted for 100 ns in absence of ions. A cubic box matching the size of the PET bulk was used together with semiisotropic pressure coupling to mimic an infinite PET surface when applying periodic boundary conditions. Conformational clustering

of the PET bulk with a 3 Å cutoff yielded the most populated cluster as the starting structure for the respective following simulation, which finally included an enzyme.

1.5 Simulating enzymes with PET bulk

The LCC and PES-H1 were subjected to MD simulations in a system with PET bulk to sample the initial adsorption to PET. The same x and y cubic box boundaries as for the PET bulk simulations as well as semiisotropic coupling in x and y direction were chosen to mimic an infinite PET surface under application of periodic boundary conditions. For each simulation, the box size in z direction was increased to make space for the incorporation for the enzyme, which was placed at least 10 Å minimum distance above the PET bulk in a random orientation using PyMOL.[25] Six different starting conformations were generated per enzyme to reduce the risk of a biased initial contact site and to increase statistical significance. An additional energy minimization was performed *in vacuo* to relax the structure prior to solvation. Simulations were carried out for 1.5 µs and the three most promising of the six simulations per enzyme, characterized by a minimum distance below 12 Å between the catalytic serine and PET, were elongated to 2 µs (LCC: 1st, 2nd, 4th; PES-H1: 1st, 2nd, 3rd MD run), yielding a total simulation time of 10.5 µs per enzyme.

1.6 Triple-mutant MD simulations

Variants of LCC^{IG} and PES-H1^{FY} were generated using PyMOL[25] to analyze the influence of charge and polarity on PET binding: T11V/S13A/S14A, S13A/R19E/R75E and Q26L/T27V/T28V for PES-H1^{FY}, and R143E/S145A/R151E, L66A/S67A/S69A and T211V/S216A/N239L for LCC^{IG}. As a starting conformation, we extracted the enzyme–PET bulk configuration in which PET was closest to these mutation sites from the preceding 1.5 µs MD simulations of the WT enzymes. In addition to the LCC^{IG} and PES-H1^{FY} triple mutants, we also simulated their respective parent enzyme, i.e., LCC^{IG} and PES-H1^{FY}. All of these simulations were performed in triplicate to compare their interaction with PET and

PET contact progression with statistical significance. The box size was set according to the x and y boundaries of the extracted snapshots to fit the PET bulk conformation, but reduced in z direction to decrease computational demand (which is possible since the enzymes are already adsorbed on the PET surface here). An additional energy minimization was performed *in vacuo* prior to solvation and addition of ions. The pressure was scaled semiisotropically to allow for an infinite PET bulk surface under application of periodic boundary conditions. Simulations were performed for 100 ns each.

1.7 Hamiltonian replica exchange MD (HREMD) simulations

In the MD simulations, adsorption of LCC and PES-H1 onto the PET bulk was observed with high retention near the catalytic site, but without PET penetrating into the binding cleft. To sample the entrance to the binding cleft, conformations with at most 5 Å distance between the catalytic serine and PET were extracted from the MD simulations that had been elongated to 2 µs, in which long retention of PET close to the active site took place. This yielded one PET pose for PES-H1 (1st run, 3.25 Å after 25.6 ns) and two poses for LCC (1st run, 1.59 Å after 1,264.4 ns; 4th run, 1.69 Å after 58.8 ns), which were used for further study. However, only the enzyme and the one PET chain closest to the catalytic serine were kept, which was further reduced from nine to the five PET units closest to the catalytic serine to reduce the computational demand of the following HREMD simulations. To increase the number of starting configurations to three per enzyme, the two LCC-PET poses were also used for PES-H1 by replacing LCC with PES-H1 after superposition of the enzymes, and vice versa the original PES-H1-PET configuration was copied to LCC, denoted as 1stP (from the 1st PET bulk simulation with PES-H1) and 1stL and 4thL (from the 1st and 4th bulk simulations with LCC). The simulations were prepared for the WT enzymes and variants listed in Tab. S1 using the standard equilibration MD protocol described above. This was followed by an additional simulation step, which was conducted for 10 ns using the same conditions as for NpT equilibration but without position-restraining the enzyme

to relax the protein structure and ensure system stability prior to the HREMD production run, which was conducted for 115 ns per replica using GROMACS version 2016.4 patched with the PLUMED 2.4.6 plugin.[8,34,35] Here, the v-rescale thermostat[13] is used instead of the Nosé-Hoover thermostat[15,16] as it is recommended for the HREMD method.[35] Six replicas per HREMD simulation were used, where the Hamiltonian of PET's non-bonded interactions was perturbed by applying λ scaling factors of 1.00, 0.87, 0.76, 0.66, 0.57, and 0.50, corresponding to temperatures ranging from 300 to 600 K. Exchange rates of approx. 30% were obtained with exchanges between replicas being attempted every 0.2 ps. For some of the variants, multiple HREMD simulations were performed, which were initiated with different initial velocities. In total, we run 37 and 31 HREMD simulations corresponding to 25.53 and 21.39 µs of sampling for variants of LCC and PES-H1, respectively (Tab. S1).

Besides the HREMD production run, conventional MD production runs were performed at 303 K and 343 K for the three starting structures 1stP, 1stL, and 4thL with only one PET chain (of five units), as well as one simulation for each starting structure including the whole PET bulk at 343 K. These extra MD simulations were done to ensure that the HREMD results obtained are not a consequence of reducing the PET to one chain or the HREMD settings and that they are reproducible at higher temperatures and with the inclusion of a PET bulk. The same simulation conditions as in the HREMD simulations were applied for the systems including one PET chain, while the conditions from the initial PET bulk simulations were used for the systems including PET bulk.

Table S1: Variants studied by HREMD simulations with the starting structures 1stP (taken from 1st PET-bulk simulation of PES-H1), 1stL, and 4thL (taken from the 1st and 4th PET-bulk simulations of LCC). The number of HREMD simulations performed per variant and starting structure as well as the total number of simulations are given. For both enzymes, 16 mutation positions were analyzed.

LCC	**1stP**	**1stL**	**4thL**	**total**	**PES-H1**	**1stP**	**1stL**	**4thL**	**total**
WT	1	1	3	5	WT	2	1	1	4
LCC^{IG}	2	2	1	5	$PES\text{-}H1^{FY}$	1	1	1	3
T96A	0	0	1	1	T63G	0	0	1	1
S101A	0	0	1	1	S68A	0	0	1	1
					S68D	0	0	1	1
					S68F	0	0	1	1
					S68I	0	0	1	1
					S68K	0	0	1	1
					S68Q	0	0	1	1
T121A	0	0	1	1	D93A	0	0	1	1
R124A	0	1	0	1	R91A	0	0	1	1
F125L	0	0	1	1	R98A	0	0	1	1
D126A	0	0	2	2	H129A	0	0	1	1
R131A	0	0	1	1	T157G	0	1	0	1
H164A	0	0	1	1	L175A	0	0	2	2
T192G	1	0	0	1	T177G	2	0	1	3
T211G	0	0	2	2	H184S	1	0	1	2
Q217A	0	0	1	1	S207A	0	0	1	1
H218A	0	0	1	1	L209A	1	0	0	1
S241G	0	1	1	2	N212A	0	1	1	2
N246A	3	0	0	3	T213A	0	0	1	1
total				32	**total**				31

1.8 Free energy surface (FES)

Two-dimensional FESs were generated for a temperature of 303 K using the HREMD data. The two collective variables along which the free energies ΔG were projected were calculated using tools implemented in GROMACS: *gmx select* and *gmx mindist* for the SER–C distance and *gmx energy* as well as *gmx rerun* to obtain the total interaction energy E_{int} between PET and specific residues consisting of polar Coulomb (Coul) and hydrophobic Lennard-Jones (LJ) contributions. The multistate Benett acceptance ratio (MBAR) method as implemented in the Python 3 package *pymbar*[36–38] was used to construct the FES histogram. To reduce

noise and for representing the FESs as smooth contour plots, a Gaussian filter was used as implemented in the Python module *scipy.ndimage*.

1.9 Principal component analysis (PCA)

PCA was performed using the minimum distance between the post-entry productively bound PET ester carbon and all C_α atoms that were located at least once within 10 Å of that PET carbon during entry of the PET and the first 1 ns of its inside phase. The resulting data from both enzymes were merged, taking into account corresponding C_α atoms that were identified by superimposing both enzyme structures, resulting in a total of 49 C_α positions that were used in the PCA. The dataset of distances between these C_α atoms and PET, as described above, was subjected to PCA by using the Python 3 module *PCA* as implemented in the *decomposition* package of the *scikit learn* library (*sklearn.decomposition.PCA*).[39] The resulting principal components (PCs) are thus identical for both enzymes, yet the individual datasets per enzyme were used for constructing FESs at 303 K along the two main PCs using an inhouse Python 3 script, which calculates ΔG based on the probability distribution P along the order parameter R, here the two PCs (Eq. 1).

$$\Delta G(R) = -k_B T \left[\ln P(R) - \ln P_{\max}(R)\right] \tag{1}$$

The resulting FESs were further analyzed by identifying productive and unproductive states in the PC space and by projecting individual entry events onto the FESs.

1.10 Enzyme production and purification

PES-H1^{FY} and LCC^{ICCG} variants were produced using pET28a(+) and pET26b(+) as vectors, respectively. Genes encoding PES-H1^{FY} and LCC^{ICCG} have been synthesized and codon optimized as previously described.[10] Chemically competent *E.coli* BL21 DE3 cells were transformed with the plasmids and overnight cultures containing 50 µg/ml kanamycin were inoc-

ulated from glycerol stocks. For the expression, 250 ml of ZYM-5052 autoinduction medium containing 50 µg/ml kanamycin were added into a 1 L baffled flask and 2.5 ml of overnight culture were used for the inoculation. Cell cultures were incubated at 37 °C; 120 rpm for approximately 2 h and subsequently the temperature was reduced to 21 °C. After 21 h or 23 h of incubation for PES-H1^{FY} and LCC variants, respectively, cells were centrifuged at 12,000 g for 15 min, and pellets were resuspended in 4 ml/g cell pellet of lysis buffer (50 mM Na_2HPO_4, 300 mM NaCl, pH 8.0) and lysed using ultrasonication (2x 3 min at 50% power, 50% amplitude). After subsequent centrifugation at 12,000 g for 30 min, the enzymes were purified using cobalt-ion affinity chromatography (ROTI®Garose-His/Co Beads, Carl Roth, Karlsruhe, Germany). The supernatant was applied onto a gravity flow column and washed with either 20 mM or 50 mM imidazole (pH 8.0). The proteins were eluted with an elution buffer containing 50 mM Na_2HPO_4, 300 mM NaCl and 250 mM imidazole (pH 8.0). The imidazole was removed with a PD-10 desalting column (Cytiva, Marlborough, Massachusetts, USA) changing the buffer to 50 mM Na_2HPO_4 (pH 8.0) and proteins were concentrated with 10 kDa molecular weight cutoff centrifugal concentrators (Satorius, Goettingen, Germany). The protein concentration was determined with a Nanodrop1000 spectrophotometer.

1.11 Site directed mutagenesis

Single Mutations were introduced using the Q5® Site Directed Mutagenesis Kit (New England Biolabs GmbH, Ipswich, Massachusetts, USA). Oligonucleotides used in the polymerase chain reaction (PCR) are listed in Table S2. The successful incorporation of the mutation was confirmed by Sanger sequencing (Microsynth AG, Balgach, Switzerland).

Table S2: Oligonucleotides used for site directed mutagenesis

Mutation	**Forward Primer**	**Reverse Primer**
LCC^{ICCG} H164A	GGTGGCGGGT**gcg**AGCATGGGCGG	GCCAGACGGTTGGCATCC
LCC^{ICCG} T192G	GCCGTGGCAT**ggc**GATAAAACCTTT AACACCAGCGTGC	GTCAGCGGCACCGCCGCT
LCC^{ICCG} T211G	GGAAGCCGAT**ggc**GTGGCGCCGG	GCGCCAACAATCAGCACC
LCC^{ICCG} S241G	GTGCAACGCC**ggc**CATATTGCGC	AGTTCAACATAAACTTTC GGCGTGGTG
LCC^{ICCG} N246A	TATTGCGCCG**gcg**AGCAATAACGCGG	TGGCTGGCGTTGCACAGT
PES-$H1^{FY}$ S68A	CGGTCAGGAA**gcg**ATTGCCTGGCTG GGCCC	GCGGTAAAGCCCGGGCTG
PES-$H1^{FY}$ R91A	TACCATCACC**gcg**TTTGATTATCCG GAC	TCAATGGTAATCACCACAAAG
PES-$H1^{FY}$ D93A	CACCCGTTTT**gcg**TATCCGGACAG	ATGGTATCAATGGTAATCAC
PES-$H1^{FY}$ L175A	TGGCGCGCAG**gcg**GATACCATTGCGC	ACCACCAGCGTCGGCGTG
PES-$H1^{FY}$ N212A	TCTGGTCAGC**gcg**ACGCCGGATACC ACCACC	TGGCTGGCACCGCGCAGT

1.12 Enzymatic hydrolysis of PET film

The PET-film (Goodfellow GmbH, product number ES301445) was cut into 1x 2 cm pieces (∼60 mg), which were washed once with ethanol, afterwards with dH_2O and were dried at room temperature. Degradation of PET was performed with 1x 60 mg PET film in a 2 ml reaction vessel with an enzyme load of either 1 mg enzyme/g PET or 0.5 mg enzyme/g PET and 1 M potassium phosphate-buffer was added to a total volume of 1.5 ml. The reaction mixtures were incubated at 70 °C on a ThermoMixer C (Eppendorf, Hamburg, Germany) for 24 h at 1000 rpm. Each reaction was performed at least in duplicates. After 24 h, the remaining PET-films were washed in a 0.1% SDS solution, dH_2O and absolute ethanol and subsequently dried at 50 °C for 24 h. The weight loss through PET degradation was determined gravimetrically.

1.13 Kinetic analysis

For determining the kinetic parameters, a turbidimetric assay was applied: A mixture of 3.75 ml ROTIPHORESE® gel 30, 3 ml potassium phosphate buffer (1 M, pH 8.0), 120 µl tetramethylethylenediamine (TEMED) and PET-NP suspension (1 mg·ml^{-1}) was prepared and filled up to a final volume of 15 ml with ddH_2O. PET-NP were prepared as previously described.[40–42] A total volume of 50 µl enzyme mix was prepared by combining 2 µl of a 40% (w/v) solution of ammonium persulfate (APS) with 48 µl of the enzyme. This mixture was then mixed with 150 µl of the solution containing the substrate and acrylamide. The turbidimetric assay was carried out in a microtiter plate at a temperature of 70 °C for a duration of 40 min for each variant at least in triplicate. The substrate load concentrations varied from 0-1.5 mg/ml while keeping a constant enzyme concentration of 0.7 µM for the conventional Michaelis–Menten (^{conv}MM) setting (Eq. 2).

$$^{conv}v_0 = \frac{^{conv}V_{max}[S_0]}{^{conv}K_m + [S_0]} \tag{2}$$

The inverse Michaelis–Menten (^{inv}MM) approach included enzyme concentrations varying from 0-6 µM while keeping a fixed PET-NP concentration of 0.375 mg/ml(Eq. 3).

$$^{inv}v_0 = \frac{^{inv}V_{max}[E_0]}{^{inv}K_m + [E_0]} \tag{3}$$

The turnover rate constant k_{cat} and the catalytic efficiency $^{mass}\eta$ can be obtained from the ^{conv}MM (Eq. 4 and 5).

$$k_{cat} = \frac{^{conv}V_{max}}{[E_0]} \tag{4}$$

$$^{mass}\eta = \frac{k_{cat}}{^{conv}K_m} \tag{5}$$

For a better comparability when targeting large, insoluble substrates, the catalytic efficiency is also assessed in terms of molarity ($^{\text{molar}}\eta$) instead of mass ($^{\text{mass}}\eta$). This is not possible considering only the kinetic parameters obtained from $^{\text{conv}}$MM since $^{\text{conv}}K_M$ considers only the used substrate load in terms of mass $^{\text{mass}}[S_0]$ and not in terms of molarity as in the $^{\text{inv}}$MM approach. The accessible attack sites on the PET surface ($^{\text{molar}}[S_0]$) can be obtained by defining the density of attack sites per gram PET (Γ_{attack}) (Eq. 6).

$$^{\text{molar}}[S_0] = ^{\text{mass}}[S_0] \cdot \Gamma_{\text{attack}} \tag{6}$$

Γ_{attack} can be obtained by taking the $^{\text{inv}}$MM parameters into account (Eq. 7), which then also allows to estimate a molar $^{\text{molar}}K_{\text{m}}$ for the $^{\text{conv}}$MM setting (Eq. 8) and, thus, the $^{\text{molar}}\eta$ (Eq. 9).[43,44]

$$\Gamma_{\text{attack}} = \frac{^{\text{inv}}V_{\text{max}}/[S_0]}{^{\text{conv}}V_{\text{max}}/[E_0]} \tag{7}$$

$$^{\text{molar}}K_{\text{m}} = ^{\text{conv}}K_{\text{m}} \cdot \Gamma_{\text{attack}} \tag{8}$$

$$^{\text{molar}}\eta = \frac{k_{cat}}{^{\text{molar}}K_{\text{m}}} = \frac{^{\text{mass}}\eta}{\Gamma_{\text{attack}}} \tag{9}$$

2 Supplementary Figures

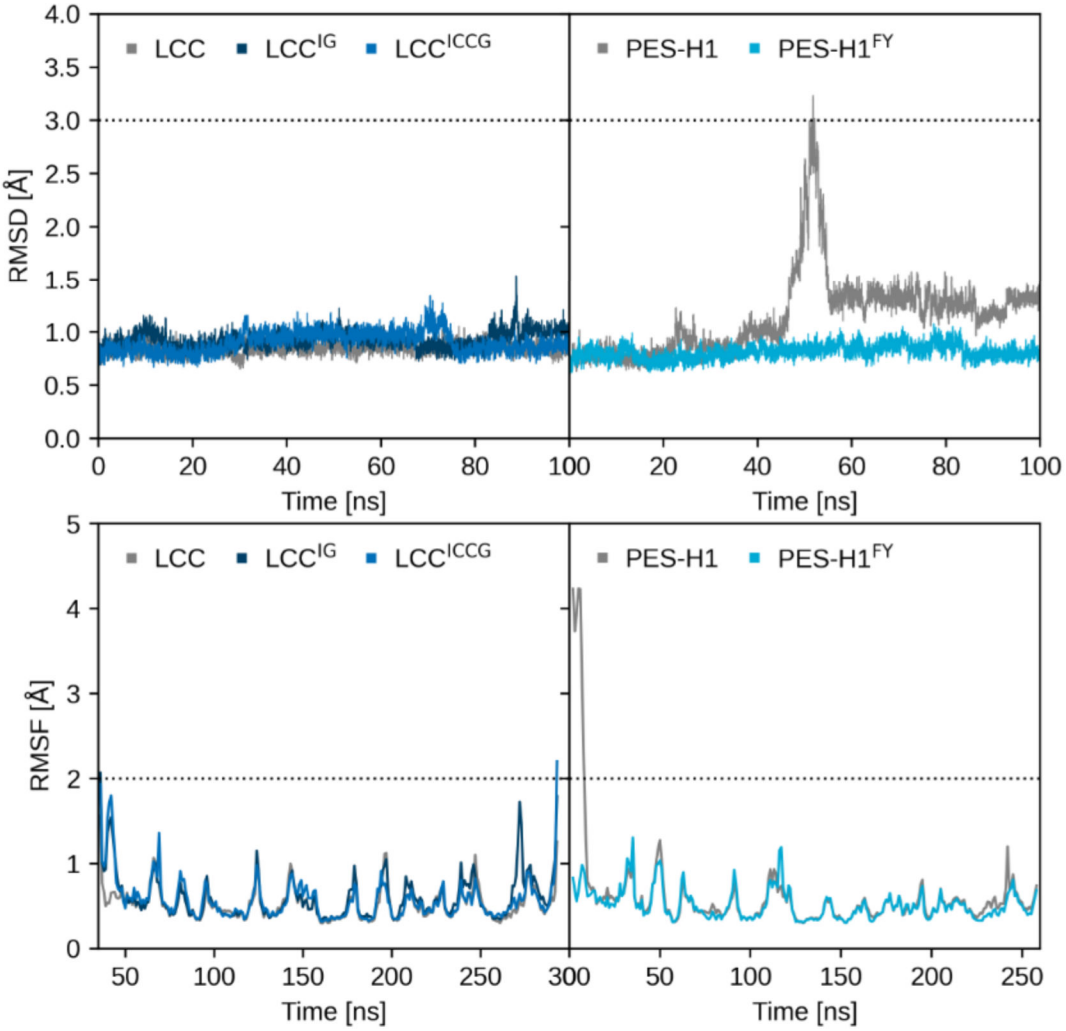


Figure S1: RMSD (top) and RMSF (bottom) of LCC, LCC^{IG} and LCC^{ICCG} (gray, darkblue and blue, left) and PES-H1 and $PES\text{-}H1^{FY}$ (gray and lightblue, right). We define an RMSD difference of 3 Åwith respect to the starting structure of the simulation as a significant structural difference, which is only observed once for PES-H1 at around 50 ns. This structural change results from structural flexibilities in the first ten disordered N-terminal residues, which can be recognized by the large RMSF values in this region. The RMSF specifies the flexibility per residue, whereby an RMSF below 2 Å defines a rigid residue and above this value a flexible one. Overall, the structures of all four proteins were consistently rigid throughout the simulations.

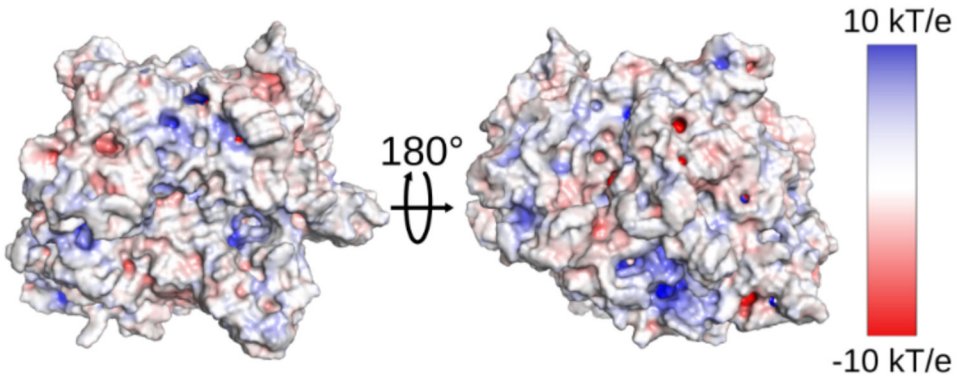


Figure S2: The EPS of the PET bulk used in this study is shown from two perspectives with a positive EPS colored in blue and a negative colored in red, while hydrophobic areas are shown in white.

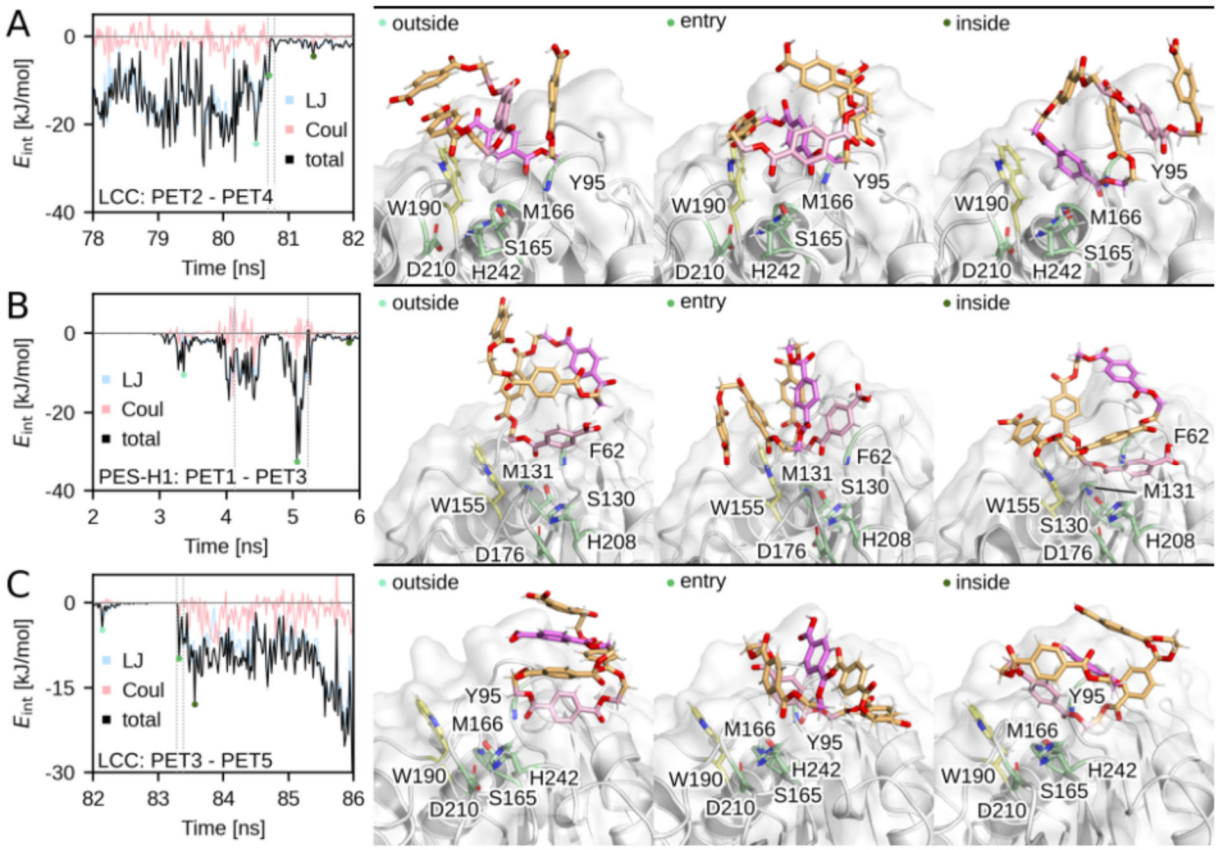


Figure S3: Examples of intramolecular PET interactions before PET entry into the binding site (A, LCC, PET2–PET4 interactions), during entry (B, PES-H1, PET1–PET3), and after entry (C, LCC, PET3–PET5). The left plots show the evolution of these interaction energies, E_{int}, which comprise polar Coulomb (Coul) and hydrophobic Lennard-Jones (LJ) interactions, during 4 ns snippets of the entry process. The actual entry phase is indicated by vertical dotted lines. Structures for each of the three entry events are shown on the right-hand side, with a snapshot from each phase (outside, entry, inside) being presented. The times at which these snapshots were sampled are indicated by green-colored spheres in the plots on the left. In the structures, the catalytic triad and the oxyanion hole are shown in green, the 'wobbling' tryptophan in yellow, PET in orange, and the two interacting PET units in light pink (lower residue ID) and dark pink (higher residue ID).

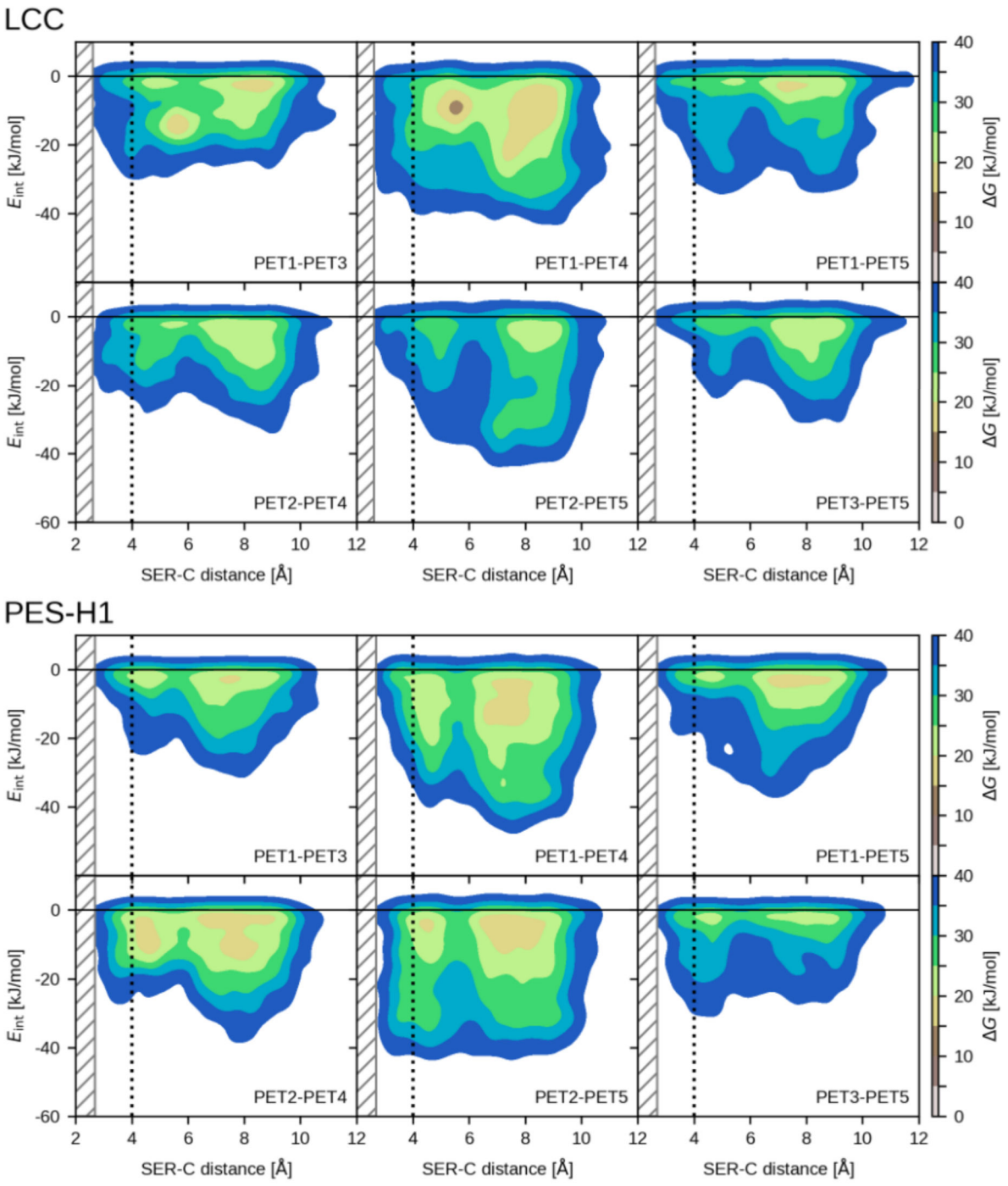


Figure S4: Free energy surfaces of PET–PET interactions over the SER–C distance sampled during LCC (top) and PES-H1 (bottom) simulations. The area with a minimum SER–C distance <4 Å harbors productive poses. The gray hatched area indicates distances that were not sampled, resulting in a truncated FES.

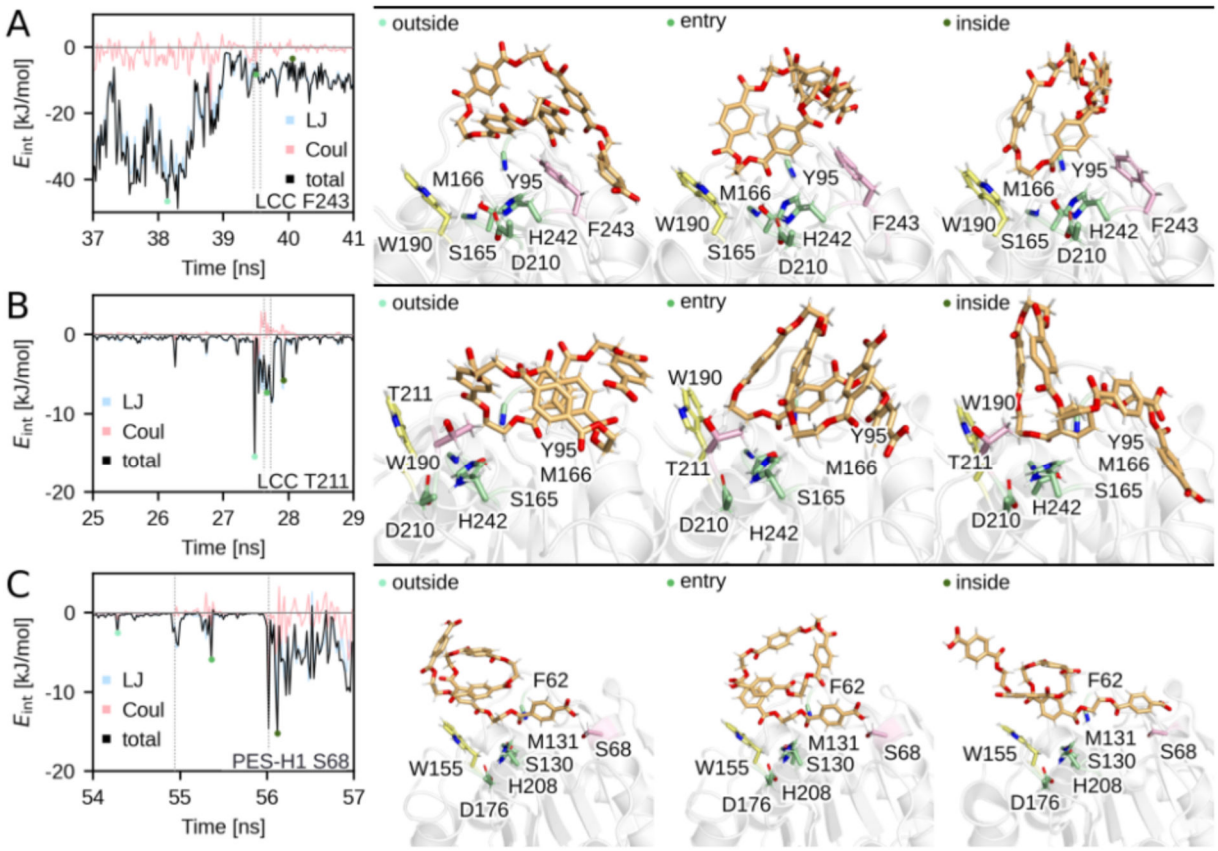


Figure S5: Examples of residues interacting with PET before PET entry into the binding site (A, with LCC F243), during entry (B, with LCC T211), and after entry (C, with PES-H1 S68). The left plots show the evolution of these interaction energies, E_{int}, which comprise polar Coulomb (Coul) and hydrophobic Lennard-Jones (LJ) interactions, during 4 ns snippets of the entry process. The actual entry phase is indicated by vertical dotted lines. Structures for each of the three entry events are shown on the right-hand side, with a snapshot from each phase (outside, entry, inside) being presented. The times at which these snapshots were sampled are indicated by green-colored spheres in the plots on the left. The catalytic triad and oxyanion hole are shown in green, the 'wobbling' tryptophan in yellow, PET in orange, and the interacting residue in pink.

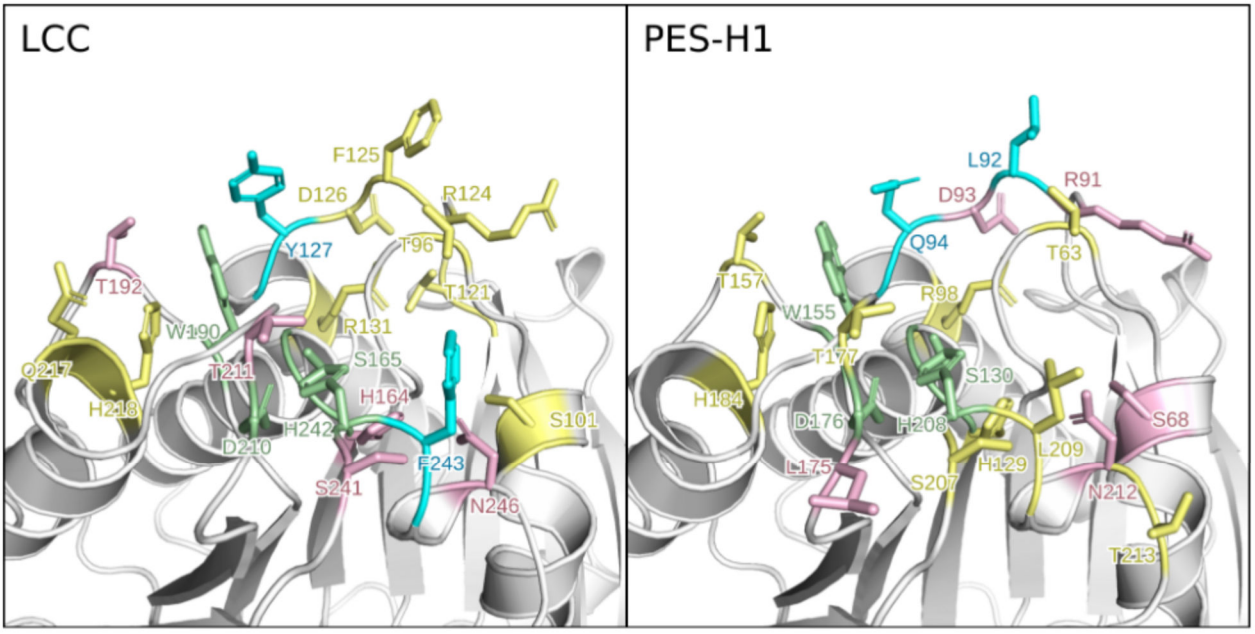


Figure S6: Mutation sites of variants addressed using the FES approach. The catalytic triad residues as well as the 'wobbling' tryptophan are shown in green, the LCC^{IG} and PES-H1^{FY} mutation sites in cyan, the experimentally evaluated mutation sites in red, and all other mutation sites in yellow.

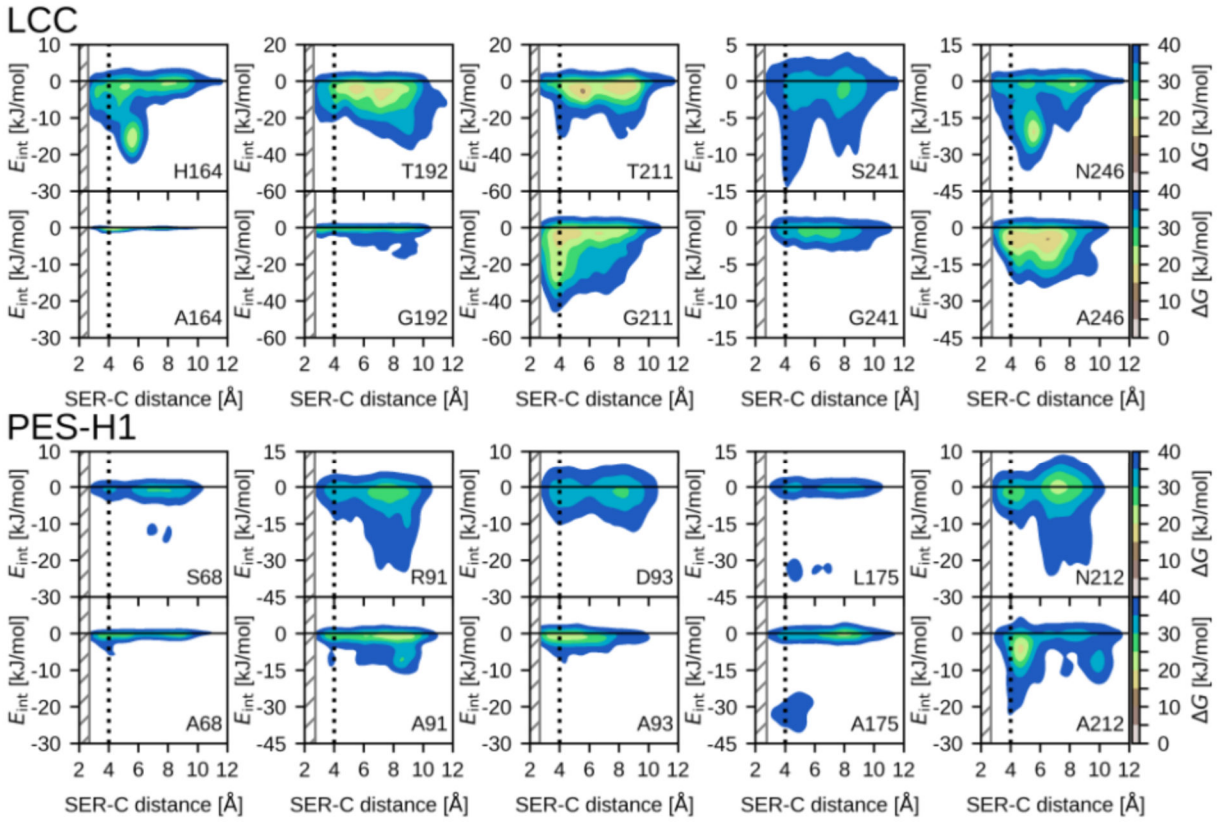


Figure S7: Free energy surfaces of PET–residue interactions over the SER–C distance sampled during LCC and PES-H1 and corresponding variant simulations. The top rows present the FES for WT residues and the bottom row for mutated residues. The area with a minimum SER–C distance <4 Å harbors productive poses. The gray hatched area indicates distances that were not sampled, resulting in a truncated FES.

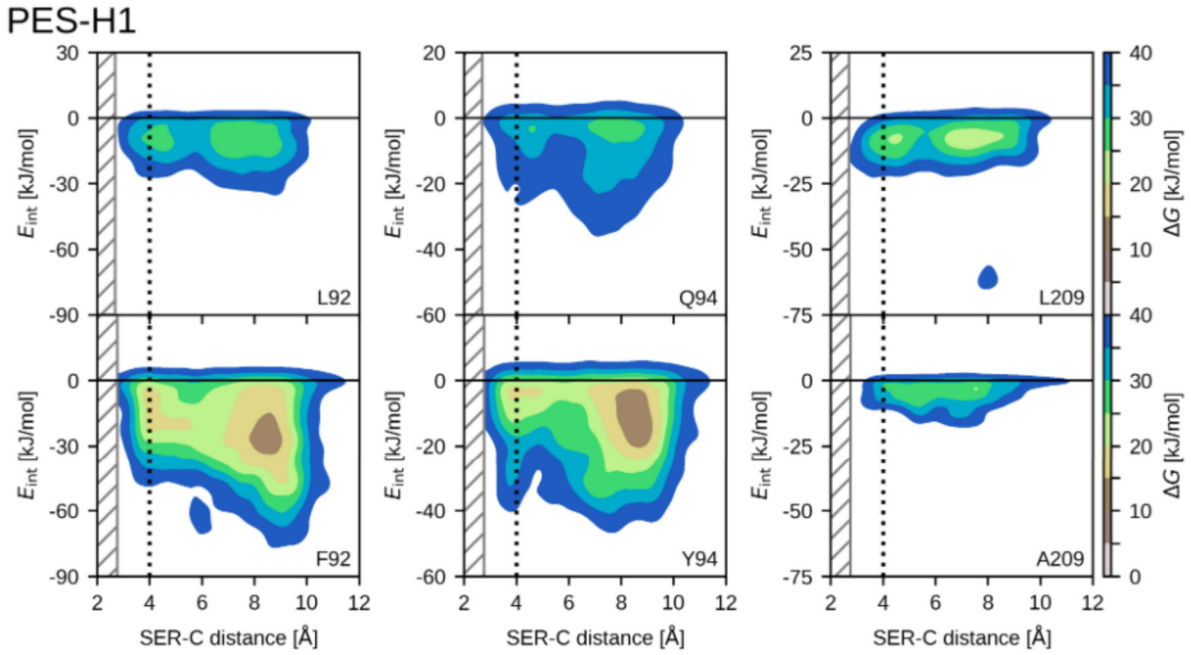


Figure S8: Free energy surfaces of PET–residue interactions at position 68 over the SER–C distance sampled during PES-H1 and corresponding PES-H1^{FY} variant simulations. The left FES shows the interaction of the WT S68 and the remaining ones of variants. The area with a minimum SER–C distance <4 Å harbors productive poses. The gray hatched area indicates distances that were not sampled, resulting in a truncated FES.

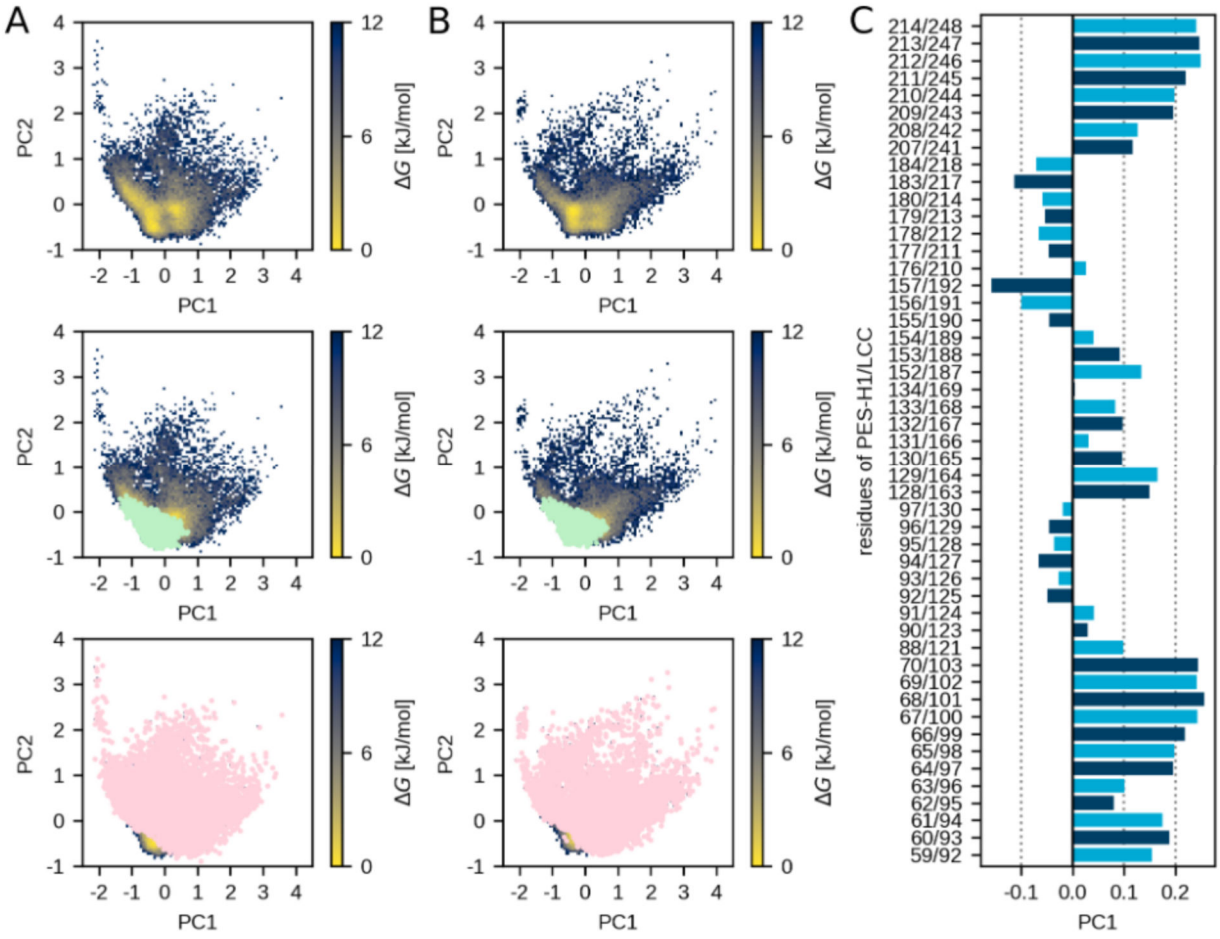


Figure S9: The FES over PC1 and PC2 of LCC (A) and PES-H1 (B), accompanied by the contribution profile of amino acid positions to PC1 (C). In the central figure of A and B, productive states of PET in the active site of each enzyme are highlighted in green, while the lower figure depicts unproductive states in red.

3 Supplementary Tables

Table S3: Maximum reaction rate $V_{\max}$ for both settings, $^{\text{conv}}$MM, $^{\text{inv}}$MM derived from the nonlinear fit to experimental data as well as $^{\text{molar}}\eta$ and Γ_{attack}.

	$^{\text{conv}}\mathbf{V}_{\max}[\mathbf{min^{-1}}]$	$^{\text{inv}}\mathbf{V}_{\max}[\mathbf{min^{-1}}]$	$^{\text{mass}}\eta[\frac{\mathbf{L^2}}{\mathbf{g \cdot min \mu mol}}$	$\mathbf{\Gamma}_{\text{attack}}\left[\frac{\mathbf{\mu mol}}{\mathbf{g}}\right]$
LCC$^{\text{ICCG}}$	0.033 ±0.003	0.029 ±0.001	0.219	1.659
LCC$^{\text{ICCG}}$ H164A	0.022 ±0.003	0.035 ±0.002	0.335	2.931
LCC$^{\text{ICCG}}$ T211G	0.029 ±0.005	0.039 ±0.003	0.462	2.450
LCC$^{\text{ICCG}}$ S241G	0.038 ±0.003	0.029 ±0.002	0.217	1.433
PES-H1$^{\text{FY}}$	0.062 ±0.006	0.088 ±0.003	0.226	2.646
PES-H1$^{\text{FY}}$ S68A	0.059 ±0.007	0.064 ±0.003	0.234	2.038
PES-H1$^{\text{FY}}$ D93A	0.028 ±0.004	0.072 ±0.007	0.079	4.860
PES-H1$^{\text{FY}}$ N212A	0.047 ±0.007	0.082 ±0.006	0.140	3.250

References

(1) Frisch, M. J. et al. Gaussian 09 Revision E.01. Gaussian Inc. Wallingford CT 2009.

(2) Wang, J.; Wolf, R. M.; Caldwell, J. W.; Kollman, P. A.; Case, D. A. Development and testing of a general amber force field. *J Comput Chem* **2004**, *25*, 1157–1174.

(3) Bayly, C. I.; Cieplak, P.; Cornell, W.; Kollman, P. A. A well-behaved electrostatic potential based method using charge restraints for deriving atomic charges: The RESP model. *J Phys Chem* **1993**, *97*, 10269–10280.

(4) Cornell, W. D.; Cieplak, P.; Bayly, C. I.; Kollman, P. A. Application of RESP charges to calculate conformational energies, hydrogen bond energies, and free energies of solvation. *J Am Chem Soc* **1993**, *115*, 9620–9631.

(5) Wang, J.; Wang, W.; Kollman, P. A.; Case, D. A. Automatic atom type and bond type perception in molecular mechanical calculations. *J Mol Graph Model* **2006**, *25*, 247 – 260.

(6) Wang, J.; Wang, W.; Kollman, P.; Case, D. ANTECHAMBER: an accessory software package for molecular mechanical calculations. *JCISD* **2000**, *222*, U403.

(7) Case, D. et al. AMBER 2021. University of California, San Francisco, 2021.

(8) Abraham, M.; Murtola, T.; Schulz, R.; Páll, S.; Smith, J.; Hess, B.; Lindahl, E. GROMACS: High performance molecular simulations through multi-level parallelism from laptops to supercomputers. *SoftwareX* **2015**, *1-2*, 19–25.

(9) Sousa da Silva, A. W.; Vranken, W. F. ACPYPE - AnteChamber PYthon Parser interfacE. *BMC Res Notes* **2012**, *5*, 367.

(10) Pfaff, L. et al. Multiple substrate binding mode-guided engineering of a thermophilic PET hydrolase. *ACS Catal* **2022**, *12*, 9790–9800.

(11) Jorgensen, W.; Chandrasekhar, J.; Madura, J.; Impey, R.; Klein, M. Comparison of simple potential functions for simulating liquid water. *J Chem Theory Comput* **1983**, *79*, 926–935.

(12) Cauchy, M. A. Méthode générale pour la résolution des systèmes d' équations simultanées. *CR Hebd Acad Sci* **1847**, *25*, 536–538.

(13) Bussi, G.; Donadio, D.; Parrinello, M. Canonical sampling through velocity rescaling. *J Chem Phys* **2007**, *126*.

(14) Berendsen, H. J. C.; Postma, J. P. M.; van Gunsteren, W. F.; DiNola, A.; Haak, J. R. Molecular dynamics with coupling to an external bath. *J Chem Phys* **1984**, *81*, 3684–3690.

(15) Nosé, S. Molecular-dynamics method for simulations in the canonical ensemble. *Mol Phys* **1984**, *52*, 255–268.

(16) Hoover, W. Canonical dynamics - equilibrium phase-space distributions. *Phys Rev A* **1985**, *31*, 1695–1697.

(17) Parrinello, M.; Rahman, A. Polymorphic transitions in single-crystals - a new molecular-dynamics method. *Mol Phys* **1981**, *52*, 7182–7190.

(18) Maier, J. A.; Martinez, C.; Kasavajhala, K.; Wickstrom, L.; Hauser, K. E.; Simmerling, C. ff14SB: Improving the accuracy of protein side chain and backbone parameters from ff99SB. *J Chem Theory Comput* **2015**, *11*, 3696–3713.

(19) Ivani, I. et al. Parmbsc1: a refined force field for DNA simulations. *Nat Methods* **2016**, *13*, 55.

(20) Hess, B.; Bekker, H.; Berendsen, H.; Fraaije, J. LINCS: A linear constraint solver for molecular simulations. *J Comput Chem* **1997**, *18*, 1463–1472.

(21) Gunsteren, W. F. V.; Berendsen, H. J. C. A leap-frog algorithm for stochastic dynamics. *Mol Simulat* **1988**, *1*, 173–185.

(22) Darden, T.; York, D.; Pedersen, L. Particle mesh Ewald - an $N \cdot log(N)$ method for Ewald sums in large systems. *J Chem Phys* **1993**, *98*, 10089–10092.

(23) Essmann, U.; Perera, L.; Berkowitz, M. A smooth particle mesh Ewald method. *J Chem Phys* **1995**, *103*, 8577–8593.

(24) Humphrey, W.; Dalke, A.; Schulten, K. VMD - Visual Molecular Dynamics. *J Mol Graph* **1996**, *14*, 33–38.

(25) Schrödinger, LLC The PyMOL molecular graphics system, Version 1.8. 2015.

(26) Rossum, G. V.; Drake, F. L. Python 3 Reference Manual. CreateSpace: Scotts Valley, CA, 2009.

(27) Daura, X.; Gademann, K.; Jaun, B.; Seebach, D.; van Gunsteren, W. F.; Mark, A. E. Peptide folding: When simulation meets experiment. *Angew Chem Int Edit* **1999**, *38*, 236–240.

(28) Grochowski, P.; Trylska, J. Continuum molecular electrostatics, salt effects, and counterion binding-a review of the Poisson-Boltzmann theory and its modifications. *Biopolymers* **2008**, *89*, 93–113.

(29) Jurrus, E. et al. Improvements to the APBS biomolecular solvation software suite. *Protein Sci* **2018**, *27*, 112–128.

(30) Sulaiman, S.; You, D.-J.; Kanaya, E.; Koga, Y.; Kanaya, S. Crystal structure and thermodynamic and kinetic stability of metagenome-derived LC-Cutinase. *Biochemistry* **2014**, *53*, 1858–1869.

(31) Olsson, M. H.; Søndergaard, C. R.; Rostkowski, M.; Jensen, J. H. PROPKA3: Consistent treatment of internal and surface residues in empirical pKa predictions. *J Chem Theory Comput* **2011**, *7*, 525–537.

(32) Søndergaard, C. R.; Olsson, M. H. M.; Rostkowski, M.; Jensen, J. H. Improved treatment of ligands and coupling effects in empirical calculation and rationalization of pKa values. *J Chem Theory Comput* **2011**, *7*, 2284–2295.

(33) Cruz-Chu, E. R.; Ritz, T.; Siwy, Z. S.; Schulten, K. Molecular control of ionic conduction in polymer nanopores. *Faraday Discuss* **2009**, *143*, 47–62.

(34) The PLUMED consortium Promoting transparency and reproducibility in enhanced molecular simulations. 2019.

(35) Bussi, G. Hamiltonian replica exchange in GROMACS: a flexible implementation. *Mol Phys* **2014**, *112*, 379–384.

(36) Shirts, M. R.; Ferguson, A. L. Statistically optimal continuous free energy surfaces from biased simulations and multistate reweighting. *J Chem Theory Comput* **2020**, *16*, 4107–4125.

(37) Chodera, J. D. A simple method for automated equilibration detection in molecular simulations. *J Chem Theory Comput* **2016**, *12*, 1799–1805.

(38) Shirts, M. R.; Chodera, J. D. Statistically optimal analysis of samples from multiple equilibrium states. *J Chem Phys* **2008**, *129*, 124105.

(39) Pedregosa, F. et al. Scikit-learn: Machine Learning in Python. *J Mach Learn Res* **2011**, *12*, 2825–2830.

(40) Vogel, K.; Wei, R.; Pfaff, L.; Breite, D.; Al-Fathi, H.; Ortmann, C.; Estrela-Lopis, I.; Venus, T.; Schulze, A.; Harms, H.; Bornscheuer, U. T.; Maskow, T. Enzymatic degradation of polyethylene terephthalate nanoplastics analyzed in real time by isothermal titration calorimetry. *Sci Total Environ* **2021**, *773*, 145111.

(41) Brott, S.; Pfaff, L.; Schuricht, J.; Schwarz, J.-N.; Böttcher, D.; Badenhorst, C. P. S.; Wei, R.; Bornscheuer, U. T. Engineering and evaluation of thermostable *Is*PETase variants for PET degradation. *Eng Life Sci* **2022**, *22*, 192–203.

(42) Pfaff, L.; Breite, D.; Badenhorst, C. P.; Bornscheuer, U. T.; Wei, R. In *Enzymatic Plastic Degradation*; Weber, G., Bornscheuer, U. T., Wei, R., Eds.; Methods in Enzymology; Academic Press, 2021; Vol. 648; pp 253–270.

(43) Bååth, J. A.; Borch, K.; Jensen, K.; Brask, J.; Westh, P. Comparative biochemistry of four polyester (PET) hydrolases**. *ChemBioChem* **2021**, *22*, 1627–1637.

(44) Kari, J.; Andersen, M.; Borch, K.; Westh, P. An inverse Michaelis–Menten approach for interfacial enzyme kinetics. *ACS Catal* **2017**, *7*, 4904–4914.

bioRxiv preprint doi: https://doi.org/10.1101/2024.04.30.591886; this version posted April 30, 2024. The copyright holder for this preprint (which was not certified by peer review) is the author/funder, who has granted bioRxiv a license to display the preprint in perpetuity. It is made available under aCC-BY 4.0 International license.

Influence of Wobbling Tryptophan and Mutations on PET Degradation Explored by QM/MM Free Energy Calculations

Anna Jäckering,[†,‡] Marc van der Kamp,[¶] Birgit Strodel,[*,†,‡] and Kirill Zinovjev[*,§]

[†]*Institute of Theoretical and Computational Chemistry, Heinrich Heine University, Düsseldorf, Universitätsstr. 1, 40225 Düsseldorf, Germany*

[‡]*Institute of Biological Information Processing: Structural Biochemistry (IBI-7), Forschungszentrum Jülich, Wilhelm-Johnen-Straße, 52428 Jülich, Germany*

[¶]*School of Biochemistry, University Walk, University of Bristol, Bristol BS8 1TD, United Kingdom*

[§]*Departament de Química Física, Universitat de València, 46100 Burjassot, Spain*

E-mail: b.strodel@fz-juelich.de; kirill.zinovjev@uv.es

Abstract

Plastic-degrading enzymes, particularly poly(ethylene terephthalate) (PET) hydrolases, have garnered significant attention in recent years as potential eco-friendly solutions for recycling plastic waste. However, understanding of their PET-degrading activity and influencing factors remains incomplete, impeding the development of uniform approaches for enhancing PET hydrolases for industrial applications. A key aspect of PET hydrolase engineering is optimizing the PET-hydrolysis reaction by lowering the associated free energy barrier. However, inconsistent findings have complicated these efforts. Therefore, our goal is to elucidate various aspects of enzymatic PET degradation by means of quantum mechanics / molecular mechanics (QM/MM) reaction simulations

bioRxiv preprint doi: https://doi.org/10.1101/2024.04.30.591886; this version posted April 30, 2024. The copyright holder for this preprint (which was not certified by peer review) is the author/funder, who has granted bioRxiv a license to display the preprint in perpetuity. It is made available under aCC-BY 4.0 International license.

and analysis, focusing on the initial reaction step, acylation, in two thermophilic PET hydrolases: LCC and PES-H1, along with their highly active variants, LCC^{ICCG} and PES-H1^{FY}. Our findings highlight the impact of semi-empirical QM methods on proton transfer energies, affecting the distinction between a two-step reaction involving a metastable tetrahedral intermediate and a one-step reaction. Moreover, we uncovered a concerted conformational change involving the orientation of the PET benzene ring, altering its interaction with the side-chain of the 'wobbling' tryptophan from T-stacking to parallel π-π interactions, a phenomenon overlooked in prior research. Our study thus enhances the understanding of the acylation mechanism of PET hydrolases, in particular by characterizing it for the first time for the promising PES-H1^{FY} using QM/MM simulations. It also provides insights into selecting a suitable QM method and a reaction coordinate, valuable for future studies on PET degradation processes.

1 Introduction

Synthetic polymers, commonly referred to as plastics, have gained significant attraction in the global market due to their durability, affordability, and versatility.[1,2] Presently, degradation methods for the immense amount of accumulated plastic waste are both environmentally and economically costly, pressing the need for an eco-friendly and efficient alternative.[3] Enzymatic degradation emerges as a promising solution, particularly focusing on poly(ethylene terephthalate) (PET), a widely used plastic in packaging and textiles.[4,5] The discovery of enzymes capable of PET degradation in 2005[6] and the identification of *Ideonella sakaiensis* as an organism metabolizing PET[7] in 2016 have paved the way for enzymatic degradation.

Enzymes with PET-degradation function are often found among hydrolases (EC 3.1.1.x) and specifically cutinases (EC 3.1.1.74), but are now often categorized into the novel class of polyester hydrolases (EC 3.1.1.101).[7–9] These enzymes share an α/β-hydrolase fold characterized by a core comprising eight β-strands and six α-helices with a surface-exposed catalytic triad typically composed of serine, aspartate, and histidine, facilitating PET hydrolysis.[10,11]

bioRxiv preprint doi: https://doi.org/10.1101/2024.04.30.591886; this version posted April 30, 2024. The copyright holder for this preprint (which was not certified by peer review) is the author/funder, who has granted bioRxiv a license to display the preprint in perpetuity. It is made available under aCC-BY 4.0 International license.

Despite some wild-type (WT) enzymes exhibiting high activities, enzyme engineering is necessary to enhance efficiency and stability to facilitate industrial application, yielding two of the currently most active PET-degrading enzymes, the leave-branch compost cutinase F243I/D238C/S283C/Y127G (LCC^{ICCG}) and polyester hydrolase I L92F/Q94Y ($PES\text{-}H1^{FY}$) variants.[5,12,13] Notable, these two variants share a mutation at the same position, yet with divergent effects: activity of LCC could be enhanced by elimination of tyrosine (Y127G) in addition to other mutations present in the LCC^{ICCG} variant, while an introduction of tyrosine (Q94Y) in combination with introduction of phenylalanine in close proximity yielded the $PES\text{-}H1^{FY}$ variant with increased activity.[5,13] We previously found that the entry of PET into the active binding cleft and the subsequent Michaelis complex (MC) formation is promoted by the LCC F243I/Y127G (IG) variant[14] but the precise effect remains unclear and demands elucidation of the energy profile of the first reaction step, the acylation, to fully understand MC stabilization.

The catalytic hydrolysis reaction of several PET-degrading enzymes was investigated using quantum mechanics/molecular mechanics (QM/MM) simulation studies, which enable investigation of the region contributing to the target reaction at the QM level for bond breaking and formation, while managing the computational demand by treating the remaining part of the system at the MM level.[15–17] These studies revealed two predominant binding poses of PET: pro-S[18–20] and pro-R.[5,21] An energetic preference for catalysis starting from the pro-S pose is proposed, which allows for T-stacking π-π interactions between PET's benzene ring and a conserved tryptophan positioned at one end of the catalytic binding cleft, which is also called 'wobbling' tryptophan (LCC: W190, PES-H1: W155).[15,22] The catalysis mechanism after substrate binding can be divided into two main processes: acylation and deacylation (Fig. 1).[15–17,23–26]

bioRxiv preprint doi: https://doi.org/10.1101/2024.04.30.591886; this version posted April 30, 2024. The copyright holder for this preprint (which was not certified by peer review) is the author/funder, who has granted bioRxiv a license to display the preprint in perpetuity. It is made available under aCC-BY 4.0 International license.

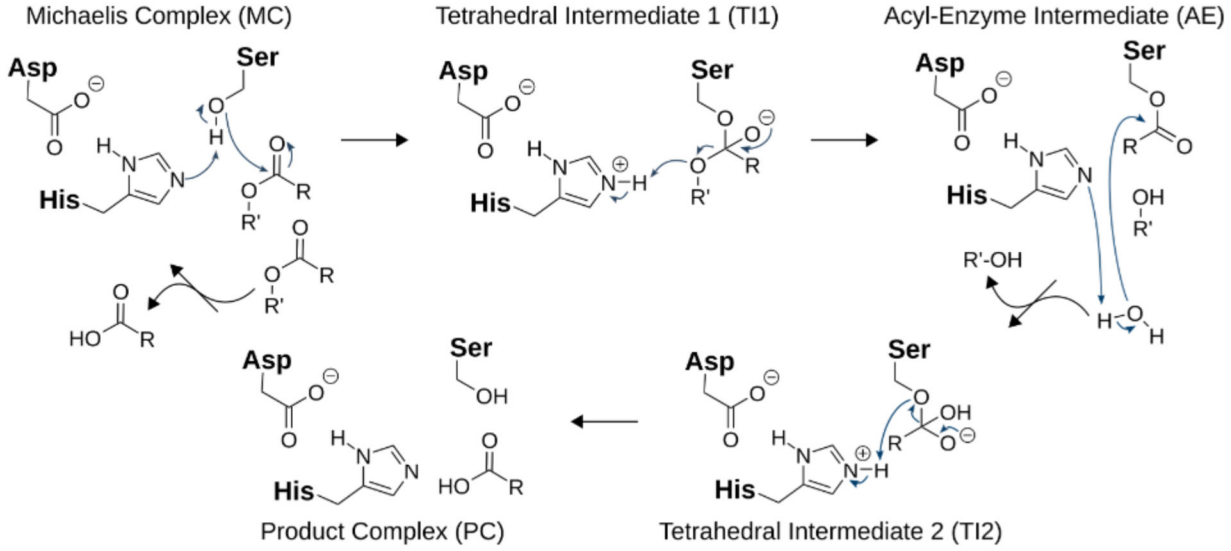


Figure 1: Mechanism of PET-degradation as proposed by Boneta *et al.*[15] The mechanism can be divided into two steps: First, the acylation of the Michaelis complex (MC) yielding the acyl-enzyme intermediate (AE) and second, the hydrolysis yielding the product complex (PC), both incorporating a tetrahedral intermediate (TI).

During acylation, the catalytic serine's nucleophilicity increases via proton transfer to the catalytic histidine, which is polarized by the catalytic aspartate. This facilitates nucleophilic attack on the ester's carbonyl carbon, with the resulting oxyanion stabilized by the oxyanion hole. Subsequent cleavage of the ester bond yields the acyl-enzyme intermediate (AE), releasing an alcohol molecule from the active site after a proton transfer from the catalytic histidine to the resulting oxyanion. In deacylation, a water molecule's oxygen nucleophilically attacks the carbonyl carbon of AE, generating a second tetrahedral intermediate (TI) and reprotonating the catalytic histidine. Finally, the AE bond breaks, yielding the second product with a carboxyl group, while the serine is reprotonated, restoring the initial state. Products comprise smaller PET oligomers, as well as mono(2-hydroxyethyl) terephthalic acid (MHET), bis(2-hydroxyethyl) terephthalic acid (BHET) and the final monomers terephthalic acid (TPA) and ethylene glycol (EG).[27–29]

There is debate over whether acylation and deacylation occur in one or two steps, with the TI potentially representing a tetrahedral transition state (TS).[15,16] Identifying the rate-determining step remains challenging, with some studies suggesting acylation and others

bioRxiv preprint doi: https://doi.org/10.1101/2024.04.30.591886; this version posted April 30, 2024. The copyright holder for this preprint (which was not certified by peer review) is the author/funder, who has granted bioRxiv a license to display the preprint in perpetuity. It is made available under aCC-BY 4.0 International license.

deacylation.[15,17,23–26,30,31] Product diffusion from the active site, necessary for subsequent substrate hydrolysis, may also be rate-limiting, as suggested by Shrimpton-Phoenix *et al.*,[31] though other simulations contest this notion.[26] Various studies discuss the catalytic histidine's polarisation mechanisms, considering proton transfer in addition to pure polarisation.[20,25,31] QM/MM studies highlight the role of specific amino acids (Ser, Ile, Ala) near the catalytic aspartate in stabilising the histidine, influencing proton transfer dynamics.[23,32] The choice of the QM region significantly impacts observations, with larger regions offering greater accuracy but escalating computational costs. Mutation experiments confirm the importance of isoleucine, with alanine substitutions resulting in activity loss.[23] Such insights are crucial for evaluating mutation sites, particularly in enzyme redesign aiming to lower the free activation energy by stabilising transition states, beyond substrate binding.[33,34]

Another interesting residue is a conserved tryptophan, the 'wobbling' tryptophan, which exhibits three different conformations in the mesophilic *Ideonella sakaiensis* PETase (*Is*PETase), while maintaining a single conformation in other, mostly thermophilic polyester hydrolases.[20,35] This rigidity is attributed to steric hindrance by a nearby histidine, which in *Is*PETase is substituted by a serine. Extensive MD and metadynamics simulations, coupled with experimental analyses, have revealed that the presence of this serine and an adjacent isoleucine in *Is*PETase, instead of histidine and phenylalanine in other PET-degrading enzymes, enhances the flexibility of the tryptophan and loop regions within the active site, positively impacting activity.[36,37] Moreover, the conformational flexibility of tryptophan allows T-shaped π-π interactions with PET's benzene ring, thereby expanding the space within the active site and favoring PET binding. Following hydrolysis, suggested conformational changes of the PET benzene ring lead to energetically less favored face-to-face stacking and promote product release.[20,35,37]

The detailed impact of the 'wobbling' tryptophan on the reaction energetics remains unexplored. Moreover, prior publications propose inconsistent conclusions regarding whether the acylation and deacylation mechanism occurs as a one- or two-step process.[15–17,26] To

bioRxiv preprint doi: https://doi.org/10.1101/2024.04.30.591886; this version posted April 30, 2024. The copyright holder for this preprint (which was not certified by peer review) is the author/funder, who has granted bioRxiv a license to display the preprint in perpetuity. It is made available under aCC-BY 4.0 International license.

address these questions, we aim to elucidate the conformational changes of the benzene ring of PET that alter its interaction with the 'wobbling' tryptophan, and to shed light free energy profile of the acylation reaction to distinguish between one- and two-step mechanisms.

For this reason, we performed QM/MM simulations of the acylation step of PES-H1 and LCC as well as their variants, PES-H1^{FY} and LCC^{IG}, the latter representing LCC^{ICCG} excluding the stabilizing disulfide bridge. This is the first QM/MM investigation of PES-H1, and provide additional insights into the LCC, which has been analyzed in several previous studies and thus allows for comparison and validation of our results.[15,17,22,24,32] The QM/MM method is used in combination with the adaptive string method (ASM),[38] which offers a flexible approach for incorporating collective variables to delineate the reaction pathway. This methodology sheds light on the previously overlooked impact of the 'wobbling' tryptophan, addressing gaps in our understanding of PET degradation mechanisms, thus helping to drive the development of industrially applicable enzymes.

2 Methods

2.1 Parameterisation

The parameterisation of a small PET analogue, comprised of three units, has been previously documented by Pfaff and colleagues.[13] To model the analogue of AE, three residues additional were parameterised using the same methodology applied to PET. These residues specifically represent the serine bonded to PET and two residues corresponding to the units subsequent to the cleavage of the connecting ester bond.

The parameterisation procedure involved quantum mechanics calculations conducted at the HF/6-31G* level using Gaussian 09.[39] This was undertaken to establish generalised AMBER force field (GAFF)[40] parameters for both the terminal and central units. Subsequently, restrained electrostatic potential (RESP) calculations[41,42] were executed through the antechamber tool[43,44] available in AmberTools 21.[45] This step aimed to derive partial

bioRxiv preprint doi: https://doi.org/10.1101/2024.04.30.591886; this version posted April 30, 2024. The copyright holder for this preprint (which was not certified by peer review) is the author/funder, who has granted bioRxiv a license to display the preprint in perpetuity. It is made available under aCC-BY 4.0 International license.

charges, which were then redistributed using prepgen to achieve a zero net charge for each PET unit. Finally, input files for the GROMACS simulation software[46] were generated using the ACPYPE tool.[47]

2.2 Preparation of Input Structures

For each enzyme, namely LCC and PES-H1, the pro-*S* conformation with the minimal distance between the PET ester carbon and the catalytic serine's γ-oxygen was extracted from the WT HREMD simulations, as detailed in a previous publication.[14] These starting structures comprised a single PET molecule involving five units besides the enzyme. To ensure compatibility with the AMBER software utilised in this study, the system was resolvated and setup using *tleap*, as the solvated box generated from GROMACS[46] is not congruent with the box types employed in AMBER.[48] Starting structures for the variants were obtained by introducing mutations to the WT structures, ensuring similar PET binding poses for improved comparability. The system was solvated and neutralised by the addition of TIP3P water and sodium or chloride ions, respectively. The system was represented using the AMBER14SB force field, and parameters for all three PET unit types were incorporated using *tleap* as implemented in AMBER. The protonation states of titratable amino acids were maintained as originally suggested by Propka 3.4,[49,50] resulting in a net charge of +5 for LCC and LCC IG, and –5 for PES-H1 and PES-H1 FY.[14] The final system's energy was locally minimised using the steepest descent algorithm[51] followed by the conjugate gradient algorithm.[52] Subsequent equilibration runs were performed at a temperature of 303 K and pressure of 1 bar in the NVT and NPT ensemble, utilising the Langevin thermostat[53] and the Berendsen barostat,[54] respectively, with restraints applied to the position of the protein and PET. The production run spanned 20 ns in the NPT ensemble, incorporating one-sided harmonic distance restraints to maintain the PET ester in a productive pose. The harmonic restraint, up to 20 kcal/mol/Å^2, was initiated for a distance above 3.5 Å between the catalytic serine's γ-oxygen and PET's ester carbon, and for a distance above 3 Å between PET's ester

bioRxiv preprint doi: https://doi.org/10.1101/2024.04.30.591886; this version posted April 30, 2024. The copyright holder for this preprint (which was not certified by peer review) is the author/funder, who has granted bioRxiv a license to display the preprint in perpetuity. It is made available under aCC-BY 4.0 International license.

carbonyl-oxygen and the centre of mass of the backbone amine's nitrogen of the oxyanion hole residues, respectively. This restraint becomes linear for distances above 10 Å. A periodic box was employed for all runs, SHAKE algorithm was used[55] to constrain hydrogen bonds. To reduce computational demand, a cutoff at 8 Å for short-range non-bonded interactions was introduced, and the PME method[56,57] was applied to treat electrostatic interactions.

The AE was created from the reactant's structure after the MM production run using PyMOL, retaining water molecules, ions, and box dimensions. The same protocol as for the reactants was followed to obtain the preferred PET benzene ring orientation and corresponding tryptophan–PET dihedral angle from the 20 ns production run, in which the CV distances were restrained to keep the two PET units adjacent to the broken ester bonds within the AE basin. As the overall conformation of PET was altered due to conformational changes of the remaining units of the long, flexible PET chain during the MM production run, the AE structure was subjected to the QM/MM preparation right after MM minimisation diminishing the MM equilibration and MM production run steps. This involved a QM/MM optimisation using steepest descent and conjugate gradient for both, reactant and AE. Only for the AE, a 50 ps QM/MM run was performed in the NVT ensemble applying a one-sided harmonic restraint to adjust the tryptophan–PET angle to the prevalent one during the MM production run. For the PES-H1 FY variant, this step was skipped as the preferred tryptophan–PET angle was already obtained after MM MD and was, thus, already existent after QM/MM optimisation. The last step before the actual ASM run comprised an unrestrained 50 ps QM/MM relaxation in the NVT ensemble reactant and AE. The QM region comprised 66 atoms, including the two PET units connected by the scissile ester bond, and the sidechains of the catalytic serine, histidine, and aspartate (Fig. 2). It was described by the DFTB3 method without using the SHAKE algorithm to allow for proton transitions.[58] The non-bonded cutoff was increased to 10 Å for minimisation and to 9,999 Å for relaxation.

bioRxiv preprint doi: https://doi.org/10.1101/2024.04.30.591886; this version posted April 30, 2024. The copyright holder for this preprint (which was not certified by peer review) is the author/funder, who has granted bioRxiv a license to display the preprint in perpetuity. It is made available under aCC-BY 4.0 International license.

2.3 ASM

The analysis of PET deacylation was conducted using the ASM, as implemented in AMBER.[38] The initial and final states for the pathway connecting the reactant and the AE in CV space were defined through QM/MM relaxation simulations. Five relevant distances describing the reaction and one dihedral representing the ring orientation change were employed as CVs, as well as two point-to-plane distances reflecting the hybridisation state of the PET ester's carbon to enhance convergence (Fig. 2). MD simulations were initiated from a total of 96 nodes, equidistantly positioned along the initial guess. Half of these simulations started from the reactant state, while the other half began from the AE state. The structures were brought to the corresponding node positions during 1 ps by gradually increasing the force constants from zero to the target value.

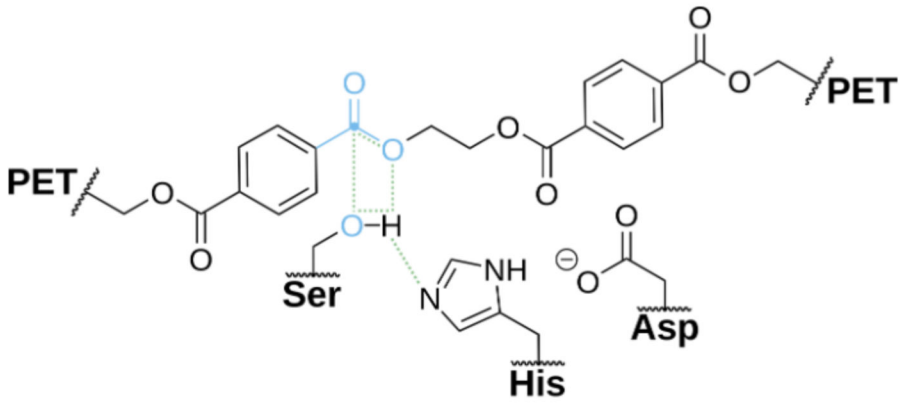


Figure 2: QM region and CVs employed in this study. The QM region includes two PET units connected via the scissile ester bond and the side chains of the three catalytic triad residues (PES-H1: S130, D176, H208; LCC: S165, D210, H242). The distance CVs are highlighted in green, and the point-to-plane CVs are in blue, with the PET ester's carbon corresponding to the point marked by a blue circle. The remaining atoms forming the plane include those in the ester between the PET units in the MC and the ester between PET and the catalytic serine in the AE, respectively. An additional dihedral CV is included, which is highlighted in figure 4.

bioRxiv preprint doi: https://doi.org/10.1101/2024.04.30.591886; this version posted April 30, 2024. The copyright holder for this preprint (which was not certified by peer review) is the author/funder, who has granted bioRxiv a license to display the preprint in perpetuity. It is made available under aCC-BY 4.0 International license.

Upon convergence of the string to the MFEP, a path-CV was defined, illustrating the progress along the MFEP and consequently, the advancement along the reaction. umbrella sampling MD (USMD) simulations[59,60] were then performed, restraining each replica to the corresponding node on the string for the US windows using an automatically defined potential. The PMF was obtained via umbrella integration (UI),[61–63] and assumed to be converged when the 95% confidence interval at the TS fell below 1 kcal·mol^{-1}.

2.4 DFT correction

The PMF obtained from the ASM runs was corrected to M06-2x/6-31+G(d,p) level of theory[64] by applying a cubic splines correction based on single point energy estimates for relaxed structures along the reaction path. Single-point calculations were carried out for the resulting optimised structures using the DFTB3 method and, additionally, the M06-2X functional[64] with the 6-31+G(d,p) basis set, employing the Gaussian 09 software.[39] The energy difference ($\Delta E = E_{DFT} - E_{DFTB3}$) was then interpolated and subtracted from the original PMF values to obtain the corrected PMF.

3 Results and Discussion

RC and AE prefer different PET ring orientations To conduct QM/MM simulations of PET acylation, we extracted starting structures of PET–enzyme complexes from Hamiltonian replica exchange MD (HREMD) simulations as detailed in our previous work.[14] These structures involved a PET chain with 5 units and either LCC or PES-H1. The initial configurations for the LCC^{IG} and PES-H1^{FY} variants were derived by introducing corresponding mutations to the WT enzymes, ensuring a consistent starting point for comparison. Analysis of the binding poses revealed that the PET units sharing the scissile ester bond are tightly bound, whereas units further away exhibit looser interactions with the enzyme. This contradicts assumptions of simultaneous binding of several PET units.[65]

bioRxiv preprint doi: https://doi.org/10.1101/2024.04.30.591886; this version posted April 30, 2024. The copyright holder for this preprint (which was not certified by peer review) is the author/funder, who has granted bioRxiv a license to display the preprint in perpetuity. It is made available under aCC-BY 4.0 International license.

Four resultant Michaelis complexes (MC)s underwent 20 ns MM simulations, confirming the stability of chosen binding poses. However, chain termini remained flexible (Fig. S1). The final structures served as templates to manually generate AE structures using PyMOL. Subsequently, they were subjected to 20 ns MM simulations with restraints to prevent the leaving group from diffusing away from the AE. Two notable findings emerged: Firstly, loosely bound PET units exhibited greater flexibility compared to those near the scissile ester bond, resulting in conformations unsuitable for subsequent QM/MM simulations using the ASM due to the difference to MC conformations (Fig. 3).

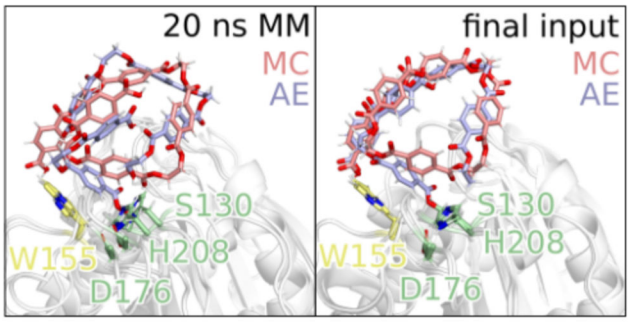


Figure 3: PET conformations of the MC (red) and AE (blue) for PES-H1 after 20 ns MM production run (left) with prior two-step equilibration and the final structures used as input for the ASM run (right). Here, an additional QM/MM optimisation and 50 ps relaxation followed the 20 ns production run for the MC. The AE was generated from the MC structure after 20 ns MM production run and subjected to MM minimisation, QM/MM optimisation and two 50 ps QM/MM simulations, of which the first included restraints to set the dihedral angle to that observed during the 20 ns MM production run while the second was performed without restraints to relax the structures prior to ASM.

Secondly, the benzene ring of PET bound to the catalytic serine in the AE demonstrated a preference for a parallel orientation with respect to the 'wobbling' tryptophan, whereas the MC favoured a T-stacked orientation. This transition from T-stacked to parallel π-π interactions was observed during MM minimisation (PES-H1^{FY}) and during the beginning (LCC, LCC^{IG}) or middle (PES-H1) of the MM production run. This shift, previously discussed by Han *et al.*[20] in the context of product liberation, was not specifically mapped to a reaction step. Our results suggest that this transition occurs during the acylation phase. To address these findings, we conducted MM minimisation for AE structures without equi-

bioRxiv preprint doi: https://doi.org/10.1101/2024.04.30.591886; this version posted April 30, 2024. The copyright holder for this preprint (which was not certified by peer review) is the author/funder, who has granted bioRxiv a license to display the preprint in perpetuity. It is made available under aCC-BY 4.0 International license.

libration or 20 ns production runs prior to QM/MM minimisation. This was followed by an additional 50 ps QM/MM run with restraints to enforce the transition of the benzene ring from T-stacked to parallel. However, using plane angles as restraints or CVs in the ASM run is currently not implemented. We therefore identified a dihedral angle that correlated well with the plane angle, serving both as a restraint in structure preparation and as a CV during ASM reaction simulation (Fig. 4). An angle of approximately 0° corresponds to a T-stacked orientation, while an angle of approximately 90° indicates a parallel orientation. After enforcing the preferred parallel plane–plane angle of the AE, both MC and AE structures, were subjected to a 50 ps QM/MM relaxation without restraints before conducting the final ASM run.

PET ring orientation change correlates with acylation To perform QM/MM calculations, we used the final MC and AE structures after 50 ps QM/MM relaxation as input configurations (Fig. S2). We employed the semi-empirical DFTB3 method[58] to describe the QM region, encompassing the side chains of catalytic residues (LCC and LCC^{IG}: S165, D210, H242; PES-H1 and PES-H1^{FY}: S130, D176, H208) and the two PET units sharing the scissile ester (Fig. 2). This QM method, successfully applied in previous studies in combination with ASM, offers a balanced trade-off between accuracy and computational demand.[16] Additionally, we corrected the PMF on DFT level using the M06-2X functional[64] with the 6-31+G(d,p) basis set, which has proven effective in QM/MM studies of PET hydrolases.[15,17] We used relevant distances depicting bond formations and breaking during the reaction as CVs, alongside two point-plane distances defining the hybridisation state of the PET ester's carbon, to enhance convergence.[16] Furthermore, we included the dihedral defining the plane angle change as a CV. Average values for each CV, as well as the plane angle were calculated for each node after the ASM string was converged (Fig. 5 and 6).

A smooth transition from approximately 0° (T-stacking) to approximately ±90° (parallel orientation) towards the ring plane of the 'wobbling' tryptophan was revealed, showing

bioRxiv preprint doi: https://doi.org/10.1101/2024.04.30.591886; this version posted April 30, 2024. The copyright holder for this preprint (which was not certified by peer review) is the author/funder, who has granted bioRxiv a license to display the preprint in perpetuity. It is made available under aCC-BY 4.0 International license.

good correlation with the plane angle change during the reaction. This smooth transition underscores the importance of including the plane angle change as a dihedral CV. As a proof of concept, we performed the same ASM calculation for PES-H1^{FY} without including the dihedral CV. Here, the dihedral for MC and AE was not fixed, allowing for more flexibility and a mixture of parallel and T-stacked conformations when approaching the product. This T-stacked conformation is adopted after 180° rotation, so that the PET ring atom defining the dihedral points away from the 'wobbling' tryptophan instead of towards it as in the MC (Fig. 7). Thus, the change in ring orientation happens even when it is not included in the CVs, highlighting the link between this change and the reaction.

The progression of the distance CVs in combination with the PMFs describes the course of the reaction and enables mapping the ring orientation change to a specific step (Fig. 5 and 6). The reaction mechanism matches that from previous works, suggesting a two-step acylation with the tetrahedral intermediate state a shallow minimum on the free energy surface.[15,17,22–25,30,32] Firstly, the catalytic histidine abstracts a proton from the catalytic serine, resulting in TS1. Then, the serine attacks the ester carbon, yielding the tetrahedral intermediate with its oxyanion stabilised by the oxyanion hole. The oxyanion is then converted back into a carbonyl oxygen by breaking the ester bond between the two PET units, generating a new oxyanion. The second transition state corresponds to the second proton transfer from the catalytic histidine to this oxyanion of the leaving group, liberating an alcohol and resulting in the AE. The steepest change of the plane and dihedral angles begins with the formation of the tetrahedral intermediate, and in the case of LCC^{IG}, starts after the second proton transfer, and is thus concerted with the acylation (Fig. 5 and 6). Comparing the PMF of the ASM runs with and without the dihedral CV shows that the barriers in the corrected PMFs are somewhat larger when the dihedral CV is not included, suggesting that the conformational change during reaction is energetically favourable, which is neglected when the corresponding CV is omitted (Fig. 7).

bioRxiv preprint doi: https://doi.org/10.1101/2024.04.30.591886; this version posted April 30, 2024. The copyright holder for this preprint (which was not certified by peer review) is the author/funder, who has granted bioRxiv a license to display the preprint in perpetuity. It is made available under aCC-BY 4.0 International license.

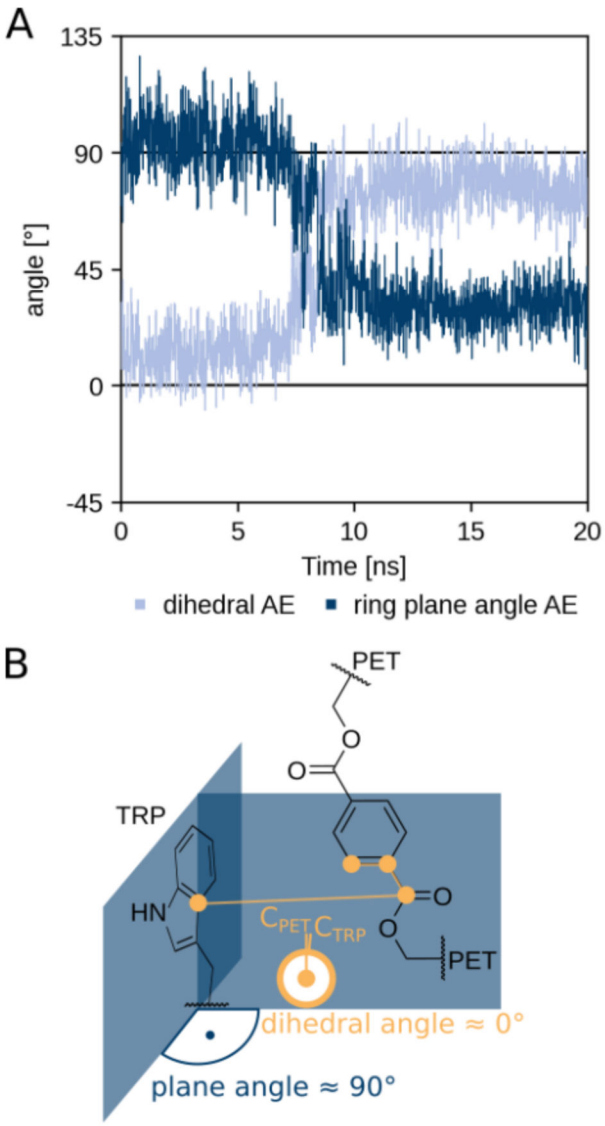


Figure 4: Dihedral angle and the angle between the tryptophan and PET ring planes during the 20 ns MM production run of the AE (lightblue, darkblue) of PES-H1 (A). The definition of the dihedral (orange) and the ring plane angles (blue) is highlighted schematically for the MC state preferring an approx. T-stacked orientation with a plane angle of approx. 90°, which correlates with a dihedral angle of approx. 0° (B).